TOPICS IN CURRENT CHEMISTRY 293

Volume Editor M. Schröder

Functional Metal-Organic Frameworks: Gas Storage, Separation and Catalysis

Springer

293

Topics in Current Chemistry

Topics in Current Chemistry

Recently Published and Forthcoming Volumes

Functional Metal-Organic Frameworks: Gas Storage, Separation and Catalysis
Volume Editor: Martin Schröder
Vol. 293, 2010

C-H Activation
Volume Editors: Jin-Quan Yu, Zhangjie Shi
Vol. 292, 2010

Asymmetric Organocatalysis
Volume Editor: Benjamin List
Vol. 291, 2010

Ionic Liquids
Volume Editor: Barbara Kirchner
Vol. 290, 2010

Orbitals in Chemistry
Volume Editor: Satoshi Inagaki
Vol. 289, 2009

Glycoscience and Microbial Adhesion
Volume Editors: Thisbe K. Lindhorst, Stefan Oscarson
Vol. 288, 2009

Templates in Chemistry III
Volume Editors: Broekmann, P., Dötz, K.-H., Schalley, C.A.
Vol. 287, 2009

Tubulin-Binding Agents: Synthetic, Structural and Mechanistic Insights
Volume Editor: Carlomagno, T.
Vol. 286, 2009

STM and AFM Studies on (Bio)molecular Systems: Unravelling the Nanoworld
Volume Editor: Samorì, P.
Vol. 285, 2008

Amplification of Chirality
Volume Editor: Soai, K.
Vol. 284, 2008

Anthracycline Chemistry and Biology II
Mode of Action, Clinical Aspects and New Drugs
Volume Editor: Krohn, K.
Vol. 283, 2008

Anthracycline Chemistry and Biology I
Biological Occurence and Biosynthesis, Synthesis and Chemistry
Volume Editor: Krohn, K.
Vol. 282, 2008

Photochemistry and Photophysics of Coordination Compounds II
Volume Editors: Balzani, V., Campagna, S.
Vol. 281, 2007

Photochemistry and Photophysics of Coordination Compounds I
Volume Editors: Balzani, V., Campagna, S.
Vol. 280, 2007

Metal Catalyzed Reductive C–C Bond Formation
A Departure from Preformed Organometallic Reagents
Volume Editor: Krische, M.J.
Vol. 279, 2007

Combinatorial Chemistry on Solid Supports
Volume Editor: Bräse, S.
Vol. 278, 2007

Creative Chemical Sensor Systems
Volume Editor: Schrader, T.
Vol. 277, 2007

In situ NMR Methods in Catalysis
Volume Editors: Bargon, J., Kuhn, L.T.
Vol. 276, 2007

Functional Metal-Organic Frameworks: Gas Storage, Separation and Catalysis

Volume Editor: Martin Schröder

With Contributions by

M. Banerjee · N. R. Champness · A. I. Cooper · S. Das · R. A. Fischer · J.-X. Jiang · K. Kim · S. Kitagawa · W. Lin · X. Lin · L. Ma · V. Mugnaini · N. Roques · F. Schröder · M. Schröder · T. Uemura · J. Veciana · M. Yoon

Springer

Editor
Prof. Dr. Martin Schröder
University of Nottingham
Faculty of Science
School of Chemistry
University Park
NG7 2RD Nottingham
United Kingdom
m.schroder@nottingham.ac.uk

ISSN 0340-1022 e-ISSN 1436-5049
ISBN 978-3-642-14612-1 e-ISBN 978-3-642-14613-8
DOI 10.1007/978-3-642-14613-8
Springer Heidelberg Dordrecht London New York

Library of Congress Control Number: 2010933723

Cover design: WMXDesign GmbH, Heidelberg, Germany

Printed on acid-free paper

Springer is part of Springer Science+Business Media (www.springer.com)

Volume Editor

Prof. Dr. Martin Schröder

University of Nottingham
Faculty of Science
School of Chemistry
University Park
NG7 2RD Nottingham
United Kingdom
m.schroder@nottingham.ac.uk

Editorial Board

Topics in Current Chemistry Also Available Electronically

Topics in Current Chemistry is included in Springer's eBook package *Chemistry and Materials Science*. If a library does not opt for the whole package the book series may be bought on a subscription basis. Also, all back volumes are available electronically.

For all customers who have a standing order to the print version of *Topics in Current Chemistry*, we offer the electronic version via SpringerLink free of charge.

If you do not have access, you can still view the table of contents of each volume and the abstract of each article by going to the SpringerLink homepage, clicking on "Chemistry and Materials Science," under Subject Collection, then "Book Series," under Content Type and finally by selecting *Topics in Current Chemistry*.

You will find information about the

– Editorial Board
– Aims and Scope
– Instructions for Authors
– Sample Contribution

at springer.com using the search function by typing in *Topics in Current Chemistry*.

Color figures are published in full color in the electronic version on SpringerLink.

Aims and Scope

The series *Topics in Current Chemistry* presents critical reviews of the present and future trends in modern chemical research. The scope includes all areas of chemical science, including the interfaces with related disciplines such as biology, medicine, and materials science.

The objective of each thematic volume is to give the non-specialist reader, whether at the university or in industry, a comprehensive overview of an area where new insights of interest to a larger scientific audience are emerging.

Thus each review within the volume critically surveys one aspect of that topic and places it within the context of the volume as a whole. The most significant developments of the last 5–10 years are presented, using selected examples to illustrate the principles discussed. A description of the laboratory procedures involved is often useful to the reader. The coverage is not exhaustive in data, but rather conceptual, concentrating on the methodological thinking that will allow the non-specialist reader to understand the information presented.

Discussion of possible future research directions in the area is welcome.

Review articles for the individual volumes are invited by the volume editors.

In references *Topics in Current Chemistry* is abbreviated *Top Curr Chem* and is cited as a journal.

Impact Factor 2009: 4.291; Section "Chemistry, Multidisciplinary": Rank 20 of 138

Preface

The study of metal–ligand coordination polymers, also termed metal-organic frameworks (MOFs) and porous coordination compounds (PCPs), is a field of research that has risen rapidly over recent years to the forefront of modern chemistry and materials science. The field has grown out of coordination chemistry through supramolecular chemistry and crystal engineering to the discovery of porous hybrid materials via the design and implementation of new synthetic strategies, and of structural, theoretical, and topological analysis and modeling. A range of new fascinating porous materials showing specific and unprecedented properties and function are now emerging.

This volume focuses on recent advances in research on porous framework materials covering chiral separations, catalysis and activation, fuel gas storage and capture, reactivity in porous hosts, and magnetism. The control of chemistry within confined, nanoscale environments is an expanding platform technology for the future, which will be vital for the delivery of new sustainable processes, energy portals, and healthcare. Synthesis and materials design has never been more important.

Nottingham, Summer 2010 Martin Schröder

Contents

Top Curr Chem (2010) 293: 1–33
DOI 10.1007/128_2009_5

Published online: 01 September 2009

Microporous Organic Polymers: Design, Synthesis, and Function

Jia-Xing Jiang and Andrew I. Cooper

Abstract Microporous organic polymers (MOPs) can be defined as materials with pore sizes smaller on average than 2 nm which are comprised of light, non-metallic elements such as C, H, O, N, and B. We describe here the main classes of MOPs which are conveniently sub-divided into amorphous and crystalline groups. We present an overview of the synthesis of these materials, along with some general design criteria for producing MOPs with high surface areas and micropore volumes. The advantages and disadvantages of MOPs with respect to inorganic materials such as zeolites and hybrid materials such as metal organic frameworks are discussed throughout, particularly in terms of practical applications such as catalysis, separations, and gas storage. We also discuss future opportunities in this area as well as the potential to unearth "undiscovered" MOPs among the large number of rigid backbone polymers and networks reported in the literature.

Keywords Microporous • Nanoporous • Networks • Polymers

Contents

Jia-Jiang and A.I. Cooper (✉)
Department of Chemistry and Centre for Materials Discovery, University of Liverpool, Crown Street, Liverpool, L69 3BX, UK
e-mail: aicooper@liv.ac.uk

Abbreviations

BET	Brunauer-Emmett-Teller
CMP	Conjugated microporous polymer
COF	Covalent organic framework
HCP	Hypercrosslinked polymer
MOF	Metal organic framework
MOP	Microporous organic polymer
PAE	Poly(aryleneethynylene)
PIM	Polymer of intrinsic microporosity
PPB	Poly(phenylene butadiynylene)
PPV	Polyphenylenevinylene
ZIF	Zeolitic imidazolide framework

1 Introduction

Microporous materials are important in a wide range of applications such as catalysis and separation science [1]. They can exhibit very high physical surface areas and the pores have dimensions that are comparable to small molecules. There are several well-known classes of microporous material [1] including zeolites, activated carbons, silica, and metal organic frameworks (MOFs) – the latter of which is the main focus of this volume [2–5]. In this chapter, we will discuss the design, synthesis, and function of microporous organic polymers (referred to hereafter as "MOPs"). We define "organic" polymers broadly as materials, which are composed predominantly of light, non-metallic elements such as carbon, hydrogen, boron, and nitrogen. We do not include (other than for comparison) metal-based species (e.g. MOFs) [2–5], although we do discuss phthalocyanine and porphyrin networks (Sect. 2.2.3). Microporous inorganic materials such as silica, metal oxides, and

zeolites, are not covered; neither are "hybrid" materials such as polysilsesquioxanes [6]. We will restrict the discussion to microporous polymers following the current IUPAC definition – that is, materials with pores that are mostly smaller than 2 nm in diameter. Moreover, this review is focused on materials with interconnected porosity, which are *physically accessible* to other molecules and can be measured, for example, by gas sorption analysis. This contrasts with the closed porosity and channel structures found in supramolecular organic structures and some crystalline polymers [7]. A summary of the main types of MOPs and their typical properties is given in Table 1.

Unambiguous classification is challenging for MOPs, even when the subject is delineated as above. We have divided materials into amorphous (Sect. 2) and crystalline (Sect. 3) groups since this distinction is clear-cut. Within amorphous MOPs, classification is more problematic and several "classes" overlap. For example, many network-type MOPs may be classified in principle as "hypercrosslinked," although this term has been confined in the literature to only a few polymers (Sect. 2.1).

1.1 Advantages of MOPs

MOPs have a range of potential advantages for specific applications. There are also a number of challenges in terms of developing and improving the properties of MOPs. As such, this is a fertile area of research for synthetic chemists, materials chemists, and researchers working in diverse areas such as energy storage, separation science, catalysis, and sensor technology.

1.1.1 Synthetic Diversity

Perhaps the main potential advantage of MOPs is the synthetic diversity that is possible. First, a very wide range of synthetic polymer methodologies has been developed, many of which can be adapted to the synthesis of MOPs. Examples of chemistry used to generate MOPs includes Friedel–Crafts alkylation [8], dibenzodioxane formation [9], imidization [10], amidation [10], Sonagashira–Hagihara cross-coupling [11] and homocoupling [12], Gilch coupling [13], boroxine- and boronate-ester formation [14], and nitrile cyclotrimerization [15]. Second, there is enormous scope for polymer post-modification to introduce specific chemical functionalities. This is possible because most MOPs are quite chemically and thermally stable (Sect. 1.1.2). They can therefore be handled and derivatized under standard wet chemical conditions without problems such as framework degradation or loss of microporosity. Indeed, most of the combinatorial chemistry developed for resin-based supports may be translated to MOPs, although some limitations could arise in terms of size exclusion of bulky reagents, particularly for ultramicroporous MOPs (pore sizes < 0.7 nm).

Table 1 Types of MOPs and summary of key properties

	Apparent BET SA ($m^2 g^{-1}$)	Micropore volume ($cm^3 g^{-1}$)	Stability	Special features	Key references
Hypercrosslinked polymers (HCPs; Sect. 2.1)	330–2,090	>0.5	Both thermal and chemical stability high	Swelling in non-solvents for network	[8, 21, 22, 24, 25, 31, 33, 34]
Polymers of intrinsic microporosity (PIMs; Sect. 2.2)	500–1,064	[a]	Both thermal and chemical stability high	Linear PIMs are solution-processable	[9, 46]
Phthalocyanine and porphyrin networks (Sect. 2.2.3)	450–1,000	Up to 0.29	Both thermal and chemical stability high	Networks can bind metals	[50, 51]
Conjugated microporous polymers (CMPs; Sect. 2.3)	512–1,018	0.16–0.38	Both thermal and chemical stability high	Conjugated nature; tunable pore sizes	[11–13, 19, 63]
Covalent organic frameworks (COFs; Sect. 3.1)	711–4,210	0.32–1.66[b]	High thermal stability; porosity sensitive to air for B-containing COFs	Highest MOP surface areas; crystalline; tunable pores	[14, 20, 67]
Triazine frameworks (Sect. 3.2)	584–2,475	0.29–2.44[c]	Both thermal and chemical stability high	Substantial crystallinity; stability	[15]

[a]Not generally reported; PIM-1 has a total pore volume of 0.78 $cm^3 g^{-1}$ at $P/P^0 = 0.99$;[9]

[b]COF-8–COF-10 are mesoporous [67]

[c]Again, these are total pore volumes at $P/P^0 = 0.99$ – micropore volumes are presumably smaller

1.1.2 Chemical and Physical Stability

The very high physical surface area exhibited by microporous materials is the key to many applications; but this also presents a potential challenge in terms of stability. For example, surface degradation reactions are greatly accelerated in a material that is "all surface." Some microporous materials such as activated carbon have very good thermal and chemical stability but there is relatively limited scope for synthetic diversification (Sect. 1.1.1). Zeolites can be extremely stable thermally but may be degraded (or indeed dissolved) under certain chemical conditions. Reports suggest that MOFs have widely varying chemical stability: some materials lose porosity on brief exposure to air, while others are reported to be quite stable under standard atmospheric conditions for extended periods. Zeolitic imidazolide frameworks (ZIFs) [16, 17] are stable even towards harsh chemical conditions.

The chemical and thermal stability of MOPs are also variable. In general, though, organic main-chain aromatic polymers have very good chemical stability and moderate-to-good thermal stability. For example, hypercrosslinked polymers (HCPs) (Sect. 2.1), polymers of intrinsic microporosity (PIMs) (Sect. 2.2), and conjugated microporous polymers (CMPs) (Sect. 2.3) all tend to be stable, for example, to acids and bases. These materials also exhibit quite good thermal stability, although less so than inorganic materials such as silica. Covalent organic frameworks (Sect. 3) based on boroxines show good thermal stability but porosity has been reported to be degraded by exposure to air [18].

1.1.3 Cost and Scalability

Some MOPs – for example, HCPs (Sect. 2.1) – are relatively low cost and have already been commercialized. It does not follow however, that MOPs are in general less expensive than "exotic" materials such as MOFs, some of which are synthesized from fairly inexpensive metal salts and organic linkers. For example, most of the monomers used to synthesize the CMPs developed in our laboratory [11, 12, 19] (Sect. 2.3) are expensive, as is the palladium catalyst used for the coupling chemistry. As such, cost must be appraised in terms of specific technical benefit on a case-by-case basis. In general, organic polymers are a well-proven and scalable technology. Cost is unlikely to be totally prohibitive for all MOPs, particularly in cases where unique molecular function can be achieved to distinguish these materials from cheaper high surface area materials.

1.2 Challenges

In addition to numerous advantages, MOPs present a range of challenges. So far few organic polymers have been synthesized which match the highest micropore volumes and surface areas exhibited by MOFs (apparent BET surface areas $>4{,}000\ m^2 g^{-1}$),

although boroxine- and boronate-ester-linked COFs [14, 20], in particular, show strong promise in this regard. Some MOPs are relatively expensive (Sect. 1.1.3). An associated problem is environmental impact, since most organic polymer chemistry are carried out using volatile organic solvents. Likewise, atom economy is low for some MOP chemistries – for example, the Friedel–Crafts alkylation route used to generate HCPs [8, 21, 22] (Sect. 2.1) uses non-catalytic concentrations of $FeCl_3$ and produces HCl as the condensate molecule. From a longer-term "life cycle" perspective, the environmental degradability of the aromatic units that comprise most MOPs is poor, although this may also apply to aromatic MOFs, for example. A significant challenge in developing ordered crystalline MOPs (Sect. 3) is to identify covalent linking chemistries that are sufficiently reversible to form structures under thermodynamic control (Sect. 1.3.3) while generating stable and robust microporous structures.

1.3 Design Rules for MOPs

Although it is difficult to formulate generic "design rules" for MOPs, a number of criteria are clearly important in terms of producing polymers with high physical surface areas and interconnected micropore structures.

1.3.1 Polymer Rigidity and Free Volume

All organic polymers exhibit free volume – that is, molecular spaces between polymer chains – to a greater or lesser degree [23]. However, with the exception of certain ultra-high free volume polymers such as poly(1-trimethylsilyl-1-propyne) and PIMs [9] (Sect. 2.2), the vast majority of linear polymers do not exhibit sufficient interconnected free volume to be classified as permanently microporous. Network-type or "crosslinked" organic polymers can exhibit permanent microporosity but this is not generic; it is easy to synthesize organic polymer networks which are entirely non-porous. In general, both linear PIMs and network polymers must be composed of rigid molecular linkers in order to "lock in" microporosity in the dry state. A good example of this can be found in HCPs (Sect. 2.2): linear polystyrene crosslinked with chloromethyl methyl ether or tris-chloromethyl mesitylene was found to exhibit an apparent BET surface area of >1,000 $m^2 g^{-1}$, while comparable materials crosslinked using a more flexible linker, bischloromethyl diphenylbutane, were non-porous [21]. Likewise, linear PIMs (Sect. 2.2.1) exhibit permanent microporosity as a function of both their rigid polymer backbones and the contorted structures (for example, introduced via spiro linkages) [9], which prevent the chains from packing efficiently in the solid state. A degree of molecular rigidity is generally necessary to expect permanent microporosity in organic polymers, whether they be ordered or disordered (Sect. 1.3.2), linear or networks. There are no fixed

rules, however, about what constitutes a sufficiently rigid covalent bond. Rigid aromatic groups are clearly advantageous, as found for MOFs; and most MOPs reported thus far are aryl-type polymers. Boroxines [14, 20] (Sect. 3.1) and triazine units [15] (Sect. 3.2) are also rigid and impose a planar 1,3,5-geometry. Examples of aliphatic linkages in MOPs all tend to have low conformational flexibility – for example, methylene, tetraphenylmethane [24], and triphenylmethanol [24] (Sect. 2.2). In our laboratory, we have exploited aryleneethynylene [11] and butadiynylene [12] linkers (Sect. 2.4). These units are quite rigid although there is significant conformational freedom in terms of rotation about the alkyne bond.

1.3.2 Order Versus Disorder

There are two broad classes of MOPs – disordered, amorphous MOPs (Sect. 2.2–2.5) and ordered, crystalline MOPs (Sect. 3). The nature of the covalent bond-forming chemistry tends to govern possibilities here. Crystalline MOPs will in general, necessitate chemistry that is reversible to allow ordered, thermodynamic products to be accessed. Examples of this include boroxine- and boronate-ester formation [14, 20] and nitrile cyclization [15]. Irreversible chemistry – for example, Sonagashira–Hagihara cross-coupling [11, 19] – will tend to produce amorphous, kinetic products, at least in the absence of very strong templating which could in principle direct such chemistry to give crystalline MOPs. This situation is unsymmetrical; reversible bond-forming chemistry might produce amorphous, kinetic-product MOPs under certain reaction conditions, whereas it is harder to conceive conditions where irreversible chemistry forms ordered, crystalline MOPs.

It cannot be said that one particular strategy – order versus disorder – is "better" than the other, and the choice will depend on the desired application. There are a number of potential advantages for crystalline MOPs. Structural uniformity makes it possible to design materials with very narrow pore size distributions and thus, conceivably, gain some of the advantages associated with zeolites [1] – for example, molecular specificity in catalysis. Crystalline MOPs can also be characterized structurally at the molecular level by X-ray diffraction [14, 15, 20] in a manner that is not possible for amorphous materials. At the time of writing, the highest apparent BET surface areas reported for MOPs (up to 4,210 $m^2 g^{-1}$) were found for ordered, crystalline COFs [20].

Given the advantages of crystalline MOPs, why, then, would one consider disordered systems? First, there are properties and functions that cannot currently be accessed with ordered crystalline materials. For example, linear PIMs [9] (Sect. 2.2) can be cast from solution to form microporous membranes for gas separation, which have good mechanical properties. High surface area *conjugated* MOPs [11–13, 19] may be useful in a range of electronic and optoelectronic applications, but the chemistry employed to prepare conjugated polymers is usually irreversible. Thus, crystalline conjugated MOPs may be hard to access, although this is certainly a very interesting challenge. The highest apparent BET surface areas reported thus far for amorphous MOPs are exhibited by hypercrosslinked materials (>2,000 $m^2 g^{-1}$) [25]. Molecular

simulations in our laboratory suggest that much higher surface areas are in theory possible for amorphous MOPs and that *density* is the primary limiting factor. That is, the highest surface area COFs [14, 20] (and MOFs) exhibit lower densities and higher pore volumes than are typically observed in amorphous MOPs. In principle, better molecular design and more sophisticated templating strategies may allow the formation of amorphous MOPs with less chain interpenetration and higher micropore volumes (Sect. 1.3.3). Pore size is harder to control precisely in most amorphous MOPs because the average pore size is statistically related to the chemical structure rather than defined crystallographically.. We have shown recently, however, that fine synthetic control over pore size can be achieved for poly(aryleneethynylene) (PAE) networks (Sect. 2.3) [11, 19]. Amorphous MOPs may have stability advantages in some applications by virtue of the irreversible covalent bond-forming reactions used to generate these materials. It is not a coincidence, for example, that the most synthetically-versatile microporous MOF [2] and COF [14, 20] routes give rise to high surface area materials where chemical lability and physical stability are potential practical issues. To achieve the best of both worlds – that is, the molecular design of highly-robust, high surface area MOPs – remains a difficult synthetic challenge.

1.3.3 Templates and Porogens

The role of solvent and other additives in pore formation in MOPs is likely to be very important but is poorly understood. Templating effects are commonly invoked for microporous MOFs and similar considerations would apply to crystalline microporous COFs [14, 20], for example. Likewise, the influence of solvents and other species as "porogens" in porous polymer synthesis is well-known [26] but mostly understood at a qualitative level. Indeed, there is relatively little detailed information to hand for MOPs and this issue requires further attention.

Solvent porogen effects for macroporous resins are often explained in terms of the degree of solvation imparted to the incipient polymer network, the point at which phase separation takes place, and the resultant degree of "in filling" between primary particles [26]. This may play a role in some amorphous MOPs (for example, micro/mesoporous PPV [13]); however other systems such as HCPs (Sect. 2.1) do not undergo phase separation in this way [21, 22]. This basic mechanistic difference also accounts for the apparent independence of surface area on monomer concentration for conjugated microporous PAE networks [19], for example, in comparison with macroporous polymer resins where surface area may be strongly concentration dependent.

A few MOPs – for example, linear PIMs [9] – can be dissolved and precipitated an indefinite number of times from a range of solvents. As we know, the effect of changing solvent or drying time on micropore properties has not been reported in detail.

The solvothermal conditions used to synthesize boroxine- and boronate-ester COFs (temperature, solvent, solvent-to-head-space ratio) have a strong effect on the product morphology [14, 20] and it seems that particular solvents give rise to ordered crystalline materials whereas others do not. In principle, this may be understood in terms of templating effects but could equally arise from differences in monomer solubility, for example, which in turn affects the rate of network formation.

Triazine-based networks have been produced under ionothermal conditions in molten $ZnCl_2$, followed by extraction of residual salt from the materials [15]. It is certainly possible that the salt acts here as a template for pore formation; indeed, $ZnCl_2$ has been used previously as a "porogen" for the formation of activated carbon [27–29].

1.3.4 Molecular Simulations for MOPs

It is desirable to use molecular simulations to design new MOPs with particular properties. There are two interrelated strategies – predictive simulations (to anticipate wholly new structures) and explanatory simulations (to rationalize the properties of materials that have been synthesized).

Truly predictive simulations are challenging for both amorphous and crystalline MOPs. For amorphous materials, it is very difficult to simulate *ab initio* the density of a disordered MOP network. Pore sizes and surface areas are highly dependent on small changes in simulated density. As such, a major challenge exists in accurately predicting micropore properties for amorphous MOPs, even if one can simulate precisely the polymer network growth mechanism and underlying chemistry (in itself a non-trivial task). The scope of predictive simulation for ordered, crystalline MOPs is rather greater, although again numerous difficulties exist. For example, it may be hard to establish whether a putative ordered MOP structure is more stable than, for example, an alternative catenated and non-porous form.

Explanatory simulations are more readily achieved, particularly for ordered materials such as MOFs. For example, it was shown recently that calculated geometric surface areas for MOFs agree well with both simulated and actual BET surface areas [30]. Geometric surface areas can be calculated simply and quickly in comparison with BET surface areas derived from Grand Canonical Monte Carlo (GCMC) gas sorption simulations. This simple geometric approach may therefore be widely applicable as an in silico screening tool for the design of COFs (Sect. 3) and other crystalline MOPs, so long as an appropriate surface is defined – that is, an accessible surface, as opposed to a Connolly surface. Simulations for known amorphous MOPs are again more problematic and there are relatively few examples in the literature [31]. Micropore volumes (and hence densities) can be determined with some precision by gas sorption; as such, it is possible to set a "target" density for simulations, thus addressing one of the most important variables in terms of predicting micropore volume. It is clear, however, that identical simulated densities can be obtained for materials with very different pore connectivities and, hence, different simulated accessible pore volumes and surface areas. An example of a molecular simulation for a hypercrosslinked polydichloroxylene network is shown in Fig. 1.

For the few soluble, linear MOPs which exist (i.e. PIMs [9], Sect. 2.2), it should be possible to define chemical structures with good fidelity within simulations, although the quantitative representation of molecular weight distribution requires some thought. Amorphous network-type MOPs such as HCPs present a range of challenges. Most significantly, it is difficult to build a single, unambiguous model of the covalent network structure, even when high-quality solid state ^{13}C NMR data are obtained. For example, we have simulated the micropore structure for

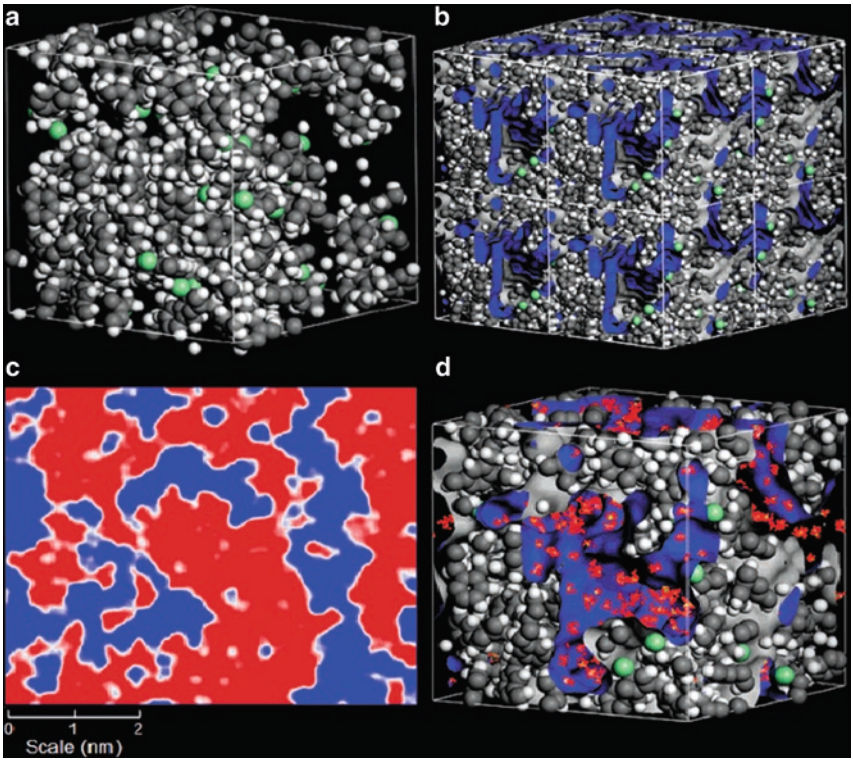

Fig. 1 Molecular simulation of a microporous hypercrosslinked polydichloroxylene network (**a**–**c**) and simulation of hydrogen sorption within the micropores (**d**) [31]. This model simulates properties such as pore volume, density, and average pore size quite well. Hydrogen sorption is overestimated by the simulation shown in (**d**) because a Connolly surface, rather than a solvent accessible surface [30], is used to calculate the H_2 uptake

polyxylylene materials [31] based on a combination of measured pore volumes, solid state ^{13}C NMR data, and elemental analysis (Fig. 1); but even with this range of data it is only possible to define average atomic connectivities and substitution patterns for the polyxylylene network.

2 Amorphous Microporous Polymers

2.1 Hypercrosslinked Polymers

Permanently porous vinyl polymer resins – for example, as produced from styrene/divinylbenzene – are well-known and are used for ion exchange applications and as supports for various reagents and catalysts [26]. These materials are often mesoporous

or macroporous (pore sizes >2 nm) and have a relatively broad pore size distributions. We do not therefore define these materials as MOPs, although resins have been produced with significant microporosity and surface areas up to around 1,000 $m^2 g^{-1}$. (The term "macroporous" here is used in the non-IUPAC sense of "permanently porous in the dry state," although to confuse matters further, macroporous resins do often exhibit IUPAC-style macroporosity with pore sizes of >50 nm [26]) HCPs are in most cases predominantly microporous and tend to exhibit Type I gas sorption isotherms. HCPs can be produced in two ways – by intermolecular and intramolecular crosslinking of preformed polymer chains (either linear chains or lightly crosslinked gels), and by direct step growth polycondensation of suitable monomers.

2.1.1 HCPs by Post-Crosslinking of Polymers

The most well-known HCPs derived from polystyrene (or related polymers) are produced by extensive crosslinking via Friedel–Crafts alkylation [8]. Tsyurupa and Davankov [21, 22] have reviewed this class of material in depth and only the main features will be described here. In the simplest case, linear polystyrene is extensively crosslinked with a crosslinking agent such as monochlorodimethyl ether (MCDE) which contributes a methylene bridge between two chains, or intramolecularly within a single chain [32]. Extensive single-phase crosslinking occurs in the presence of a solvating medium (Sect. 1.3.4.), to generate a relatively uniform network, which cannot collapse into a non-porous state upon removal of the solvent. Hypercrosslinked polystyrene has been studied by SEM, TEM and X-ray diffraction and there is no indication of heterogeneity; it is therefore likely to be a homogeneous, single-phase material, quite unlike the macroporous polymer resins referred to above [26]. The same approach can be applied to solvent-swollen, lightly crosslinked styrene–divinylbenzene gels, and the methylene bridge can be "built in" to the prepolymer – for example, by using poly(chloromethyl styrene) linear homopolymer or gel [25, 33–36]. The molecular structure of these materials is complicated; depending on the chemistry, a variety of crosslinks can be introduced including both single and double methylene bridges [37] (Fig. 2).

Solid state ^{13}C NMR is the method of choice for elucidating these structures [33, 37] but it is quite difficult to determine anything more precise than average ring-substitution patterns for such polymers.

Apparent BET surface areas for hypercrosslinked polystyrenic materials can be as high as 2,090 $m^2 g^{-1}$ in some cases [25] and these materials can be produced as monoliths, powders, suspension polymerized beads, or by surfactant-free emulsion polymerization as spherical particles with diameters of around 500 nm [35]. Some care must be exercised when interpreting gas sorption isotherms for HCPs using sorbates such as nitrogen and argon as they exist in a "non-classical" [38] physical state and can exhibit unusual swelling characteristics (Fig. 3).

For example, hypercrosslinked polystyrene swells significantly in non-solvents for the equivalent linear polymer (e.g. water, methanol [21]) and, conceivably, can

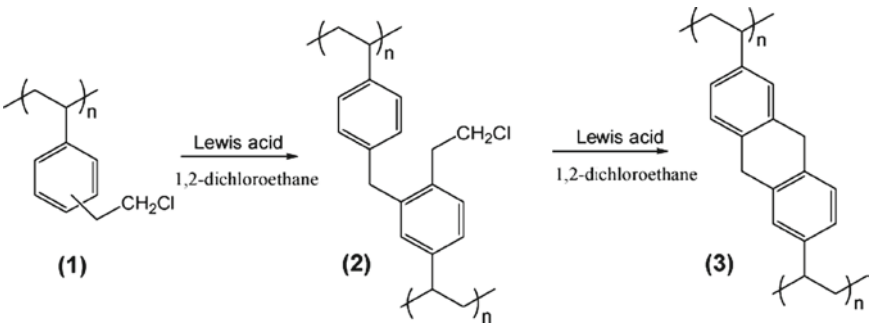

Fig. 2 Formation of a hypercrosslinked network by Friedel–Crafts alkylation. A simplified scheme is shown [25]; in reality, a diverse range of crosslinks, macrocycles (also Fig. 3) and end groups can exist in these networks [25, 31]

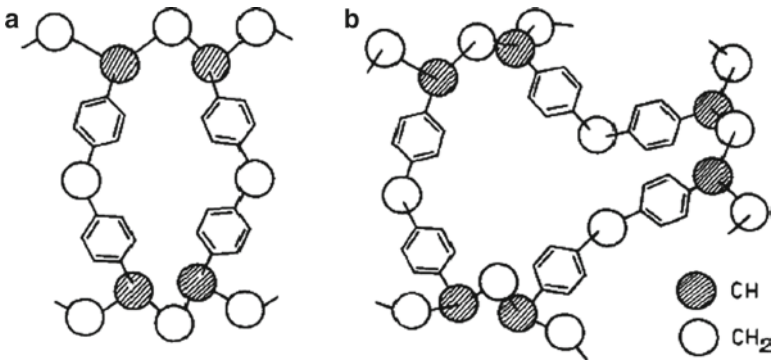

Fig. 3 Schematic representation of a stressed (**a**) and unstressed (**b**) macrocycle in a hypercrosslinked polystyrene network [8]. The cooperative conformational rearrangement of a large ensemble of such macrocycles may allow the substantial swelling observed for these networks in a wide range of solvents

also swell in liquid nitrogen or dense argon. This property may be exploited in principle for the storage of gases such as methane (Sects. 4.3 and 5.3) [39].

2.1.2 HCPs by Direct Polycondensation

HCPs have also been produced by the direct polycondensation of small molecule monomers (Fig. 4). Polyxylene networks – for example, produced from dichloroxylene (DCX) [21, 31] – are analogous to the Friedel–Crafts linked polystyrene materials described in Sect. 2.1.1 and can exhibit apparent BET surface areas up to 1,431 $m^2 g^{-1}$ [31].

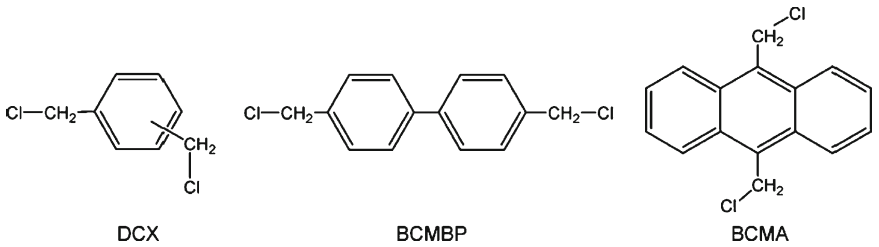

Fig. 4 Three bischloromethyl monomers used for the preparation of HCPs by direct polycondensation [31]. Monomer BCMBP gave rise to the highest surface area materials (>1,900 $m^2 g^{-1}$)

We have shown that similar networks formed from bis(chloromethyl)biphenyl (BCMBP) exhibit surface areas as high as 1,904 $m^2 g^{-1}$ [31]. Webster and coworkers have prepared HCPs by treating 4,4′-dilithiobiphenyl (as well as other multi-lithiated aromatic compounds) with dimethylcarbonate to generate polymeric carbinol networks with surface areas of 400–1,000 $m^2 g^{-1}$ [24]. More recently, polysilane "element–organic frameworks" was synthesized via a lithiation route to yield microporous networks with BET surface areas in the range 780–1,046 $m^2 g^{-1}$ [40].

2.2 *Polymers of Intrinsic Microporosity*

For the purposes of this review, we restrict the definition of PIMs to organic polymers which have interconnected pore structures and which exhibit appreciable apparent inner surface areas by gas sorption analysis. PIMs can be linear polymers (Sect. 2.2.1) or networks (Sect. 2.2.2). While other network polymers may be microporous (e.g. Sect. 2.1 and 2.4), it is this porosity of the linear analogues that distinguishes PIMs. Again, the area of PIMs has been reviewed quite recently [41, 42] so relatively brief details are given here.

2.2.1 Soluble, Linear PIMs

A unique advantage of PIMs is the ability to prepare linear polymers which are solution-processable and microporous in the dry state when cast as films [9, 43]. This gives rise to a range of potential applications, particularly in areas such as gas separation (Sect. 4.2.2), where thin films and high gas flux are desirable. Most PIMs have been synthesized via a highly efficient dibenzodioxane-forming reaction using bis catechol type monomers; the structure of PIM-1 is shown in Fig. 5 [9]. Analogous soluble PIMs were formed from bis(phenazyl) monomers [44]. Soluble spirobifluorene-linked polyamides and polyimides have also been shown

to exhibit microporosity (BET surface areas up to 550 $m^2 g^{-1}$) [10]. Limited gas sorption was observed in hyperbranched thermosetting poly(imide-ester)s although the sorption isotherms presented (N_2 and CO_2) did not suggest a high degree of microporosity [45].

2.2.2 Insoluble PIM Networks

Insoluble PIM networks can also be produced using similar chemistries [46–48]. By and large, these materials exhibit higher surface areas than their linear counterparts (up to 1,065 $m^2 g^{-1}$) [48], as evidenced, for example, by larger hydrogen storage capacities (Sect. 4.3.1). This is most likely due to greater retention of micropore volume because of their highly linked covalent network structures. Three-connected branching monomers used to create these PIM networks include hexaazatrinaphthalyene (HATN) [47], cyclotricatechylene (CTC) [46], and 9,10-diethyl-2,3,6,7,12,13-hexahydroxytriptycene (Trip) [48] (Fig. 5). Significant sorption hysteresis was observed for N_2 with some of these networks – most notably the Trip-based PIM [48]. This suggests activated sorption occurs [48] either due to network swelling (c.f., discussion for HCPs, Sect. 2.1) or restricted access of N_2 molecules to narrow pore openings (i.e. a degree of kinetic trapping).

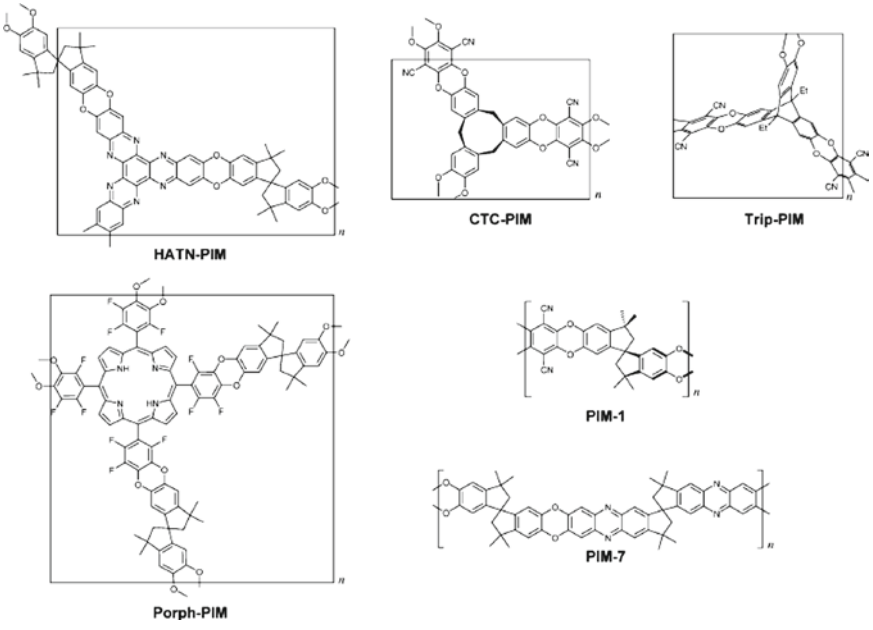

Fig. 5 Molecular repeat unit structures for various linear, soluble PIMs (PIM-1, PIM-7) and insoluble PIM networks (HATN-PIM, CTC-PIM, Trip-PIM, Porph-PIM) [79]

2.2.3 Phthalocyanine and Porphyrin Networks

Phthalocynanine-containing polymers are well-known [49]; but till relatively recently, phthalocynanine-containing network polymers were generally rendered non-porous by strong non-covalent π-π stacking between sub-units. The introduction of contorted spiro centres allowed the preparation of phthalocynanine networks with BET surface areas in the range 500–1,000 $m^2 g^{-1}$ (Fig. 6) [41, 50]. These materials also demonstrated marked gas sorption hysteresis [50]. In the same study, dioxane-linked porphyrin network PIMs were produced with high BET surface areas (900–1,100 $m^2 g^{-1}$) [51]. An important aspect of these network polymers is their potential use in catalysis [52] (Sect. 4.1).

2.3 Conjugated Microporous Polymers

Conjugated organic polymers were studied intensively in the last 20 years because of their potential applications in organic electronics and optoelectronics [53, 54]. Surprisingly, to the best of our knowledge, no explicit examples of the synthesis of CMPs were available until very recently [11, 19, 55]. The production of well-defined CMPs with high surface areas opens up a range of technological possibilities in areas such as sensors, solar energy conversion, and hybrid conjugated materials.

2.3.1 Poly(aryleneethynylene)s and Poly(phenylene butadiynylene)s

PAEs are versatile materials [56, 57] with applications that include photoluminescence [58], light-emitting diodes (LEDs) [59], molecular wires [60], sensors [60],

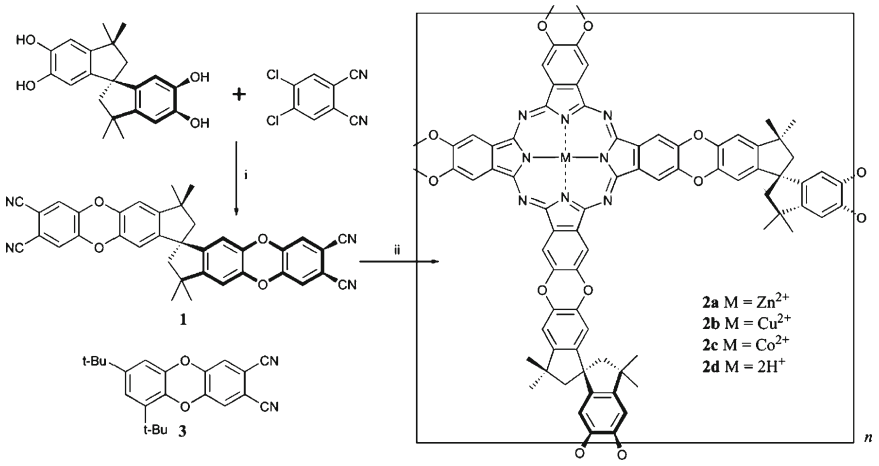

Fig. 6 Reaction scheme for synthesis of microporous phthalocynanine-containing network polymers [50]

and rapid bacterial identification [61]. In our laboratory, we have used Sonogashira–Hagihara Pd-catalysed cross-coupling chemistry to synthesize a range of CMPs based on branched PAE networks [11, 19]. The materials exhibit BET surface areas of 1,000 $m^2 g^{-1}$ or more. Excluding any microporous materials that may have been prepared inadvertently and not recognized as such (Sect. 5.1), these represent the first examples of CMPs. A series of five CMPs was prepared by this method (Fig. 7) and it was shown that the average micropore size, the micropore volume, and the BET surface area could be fine tuned by varying the "strut" length in the PAE network [11, 19]. This systematic synthetic variation in pore structure has been achieved for isoreticular MOFs [4, 62] but this is the first comparable example for an amorphous MOP [55]. Moreover, it was also shown that these physical properties can be tuned to an even finer degree by copolymerization of "short" and "long" struts [19] (Figs. 8 and 9). This can be achieved with amorphous statistical copolymer networks in a manner that would be impossible with crystalline frameworks. These microporous CMP networks are non-conducting as prepared (pressed-pellet conductivity for CMP-1 approx. 10^{-12} S cm^{-1}) but there is broad synthetic scope for modifying these network structures and also for post-modification, for example, by doping (Sect. 5.3).

Very recently, microporous poly(*p*-phenylene) and poly(phenyleneethynylene) materials based on a spirobifluorene building block were reported (BET surface areas 450–510 $m^2 g^{-1}$) [63]. These interesting materials exploit two of the aforementioned design strategies – that is, spiro linkers (as found in soluble PIMs [9, 10], Sect. 2.2.1) combined with rigid phenylene [24] and phenylene ethynylene [11] struts.

In separate but related studies, microporous pyrolytic polymers were prepared by heat treatment (350–900°C) of a variety of branched alkyne-linked networks [64]. The precursor networks were designed to bear degradable side chains to produce microporosity upon thermal degradation (a kind of "intramolecular porogen," see Sect. 1.3.4). In general, heat treatment to 400°C led to "pyrolytic polymers" and further heating to 900°C caused carbonization. Molecular level characterization (e.g. solid state ^{13}C NMR) was not given for the precursors nor the pyrolytic polymers. No porosity data was given for the precursor networks prior to heating, although an equivalent of CMP-1 [11] (P6a in this study [64]) was prepared. Interestingly, P6a exhibited much lower surface area than CMP-1 after heating to 450°C (360 versus 834 $m^2 g^{-1}$). By comparison with our own findings [11, 12], it is conceivable that some of these pyrolytic networks [64] were in fact more porous *prior* to heat treatment and subsequent carbonization.

In addition to Pd-catalysed cross-coupling, we have also used homocoupling routes to produce microporous conjugated poly(phenylene butadiynylene)s (PPBs) [12]. These materials also exhibit high BET surface areas (842 $m^2 g^{-1}$). The structures are more complex than found for PAEs [11, 19]; in particular, the networks do not solely comprise of butadiynylene linkages but also incorporate head-to-tail 1,3-disubstituted enyene crosslinks [12]. Perhaps as a result of this more diverse linking chemistry, these PPB materials exhibit broader pore size distributions and mesostructure which are absent in the PAE samples [11, 19] referred to above. This

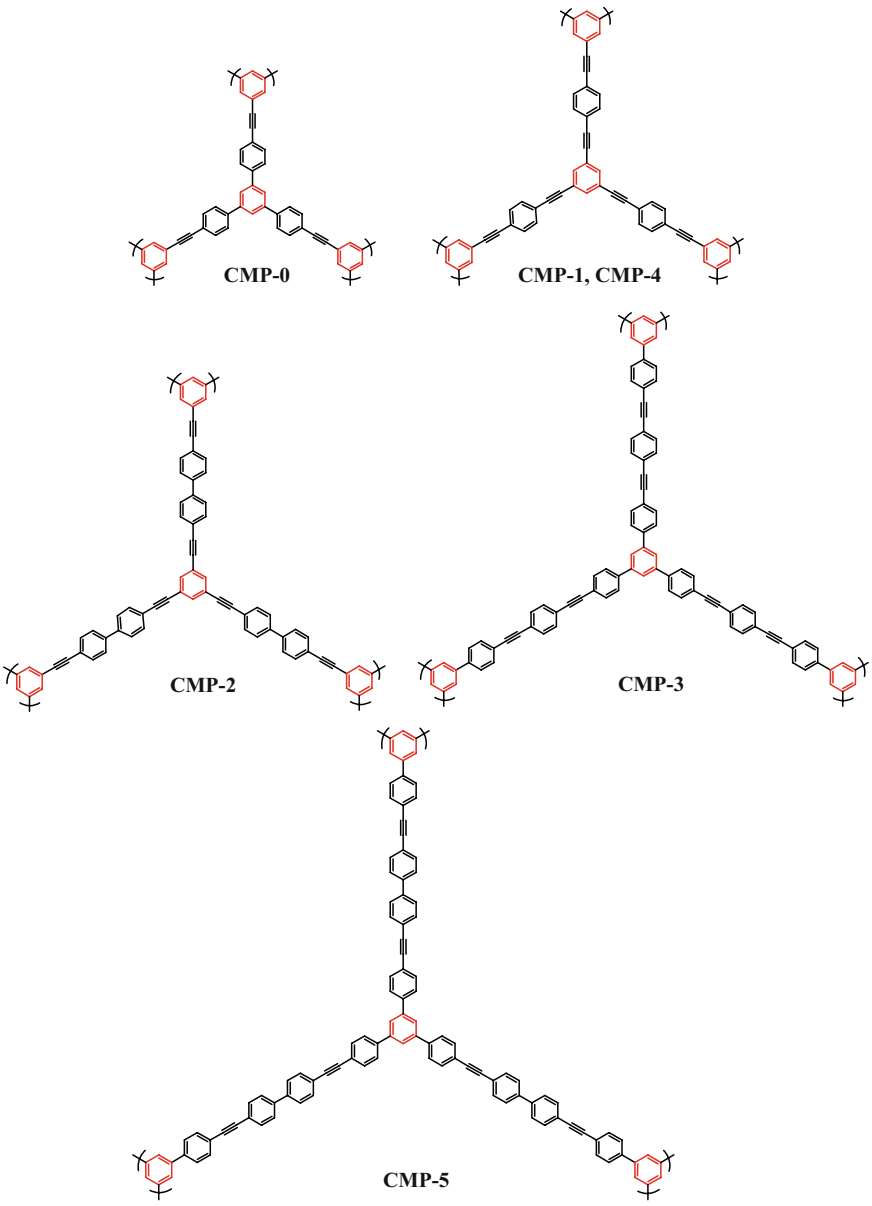

Fig. 7 "Node-strut" topology for series of CMPs networks produced by Sonagashira–Hagihara cross-coupling chemistry [19]. The benzene "nodes" are shown in *red*. The total number of ethyne plus benzene links per "strut" increases in increments of one from two (CMP-0) to six (CMP-5) in this series of samples. It should be stressed that these are simple representations of the repeat unit structures for the networks. The actual three-dimensional materials have more complex structures and include both terminal alkyne and halogen end groups (see also molecular simulations, Fig. 9)

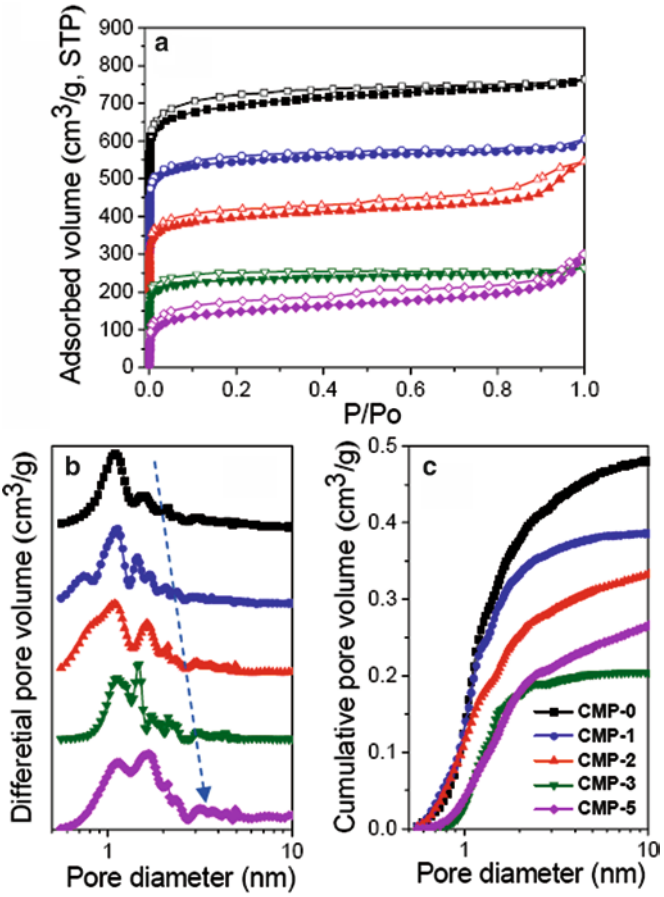

Fig. 8 Gas sorption characterization data for series of CMP polymers [19]. N_2 adsorption–desorption isotherms measured at 77.3 K (**a**), adsorption branch is labelled with *filled symbols*. For clarity, the isotherms of CMP-0, CMP-1, CMP-2, and CMP-3 were shifted vertically by 400, 300, 200, and 100 $cm^3 g^{-1}$, respectively. NL-DFT pore size distribution curves, (**b**); the *dashed arrow* indicates the shift to larger average pore size in this series. Cumulative pore volume curve calculated by application of NL-DFT, (**c**)

is manifested in the gas sorption isotherms [12] ,which deviate from the pure Type I behaviour shown by microporous PAEs [11, 19].

2.3.2 Polyphenylenevinylene

The PAE networks referred to above [11, 19] are potential precursors for microporous polyphenylenevinylene (PPV). For example, if all of the alkyne bonds in CMP-1 [11] were selectively hydrogenated to the corresponding alkenes then

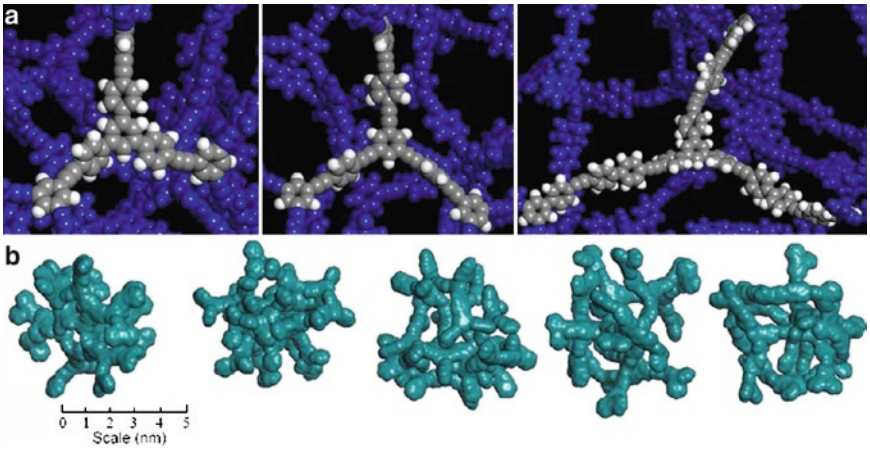

Fig. 9 Atomistic simulations for PAE networks with different strut lengths [19]. Node-strut topology for simulated network fragments for CMP-0 (*left*), CMP-1 (*centre*), and CMP-5 (*right*), (**a**). Atomistic simulations of network fragments for CMP-0, CMP-1, CMP-2, CMP-3, and CMP-5 (*left to right),* (**b**). A solvent accessible surface is shown (in *green*) in each case (solvent diameter = 0.182 nm)

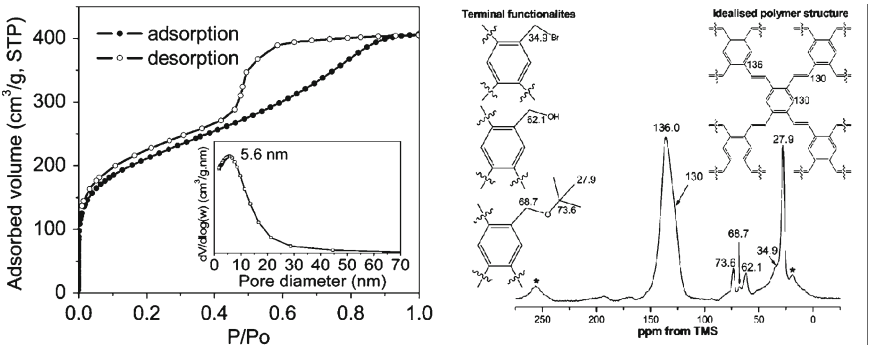

Fig. 10 Gas sorption data (*left*) and NMR spectrum (*right*) for micro/mesoporous PPV-type network [13]

the resulting material would be a hyperbranched 1,3,5-linked network variant of PPV. In principle, such a material might retain a degree of microporosity. We did not yet attempt a chemical network transformation of this kind, but we did synthesize micro/mesoporous PPV directly [13] by Gilch coupling [65] of 1,2,4,5-tetrakis(bromomethyl)benzene (TBMB) (Fig. 10). Materials were produced which exhibited some microporosity but which were predominantly mesoporous (average mesopore diameter 5.6 nm; BET surface area 761 $m^2 g^{-1}$; pore volume 0.63 $cm^3 g^{-1}$). Solid state ^{13}C NMR supported the proposed structure and revealed a

variety of end groups [13]. The material showed wide adsorption in the range 250–400 nm and fluorescence between 500 and 525 nm. Similar condensation reactions with 1,3,5-tris(bromomethyl)benzene did not yield insoluble porous networks [13], probably because of the need for a diradical with para geometry [66].

3 Crystalline MOPs

3.1 Covalent Organic Frameworks

Covalent organic frameworks [14, 20, 67, 68] are porous, shape-persistent zeolite analogues [69], which (unlike MOFs) comprised solely of non-metallic elements (C, H, O, B). The first COF (COF-1) was synthesized by self-condensation in sealed pyrex tubes of 1,4-benzenediboronic acid (BDBA) to generate a staggered $P6_3/mmc$ hexagonal layered material linked by planar boroxine rings (Fig. 11) [14]. Choice of solvent was important, as was control over reaction rates to ensure that the thermodynamic ordered, crystalline products were obtained. These considerations (solubility, reaction rates, nucleation and growth, ability of structures to "self heal") are likely to be important in the synthesis of any ordered, crystalline MOPs.

COF-1 exhibited an apparent BET surface area of 711 $m^2 g^{-1}$, a micropore volume of 0.32 $cm^3 g^{-1}$, and an average micropore size of 1.5 nm [14]. An analogous boronate-ester linked structure (COF-5) showed a BET surface area of 1,590 $m^2 g^{-1}$ and a mesopore volume of 0.998 $cm^3 g^{-1}$ (average pore size = 2.7 nm).

Much higher surface areas were obtained by employing three-dimensional tetrahedral monomers (Fig. 12) [20]. For example, COF-103 [20] exhibited an apparent BET surface area of 4,210 $m^2 g^{-1}$, which is comparable with the highest surface areas observed in MOFs. These remarkable polymeric networks exhibit some of the lowest densities known for any crystalline material. COF materials also have excellent

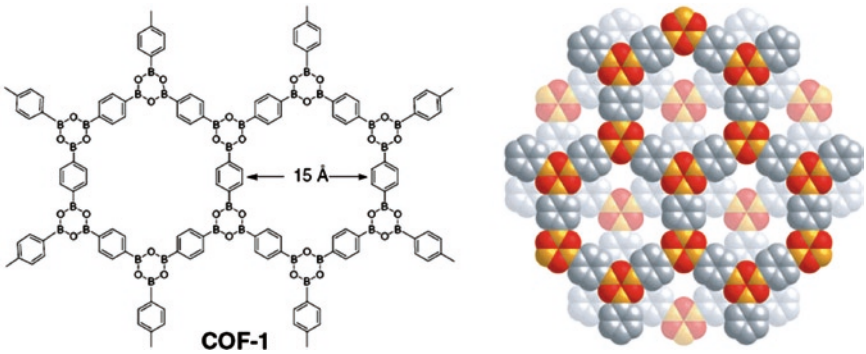

Fig. 11 Structure of crystalline two-dimensional microporous polyboroxine network, COF-1 [14]

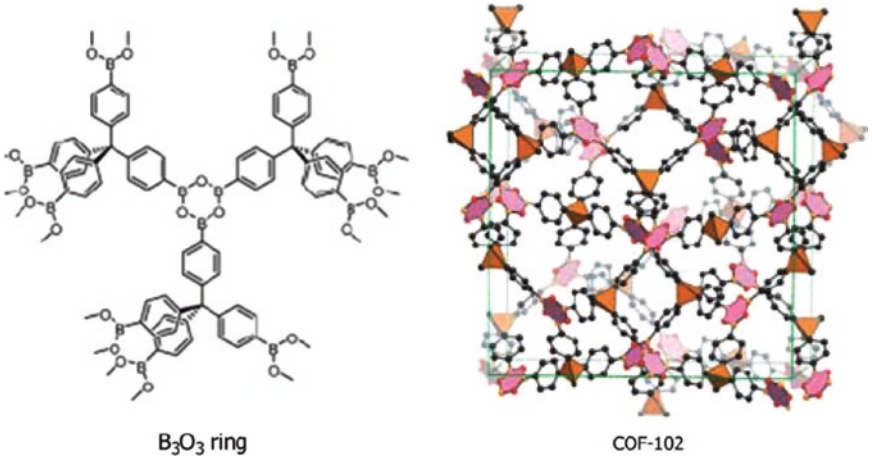

Fig. 12 Structure of crystalline three-dimensional microporous network, COF-102 [20]

thermal stabilities up to 500–600°C. There is less information at this time concerning chemical and physical stability for COFs, although an early report [18] suggests that COF-1 is unstable in moist air at 298 K. This highlights a fundamental challenge in the preparation of crystalline microporous polymers: that is, to identify bond-forming chemistry which is sufficiently reversible to access kinetic products while yielding materials with good physical and chemical stability.

3.2 Triazine-Based Frameworks

An innovative approach to the formation of ordered microporous crystalline polymers is the ionothermal cyclotrimerization of nitrile monomers to generate crystalline polytriazines [15] (Fig. 13). Nitrile monomers such as 1,4-dicyanobenzene (DCB) were reacted in molten $ZnCl_2$ at 400°C. The molten salt acts as both a solvent for the monomer and a catalyst for the trimerization reaction. Yields are generally close to 100% and black, monolithic materials are obtained [15]. The polymer produced from DCB, CTF-1, exhibited an apparent BET surface area of 791 $m^2 g^{-1}$ (very close to that found for both COF-1 [14] and CMP-1 [11, 19]) and a total pore volume of 0.4 $cm^3 g^{-1}$ (again, comparable to COF-1/CMP-1) [15]. Powder XRD analysis revealed intense reflection peaks consistent with an ordered hexagonal structure although these peaks were relatively broad, possibly suggesting limited long range order.

The molecular network structure suggested for CTF-1 is isoelectronic with the structure of COF-1 [14]. By contrast, COF-1 shows a staggered, $P6_3/mmc$ hexagonal structure prior to CTF-1 is proposed to have eclipsed *P6/mmm* symmetry [15]. No NMR data was given for these triazine networks, but elemental analysis implied partial decomposition or carbonization in some samples. For example, a network produced

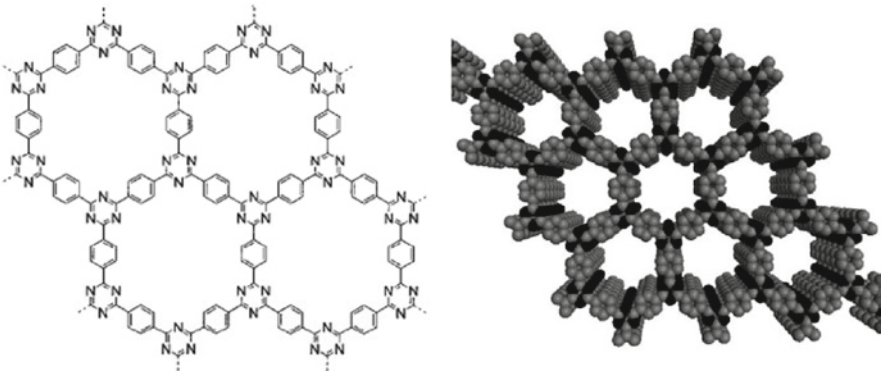

Fig. 13 Proposed structure for polytriazine CTF-1 prepared by ionothermal synthesis [15]

from dicyanobiphenyl (DCBP; surface area = 2,475 g cm^{-3}) using a larger quantity of $ZnCl_2$ exhibited a measured nitrogen content of 5.41% compared with a theoretical content of 13.72% for the idealized network. Incomplete combustion during analysis may account for this difference. Alternatively, $ZnCl_2$ is commonly used in the preparation of activated carbons [27–29] (albeit typically at much higher temperatures) and it is possible that a degree of carbonization takes place in these reactions.

4 Applications of MOPs

4.1 Catalysis

The good chemical and physical stability of many MOPs, coupled with synthetic diversity and potential for pore size control, bodes well for applications in heterogeneous catalysis. For example, microporous phthalocyanine and porphyrin network polymers are used as heterogeneous catalysts for the oxidation of cyclohexene, the decomposition of hydrogen peroxide, and the oxidation of hydroquinone [52]. Enhanced catalytic activity was observed with respect to low molar mass analogues. There is considerable scope for future development here –for example, the design of electrocatalytic materials using CMPs [11, 12, 19].

4.2 Separations

MOPs are obvious candidates for separation technology because of their high surface areas, good stabilities, and pore sizes, which have molecular dimensions. Again, the broad potential for synthetic versatility is a major advantage here in terms of designing MOPs with specific affinities.

4.2.1 Chromatography

HCPs in particular are quite well developed in terms of chromatographic separations and for the adsorption of specific components from solution mixtures. To give just a few examples, hypercrosslinked polystyrene has been used for the adsorptive removal of phenolic compounds from aqueous solutions [36, 70], as a stationary phase for HPLC [71], and as a sorbent for solid phase extraction of polar compounds from water [72]. The ability to produce bimodal pore size distributions (e.g. large "flow" macropores interconnected with micropores for surface area) [25] is a significant advantage here, as is the relatively low cost and high stability of these materials. A generic issue for chromatographic separation media is particle size control. HCPs may be produced by suspension polymerization to yield relatively well-controlled polymer beads [21]. Other materials such as PIMs, CMPs, and COFs might need to develop similar heterogeneous polymerization strategies or, alternatively, to produce these materials as coherent moulded monoliths [73–76].

4.2.2 Gas Separations

Practical gas separations tend to require relatively thin films to allow high gas fluxes. PIMs have a unique advantage here in that they can be dissolved in organic solvents and cast directly as microporous films [42]. Solution-cast PIM membranes have been used for both gas separation [41] and for pervaporation of aqueous phenol solutions [43]. A practical trade-off here is the balance between gas permeability and selectivity: in general, high gas permeabilities tend to be accompanied by low separation selectivities and *vice versa*, as illustrated by the "Robeson plot" (Fig. 14) [77].

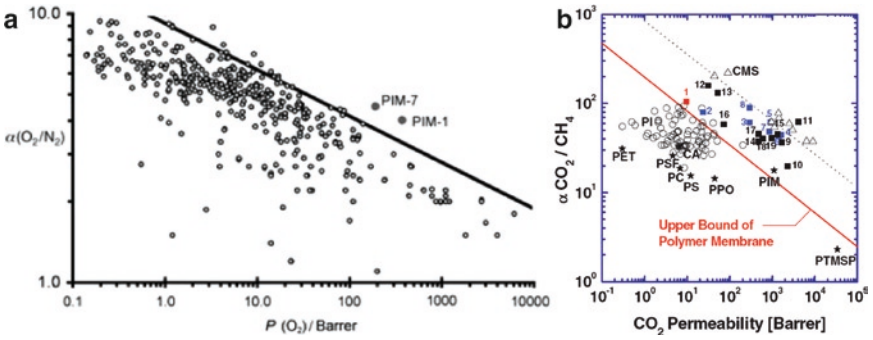

Fig. 14 Robeson plot showing high O_2/N_2 separation selectivities for PIM-1 and PIM-7, (**a**) [77]. Relation between CO_2 permeability and CO_2/CH_4 selectivity of thermally rearranged polyimides, (**b**) [78]

As shown in Fig. 14, PIM-1 and PIM-7 have been found to exhibit substantially higher O_2/N_2 selectivities ($\alpha(O_2/N_2) > 3.0$) than other polymers of similar permeability [41]. Other "thermally rearranged" [78] polyimides show excellent CO_2/CH_4 separation selectivities. These materials were also shown to function as fuel cell membranes when doped with H_3PO_4 and proton conductivities of 0.15 S cm^{-1} were observed at 130°C [78]: that is, higher than polybenzimidazole membranes.

The fine control over pore size and pore size distribution in CMPs [11, 19] suggests that these materials might also be promising for gas separation applications, although it would first be necessary to solve the non-trivial problem of synthesizing or processing these materials as defect-free thin films or as a moulded, "sandwiched" layer.

4.3 Gas Storage

Since 2006, there has been a great deal of interest in MOPs as gas storage media: indeed, this has been a key driver in the recent rapid development of this field [79, 80]. The fact that MOPs are composed of light elements – and there is potential to develop high specific surface areas – offer advantages here.

4.3.1 Hydrogen Storage

A great deal of research has focused on the use of microporous sorbents such as activated carbon [81] and MOFs [82–85] for the physisorptive storage of H_2 at low temperatures (typically 77.3 K). In 2006, it was shown that a PIM network (CTC-PIM) could adsorb up to 1.7 wt. % H_2 at 77.3 K and 10 bar [46]. Shortly afterwards, our group [33] and others [34] showed that HCPs could adsorb up to around 3 wt. % H_2 at 77.3 K/15 bar. We showed subsequently that HCPs produced via a polycondensation route (Sect. 2.1.2) adsorbed around 3.7 wt. % at 77.3 K/15 bar (~4 wt. % at 100 bar/saturation) [31]. At the time of writing, this is the highest H_2 uptake reported for a MOP although lower than observed for leading activated carbons [81] and MOFs [82, 83]. A DCBP polytriazine network [15] was shown recently to adsorb 1.55 wt. % H_2 at 77.3 K/1 bar; that is, lower than Trip-PIM [48] (1.65 wt. %) HCP **27** [31] (1.69 wt. %), or a monolithic hypercrosslinked BCMBP polymer (1.9 wt. %) [39], despite the fact that the polytriazine network exhibited an apparent BET surface area (2,475 $m^2 g^{-1}$) which was significantly higher than these other three networks. This supports prior observations [31, 80] which suggest that ultramicropore volume, rather than apparent BET surface area, is a better predictor for H_2 uptake at low pressures, well below saturation. There is at present limited data available concerning H_2 sorption in COFs. Computer simulations suggest that perfectly crystalline COF-105 may adsorb more than 8 wt. % H_2 at >10 bar/77 K [86]. A H_2 sorption capacity of 1.28 wt. % was reported recently for COF-1 at 1 bar/77.3 K [18]. COF-1 has much lower surface area than the COFs modelled in the study

above [86] and hence direct comparisons are difficult. CMP-1 (SA_{BET} = 834 $m^2 g^{-1}$, S_{micro} = 675 $m^2 g^{-1}$, pore volume = 0.33 $cm^3 g^{-1}$) [11, 19] exhibited an N_2 isotherm and pore size distribution which were both very similar to that reported for COF-1 (SA_{BET} = 711 $m^2 g^{-1}$, S_{micro} = 587 $m^2 g^{-1}$, pore volume = 0.32 $cm^3 g^{-1}$) [14]. Likewise, the reported H_2 uptakes at 1 bar/77.3 K are also similar (~1.2 wt. % for CMP-1 [11, 19] versus ~1.3 wt. % for COF-1) [14].

Larger micropore volumes and physical surface areas in MOPs would undoubtedly drive up H_2 storage capacities at cryogenic temperatures. Perhaps a more intractable problem, however, is the low isosteric heat [87] for H_2 on most microporous sorbents (including MOPs [31, 34], activated carbons [87], and MOFs [82, 83, 88]) which necessitates cryogenic temperatures that are unlikely to be compatible with practical applications. An interesting approach here is the generation of hypercrosslinked polyanilines which were shown to exhibit specific surface areas in excess of 630 $m^2 g^{-1}$ [89]. These materials showed isosteric heats (−8 to −9 kJ mol^{-1}) [89] which were somewhat higher than those found for hypercrosslinked polystyrene [31, 34], although still far below the average value required for close to ambient temperature H_2 storage (approx. −15 kJ mol^{-1}) [87]. We recently suggested a potential strategy for incorporating "naked" fluoride moieties into polymer networks in order to achieve higher energy H_2 sorption sites (Fig. 15) [90].

Calculations suggested that such moieties might impart significantly higher isosteric heats with H_2 (>10 kJ mol^{-1}) although it is synthetically challenging to produce MOPs where "naked" fluoride groups would exist in a site-isolated, charge-separated form [90]. An alternative strategy would be to introduce transition metals into MOPs such that dihydrogen [91, 92] (or dihydride [93]) complexes might be formed.

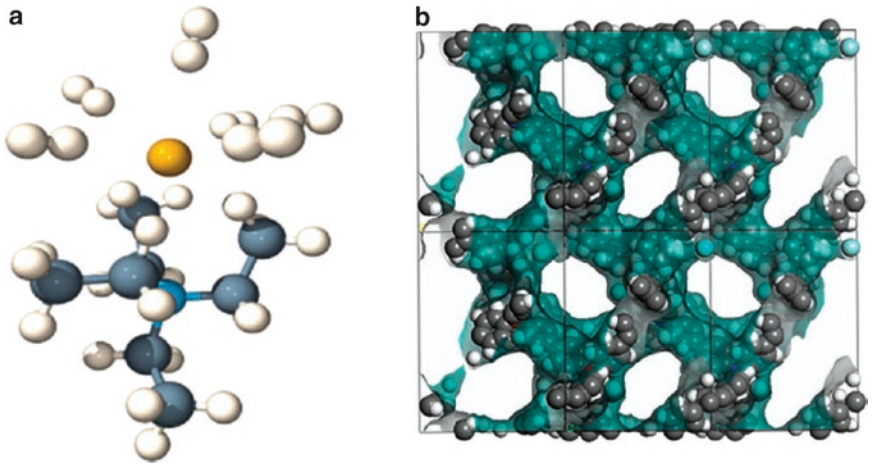

Fig. 15 Side view of molecular model showing six H_2 molecules binding to tetraethylammonium fluoride, (**a**) [90]. Molecular simulation of a hypothetical biphenyl-linked tetrabiphenylammonium fluoride MOP, (**b**). A 3×2 lattice is shown with a Connolly surface superimposed in green/grey. We have no viable synthetic route to this material at present

Certain transition metal dihydrogen complexes are known to have bond dissociation energies in the correct range for reversible H_2 storage close to ambient temperatures [91] and these species are therefore particularly appealing. Again, the formation of these reactive functionalities in a site-isolated form within a MOP is challenging, although some progress has been made recently with derivatized MOFs [94]. Other MOF strategies may also be translated to MOPs – for example, models suggest that lithiation improves H_2 binding energies for MOFs [95, 96] and COFs [97] and there is some experimental evidence for this in the case of MOFs [98]. Similar approaches might also be possible with certain CMPs [11, 12, 19], for example.

4.3.2 Methane Storage

Methane storage by physisorption is in many respects an easier problem than H_2 storage because the boiling point of CH_4 is much higher and isosteric heats of sorption with common sorbents are much more substantial. Indeed, high surface area activated carbon is a very respectable sorbent for CH_4 at ambient temperatures [87] and certain MOFs have already exceeded the DoE target of 180 v/v [62, 99]. Nevertheless, there are reasons to investigate alternative CH_4 sorbents – for example, to identify inexpensive, scaleable MOPs with enhanced physical and chemical stability (Sect. 1.1.2). We have shown recently that HCPs are promising materials for CH_4 storage [39], although initial uptakes (5.5 mmol g^{-1} at 35 bar/298 K) were significantly lower than leading MOFs [99]. Interestingly however, the isosteric heat of sorption for CH_4 with these HCPs (approx. −21 kJ mol^{-1}) [39] was found to be substantially higher than most MOFs [62, 100] and activated carbon (−16 kJ mol^{-1}) [87]. We assigned this largely to the aromatic hydrocarbon nature of the HCP material and this has been borne out recently by the discovery of an anthracene-based MOF (PCN-14) with high aromatic content and even greater isosteric heat values (−25 to −30 kJ mol^{-1}) [99]. HCPs and other MOPs therefore offer the potential to "tune" isosteric heats of sorption by synthetic diversification, perhaps to generate MOPs with enhanced CH_4 sorption capacities at significantly lower pressures [39]. It is also possible to produce HCPs [39] (and other MOPs such as CMPs [11, 12, 19]) in a moulded monolithic which may have potential advantages in terms of *volumetric* storage capacity [39].

5 Future Outlook

5.1 "Undiscovered" MOPs?

The MOPs referred to in Sects. 2 and 3 were synthesized with the aim of generating microporosity. Some materials were even "designed" [101] to an extent. It is quite likely however, that a number of other "inadvertent" MOPs exist in the literature which are undiscovered in terms of their micropore properties (Fig. 16). For example,

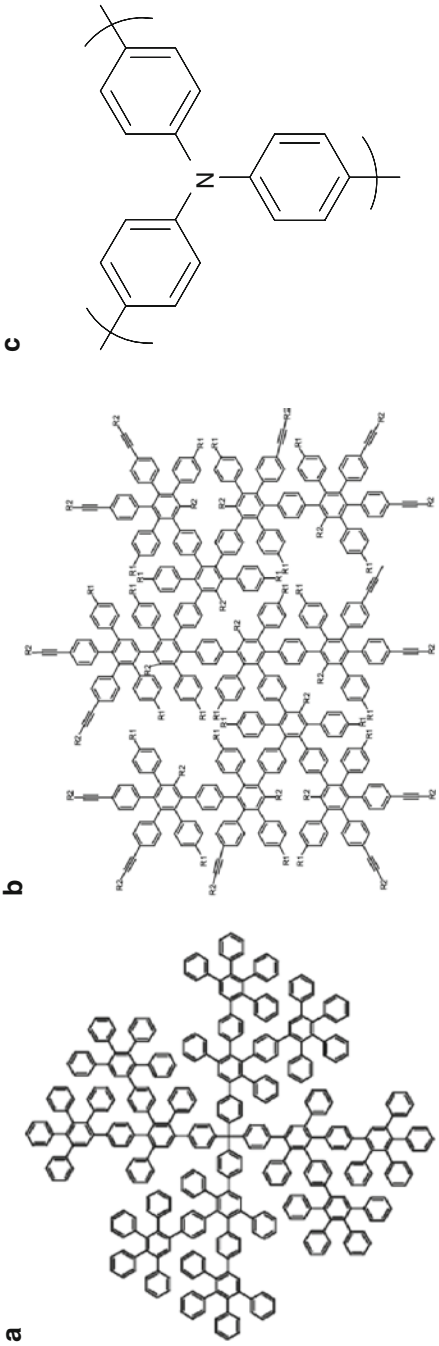

Fig. 16 Examples of potential "undiscovered" MOPs. A polyphenylene dendrimer [105] (**a**), a hyperbranched polyphenylene material [121] (**b**) and polytriphenylamine [116, 117] (**c**)

we synthesized a homocoupled "linear" PPB sample (HCMP-2), initially as a control experiment [12]. It was found not to be linear when synthesized under these conditions but rather found to contain 1,3-disubstituted enyene crosslinks and to exhibit significant micro/mesoporosity ($SA_{BET} = 827\ m^2\ g^{-1}$) [12]. Others [102, 103] had observed this crosslinking phenomenon – and very similar solid state NMR spectra – before [102, 103] but no attempt had been made to measure micropore properties. Similarly, a series of PAE networks was reported in 1986, some of which were most likely microporous, although no such measurements were made at that time [104]. It is interesting to speculate which published systems may be microporous: obvious candidates would be network polymers produced from rigid monomers (see Sect. 1.3) although soluble rigid backbone polymers cannot be discounted, particularly when efficient chain packing is inhibited in some way (e.g. other aromatic polyimides, see Sect. 2.2). While it is outside the scope of this review to survey this very broad literature in detail, a few examples of possible "good bets" are listed as follows:

- Rigid aromatic dendrimers [105–108] and dendrons (particularly higher generation or unsymmetrical materials where efficient molecular packing might be restricted); PAE dendrimers or dendrons [109, 110], especially if alkyl solubilizing groups can be minimized/omitted.
- Hyperbranched polyphenylenes [111] and other polyphenylene nanostructures [106] (potentially also hyperbranched aromatic polyesters [112], although ester groups may introduce too much conformational flexibility; hyperbranched polycarbazoles [113], again absence of alkyl solubilizing groups might enhance porosity; hyperbranched PAEs [114].
- Dendronized conjugated polymers [115] or copolymers; such materials have been designed to be non-aggregating in order to suppress formation of long wavelength emitting aggregates; such motifs might also lead in principle to the generation of permanent microporosity.
- Polytriphenylamine [116, 117] and related structures provided that substantial molecular weights/networks are achieved.

5.2 New Classes of MOPs

There are a number of interesting "crossovers" between the approaches described in the sub-sections of this chapter, which are yet to be realized. For example, it should be possible to design conjugated polymers of intrinsic microporosity (CPIMs); that is, linear (or perhaps dendritic [109, 110]/ hyperbranched [114]) conjugated polymers which are soluble in organic solvents but microporous when cast as films. This would have obvious practical advantages in terms of generating new electronic or optoelectronic devices (Sect. 5.3). A challenge here is that the alkyl functionalities typically used to solubilize such conjugated polymers might also fill free volume and reduce microporosity: as such, branched or dendritic architectures may be preferred since these are often inherently more soluble for a given system.

By varying reaction conditions, it should also be possible to utilize the boroxine- and boronate-ester-forming chemistry used to generate crystalline COFs [14, 20, 67] to synthesize *amorphous* MOPs, if desired, and perhaps even solution-processable variants. (Simulations have already suggested other nanostructures such as nanotubes and fullerene-analogues [118].) Conversely, ordered, crystalline CMPs might have very interesting physical properties (Sect. 5.3) but this would require employment of reversible chemistry or the presence of strong templating to direct the crystallization (see discussion, Sect. 1.3.2).

Certain general synthetic strategies may also be transferable across classes of MOPs. For example, Friedel–Crafts post crosslinking has been used extensively to generate HCPs (Sect. 2.1.1) but similar "prepolymer" strategies have not in general been applied to other MOPs. The synthesis of linear or branched prepolymers with pendant reactive functional groups (e.g. catechols [9], alkynes [11], nitriles [15]), followed by spin-coating and subsequent network formation could represent a broad strategy for the preparation of microporous thin films.

5.3 MOPs with New Properties

There are an increasing number of reports of useful, specific chemical and physical properties in MOPs. Recent examples include high gas separation efficiencies in PIM membranes [41, 78], catalytically-active phthalocyanine and porphyrin network polymers [52], and HCPs with elevated isosteric heats of sorption for CH_4 [39]. Many more possibilities for exploration exist – the following list suggests just a few such opportunities:

- HCPs exhibit very unusual swelling properties [38], even in weak solvents (Sect. 2.1). This suggests applications in molecular entrapment and the storage of gases (e.g. alkanes [39]) which might "solvate" these networks, even weakly.
- CMPs have been produced with high surface areas and good synthetic control over pore size (Sect. 2.3) [11, 19, 63]. An important extension of this would be the synthesis of conducting or semiconducting CMPs – for example, by using doping strategies. Potential applications here include light-harvesting and photocatalysis.
- Three-dimensional COFs have been predicted to exhibit high levels of H_2 sorption [86] (Sect. 4.3.1); the practical demonstration of this (also CH_4 for; Sect. 4.3.2) would be of significant interest.
- Ordered, crystalline CMPs might exhibit a range of unique electronic and optoelectronic properties if suitable chemistry or templating strategies can be devised (Sect. 1.3.2).
- The efficient separation and capture of CO_2 from industrial waste streams is an important societal problem. Recently, ZIFs, for example, have demonstrated excellent CO_2 selectivities in this regard [16, 17]. At present there has been little progress in this area with MOPs, despite the clear potential for the

introduction of suitable chemical functionality [119, 120]. For example, cyclic amidine structures were introduced into linear polymers bearing chloromethyl substituents [120] and this strategy might readily be translated into HCPs, for example, which are often synthesized from chloromethyl-substituted monomers [21, 25, 31, 33].

5.4 High Throughput Approaches

High throughput (HT) approaches have much to offer, both for the discovery of entirely new materials (Sect. 5.2 and 5.3) and for the optimization of new properties (Sect. 5.3) as new MOPs are discovered. HT methods were used in the synthesis of novel ZIFs using X-ray methods as a primary "screen" [16]. The HT discovery of amorphous MOPs is complicated by the lack of an equivalent structural handle. We have developed HT gas sorption methods (H_2, N_2, CH_4) to address this [31]. This accelerated methodology can be used to measure standard quantities such as apparent BET surface areas and H_2 (or CH_4) uptakes. The method is also applicable to the rapid measurement of isosteric heats of sorption for diverse libraries or for homologous series of materials [19]. Coupled with the use of automated robotic synthesizers to prepare the polymer arrays, this represents a very powerful combined strategy for the accelerated discovery of new MOPs.

6 Conclusion and Perspectives

The synthesis and application of MOPs is a flourishing area of interdisciplinary research. Recent discoveries have led to a growing understanding of the underlying structure–property relationships for this class of material although much remains to be uncovered. A key advantage of MOPs is the very broad synthetic diversity that may be achieved. This promises a range of new microporous polymers with tailored physical and chemical properties that are unobtainable in other microporous materials.

Acknowledgement We thank NWDA, the EU, and the Engineering and Physical Sciences Research Council (EPSRC) for funding via EP/C511794/1. We gratefully acknowledge the University of Liverpool for funding the recent refurbishment of our materials laboratories.

References

1. Schuth F, Sing KSW, Weitkamp J (eds) (2002) Handbook of porous solids. Wiley, New York
2. Li H, Eddaoudi M, O'Keeffe M, Yaghi OM (1999) Nature 402:276
3. Cheetham AK, Férey G, Loiseau T (1999) Angew Chem Int Ed Engl 38:3268

4. Yaghi OM, O'Keeffe M, Ockwig NW, Chae HK, Eddaoudi M, Kim J (2003) Nature 423:705
5. Kitagawa S, Kitaura R, Noro S (2004) Angew Chem Int Ed Engl 43:2334
6. Loy DA, Shea KJ (1995) Chem Rev 95:1431
7. Petraccone V, Ruiz de Ballesteros O, Tarallo O, Rizzo P, Guerra G (2008) Chem Mater 20:3663
8. Davankov VA, Tsyurupa MP (1990) React Polym 13:27
9. Budd PM, Ghanem BS, Makhseed S, McKeown NB, Msayib KJ, Tattershall CE (2004) Chem Commun:230
10. Weber J, Su O, Antonietti M, Thomas A (2007) Macromol Rapid Commun 28:1871
11. Jiang JX, Su F, Trewin A, Wood CD, Campbell NL, Niu H, Dickinson C, Ganin AY, Rosseinsky MJ, Khimyak YZ, Cooper AI (2007) Angew Chem Int Ed Engl 46:8574 see also correction, (2008) Angew Chem Int Ed Engl 47: 1167
12. Jiang JX, Su F, Niu H, Wood CD, Campbell NL, Khimyak YZ, Cooper AI (2008) Chem Commun:486
13. Dawson R, Su FB, Niu HJ, Wood CD, Jones JTA, Khimyak YZ, Cooper AI (2008) Macromolecules 41:1591
14. Côté AP, Benin AI, Ockwig NW, O'Keeffe M, Matzger AJ, Yaghi OM (2005) Science 310:1166
15. Kuhn P, Antonietti M, Thomas A (2008) Angew Chem Int Ed Engl 47:3450
16. Banerjee R, Phan A, Wang B, Knobler C, Furukawa H, O'Keeffe M, Yaghi OM (2008) Science 319:939
17. Wang B, Côté AP, Furukawa H, O'Keeffe M, Yaghi OM (2008) Nature 453:207
18. Li YW, Yang RT (2008) AIChE J 54:269
19. Jiang J-X, Su F, Trewin A, Wood CD, Niu H, Jones JTA, Khimyak YZ, Cooper AI (2008) J Am Chem Soc 130:7710
20. El-Kaderi HM, Hunt JR, Mendoza-Cortes JL, Côté AP, Taylor RE, O'Keeffe M, Yaghi OM (2007) Science 316:268
21. Tsyurupa MP, Davankov VA (2002) React Funct Polym 53:193
22. Tsyurupa MP, Davankov VA (2006) React Funct Polym 66:768
23. Budd PM, McKeown NB, Fritsch D (2005) J Mater Chem 15:1977
24. Webster OW, Gentry FP, Farlee RD, Smart BE (1992) Makromol Chem Macromol Symp 54–5:477
25. Ahn JH, Jang JE, Oh CG, Ihm SK, Cortez J, Sherrington DC (2006) Macromolecules 39:627
26. Sherrington DC (1998) Chem Commun:2275
27. Caturla F, Molinasabio M, Rodriguezreinoso F (1991) Carbon 29:999
28. Ahmadpour A, Do DD (1996) Carbon 34:471
29. Sathishkumar M, Vijayaraghavan K, Binupriya AR, Stephan AM, Choi JG, Yun SE (2008) J Coll Int Sci 320:22
30. Duren T, Millange F, Férey G, Walton KS, Snurr RQ (2007) J Phys Chem C 111:15350
31. Wood CD, Tan B, Trewin A, Niu HJ, Bradshaw D, Rosseinsky MJ, Khimyak YZ, Campbell NL, Kirk R, Stöckel E, Cooper AI (2007) Chem Mater 19:2034
32. Davankov VA, Pastukhov AV, Tsyurupa MP (2000) J Polym Sci Part B Polym Phys 38:1553
33. Lee JY, Wood CD, Bradshaw D, Rosseinsky MJ, Cooper AI (2006) Chem Commun:2670
34. Germain J, Hradil J, Fréchet JMJ, Svec F (2006) Chem Mater 18:4430
35. Macintyre FS, Sherrington DC, Tetley L (2006) Macromolecules 39:5381
36. Oh CG, Ahn JH, Ihm SK (2003) React Funct Polym 57:103
37. Law RV, Sherrington DC, Snape CE, Ando I, Kurosu H (1996) Macromolecules 29:6284
38. Pastukhov AV, Tsyurupa MP, Davankov VA (1999) J Polym Sci Part B Polym Phys 37:2324
39. Wood CD, Tan B, Trewin A, Su F, Rosseinsky MJ, Bradshaw D, Sun Y, Zhou L, Cooper AI (2008) Adv Mater 20:1916
40. Rose M, Böhlmann W, Sabo M, Kaskel S (2008) Chem Commun 2462
41. McKeown NB, Budd PM, Msayib KJ, Ghanem BS, Kingston HJ, Tattershall CE, Makhseed S, Reynolds KJ, Fritsch D (2005) Chem Eur J 11:2610

42. McKeown NB, Budd PM (2006) Chem Soc Rev 35:675
43. Budd PM, Elabas ES, Ghanem BS, Makhseed S, McKeown NB, Msayib KJ, Tattershall CE, Wang D (2004) Adv Mater 16:456
44. Ghanem BS, McKeown NB, Budd PM, Fritsch D (2008) Macromolecules 41:1640
45. Xu K, Economy J (2004) Macromolecules 37:4146
46. McKeown NB, Gahnem B, Msayib KJ, Budd PM, Tattershall CE, Mahmood K, Tan S, Book D, Langmi HW, Walton A (2006) Angew Chem Int Ed Engl 45:1804
47. Budd PM, Ghanem B, Msayib K, McKeown NB, Tattershall C (2003) J Mater Chem 13:2721
48. Ghanem BS, Msayib KJ, McKeown NB, Harris KDM, Pan Z, Budd PM, Butler A, Selbie J, Book D, Walton A (2007) Chem Commun:67
49. McKeown NB (2000) J Mater Chem 10:1979
50. McKeown NB, Makhseed S, Budd PM (2002) Chem Commun:2780
51. McKeown NB, Hanif S, Msayib K, Tattershall CE, Budd PM (2002) Chem Commun:2782
52. Mackintosh HJ, Budd PM, McKeown NB (2008) J Mater Chem 18:573
53. Müllen K, Scherf U (2006) Organic light emitting devices: synthesis, properties and applications. Wiley, New York
54. Friend RH, Gymer RW, Holmes AB, Burroughes JH, Marks RN, Taliani C, Bradley DDC, Dos Santos DA, Bredas JL, Logdlund M, Salaneck WR (1999) Nature 397:121
55. Weder C (2008) Angew Chem Int Ed Engl 47:448
56. Bunz UHF (2000) Chem Rev 100:1605
57. Hittinger E, Kokil A, Weder C (2004) Angew Chem Int Ed Engl 43:1808
58. Weder C, Wrighton MS (1996) Macromolecules 29:5157
59. Schmitz C, Posch P, Thelakkat M, Schmidt HW, Montali A, Feldman K, Smith P, Weder C (2001) Adv Funct Mater 11:41
60. Swager TM (1998) Acc Chem Res 31:201
61. Phillips RL, Miranda OR, You CC, Rotello VM, Bunz UHF (2008) Angew Chem Int Ed Engl 47:2590
62. Eddaoudi M, Kim J, Rosi N, Vodak D, Wachter J, O'Keeffe M, Yaghi OM (2002) Science 295:469
63. Weber J, Thomas A (2008) J Am Chem Soc 130:6334
64. Kobayashi N, Kijima M (2007) J Mater Chem 17:4289
65. Gilch HG, Wheelwri Wl (1966) J Polym Sci Part A Polym Chem 4:1337
66. Schwahn T, Wiesecke J, Immel S, Rehahn M (2007) Macromolecules 40:8842
67. Côté AP, El-Kaderi HM, Furukawa H, Hunt JR, Yaghi OM (2007) J Am Chem Soc 129:12914
68. Budd PM (2007) Science 316:210
69. Mastalerz M (2008) Angew Chem Int Ed Engl 47:445
70. Li AM, Zhang QX, Zhang GC, Chen JL, Fei ZH, Liu FQ (2002) Chemosphere 47:981
71. Penner NA, Nesterenko PN, Ilyin MM, Tsyurupa MP, Davankov VA (1999) Chromatographia 50:611
72. Fontanals N, Galia M, Cormack PAG, Marce RM, Sherrington DC, Borrull F (2005) J Chromatogr A 1075:51
73. Svec F, Fréchet JMJ (1992) Anal Chem 64:820
74. Svec F, Fréchet JMJ (1996) Science 273:205
75. Cooper AI, Holmes AB (1999) Adv Mater 11:1270
76. Hebb AK, Senoo K, Bhat R, Cooper AI (2003) Chem Mater 15:2061
77. Robeson LM (1991) J Membrane Sci 62:165
78. Park HB, Jung CH, Lee YM, Hill AJ, Pas SJ, Mudie ST, Van Wagner E, Freeman BD, Cookson DJ (2007) Science 318:254
79. Budd PM, Butler A, Selbie J, Mahmood K, McKeown NB, Ghanem B, Msayib K, Book D, Walton A (2007) Phys Chem Chem Phys 9:1802
80. McKeown NB, Budd PM, Book D (2007) Macromol Rapid Commun 28:995
81. Yang ZX, Xia YD, Mokaya R (2007) J Am Chem Soc 129:1673

82. Rowsell JLC, Yaghi OM (2006) J Am Chem Soc 128:1304
83. Wong-Foy AG, Matzger AJ, Yaghi OM (2006) J Am Chem Soc 128:3494
84. Zhao XB, Xiao B, Fletcher AJ, Thomas KM, Bradshaw D, Rosseinsky MJ (2004) Science 306:1012
85. Lin X, Jia JH, Zhao XB, Thomas KM, Blake AJ, Walker GS, Champness NR, Hubberstey P, Schroder M (2006) Angew Chem Int Ed Engl 45:7358
86. Garberoglio G (2007) Langmuir 23:12154
87. Bhatia SK, Myers AL (2006) Langmuir 22:1688
88. Frost H, Snurr RQ (2007) J Phys Chem C 111:18794
89. Germain J, Fréchet JMJ, Svec F (2007) J Mater Chem 17:4989
90. Trewin A, Darling GR, Cooper AI (2008) New J Chem 32:17
91. Kubas GJ (2007) Chem Rev 107:4152
92. Cooper AI, Poliakoff M (2007) Chem Commun:2965
93. Cooper AI, Poliakoff M (1993) Chem Phys Lett 212:611
94. Kaye SS, Long JR (2008) J Am Chem Soc 130:806
95. Han SS, Goddard WA (2007) J Am Chem Soc 129:8422
96. Mavrandonakis A, Tylianakis E, Stubos AK, Froudakis GE (2008) J Phys Chem C 112:7290
97. Choi YJ, Lee JW, Choi JH, Kang JK (2008) Appl Phys Lett 92
98. Mulfort KL, Hupp JT (2007) J Am Chem Soc 129:9604
99. Ma SQ, Sun DF, Simmons JM, Collier CD, Yuan DQ, Zhou HC (2008) J Am Chem Soc 130:1012
100. Duren T, Sarkisov L, Yaghi OM, Snurr RQ (2004) Langmuir 20:2683
101. Jansen M, Schon JC (2006) Angew Chem Int Ed Engl 45:3406
102. Okada S, Peng S, Spevak W, Charych D (1998) Acc Chem Res 31:229
103. Lin VSY, Radu DR, Han MK, Deng WH, Kuroki S, Shanks BH, Pruski M (2002) J Am Chem Soc 124:9040
104. Trumbo DL, Marvel CS (1986) J Polym Sci Part A Polym Chem 24:2311
105. John H, Bauer R, Espindola P, Sonar P, Heinze J, Müllen K (2005) Angew Chem Int Ed Engl 44:2447
106. Berresheim AJ, Muller M, Müllen K (1999) Chem Rev 99:1747
107. Watson MD, Fechtenkotter A, Müllen K (2001) Chem Rev 101:1267
108. Bauer R, Liu D, Heyen AV, De Schryver F, De Feyter S, Mullen K (2007) Macromolecules 40:4753
109. Devadoss C, Bharathi P, Moore JS (1996) J Am Chem Soc 118:9635
110. Peng ZH, Melinger JS, Kleiman V (2006) Photosynth Res 87:115
111. Kim YH, Webster OW (1990) J Am Chem Soc 112:4592
112. Hawker CJ, Lee R, Fréchet JMJ (1991) J Am Chem Soc 113:4583
113. Tao XT, Zhang YD, Wada T, Sasabe H, Suzuki H, Watanabe T, Miyata S (1998) Adv Mater 10:226
114. Mendez JD, Schroeter M, Weder C (2007) Macromol Chem Phys 208:1625
115. Setayesh S, Grimsdale AC, Weil T, Enkelmann V, Müllen K, Meghdadi F, List EJW, Leising G (2001) J Am Chem Soc 123:946
116. Petr A, Kvarnstrom C, Dunsch L, Ivaska A (2000) Synth Metals 108:245
117. Ishikawa M, Kawai M, Ohsawa Y (1991) Synth Metals 40:231
118. Lino MA, Lino AA, Mazzoni MSC (2007) Chem Phys Lett 449:171
119. Endo T, Nagai D, Monma T, Yamaguchi H, Ochiai B (2004) Macromolecules 37:2007
120. Ochiai B, Yokota K, Fujii A, Nagai D, Endo T (2008) Macromolecules 41:1229
121. Zhi LJ, Wu JS, Li JX, Stepputat M, Kolb U, Müllen K (2005) Adv Mater 17:1492

Top Curr Chem (2010) 293: 35–76
DOI 10.1007/128_2009_21

Published online: 26 February 2010

Hydrogen, Methane and Carbon Dioxide Adsorption in Metal-Organic Framework Materials

Xiang Lin, Neil R. Champness, and Martin Schröder

Abstract The role of porous coordination polymers (metal-organic frameworks) as storage materials for hydrogen, carbon dioxide and methane and the current state-of-the-art in this rapidly developing field are reviewed. The significant potential of porous materials to store fuel gases effectively and reversibly illustrates the great promise of engineered solid-state materials as the next generations of applied multi-functional materials.

Keywords Carbon dioxide storage · Coordination polymer · Fuel gas storage · Gas separations · Hydrogen storage · Metal-organic framework · Methane storage · Porosity

Contents

X. Lin, N.R. Champness, and M. Schröder (✉)
School of Chemistry, University of Nottingham, Nottingham NG7 2RD, UK
e-mail: Martin.Schroder@nottingham.ac.uk

Abbreviations

BET	Brunauer-Emmett-Teller
DABCO	1,4-Diazabicyclo[2.2,2]octane
diPyNI	*N*,*N*′-Di-(4-pyridyl)-1,4,5,8-naphthalenetetracarboxydiimide
diPyTz	Di-3,6-(4-pyridyl)-1,2,4,5-tetrazine
DoE	Department of Energy (USA)
H_2BDC	Benzene-1,4-dicarboxylic acid
H_2BDP	Benzene-1,4-di(4′-pyrazole)
H_2BPnDC	Benzophenone-4,4′-dicarboxylic acid
H_2BPPC	Pyridine-3,5-bis(phenyl-4-carboxylic acid)
H_2ImDC	Imidazole-4,5-dicarboxylic acid
H_2NDC	Naphthalene-2,6-dicarboxylic acid
H_2PPZ	Dihydropiperazinium cation
H_2T^2DC	Thieno[3,2-*b*]thiophene-2,5-dicarboxylic acid
H_3BTB	1,3,5-Tris-(4-carboxyphenyl)benzene
H_3BTC	Benzene-1,3,5-tricarboxylic acid
H_3BTT	Benzene-1,3,5-tris-tetrazole
H_4ABTC	Azodibenzene-3,3′,5,5′-tetracarboxylic acid
H_4BPTC	Biphenyl-3,3′,5,5′-tetracarboxylic acid
H_4MDIP	5,5′-Methylene diisophthalic acid
H_4QPTC	Quaterphenyl-3,5,3′,5′-tetracarboxylic acid
INS	Inelastic neutron scattering
IRMOF	Isoreticular metal-organic framework
LDA	Lithium diisopropylamide
MOF	Metal-organic framework
NH_2-H_2BDC	2-Amino-benzene-1,4-dicarboxylic acid
NPD	Neutron powder diffraction
PDF	Pair distribution function
Pyen	5-Methyl-4-oxo-1,4-dihydropyridine-3-carboxaldehyde
ZIF	Zeolitic imidazolate framework
ΔH_{ads}	Heat of enthalpy of adsorption

1 Introduction

Fossil fuels represent a vital energy resource for human activities and there are growing concerns that oil reserves cannot be sustained in the face of increasing worldwide demand. The increasing level of carbon dioxide (CO_2) in the atmosphere produced from the burning of fossil fuels has also raised increasing concerns over the impact on global eco-systems [1]. Ongoing research efforts to address these concerns have focussed on many aspects including capture and storage of CO_2, and

the use of cleaner energy sources such as methane (CH_4) or methanol as alternatives to petroleum or diesel in vehicular applications. The potential use of hydrogen (H_2) as an energy carrier in principle reduces or even eliminates CO_2 emissions entirely at the point of use [2–7]. For all of these applications the key target and required technological advance is the invention of new polyfunctional materials that are highly efficient for fuel gas separation, capture and reversible storage. Porous coordination polymers constructed from metal cation and cluster nodes linked by ligand linkers are an important class of new hybrid solids that show potential for such applications [8–10]. The formation of coordination polymers has been recognised for decades as a class of metal complexes [11–15] but it was only in the early 1990s that they were recognised as potential porous hosts for substrate inclusion via the formation of stable 3-D superstructures [16–18]. 2-D and 3-D coordination polymers showing permanent porosity are often named metal-organic frameworks (MOFs), but conceptually they are no different to coordination polymers constructed via the node-linker, building block [16–18] or tecton [19, 20] methodology, and can also be regarded as crystal-engineered solids [21–23].

One of the key significant scientific challenges facing "The Hydrogen Economy" [2–7] is that of inventing safe, efficient and effective stores for H_2 gas, and to replace current technologies based around the compression of H_2 as a liquid or as a gas using cryogenic temperatures or high pressures [7]. Therefore, there is major world-wide interest in meeting the United States Department of Energy (DoE) targets of 6.5 wt% gravimetric and 45 g L^{-1} volumetric H_2 storage by 2010, and 9.0 wt% and 81 g L^{-1} by 2015 for mobile applications [7]. Physisorption of H_2 within a light, porous and robust material is an especially attractive option since this maximises the possibility of highly reversible gas storage with fast kinetics and stability over multiple cycles. Although physisorption of H_2 in porous hosts can be highly reversible via changes in pressure and/or temperature, the storage involves low binding energies and isosteric heats of adsorption (typically less that 6 kJ mol^{-1}) and therefore cryogenic temperatures, typically 77 K, need to be used to achieve reasonable substrate uptake capacities. In contrast, chemisorption of H_2 involves a much higher enthalpic ΔH_{ads} contribution but may also lead to slower and poorer kinetics due to the requirement for reversible cleavage and formation of the H–H bond with concomitant generation of heat [7].

The use of CH_4 in mobile applications has similar problems to the use of H_2 although the challenges are reduced. CH_4 is a gas at room temperature but has a relatively low boiling point (−164°C). An economic and safe on-board storage system is one of major technical barriers preventing CH_4-driven automobiles from competing with traditional petroleum-driven vehicles. The US DoE target for CH_4 storage is 180v(STP)/v under 35 bar at ambient temperatures [24, 25]. This is the same energy density as that of compressed natural gas, currently used at 100 bar. Some porous carbons have capacities very close to this target [26], and some coordination polymers can out-perform these materials in CH_4 adsorption and exceed the DoE targets [27, 28].

CO_2 is one of the most important greenhouse gases and the current approach to tackling increasing levels of atmospheric CO_2 is to capture and remove CO_2 from

the flue exhaust of power plants. This is accomplished by cooling and pressurizing the exhaust or by the chemical reaction of CO_2 with aqueous amine solution. Both processes involve very high energy costs and are currently inefficient [29, 30]. Physisorption of CO_2 in porous MOFs provides a high capacity [31] but with relatively low adsorption enthalpy. Recent developments have shown that chemical modification of MOF surfaces with amine groups can offer excellent selectivity for CO_2 from mixtures of CO_2/N_2, CO_2/CH_4 and CO_2/CO [32–34].

This chapter reviews and highlights the key porous coordination compounds that show potential for gas adsorption and storage applications with particular emphasis on the fuel gases H_2, CH_4 and CO_2.

1.1 Design Principles

Micro- and meso-porous oxide-based materials such as zeolites can be designed via the use of molecular or supramolecular templates [35–39]. However, the chemical nature of the interior surface on which a target gas will be adsorbed is difficult to modify in a systematic manner. MOFs are very promising materials [40–45] that afford innovative approaches to the design and synthesis of porous light-weight materials with potentially large internal surface areas [46]. MOFs are comprised typically of metal centre(s) onto which is bound organic donor molecules (ligands) that, rather than binding to a single metal centre, bridge these metal centres to afford coordination polymers. By judicious design and choice of metal nodes and bridging ligands, specific framework topologies can be targeted, while functionalisation and modification of the ligand and metal centres can fine-tune the electronic and chemical nature of the resultant framework surface. By appropriate design of metal nodes, ligand bridges, solvent, synthetic conditions and templates, MOF materials showing porosity and open structures can be prepared [47].

Although metal-ligand coordination polymers have been known for many decades [11–15], creating novel and functional materials by design has only really developed over the past 15 years. Design principles derived from crystal engineering using the node-linker [42, 48, 49], tecton [19, 20, 50] and building-block [16–18] methodologies have underpinned this work.

The structure of the framework defines its gas adsorption properties. Thus, the modular construction of MOFs offers flexibility to manipulate and decorate the framework structure at a molecular level and, in principle, improves and refines the gas adsorption of the material on demand. The ultimate goal is to gain full control and understanding over the framework structure and synthesis at a predictive level. Such design and control remains difficult to achieve in practice [40, 51], but series of analogous materials have been successfully synthesised to afford systematic variations of pore size, shape and functional groups at the pore surface [52–57]. Such studies provide valuable data to assess the factors that affect gas adsorption, separation and uptake/release behaviour, and guide the further design of porous coordination polymers.

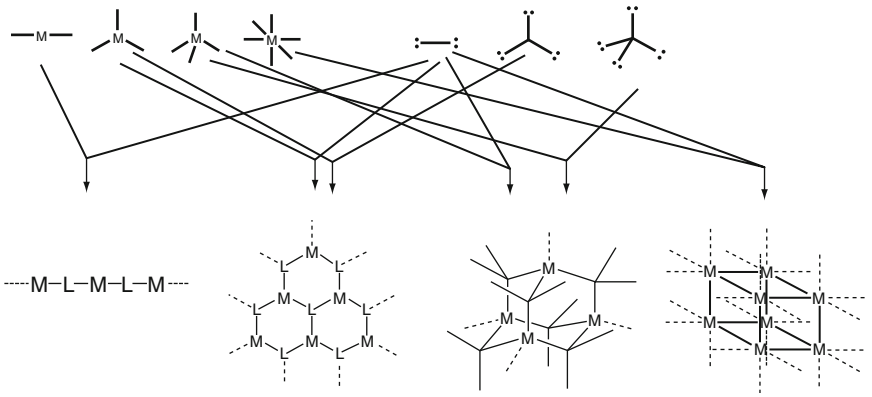

Fig. 1 Assembly of nodes and linker to form polymer structures [47]. Reproduced by kind permission of the authors

There are many excellent reviews covering various aspects of network topologies and approaches to coordination polymers [22, 42–44, 47, 49, 58–65]. The most important characteristics for nodes and linkers are their connection numbers and their overall geometries. Figure 1 illustrates some of the basic motifs generated by combinations of different metal nodes and organic linkers. For example, Cu(I) ions are known to connect in a tetrahedral stereochemistry to four 4,4′-bipyridyl ligands (L), and the resulting cationic frameworks $\{[Cu(L)_2]^+\}_\infty$ have an overall polymeric diamondoid structure [66–68]. By manipulation of metal stereochemistry and the angular nature of the ligand linkers, highly complex topologies can be generated [23, 69–71]. There is also interest in developing MOFs that mimic the topologies of zeolites [54, 55, 72–78]. For example, the angle between two coordinating vectors in the imidazolate ligand is very close to that in the Si–O–Si moiety in silicates. Thus, combinations of imidazolate and metal ions [Zn(II), In(III) or Co(II)] have afforded zeolitic imidazolate frameworks (ZIFs) [54, 55, 75–78].

2 H_2, CH_4 and CO_2 Adsorption

The first report of gas adsorption in a MOF was in 2000 and described the adsorption of CH_4 in $[Cu(4,4\text{-bipy})SiF_6]_\infty$, which shows an adsorption capacity comparable to that of zeolites and active carbons [79]. The first example of H_2 storage in a MOF was reported in 2003 [80]. A wide range of such materials have now been investigated and we summarise herein some representative compounds and systems with particular emphasis on the different classes and types of porous coordination polymers that show significant gas uptake and storage potential.

2.1 Prussian Blue Analogues

Prussian Blue, $Fe_4[Fe(CN)_6]_3 \cdot 14H_2O$, has been known for three centuries, and its crystal structure [81] incorporates octahedral Fe(II) centres bound to six cyanide ligands in an $[Fe(CN)_6]^{4-}$ moiety. The terminal N-donors of the cyanide ligands point to additional Fe(III) centres and a charge-balance of four Fe(III) centres with three $[Fe(CN)_6]^{4-}$ anions is achieved. Six of the 14 water molecules are bound to Fe(III) and the remaining 8 fill the void in the framework structure and can be removed by heat treatment *in vacuo*. A wide variety of Prussian Blue analogues $M_x[M'(CN)_6]_y \cdot zH_2O$ [M = Mn, Fe, Co, Ni, Cu, Zn; M′ = Cr, Mn, Fe, Co] can be prepared by employing different transition metal ions, and these materials have the same overall framework structure [82]. The complexes $M_3[Co(CN)_6]_2 \cdot xH_2O$ (M = Mn, Fe, Co, Cu, Zn, $x = 16$; M = Ni, $x = 15$) give stable porous framework materials on removal of water molecules, and Ar isotherms on $M_3[Co(CN)_6]_2$ give BET surface area measurements in the range of 560–870 $m^2\ g^{-1}$ comparable to zeolites. The H_2 adsorption isotherms for these species show good reversibility with an uptake of 1.4–1.8% H_2 at 890 Torr and 77 K. In the reported pressure range, no correlation between BET surface and H_2 uptake was established for these materials [82].

A series of dehydrated Prussian blue analogues $M_3[Co(CN)_6]_2$ (M = Mn, Fe, Co, Ni, Cu and Zn) has also been reported. The heats of adsorption ΔH_{ads} for H_2 in these Prussian blue analogues are in the region of 6.5–7.0 kJ mol^{-1}, except for $Mn_3[Co(CN)_6]_2$ which has a low value of 5.3 kJ mol^{-1} [82]. These binding energies are relatively low, consistent with the observation from high energy X-ray scattering experiment on an H_2-loaded samples of $Mn_3[Co(CN)_6]_2$ and time of flight neutron powder diffraction (NPD) on D_2-loaded samples of $Mn_3[Co(CN)_6]_2$ which gave no evidence for binding interactions of the adsorbed H_2 or D_2 with the accessible metal sites [83]. These experiments were carried out at 30 and 77 K, respectively, using a differential pair distribution function (PDF) to estimate the position of H_2 molecules. The most plausible position for the H_2 molecules in the $Mn_3[Co(CN)_6]_2$ framework, based upon these studies, is about a single disordered site at the centre of the pore, which maximises van der Waals interaction with the pore surface lined with highly polarisable cyanide groups.

At very low temperature (5 K), the Rietveld profile analysis of NPD data of D_2-loaded samples of $Cu_3[Co(CN)_6]_2$ reveals two possible adsorption sites [84], one at the centre of the pore, the (¼, ¼, ¼) site, which is consistent with the PDF study on $Mn_3[Co(CN)_6]_2$ [83]. The other is situated on (x, 0, 0) ($x \approx 0.183$) sites, which results from $[Co(CN)_6]^{3-}$ vacancies, suggesting a Cu–D_2 distance of 3.16 Å. The study suggested that at low loading the (¼, ¼, ¼) site is the preferred adsorption site, and the weak D_2–Cu interaction accounts for only ~25% H_2 adsorption at high loading.

2.2 Zn(II) Carboxylates

The IRMOF series of complexes is based upon $[Zn_4O]$ nodes linked by linear ditopic carboxylate ligands (Fig. 2) [80, 85–88] and is prepared by reaction of

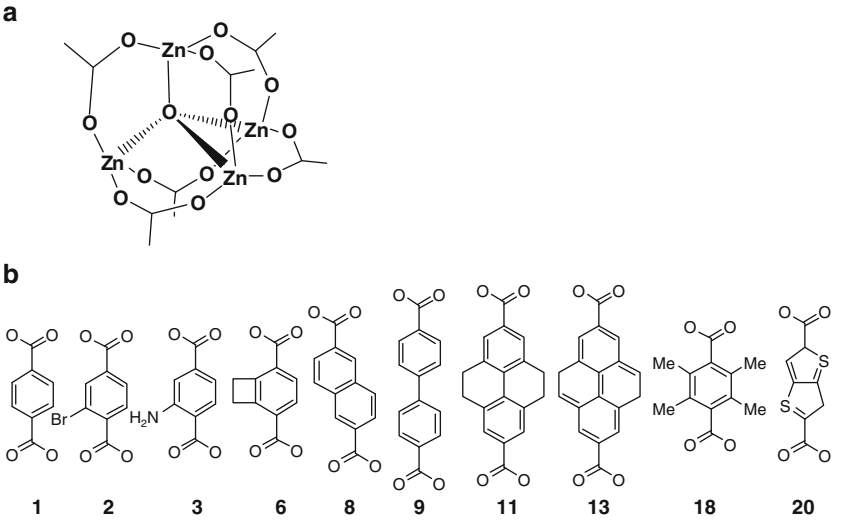

Fig. 2 View of (**a**) [Zn_4O] node; (**b**) the series of organic linkers in IRMOFs

$Zn(NO_3)_2$ with carboxylate ligands in a polar solvent typically dimethylformamide or diethylformamide at 80–120°C. Microwave-assisted synthesis or electrolysis has been reported to give faster or larger-scale synthetic procedures [89, 90]. In these materials the [Zn_4O] node is comprised of four Zn(II) ions on the vertices of a tetrahedron with an O^{2-} moiety at the centre of the tetrahedron. Each pair of Zn(II) ions is bridged by a carboxylate group (Fig. 2a), and, therefore, each [Zn_4O] node is connected to six carboxylate linkers constructing a simple cubic topology [80]. The size of the pore can be controlled by the length of the linker and number of other pendant groups on the phenyl rings. Longer linkers tend to produce larger voids and up to 80.3% of the material volume is void when thieno(3,2-)thiophene-2,5-dicarboxylic acid is used.

The pore structures of the IRMOF series can be viewed as three mutually perpendicular arrays of channels that intersect at cavities, with the sizes and shapes of the channels and cavities controlled by the linkers. The linkers in IRMOF-1, 3, 6, 8 and 18 have the same overall length, but the diameters of the channels and the cavities are affected by the functional groups on the phenyl ring only. These functional groups reduce the size of pores, and this enhances the interaction energy with adsorbed molecules when the attractive potential fields of opposite walls overlap [91]. This results in higher H_2 adsorption for IRMOF-3 and 6 than for IRMOF-1 and 2 at 1 bar (the low gravimetric uptake of IRMOF-2 is due to heavy Br atoms in the framework). However, introduction of too many functional groups, as in IRMOF-18, leads to occupation and reduction of the size of the void and this limits the uptake of H_2.

An alternative method of manipulating the pore shape and size with MOFs is to prepare interpenetrated frameworks [92]. It is well known that increasing the length

of the ligand linkers leads to interpenetration of frameworks in which the void in one net is filled by another net passing though it [93, 94]. In the series of IRMOF materials, once the length of the linker reaches two phenyl rings, interpenetration is observed and this results in lower porosity for the resultant framework material. The degree of interpenetration in these systems can be as high as fourfold when the linker contains a linear quaterphenyl chain [95]. Interpenetration significantly reduces the diameters of the pores, but can also enhance the adsorption enthalpy ΔH_{ads} of H_2 binding by increasing the overlap of the attractive potential of opposite walls [91]. Adsorption of H_2 by the interpenetrated materials IRMOF-11 and 13 is thus noticeably higher than for other IRMOFs at 1 bar (Table 1).

The saturation uptake for IRMOFs was found to be proportional to the pore volume/BET surface [88]. Thus, although introducing functional group(s) and/or interpenetration may increase the heat and strength of adsorption of the substrate, this comes at a price with a potential reduction in the available free volume available for gas adsorption due to the decrease in pore volume. Therefore, there will be an overall decrease in the maximum uptake capacities. Thus, current approaches seek to increase the length of the ligand linker to increase pore volume, but at the same time to avoid interpenetration. The length of the linkers in IRMOF-8 and 20 are longer than in IRMOF-1, 3, 6, 8 and 18, but do not induce interpenetration of frameworks. Accordingly, IRMOF-20 has the highest saturation H_2 uptake (6.7 wt%) in the IRMOF series, although its uptake at 1 bar is not especially impressive.

Preparative procedures can significantly affect the porosity and H_2 adsorption of IRMOF-1 (MOF-5). An anhydrous synthesis can make IRMOF-1 adsorb 36% more H_2 (excess uptake of 5.2 wt% vs 7.1 wt%) [87], although the improvement in BET surface area was minor (3,530 vs 3,800 $m^2\ g^{-1}$). This difference in adsorption behaviour is probably caused by the instability of IRMOF-1 to water which would be expected for a relatively labile Zn(II) centre. Thus preparation of IRMOF-1 under strictly anhydrous conditions affords one of the best performing MOF materials for H_2 adsorption. At 77 K and 100 bar, IRMOF-1 can store a total of 10.0 wt% H_2 [87].

An interesting attempt has been made to enhance the interaction of IRMOF-1 with H_2 by modifying the pore surface with $Cr(CO)_6$. The reaction of $Cr(CO)_6$ with the phenyl rings in IRMOF-1 at 160°C successfully forms "piano-stool" chromium complexes within the framework, retaining the porosity of the framework during the reaction [96]. UV irradiation of the IRMOF-1-$Cr(CO)_3$ under an H_2 atmosphere can remove one carbonyl which is replaced by H_2 molecules, which can in turn be replaced by N_2 molecules under an N_2 atmosphere. Considering the instability of molecular Cr–N_2 complexes [97], it is worth noting that the Cr–N_2 bond is stable within the IRMOF-1 framework at room temperature. Although this process does not improve the overall H_2 storage capacity of IRMOF-1, it shows a potential route to use MOFs as a matrix to stabilise active species and to introduce direct chemical binding of H_2 to a vacant metal centre within such a framework.

CH_4 and CO_2 adsorption capacities for the IRMOF series compounds are high due to their high surface areas and pore volumes. IRMOF-1 (MOF-5) and IRMOF-3

Table 1 Porosity and gas uptake data for a series of IRMOF materials

Materials	IRMOF-1 (MOF-5)	IRMOF-2	IRMOF-3	IRMOF-6	IRMOF-8	IRMOF-9[a,b]	IRMOF-11[a]	IRMOF-13[a]	IRMOF-18	IRMOF-20
A_{BET} (m^2 g^{-1})	3,362	1,722	2,446	2,476	1,466	1,904	2,340	1,551	1,501	3,409
[c]V_p (cm^3 g^{-1})	1.23	0.88	1.07	1.14	1.27	0.90	0.71	0.73	0.74	1.53
N_{H2} (1 bar)(wt%)	1.32	1.21	1.42	1.48	1.50	1.17	1.62	1.73	0.89	1.35
N_{H2} (max) (wt%)	5.2/45.4			4.8/45.3			3.5/33.7			6.7/67.3
Pressure (bar)	10.0/100									

[a]Double-interpenetrating frameworks

[b]Sample loses crystallinity upon desolvation and thus results are not comparable to others in the series

[c]Void calculated from crystal structures

can adsorb 135 and 120 v(STP)/v CO_2, respectively, at 298 K and 36 bar. The highest CH_4 storage capacity was observed on IRMOF-6, 155 v(STP)/v at 298 K and 36 bar [52], which represents 70% of the amount stored in compressed CH_4 cylinder (200 bar) in current commercial use.

CO_2 adsorption at room temperature by the IRMOF series of coordination polymers takes place via monotonic Type-I isotherms [31]. All CO_2 adsorptions reach plateau capacities at pressures over 35 bar, which qualitatively scale with their surface areas and pore volumes. IRMOF-1, 3 and 6 show 18.5, 19 and 22 mmol g^{-1} CO_2 adsorption at 298 K and 35 bar, respectively, and have greater capacities for CO_2 than other IRMOF compounds due to their larger pore volumes. Also, A theoretical study suggests that there is no structural change in IRMOF-1 on CO_2 loading although the CO_2 adsorption in IRMOF-1 exhibits inflections assigned to phase change behaviour of adsorbed CO_2 [98].

2.2.1 High H_2 Adsorption Density

MOF-74 was synthesised by the reaction of $Zn(NO_3)_2 \cdot 4H_2O$ and dihydroxyl-1,4-benzenedicarboxylic acid in a mixture of DMF, 2-propanol and water. Zn(II) cations are bridged by carboxylate and hydroxyl groups to give a hexagonal 1-D channels [86]. The BET surface area (870 m^2 g^{-1}) and H_2 uptake (1.7 wt% at 77 K and 1 bar) of MOF-74 are modest compared to other IRMOF materials, but MOF-74 has very high H_2 uptake at low pressure. It can adsorb 1.0 wt% H_2 at 100 mbar, which is at least five times the capacity of other IRMOF materials (Fig. 3a). The H_2 adsorption enthalpy (8.8 kJ mol^{-1}) in MOF-74 is also higher than the others and it does not alter below loadings of 0.5 wt% H_2 [86]. These observations indicate a

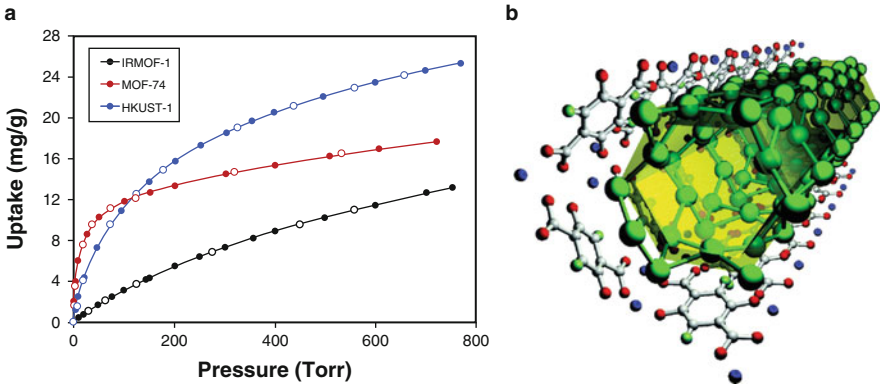

Fig. 3 (**a**) Comparison of H_2 adsorptions of MOF-74 and IRMOF-1 and HKUST-1 at 77 K. (**b**) The green balls show the close packing of D_2 molecules inside the channels of MOF-74, which was revealed by refinement based on NPD experiments [99]. Reproduced by kind permission of the authors

strong H_2-framework interaction at low H_2 loading. The Rietveld profile analysis of NPD on D_2 loaded MOF-74 (Fig. 3b) revealed that the D_2–D_2 intermolecular distances in the first layer vary from 2.85 to 4.2 Å with an average of 3.4 Å, which is shorter than the 3.6 Å found for solid D_2 [99], indicating that the packing density of D_2 on the surface of MOF-74 can be higher than that of solid D_2. Quantum mechanical calculations also suggested that such short D_2–D_2 distances are reasonable in the potential well created in MOF-74 (see also Sect. 2.3.6).

2.2.2 Framework Based on a Tri-Branched Carboxylate Ligand: MOF-177

The design of new framework topologies and structures seeks to avoid interpenetration in order to maximise total H_2 uptake. Combination of the 6-connected [Zn_4O] node, as in the IRMOF series, with the 3-connected tri-branched linker 1,3,5-tris-(4-carboxyphenyl)benzene (BTB^{3-}) produces a (6,3)-net, MOF-177, which incorporates a large void in the framework [85, 100] (Fig. 4). The Langmuir surface area for MOF-177 is estimated from N_2 isotherms as over 4,500 $m^2\ g^{-1}$ and the pore volume of 1.59 $cm^3\ g^{-1}$ is the highest in the Zn-based MOFs. H_2 uptake in MOF-177 at 77 and 1 bar is not impressive, only 1.24%, but the large pore volume offers a great potential at high pressure with a 7.5% uptake at 77 K and 70 bar.

The large pore volume of MOF-177 makes it an ideal material for CO_2 adsorption and it has much higher CO_2 adsorption capacity than the IRMOF series compounds discussed above. At 298 K and 42 bar, MOF-177 can adsorb 33.5 mmol g^{-1} CO_2, which is also higher than the best CO_2 capacity reported for a zeolite (7.4 mmol g^{-1} for zeolite 13X) and activated carbon (25 mmol g^{-1} for MAXSORB) [31].

CH_4 adsorption on MOF-177 is less impressive than its CO_2 adsorption capacity. MOF-177 adsorbs 70v(STP)/v of CH_4 at 298 K, 35 bar, which is similar to activated

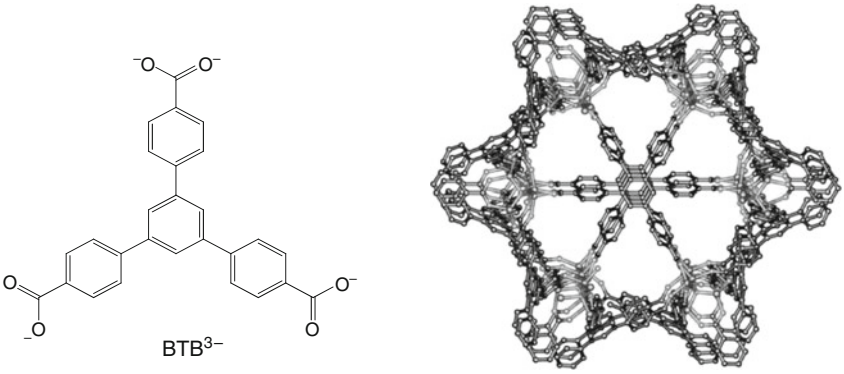

Fig. 4 View of the linker BTB^{3-} and the structure of MOF-177 [100]. Reproduced by kind permission of the authors

carbon, and only at higher pressures does MOF-177 out-perform activated carbon and even then only marginally [10a]. Interestingly, Cu(II)-carboxylate-based materials have been found to be more efficient for CH_4 adsorption than Zn(II)-carboxylate based systems (see Sect. 2.3).

2.3 Cu(II) Carboxylates

2.3.1 HKUST-1: Cu(II) with Benzene-1,3,5-tricarboxylate

Carboxylate ligands can bridge metal cations to form square paddlewheel $M_2(O_2CR)_4$ moieties and these can act as 4-connected nodes in coordination polymer construction. Such bimetallic tetracarboxylate units are common and are often highly stable [101, 102]. Combination of the 4-connected node $M_2(O_2CR)_4$ with the 3-connected anionic linker benzene-1,3,5-tricarboxylate (BTC^{3-}) affords $[Cu_3(BTC)_2]_\infty$ (HKUST-1) [103–105] and $[Mo_3(BTC)_2]_\infty$ (TUDMOF-1) [106] both having (3,4)-framework structures analogous to Pt_3O_4-type nets. HKUST-1 was prepared by reaction of $Cu(NO_3)_2$ and H_3BTC in DMF/H_2O/ethanol mixture at 85°C, while TUDMOF-1 was synthesised with $Mo(CO)_6$ and H_3BTC in refluxing DMF at 156°C under an Ar atmosphere. Although the synthetic conditions for these two materials are different, they have similar structures and show similar gas adsorption behaviours. The BET surface areas estimated from N_2 isotherms are 1,507 and 1,280 $m^2\ g^{-1}$ for HKUST-and TUDMOF-1, respectively. Considering the higher molecular weight of TUDMOF-1, the difference between these materials is less than 5%, suggesting very similar behaviour for the N_2 molecules within the pores of the framework. HKUST-1 can adsorb 2.54 wt% H_2 at 1 bar and 77 K while TUDMOF-1 adsorbs 1.75 wt%. Considering the difference in the formula weight, the copper-based framework HKUST-1 can adsorb 25% more H_2 than the molybdenum-based framework (TUDMOF-1), suggesting that choice of metal centre node can play an important role in maximizing gas uptake.

The D_2 adsorption in HKUST-1 under 4 K has been studied in detail by INS and NPD [107–109]. NPD revealed that the strongest adsorption site is at the exposed Cu(II) with a Cu–D_2 distance of 2.40 Å. The filling of the pores follows the order of smaller preceding large pores, consistent with the theory of micropore filling. Further analysis by INS suggested that H_2 has a tendency to lie in a plane perpendicular to the Cu–Cu bond in the $\{Cu_2\}$ node [108], and the INS peaks at 9.1, 12.75 and 14.0 meV were assigned to rotational transitions of D_2 from $J = 0$ to 1, $M = \pm 1$.

Significantly, HKUST-1 adsorbs considerable amounts of CH_4 [109 v(STP)/v at 35 bar, 298 K and 228 v(STP)/v at 150 bar, 298 K] [110], higher than the other more porous materials such as Zn-based MOF-177, Cr-based MIL-101 and activated carbon. CH_4 uptake by HKUST-1 has a significant non-linearity below 50 bar, suggesting significant interaction between the Cu(II)-based pores and CH_4.

2.3.2 The NOTT-xxx Series: Cu(II) with Linear Di-isophthalate Ligands

The 4-connected di-copper node $Cu_2(O_2CR)_4$ can be combined with other linkers [56, 57, 111–113] to produce more complex frameworks. For example, reaction of biphenyl-3,5,3′,5′-tetracarboxylic acid, an angular 4-connected linker, with $Cu_2(O_2CR)_4$ leads to the construction of a (4,4)-net which has a simplified NbO topology [56, 57, 113]. This structure prevents interpenetration compared to the cubic topology of the IRMOF series, and so the length of the linker can be readily varied from biphenyl, terphenyl to quaterphenyl backbones, all linkers producing frameworks with the same topology without interpenetration (Fig. 5) [56, 57]. The desolvated materials have the same stoichiometry $[Cu_2(L)]_\infty$, and Table 2 lists their BET surface areas and H_2 uptake data. However, when the phenyl number in the ligand increase to five, the double interpenetrated framework NOTT-104 is formed; framework NOTT-104 is however not stable to de-solvation.

The pore sizes estimated from the N_2 isotherms are 6.5, 7.3 and 8.3 Å for NOTT-100, NOTT-101 and NOTT-102, respectively. Accordingly, NOTT-100 can adsorb 2.57 wt% of H_2 at 1 bar, NOTT-101 absorbs 2.52 wt%, while the most porous NOTT-102 can only adsorb 2.24 wt% at 1 bar. These uptakes are significantly higher than those for Zn-based IRMOF materials. At 1 bar, the adsorption is far from reaching saturation. Thus, a small pore can provide a high attractive force to adsorb H_2 molecules due to greater overlap of the potential field leading to the small-pored NOTT-100 adsorbing more H_2 than NOTT-101 and NOTT-102 at low pressures. At 20 bar, NOTT-100 nearly reaches its adsorption saturation at 4.02 wt % uptake of H_2, while NOTT-101 and NOTT-102 adsorb 6.06 and 6.07 wt% H_2, respectively, comparable to 6.08 wt% measured for MOF-177. However, NOTT-101 and NOTT-102 have smaller pore volumes than MOF-177 and thus MOF-177 has a higher H_2 uptake at higher pressures.

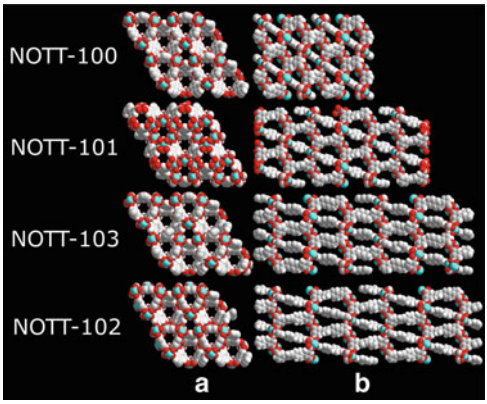

Fig. 5 Space-filling views of NOTT frameworks, in which water molecules have been removed from Cu(II) sites to show the two types of window in the frameworks: (**a**) view along the *c*-axis; (**b**) view along the *a*-axis [56]. Reproduced by kind permission of the authors

Table 2 Gas adsorption data for NOTT-xxx and PCN-14 materials

Compound	NOTT-101	NOTT-102	NOTT-103	NOTT-105	NOTT-106	NOTT-107	NOTT-110	NOTT-111	PCN-14
BET surface area ($m^2\ g^{-1}$)	2,316	2,942	2,929	2,387	1,855	1,822	2,960	2,930	1,718
Pore diameter (Å)	7.3	8.3	8.0	7.3	7.3	7.0	8.0	8.0	
Pore volume (cc g^{-1})	0.886	1.138	1.142	0.898	0.798	0.767	1.22	1.19	0.870
Total H_2 adsorption in mg g^{-1} (1 bar/20 bar/ 60 bar)	2.52/6.06/6.60	2.24/6.07/7.20	2.63/6.51/7.78	2.52/5.40	2.29/4.50	2.26/4.46	2.64/6.59/7.62	2.56/6.48/7.36	2.70/4.00/4.42

The Rietveld profile analysis of NPD on a D_2-loaded sample of NOTT-101 shows a Cu–D_2 distance of 2.50 Å [56], slightly longer than that observed in HKUST-1 (2.40 Å) [108]. Two other adsorption sites, one located in the middle of a window and the other in the cusp of three phenyl rings, were identified close to the centre of three {Cu_2} paddle wheels in NOTT-101, but the filling order for these sites is not as clear-cut as in HKUST-1. This is reasonable as the pores in NOTT-101 are larger than in HKUST-1 and thus afford more similar sites in terms of H_2-framework affinity.

2.3.3 Modification of NOTT-101 and NOTT-102

The high porosity of NOTT-101 and NOTT-102 can accommodate functional groups onto the central phenyl groups and the resultant materials retain porosity. This allows the systematic study of the relationship between the functional groups and H_2 uptake (Fig. 6). Table 2 summarises the variation of H_2 adsorption in these Cu(II) materials. NOTT-105, 106, and 107 have the same ligand length and network topology and, therefore, their results are readily comparable [56]. Compared to NOTT-101, modest changes in H_2 uptake in these materials were observed. The small differences observed at 1 bar can be attributed to the changes of pore size with the reduced H_2 uptake at high pressures a result of reduced pore volume due to the additional functional groups. This is also supported by the fact that all adsorption enthalpies are increased in the functionalised material but drop rapidly with increasing H_2 loading. PCN-14 [114] has the highest H_2 uptake of 2.70 wt% at 1 bar and 77 K and this is probably due to the large aromatic surface, while its H_2 uptake at high pressure is not as impressive due to the relative small pore volume caused by introduction of the bulky anthracene group.

Increasing the ligand aromatic surface seems have a positive effect on H_2 adsorption. NOTT-103 contains a naphthalene group and NOTT-110 [115] a phenanthrene group. At 1 bar and 77 K, NOTT-103 adsorbs 2.63 wt% H_2 and NOTT-110 adsorbs 2.64 wt% H_2, which are higher than NOTT-102, albeit they have very similar BET surface areas and pore volumes. Due to the large pore volume, the H_2 adsorptions at 60 bar and 77 K are 7.78 and 7.62 wt% for NOTT-103 and NOTT-110, respectively, which are amongst the highest uptakes reported so far. Replacing the phenanthrene group in NOTT-110 with 9,10-dihydrophenanthrene group only has a minor impact on the H_2 adsorption capacity; however, the heat of adsorption for H_2 uptake in NOTT-111 is ~1.0 kJ mol^{-1} higher than NOTT-102 and NOTT-110 at all the measured loadings [115]. This suggests that higher uptake capacities may not necessarily be related to higher heats of adsorption.

It is worth noting that PCN-14 shows exceptionally high CH_4 storage capacity [27]. At 35 bar and 290 K, the excess adsorption capacity of CH_4 in PCN-14 is 220 v(STP)/v, which is 22% high than the DoE target of 180 v(STP)/v. The heat of CH_4 adsorption is 30 kJ mol^{-1} at low loading and decreases slowly with increasing

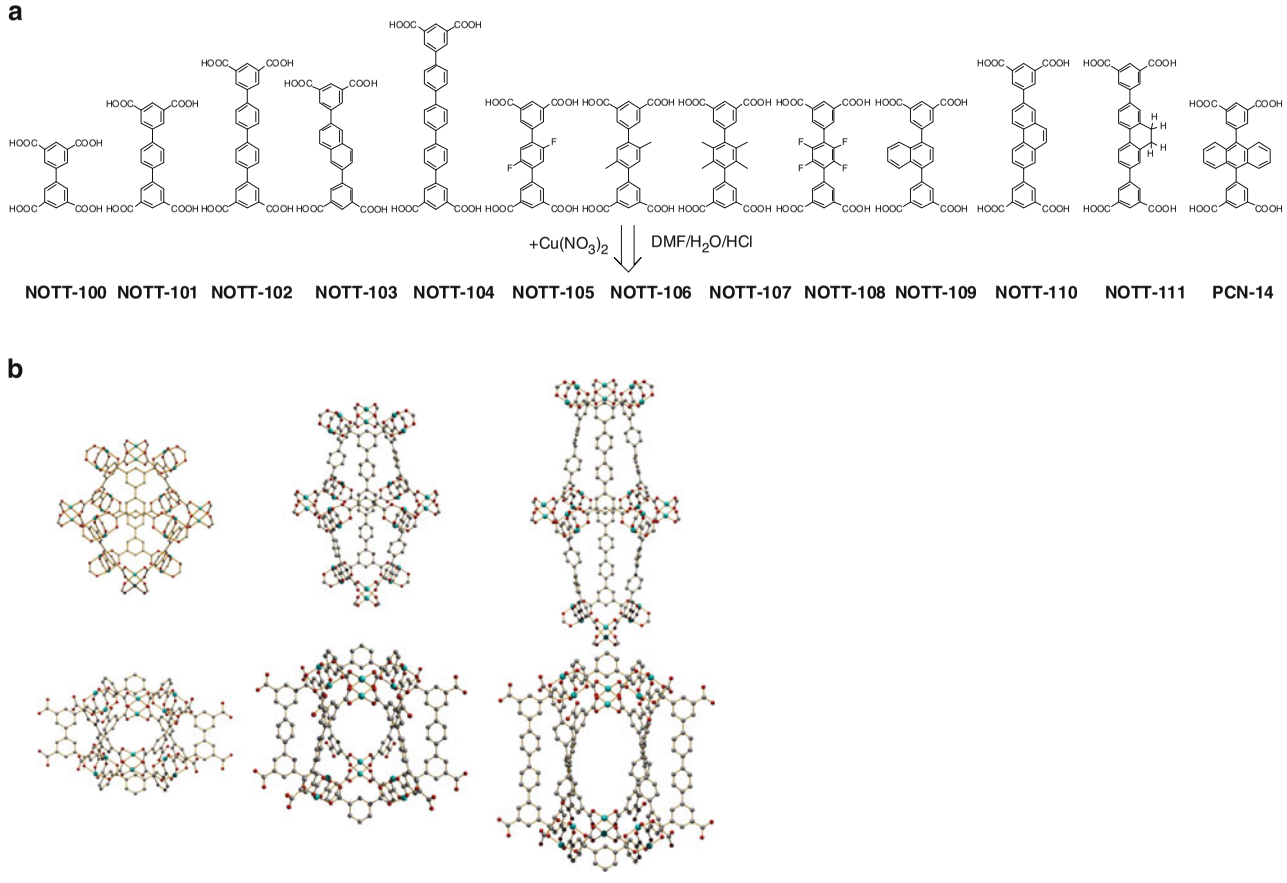

Fig. 6 (**a**) Organic linkers in the NOTT-xxx series of materials; (**b**) the size of cages in NOTT-xxx materials are predefined by the length of ligands [56]. Reproduced by kind permission of the authors

loading. Interestingly, the adsorption enthalpy increases gradually after CH_4 loading of 1 mmol g^{-1}, indicating that CH_4–CH_4 interactions start to dominate the adsorption process. This is supported by single crystal structure analysis of CH_4-loaded $[Zn_2(BDC)_2(DABCO)]$ (H_2BDC = benzene-1,4-dicarboxylic acid, DABCO = 1,4-diazabicyclo[2,2,2]-octane) [116, 117], which suggest that CH_4 can form π-HC interaction with phenyl rings, with the CH_4 molecules stabilised by van der Waals interactions with neighbouring CH_4 molecules.

2.3.4 Cu(II) with Triangular Hexa-carboxylate Ligands

The linear tetra-carboxylate ligand design can be modified to triangular hexa-carboxylate ligands such as 1,3,5-tris-(3,′5′-dicarboxy[1,1″biphenyl]-4-yl)benzene (Fig. 7). The reaction of this ligand and $Cu(NO_3)_2$ in DMSO produces a highly porous crystalline material NOTT-112 [118]. The combination of 4-connected $\{Cu_2\}$ paddle-wheel units and the triangular ligand builds up a spectacular cage structure (Fig. 7) comprising three types of cage of diameters of 13, 13.9 and 20 Å, respectively, tiling 3-D space. Although similar network topologies have been reported [119, 120], the framework NOTT-112 shows good stability and extraordinary gas adsorption capacity with a BET surface area of 3,800 m^2 g^{-1} and total pore volume of 1.62 cm^3 g^{-1}. This is one of the most porous materials discovered so far; only IRMOF-1 (prepared under anhydrous conditions) [87], MOF-177 [88, 121] and MIL-101 [122, 123] have similar BET surface areas and pore volumes. The total H_2 uptake of NOTT-112 is over 10.0 wt% above 80 bar and 77 K, comparable to IRMOF-1 and MOF-177. Interestingly, NOTT-112 out-performs these phases at lower pressure of H_2 and shows a total uptake of 7.8 wt% at 20 bar and 77 K. At 1 bar and 77 K, NOTT-112 can adsorb 2.3 wt% H_2, which is nearly double the levels of IRMOF-1 (1.32 wt%) and MOF-177 (1.25 wt%). NOTT-112 represents an interesting case that mixes excellent H_2 adsorption performance in both low pressure and high pressure regions; this is due to the exposed Cu(II) centres and the mix of varied sized cavities within the structure.

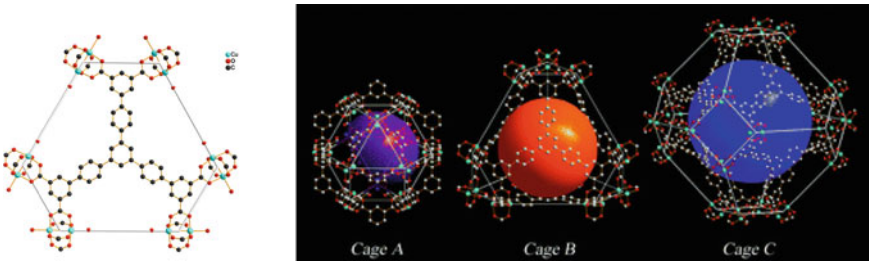

Fig. 7 The structures of ligand and cages in NOTT-112 [62]. Reproduced by kind permission of the authors

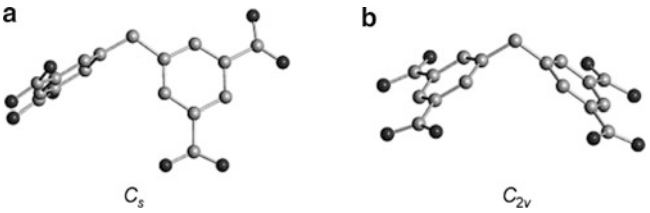

Fig. 8 C_s and C_{2v} configuration of $MDIP^{4-}$ ligand in PCN-12 and PCN-12′

2.3.5 Cu(II) with Angular Di-isophthalate Ligands

The network topology of Cu-isophthalate frameworks can be further modified by employing a non-linear ligand 5,5′-methylene diisophthalate ($MDIP^{4-}$) (Fig. 8). The reaction of H_4mdip and $Cu(NO_3)_2$ can produce two kinds of materials, PCN-12 and PCN-12′, depending on the reaction temperature and solvent used [124]. Although the chemical composition of the PCN-12 and PCN-12′ frameworks are the same, [Cu_2(MDIP)], the configuration of $MDIP^{4-}$ ligands are different in the two materials. In PCN-12 and PCN-12′, $MDIP^{4-}$ adopts C_s and C_{2v} configurations, respectively, with formula [Cu_6(C_s-MDIP)$_2$(C_{2v}-MDIP)(H_2O)$_6$] for PCN-12 and [Cu_2(C_{2v}-MDIP)] for PCN-12′. PCN-12 has a BET surface area of 1,943 $m^2\ g^{-1}$ and pore volume of 0.94 cc g^{-1}, comparable to other di-isophthalate-Cu(II) materials [56]. Interestingly, its H_2 uptake at 1 bar and 77 K is the highest reported so far at 3.0 wt%. The authors proposed that the exceptional H_2 uptake at 1 bar and 77 K relates to the unique alignment of open metal sites in the cuboctahedral cages in PCN-12, with exposed Cu(II) centres pointing into the cage, the collective effect of these Cu(II) centres generating high framework-H_2 interactions [124]. INS results support this postulate with two principal bands observed at 7.7 and 8.6 meV, lower than for analogous {Cu_2} sites in HKUST-1 (9.2 meV) and NOTT-101 (9.2 meV), indicating a stronger interaction of H_2 with the Cu sites in PCN-12.

2.3.6 Cu(II) with Polyfunctional Ligands

A 3-D (3,6)-connected biporous coordination framework incorporating two different channels (A and B in Fig. 9) has been synthesized using a designed polytopic ligand 3,5-dicyano-4-(4-carboxyphenyl)-2,2′,6′,4″-terpyridine (HDCCPTP). The framework, [Cu(DCCPTP)(NO_3)]·0.5(1,4-dioxane)·0.5MeOH, incorporates both free nitrile and free amine groups decorating the pore walls [125]. The desolvated framework absorbs 1.01 wt% H_2 at 0.2 bar and this reaches a value of 1.91 wt% at 20 bar at 77 K. Although the maximum uptake of H_2 is modest, the H_2 adsorption density and the relative H_2 absorption at low pressure (below 1 bar) is especially high [125]. [Cu(DCCPTP)(NO_3)] represents a rare example of a framework with two different free functional groups within a porous structure.

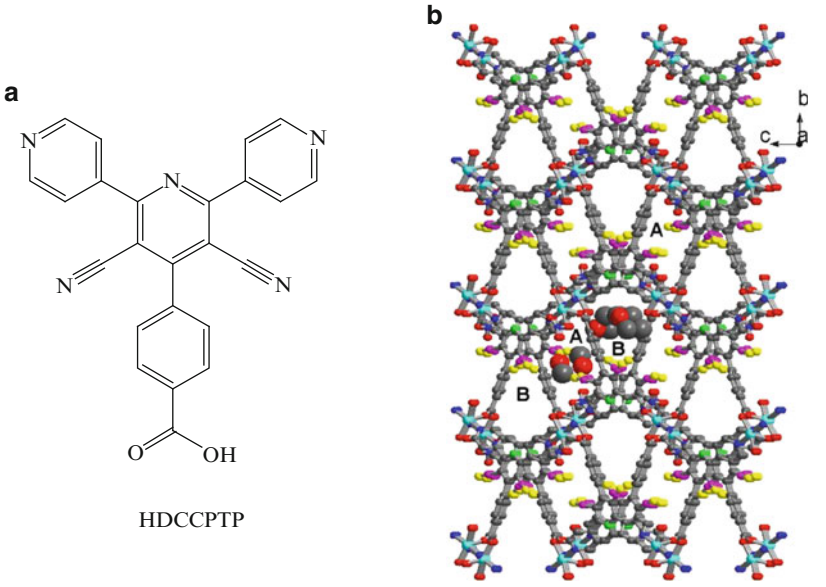

Fig. 9 View of (**a**) HDCCPTP and of (**b**) the (3,6)-connected biporous framework in [Cu(DCCPTP)(NO_3)]·0.5(1,4-dioxane)·0.5MeOH viewed close to [100] direction. The two types of channel (A and B) are identified with their respective MeOH and 1,4-dioxane guests [125]. Reproduced by kind permission of the authors

A related bifunctional porous co-ordination polymer based upon Co(II) incorporating both uncoordinated carboxyl and pyridyl groups within its pores has been prepared [126]. Gas adsorption measurements on the desolvated material reveal not only high capacity uptakes for H_2, CO_2, C_2H_2 and CH_4, but also selective CO_2 adsorption over C_2H_2 and CH_4 due to the increased interactions between CO_2 and uncoordinated organic groups [126].

2.4 Cr(III) Carboxylates

2.4.1 The MIL Series: MIL-100, 101 and Analogues

Assembly of carboxylate ligands and tri-nuclear [Cr_3O] cluster units can form materials of exceptionally high porosity. MIL-100 and MIL-101 are constructed from [Cr_3O] cluster nodes and 1,3,5-benzenetricarboxylate or 1,4-benezenedicarboxylate, respectively. The structures are based on supertetrahedra, which consist of trinuclear [$Cr_3(OH)(H_2O)(\mu\text{-}O)$] units linked by 1,3,5-benzenetricarboxylate along the faces in MIL-100, and along the edges by benezene-1,4-dicarboxylate in MIL-101. These show an augmented Mobil Thirty-Nine (MTN) zeotype structure (Fig. 10) [122, 127, 128]. Both compounds have large pore sizes with a large cage

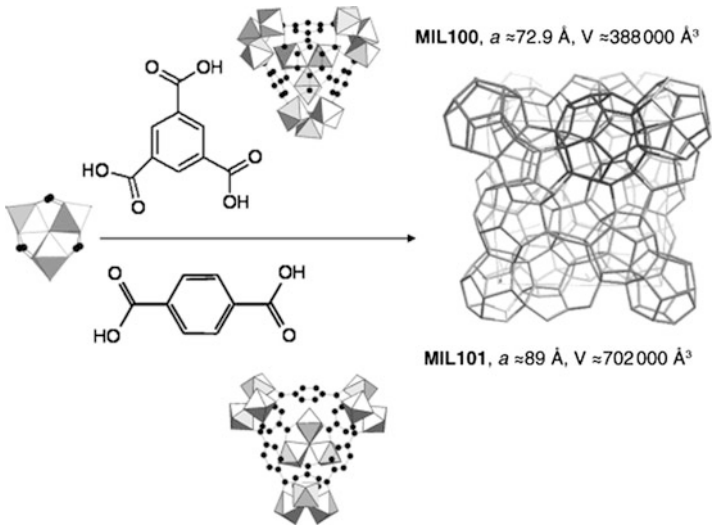

Fig. 10 Structure of MIL-100 and MIL-101 [122]. Reproduced by kind permission of the authors

of diameter ~29 Å in MIL-100 and ~34 Å in MIL-101, with pore volumes of 1.0 $cm^3\ g^{-1}$ for MIL-100 and 1.9 $cm^3\ g^{-1}$ for MIL-101. MIL-101 has a very large Langmuir surface area (5,500 $m^2\ g^{-1}$) and BET surface area (4,230 $m^2\ g^{-1}$). However, the H_2 adsorption capacities for these materials are not especially high: at 77 K; MIL-100 reaches saturation at 25 bar at 3.3 wt% uptake, and MIL-101 can adsorb 6.1 wt% H_2 at 80 bar. This suggests that the large sized pores (>10 Å) in MIL-100 and MIL-101 are not necessarily favourable or optimised for H_2 storage. MIL-101_NDC [129], an analogue of MIL-101 with the same framework topology but with 2,6-naphthalenedicarboxylate replacing 1,4-benezenedicarboxylate, incorporates larger cages than MIL-101. The diameter of the largest cage in MIL-101_NDC is ~46 Å. However, there have been no reports of H_2 adsorption by MIL-101_NDC possibly due to the difficulty in preparing pure phases of this material.

MIL-100 can absorb large amounts of CH_4 and CO_2. At 35 bar and 303 K, 119 v (STP)/v of CH_4 is adsorbed [28] below the DOE target of 180v(STP)/v and the best MOF {PCN-14, 220 v(STP)/v at 35 bar and 290 K [27]}. This is due to the weak interaction between CH_4 and MIL-100 which shows an adsorption enthalpy of 20 kJ mol^{-1} at zero loading and decreases with increasing coverage. This is in contrast to the higher adsorption enthalpy of 30 kJ/mol at zero loading (with little decrease on increasing gas coverage) of CH_4 in PCN-14 [27]. At 50 bar and 303 K, 18 mmol g^{-1} of CO_2 is adsorbed in MIL-100. Although MIL-101 has a larger BET surface area and pore volume than MIL-100, the CH_4 storage capacity of MIL-101 [100v (STP)/v at 35 bar and 303 K] is lower than that of MIL-100. However, MIL-101 shows better CO_2 adsorption capacity than MIL-101 [28]. At 304 K and 40 bar, MIL-101 adsorbs 35 mmol g^{-1} CO_2, the highest value obtained for MOFs and exceeding the value reported for MOF-177 of 33.5 mmol g^{-1} at 298 K and 42 bar.

It is worth noting that MIL-100 and MIL-101 have very high CO_2 adsorption enthalpies (63 kJ mol^{-1} for MIL-100 and 45 kJ mol^{-1} for MIL-101) near zero coverage, which is the highest for a non-amine decorated MOF material, but decreases rapidly when the loading of CO_2 increases. At CO_2 loading above 3 mmol g^{-1}, the adsorption enthalpies for MIL-100 and MIL-101 are around 25 kJ mol^{-1}, similar to other framework materials. This indicates a strong interaction between CO_2 molecules and exposed metal sites in MIL-100 and MIL-101, which is supported by the IR spectra characterizing the potential formation of CO_2-coordinated species on Lewis acid sites (O=C=O. . .Cr^{3+}) [28].

2.4.2 MIL-53 (Al, Fe or Cr)

MIL-53 has three isomers containing Cr(III), Al(III) and Fe(III) as metal ions, respectively [130–132], with a V(III) analogue MIL-47 also reported [133]. These frameworks consist of corner-sharing metal clusters (Cr, Al, Fe or V) interconnected with benzene-1,4-dicarboxylate (BDC^{2-}) ligands and are very flexible with their unit cells and pore sizes changing significantly during dehydration/hydration processing. MIL-53 (Cr and Al) have been studied extensively [134], which shows a hydrated phase with contracted pores and a dehydrated phase with open pores. This dehydration corresponds to an overall expansion of the unit cell volume by 480 $Å^3$. However, loss of water from MIL-53(Fe) results in a closing of structure to form a metastable phase followed by a small opening of the structure, during which the volume change is much smaller, around 87 $Å^3$ [130].

The dehydrated MIL-53 compounds have moderate H_2 adsorption capacities of 2.8 wt% for MIL-53(Cr) and 3.8 wt% for MIL-53 (Al) [131]. Significant adsorption/desorption hysteretic behaviour was observed in the H_2 isotherm which is clearly due to the dynamic behaviour of MIL-53.

The dynamic nature of the frameworks in MIL-53 (Cr and Al) also results in very interesting CO_2 and CH_4 adsorption behaviours (Fig. 11) [133]. CH_4 adsorption isotherms for MIL-53 are typical of those obtained with microporous materials such as zeolites and activated carbon. At 35 bar and 304 K, the amount adsorbed is 155 (Al) and 165 (Cr) v(STP)/v. The adsorption enthalpy of CH_4 remains almost constant at 17 kJ mol^{-1} from 0 to 10 bar, which is well above the liquefaction enthalpy of CH_4 (8.2 kJ mol^{-1}). The maximum CO_2 adsorption is 10 mmol g^{-1} for MIL-53(Al), observed at 304 K and 30 bar. This is a moderate capacity; however, the shape of the CO_2 adsorption isotherm is very unusual and shows a first adsorption step below 1 bar adsorbing 2 mmol g^{-1} CO_2, followed by a second adsorption step at around 6 bar. Interestingly, no steps were found to be present in the CO_2 desorption process. The corresponding adsorption enthalpy for CO_2 on MIL-53(Al) is around 35 kJ mol^{-1} during the initial adsorption process up to 6 bar, which is followed by a sharp decrease to around 17 kJ mol^{-1}, close to the liquefaction enthalpy of CO_2 (17.2 kJ mol^{-1}). MIL-53(Cr) exhibits similar behaviour in CO_2 adsorption: the first step in CO_2 adsorption in dehydrated MIL-53(Cr) disappears if the sample is hydrated [135]. For hydrated MIL-53(Cr) CO_2

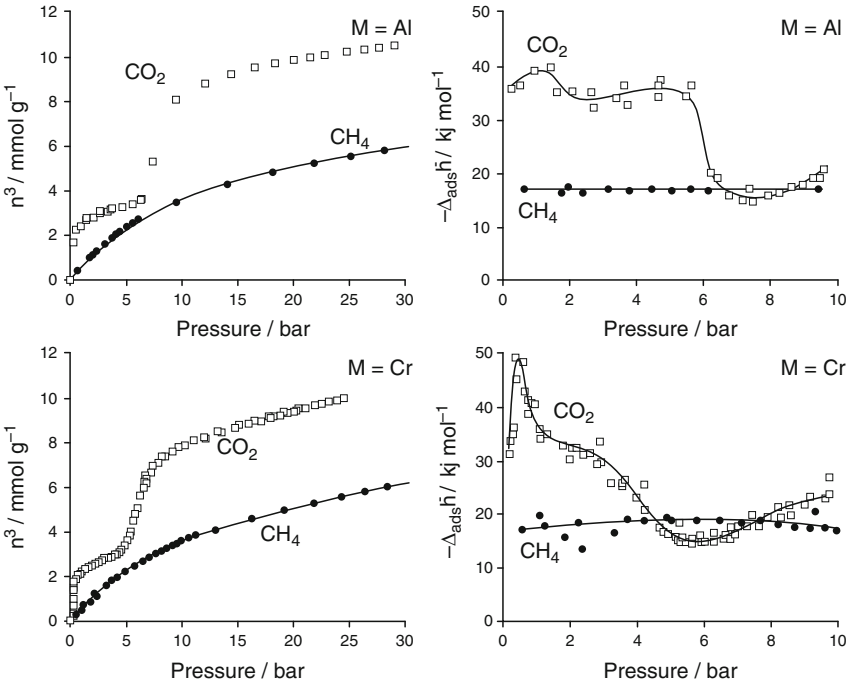

Fig. 11 Two-step CO_2 adsorption behaviour MIL-53 (Al and Cr) and their CH_4 adsorption and adsorption enthalpies [133]. Reproduced by kind permission of the authors

adsorption only occurs above 10 bar, corresponding to the second adsorption step for dehydrated MIL-53(Cr), but no CH_4 adsorption is observed in hydrated MIL-53 (Cr). Changes in the PXRD pattern for MIL-53 suggests that the quadrupole moment of CO_2 can trigger pore opening in hydrated MIL-53 at 10 bar, allowing the entry of CO_2 molecules, whilst the interaction of CH_4 and MIL-53(Cr) is simply too weak to open pores entrances. Thus, a framework contraction may contribute to the strong adsorption of CO_2 in MIL-53(Cr) [135–139].

Functionalising MIL-53(Al) with amino groups leads to an increased selectivity for CO_2 over CH_4 [32]. The amino-MIL-53(Al) was synthesised using 2-aminoterephthalic acid as a linker [33, 34], and the initial CO_2 adsorption enthalpy in amino-MIL-53(Al) is 38.4 kJ mol^{-1}, significantly higher than that for CH_4 (20 kJ mol^{-1}). Such differences result in a separation factor of 60 for CO_2 over CH_4, 5 times higher than the parent material MIL-53(Al).

2.5 Non-Transition Metal Carboxylates

A MOF containing the tri-nuclear cluster M_3O unit has been very recently obtained via the synthesis of the highly porous $[In_3O(ABTC)_{1.5}(H_2O)_3](H_2O)_3(NO_3)$

(H_4ABTC = azodibenzene-3,3′,5,5′-tetracarboxylic acid) [140]. In this material three In(III) cations are bridged by six 4-connected planar carboxylate ligands to afford 6-connected $[In_3O(O_2R)_6]$ moieties leading to an overall *soc* (square-octahedral) topology. The desolvated framework has a Langmuir surface area of 1,417 $m^2\ g^{-1}$ and a pore volume of 0.50 $cm^3\ g^{-1}$, with an H_2 uptake of 2.61 wt% at 78 K and 1.2 bar. This is a high uptake considering the pressure, but potential saturation adsorption is limited due to the relatively low pore volume of the framework. INS studies on $[In_3O(ABTC)_{1.5}](NO_3)$ indicate occupation of multiple sites in the material. This is also in agreement with analysis of ΔH_{ads} from H_2 isotherms, which shows a nearly constant value (6.5 kJ mol^{-1}) at loadings below 1.8 wt%. In this case with In(III) cations present at the node, open metal sites do not necessarily out-perform other sites within the polymer structure, and the geometry of the pores and framework topology are key factors in determining strong interaction between H_2 and the framework material. Other examples of H_2 uptake as a function of cation exchange in anionic In(III) frameworks are discussed in Sect. 2.9.

New porous materials derived from carboxylate ligands and lighter Mg(II) centres have been reported [141] and these have been shown to have high isosteric heats of absorption of 7.0–9.5 kJ mol^{-1} reflecting the increased van der Waals contact area associated with a small pore and possible interactions with the Mg(II) centre. Other examples of porous materials derived from carboxylate ligands and light Mg(II) [142–145] and Al(III) [131, 146–148] centres have been reported.

2.6 Complexes of Tetrazolate Ligands

Benzene-1,3,5-tris-tetrazole is a tri-branched linker incorporating three N-donors that can bridge two metal centres (Fig. 12a). This is analogous to the carboxylate group which can also stabilise multi-nuclear metal nodes. Reaction of benzene-1,3,5-tris-tetrazole (H_3BTT) and $MnCl_2$ in DMF affords $[Mn(DMF)_6]_3[(Mn_4Cl)_3(BTT)_8(H_2O)_{12}]_2{\cdot}42DMF{\cdot}11H_2O{\cdot}20CH_3OH$ which incorporates an 8-connected $[Mn_4Cl]^{7+}$ node linked by 3-connected BTT^{3-} ligands [149]. The fundamental building unit in the structure is a truncated octahedron sharing square faces to generate a cubic framework structure as in sodalite (Fig. 12). In the solvated material, the encapsulated Mn(II) cations are coordinated by organic solvents, DMF and methanol. To generate a porous material, the DMF was exchanged with methanol followed by desolvation *in vacuo* to afford a material with partially desolvated Mn(II) cations and exposed coordination sites. The material has a BET surface area of 2,100 $m^2\ g^{-1}$ and can adsorb 6.9% wt% H_2 at 90 bar and 77 K. Significantly, the excess volumetric adsorption reaches 60 g L^{-1} of H_2 which is well above the 45 g L^{-1} of DoE 2010 criteria, and only 11 g L^{-1} lower than the density of liquid H_2 (71 g L^{-1} at 1 bar and 20 K). This raises a possibility of replacing current liquid H_2 storage systems with a liquid N_2 coolant at moderate pressures. Using $CuCl_2$ in the same reaction produces a product that is isostructural with the Mn material [150]. The Cu complex $H[Cu(dmf)_6][(Cu_4Cl)_3(BTT)_8(H_2O)_{12}]{\cdot}$

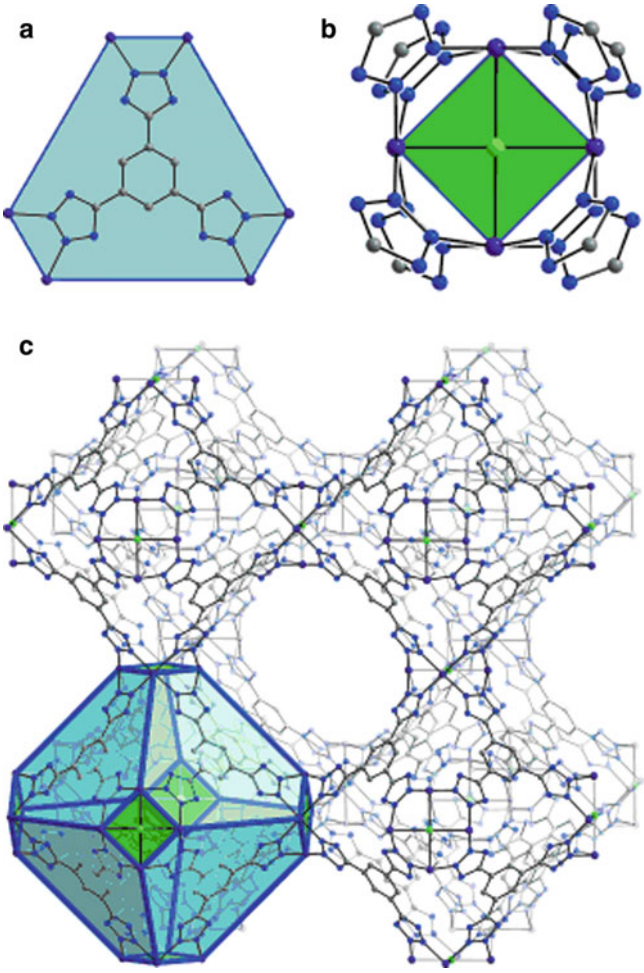

Fig. 12 Views of (**a**) (**b**) BTT^{3-} linker and its connection to metal ions; (**c**) the crystal structure of sodalite structure in $[Mn]_3[(Mn_4Cl)_3(BTT)_8]_2$ [150]. Reproduced by kind permission of the authors

$3.5HCl{\cdot}12H_2O{\cdot}16CH_3OH$ can be completely desolvated under reduced pressure and heating to 120°C. Significantly, the Cu-based material has a lower BET surface area (1,710 $m^2\ g^{-1}$) than its Mn analogue and, accordingly, adsorbs less H_2 with an overall capacity of 5.7 wt% at 90 bar at 77 K.

Strong binding of D_2 to exposed metal sites in $[Mn]_3[(Mn_4Cl)_3(BTT)_8]_2$ has been established by NPD studies at 3.5 K [149]. A Mn(II)–D distance of 2.27 Å suggest that D_2 molecules interact significantly with exposed Mn(II) sites, but this distance is significantly longer than distances reported for σ-bonded η^2-H_2 complexes of group 6 metal ions (M-H ca. 1.7–2.0 Å). NPD also reveals that once the exposed Mn(II) sites are saturated, D_2 molecules are sited at the surface of cavities created by the tetrazolate linkers. The Mn–D_2 binding appears to be consistent with

the high adsorption enthalpy of H_2 observed for $[Mn]_3[(Mn_4Cl)_3(BTT)_8]_2$. In the low H_2 coverage region, $\Delta H_{ads} = 10.1$ kJ mol^{-1}, which is higher than the value of 5.9 kJ mol^{-1} observed for $Mn_3[Co(CN)_6]_2$. In the high H_2 coverage region, however, the adsorption enthalpy of H_2 in $[Mn]_3[(Mn_4Cl)_3(BTT)_8]_2$ (5.7 kJ mol^{-1}) and $Mn_3[Co(CN)_6]_2$ (5.3 kJ mol^{-1}) are very similar. Neutron scattering experiments were conducted at 3.5 K with D_2 condensed inside the micropores of the $[Mn]_3[(Mn_4Cl)_3(BTT)_8]_2$ framework. Although these experiments confirm the binding of H_2 molecules at exposed Mn(II) sites at 3.5 K, it is still difficult to speculate upon the strength of such an interaction at 77 K [149].

NPD studies on the Cu analogue of $[Mn]_3[(Mn_4Cl)_3(BTT)_8]_2$ gave a Cu–D_2 distance of 2.47 Å [150]. Compared to $[Mn]_3[(Mn_4Cl)_3(BTT)_8]_2$, the longer Cu–$D_2$ distance is in agreement with the slightly lower adsorption enthalpy of 9.5 kJ mol^{-1} for the Cu material. At H_2 loading of 1.6 wt% the heats of adsorption for the Mn and Cu materials are the same [6.0 kJ mol^{-1}], suggesting adsorption of H_2 at high loading is controlled primarily by pore size and shape.

The Mn(II) cations in $[Mn]_3[(Mn_4Cl)_3(BTT)_8]_2$ can be partially exchanged with Fe(II), Co(II), Ni(II), Cu(II), Zn(II), Li(I) and Cu(II) ions, and the resultant materials remain porous [151]. Cation exchange has a small impact on the adsorption enthalpy of H_2 at zero loading, with adsorption enthalpies being similar at 1.2 wt% loading. This suggests that the interaction of H_2 and exposed metal cations mostly affects adsorption at low H_2 loading. Exchanging Mn(II) with Co(II) and Fe(II) increases the initial H_2 adsorption enthalpy slightly from 10.1 to 10.2 and 10.5 kJ mol^{-1}, respectively. However, replacement with other cations results in a decrease in adsorption enthalpy. This gives an interesting profile for the interaction between metal cations and H_2 suggesting an order of H_2–M binding strength within this Mn-BTT framework of $Co^{2+}>Fe^{2+}>Mn^{2+}>Cu^{+}>Zn^{2+}>Ni^{2+}>Li^{+}>Cu^{2+}$.

The exposed Cu(II) site in $H_3[(Cu_4Cl)_3(BTT)_8]$ can be occupied by ethylenediamine (en), and this amine modified surface shows very high affinity to CO_2 compared to the unmodified parent material [152]. The initial adsorption enthalpy of CO_2 in the amine functionalised material is as high as 90 kJ mol^{-1}, which is almost five times higher than the value of 19 kJ mol^{-1} observed for $H_3[(Cu_4Cl)_3(BTT)_8]$ and also the highest adsorption enthalpy observed in a MOF material. Such a high adsorption enthalpy indicates a chemisorption interaction between CO_2 and Cu-BTT-en system. CO_2 can thus be captured at low pressure from a CO_2/N_2 mixture, and the material recycled by passing over N_2 to remove CO_2 at 30°C.

Reaction of $Co(CF_3SO_3)_2$ and benzene-1,4-di(4′-pyrazole) (H_2BDP) in *N*,*N*-diethylformamide produces crystalline [Co(BDP)·DEF·H_2O] [153], the crystal structure of which shows a 10 × 10 Å square channel running along the *c*-axis of the crystal. This material undergoes a phase change after desolvation, although the structure of the phase after desolvation has not been identified. N_2 adsorption of the desolvated materials at 77 K has five distinct adsorption steps in the pressure region of $0 < P/P_0 < 0.05$ (Fig. 13a). At 87 K, the five steps are shifted to higher pressures. Desorption of N_2 revealed hysteresis at both temperatures, but the hysteresis is much more apparent at 87 K. This is very unusual as the hysteresis

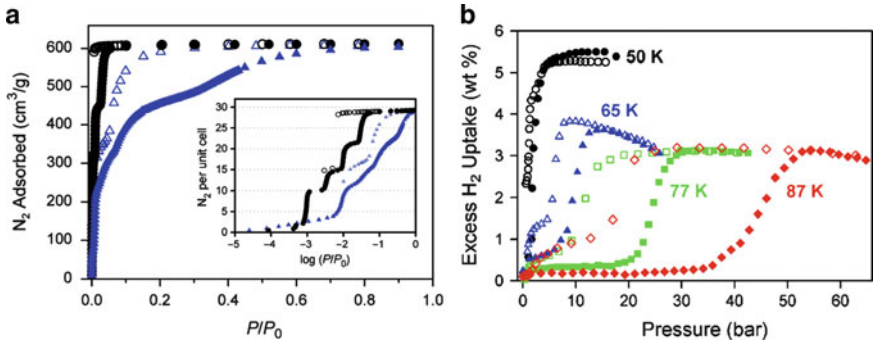

Fig. 13 (**a**) Multi-steps N_2 isotherms and (**b**) high pressure hysteretic H_2 adsorption–desorption in [Co(BDP)] [153]. Reproduced by kind permission of the authors

in N_2 uptake/release in microporous materials is normally related to a high diffusion barrier and such hysteresis becomes smaller with increasing temperature. Similar unusual adsorption–desorption behaviour is also observed in the H_2 isotherm (Fig. 13b). The material adsorbs no H_2 at 77 K at low pressures and the pore opens at 20 bar and reaches a maximum of 3.1 wt% at 28 bar. Interestingly, the adsorbed H_2 cannot be released until the pressure drops to 15 bar, resulting in a hysteresis loop with a width of 13 bar. In agreement with the temperature-dependent hysteretic N_2 isotherms, the width of the hysteresis of H_2 isotherm increases to 27 bar as the temperature rises to 87 K [153].

The adsorption enthalpy for H_2 binding of [Co(BDP)] is low, 3.2 kJ mol^{-1} for adsorption and 2.6 kJ mol^{-1} for desorption. The authors considered that this behaviour is due to part of the adsorption enthalpy being consumed during the pore-opening process. Based on this assumption, the enthalpy of the pore-opening or phase-change of [Co(BDP)] lies in the range 2–8 kJ mol^{-1}. Analysis of diffusion kinetics of H_2 in the pores of [Co(BDP)] shows a very small diffusion barrier of 0.62 kJ mol^{-1}. This also supports the argument that the large hysteresis observed in the H_2 and N_2 isotherms on [Co(BDP)] is due to the phase change rather than a diffusion kinetic trap.

Materials based on Mn-formate [154] and Co-triazine [155] and Pd- and Cu-pyrimidine [156] linkers have also been found to show H_2 storage capabilities.

2.7 *Complexes of Imidazolate Ligands*

There has been interest in developing porous coordination polymers that mimic the topology and structures of zeolites. The bridging angles of imidazolate (IM) in <M–IM–M units is coincident with the Si–O–Si angle in zeolites (Fig. 14) and this has led to the use of imidazole and related ligands as tectons to form so-called ZIFs.

MIL-100 and MIL-101 (see Sect. 2.4.1) show an augmented MTN zeotype structure (Fig. 10) [122, 127, 128], but the first examples of ZIF materials in the

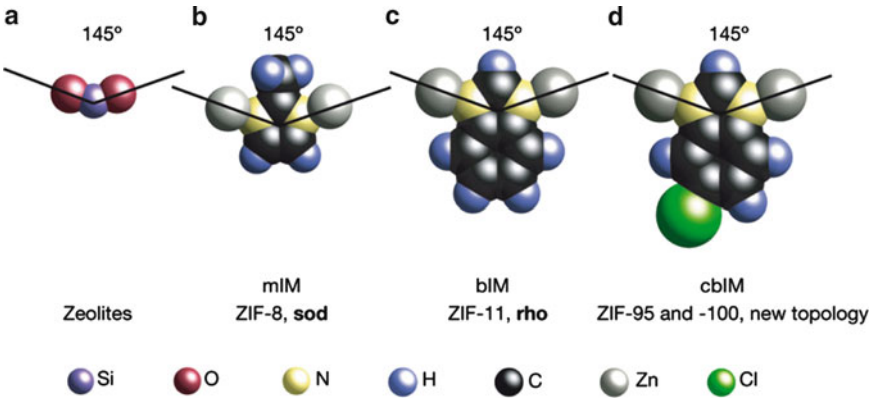

Fig. 14 Bridging angles and girths in zeolites and imidazole (IM) [73]. Reproduced by kind permission of the authors

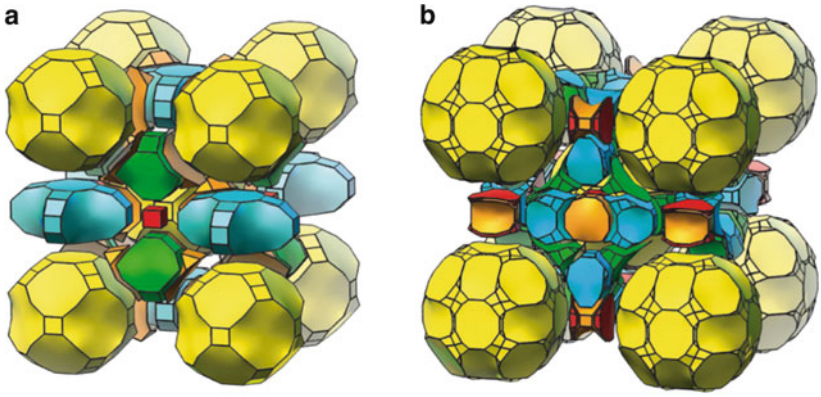

Fig. 15 Packing of cages in 3-D space in (**a**) ZIF-95 and (**b**) ZIF-100 [73]. Reproduced by kind permission of the authors

literature were reported by Tian and co-workers [75–78]. Subsequently, further example based upon substituted imidazolate and tetrahedral metal ions were reported [54, 55, 72–74]. Some of these coordination polymers have the same topologies as those found in zeolites and some new topologies not previously observed in zeolites were discovered. The connection topologies of imidazolate ligands and metal ions are (as in many syntheses of coordination polymers) highly sensitive to reaction conditions used (solvent, substrate, temperature, reaction time) and the nature of the imidazolate derivatives used in the synthesis. These materials show many structural varieties and types, and many have been well characterised by single crystal X-ray diffraction. The common feature in all ZIFs is that the metal nodes are tetrahedrally coordinated by imidazolate and the 4-coordinated net of linked metal atoms form varied cage structures. Figure 15 illustrates the basic cage

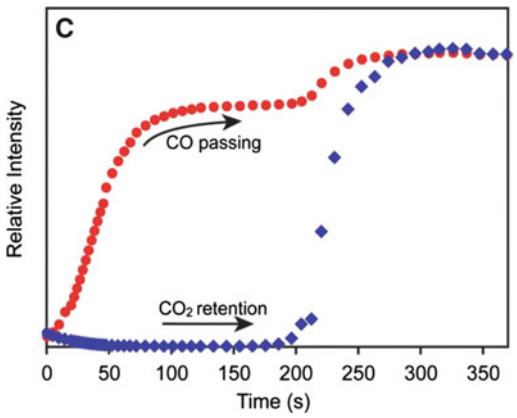

Fig. 16 Flow of a CO_2/CO mixture passing through a sample of ZIF-68 showing the retention of CO_2 in the pores and passage of CO [54]. Reproduced by kind permission of the authors

structures formed in ZIF-95 and ZIF-100 and how the packing of these cages defines different structures.

Although many ZIF materials incorporate large pores, their surface areas are below 2,000 $m^2\ g^{-1}$. The BET surface area of ZIF-8 is 1,630 $m^2\ g^{-1}$ and pore volume 0.636 $cm^3\ g^{-1}$, the highest yet reported for ZIFs. These numbers are lower than for MOFs constructed from longer and multi-branched organic ligands. Also, the relatively short ligand span of imidazolates and the zeolitic topology requires a high relative percentage of 4-connected metal centres.

H_2 adsorption on ZIF-11 was reported to be 1.4 and 1.3 wt% for ZIF-8 at 1 bar and 77 K [55]. The total maximum gas uptakes in these materials are not impressive compared to other more porous metal-organic polymers due to their relative low BET surface areas and pore volumes. However, the ZIF series provides a number of candidates for selective gas capture and adsorption. ZIF-68, 69 and 70 have the same topology (**gme**) and large pores of 7.2, 10.2 and 15.9 Å diameter, respectively, connected through tunable windows of 4.4, 7.5 and 13.1 Å diameter, respectively. Under a mixed stream of CO_2 and CO, ZIF-68, 69 and 70 show retention of CO_2 with CO passing through the material with no adsorption (Fig. 16). The CO_2 vs CO selectivity of ZIF-70 is the highest observed for these types of materials and also five times better than the state-of-the-art material BPL carbon. Similarly, ZIF-78 and 82 show high selectivity for CO_2 vs CH_4, N_2 and O_2 and out-performs BPL carbon [54].

2.8 Mixed Ligand Systems

2.8.1 Pyridine-Carboxylate Ligands

Another approach in preparing porous materials is to combine two types of linker ligands within the same structure. Thus, bimetallic tetracarboxylate units $M_2(O_2CR)_4$

a

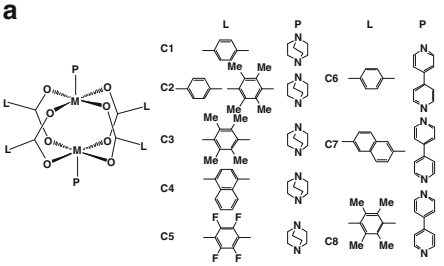

b

	Vp(cm³/g)	BET surface area (m²/g)	H_2 uptake (1bar, 77 K)
C1	0.75	1450	2.01
C2	0.59	1100	2.08
C3	0.50	920	1.85
C4	0.52	1000	1.70
C5	0.57	1070	1.78
C8	0.62	1120	1.68

Fig. 17 (**a**) Views of different linkers binding to a bimetallic node from axial and equatorial directions to form frameworks [53]. (**b**) Gas adsorption data for the resultant frameworks

can be combined with linear ditopic amine linkers that bind at the two axial sites of the paddlewheel (Fig. 17a). In these materials, the square-planar 4-connected bimetallic nodes are, therefore, bound by linear linkers L^{2-} defining a 4 × 4 2-D grid, and these sheets are then pillared by linker P to form a porous 3-D framework. A series of Zn(II) complexes have been synthesised using this methodology [53, 157] and they all have stable frameworks on removal of crystallised solvent, except **C6** and **C7** (Fig. 17). **C1** has the highest BET surface area (1,450 $m^2\ g^{-1}$) and the others have similar BET surface areas of ca. 1,000 $m^2\ g^{-1}$. The H_2 adsorption curves confirm that the pendant arms on the linker L^{2-} can help to take up more H_2 at low pressure, but they also limit the potential of these materials in terms of total H_2 capacity. The material **C1** has the highest pore volume and, therefore, shows good potential for H_2 storage at higher pressure.

The above strategy of building pillared structures can result in highly porous frameworks. For example, SNU-6 is a framework built from benzophenone-4,4′-dicarboxylic acid (H_2BPnDC), 4,4′-bipyridine and Cu(II) [158]. The solvent-accessible volume for this material is 83.7% with a BET surface area of 2,590 $m^2\ g^{-1}$. The structure has very large pores which are estimated to be distributed between 14 and 20 Å. The large pores result in modest H_2 uptake at 1 bar (1.68 wt% at 77 K), but high uptake at 70 bar (excess: 4.87 wt%, total: 10.0 wt%). There are no high pressure CO_2 adsorption data available for SNU-6; however, the CO_2 adsorption at 195 K and 1 bar reaches 25.8 mmol g^{-1} suggesting good potential for CO_2 adsorption at room temperature and high pressure [158].

A further approach involves incorporation of both pyridyl and carboxylate donors within the same angular ligand. The pyridyl group can act as a terminal group to replace solvent molecules in the metal cluster nodes [159–162]. This methodology can also, in principle, produce framework materials of especially high connectivity with the pyridyl and carboxylate linkers limiting interpenetration when the length of the linker is increased [163, 164]. The 12-connected frameworks $[Ni_3(OH)(BPPC)_3]\cdot 8DMF\cdot 10H_2O$ and $[Fe_3(O)(BPPC)_3]\cdot 3DMF\cdot 17H_2O$ have been constructed using the tri-branched linker pyridine-3,5-bis(phenyl-4-carboxylic acid) (H_2BPPC) bound to the tricapped trigonal prismatic polyhedral metal nodes $[Ni_3(OH)]$ or $[Fe_3O]$, respectively[165]. The overall topology of these highly

unusual 12-connected frameworks is $3^{18}4^{42}5^6$, and desolvation affords highly porous materials with large surface areas (1,553 $m^2\ g^{-1}$ for Ni complex and 1,200 $m^2\ g^{-1}$ for Fe complex). Their H_2 adsorption capacities are proportional to their surface areas with the Ni complex adsorbing 4.15 wt% H_2 at 77 K and 20 bar, with 3.05 wt% uptake for the Fe complex under the same conditions. Another successful approach to preparing porous materials has involved the linking of Ni(II) amine macrocyclic units with bridging carboxylic linkers [166].

2.8.2 Mixed Carboxylate Ligands

Porous coordination polymers with more complicated topologies can be formed by introducing three different building units such as ditopic terephthalic acid (H_2BDC) and tri-branched 1,3,5-tris-(4-carboxyphenyl)benzene (H_3BTB) with 4-connected [Zn_4O] units. [$Zn_4O(BDC)(BTB)_{4/3}$] (UMCM-1) is a mesoporous coordination polymer which has a 1-D hexagonal channel 2.7 nm × 3.2 nm [167]. Using the longer ditopic carboxylate thieno[3,2-*b*]thiophene-2,5-dicarboxylate (T^2DC^{2-}) affords [$Zn_4O(T^2DC)(BTB)_{4/3}$] UMCM-2 [168]. UMCM-2 has a BET surface area of 5,200 $m^2\ g^{-1}$ and can adsorb 6.9 wt% H_2 at 46 bar at 77 K. The H_2 adsorption enthalpy in UMCM-2 is between 4.6 and 6.2 kJ mol^{-1} at low loading, similar to other Zn(II)-carboxylate-based materials. The large pore in UMCM-1 provides an ideal space for post-synthesis and modification to the framework. An analogue of UMCM-1 has been synthesised by using 2-amino-benzene-1, 4-dicarboxylic acid (NH_2–H_2BDC) producing UMCM-1-NH_2. Subsequent Schiff-base condensation of UMCM-1-NH_2 with 2-pyridinecarboxaldehyde forms chelate sites, which can be used to bind metal cations, such as Pd(II), thus generating dangling metal sites inside the mesopores [169]. Although no gas adsorption was reported on this metalated framework, it is an interesting and promising route for incorporating metal ions without affecting the rigidity of the framework.

2.9 Modification of Coordination Polymers by Li^+ Exchange or Doping

The major shortcoming of porous coordination polymers and other physisorption-based materials for H_2 storage is the weak H_2-adsorbent binding energy, which prevents such materials from adsorbing high levels of H_2 at room temperature. The adsorption enthalpy of H_2 in most porous MOFs is in the range 5–9 kJ mol^{-1}. Although the adsorption enthalpy can reach 13 kJ mol^{-1} at zero coverage in some materials, the enthalpy often decreases rapidly with increasing H_2 loading, and the pore volume in microporous materials is too limiting to achieve high capacity H_2 storage. Theoretical studies have suggested that introducing light, non-transition metal species such as Li, Na or Mg can afford higher H_2-framework interactions

[170–177], and thus produce a hybrid chemi-physi-sorption material to promote H_2 adsorption at ambient temperatures.

$[Me_2NH_2][In(BPTC)]$ (H_4BPTC = biphenyl-3,3′,5,5′-tetracarboxylic acid) has a PtS-like anionic framework with 4-connected In(III) cation and $BPTC^{4-}$ ligand nodes [178]. The $[Me_2NH_2]^+$ cation can be exchanged with Li^+ by soaking a sample in saturated LiCl solution. The resulting material, Li[In(BPTC)], has a larger pore volume (0.42 $cm^3\ g^{-1}$ vs 0.33 $cm^3\ g^{-1}$) and BET surface area (1,024 $m^2\ g^{-1}$ vs 820 $m^2\ g^{-1}$) than $[Me_2NH_2][In(BPTC)]$ due to Li^+ having a smaller volume than the $[Me_2NH_2]^+$ cation and the exchange makes the pore more accessible to N_2 molecules. Accordingly, H_2 adsorption capacity at 77 K and 20 bar was enhanced from 2.36 to 2.88 wt% on exchange of $[Me_2NH_2]^+$ with Li^+. However, the initial adsorption enthalpies for H_2 binding in $[Me_2NH_2][In(BPTC)]$ and Li[In(BPTC)] are reduced from 7.6 to 6.1 kJ mol^{-1}, consistent with reduction in adsorption enthalpy with increasing pore size [56].

Similar results have been reported for Li^+ and Mg^{2+} exchanged products derived from the anionic framework $[In(ImDC)_2]^-$ (H_2ImDC = imidazole-4,5-dicarboxylic acid) [179]. $[In(ImDC)_2]^-$ has a rigid **rho**-zeolitic structure (**rho**-ZMOF = $[In(ImDC)_2]^-$) and the as-synthesised material incorporates $[Me_2NH_2]^+$ cations within the anionic $[In(ImDC)_2]^-$ framework. The $[Me_2NH_2]^+$ cations can be exchanged with Li^+ or Mg^{2+} to produce Li-**rho**-ZMOF and Mg-**rho**-ZMOF, respectively. No enhancement of H_2 adsorption capacity or adsorption enthalpy was observed in the Li^+ or Mg^+ exchanged **rho**-ZMOF. The positions of the Mg(II) cations were identified by single crystal X-ray diffraction in a sample of Mg-In[ImDc]$_2$ which had been activated at 115°C. The Mg(II) centre at 115°C for H_2 adsorption. The Mg(II) centre was found to be coordinated by water molecules and apparently H_2 is restricted from access to these cations in Mg-**rho**-ZMOF. The INS spectra of H_2 loaded Li^+, Mg^{2+} and $[Me_2NH_2]^+$-**rho**-ZMOF are very similar, suggesting that no strong adsorption site is created by the cation exchange with Li^+ or Mg^{2+}. This was rationalised by the decomposition temperature of the **rho**-ZMOF framework being lower than the dehydration temperature of the Li^+ and Mg^{2+} centres thus preventing full desolvation. Thus, no exposed Li^+ or Mg^{2+} surfaces were generated and no interaction between H_2 and Li^+ or Mg^{2+} centres observed [179].

Alkali metal doping has been achieved by reaction of Li, Na or K metal with Zn(II) framework materials [180, 181]. Alkali metal doping in framework $[Zn_2(NDC)_2(diPyNI)]$ (H_2NDC = naphthalene-2,6-dicarboxylic acid; diPyNI = *N*,*N*′-di-(4-pyridyl)-1,4,5,8-naphthalenetetracarboxydiimide) led to a slightly enhanced adsorption enthalpy for H_2 uptake, but much smaller enhancements than those predicted from computational analyses [181]. It was concluded that any enhancement was most likely caused by reduction of the framework by Li metal. Indeed, high dopant concentration in $[Zn_2(NDC)_2(diPyNI)]$ leads to decreases in BET surface area, H_2 adsorption capacity and adsorption enthalpy compared to non-doped samples [180]. This suggests that changes in the gas adsorption properties brought about by alkali metal doping in $[Zn_2(NDC)_2(diPyNI)]$ is unlikely to be caused by any noticeable H_2–alkali metal interaction, but from the subtle structural changes or breathing of the framework. The same conclusion was also drawn from Li^+, Na^+ and K^+ doped

samples of the interwoven framework $[Zn_2(NDC)_2(diPyTz)]$ (diPyTz = di-3,6-(4-pyridyl)-1,2,4,5-tetrazine) [182].

Fixing Li^+ on the internal surface of MOFs can potentially stabilise a partially exposed Li^+, and some recent reports have indicated that this is a viable route to improving H_2 adsorption enthalpy. $H_2PPZ[In(QPTC)]$ (H_2PPZ = dihydropiperazinium cation, H_4QPTC = quaterphenyl-3,5,3′,5′-tetracarboxylic acid) has an anionic interpenetrated diamondoid framework structure. In the as-synthesised material the $[H_2PPZ]^{2+}$ cation is bound to the O-centres of the $QPTC^{4-}$ ligands via N–H. . .O hydrogen bonding [183, 184]. Li^+ exchange can remove all $[H_2PPZ]^{2+}$ cations to give Li[In(QPTC)], the single crystal structure of which reveals Li^+ coordinated by two O-centres from carboxylate groups from the framework and two from two water molecules (Fig. 18). IR spectroscopy confirms that the water molecules can be removed at 150°C leaving partially exposed Li^+. The adsorption enthalpy of Li[In(QPTC)] was found to be 10 kJ mol^{-1} at zero loading, enhanced from 9 kJ mol^{-1} in $H_2PPZ[In(QPTC)]$, confirming the enhancement of H_2 adsorption enthalpy upon the incorporation of exposed Li^+ cations [183].

An analogue of MIL-53(Al) can be synthesised with H_2BDC–OH incorporating a pendant hydroxy group in the framework [185]. The material MIL–53(Al)–OH was treated with lithium diisopropylamide and the presence of Li^+ within the framework material confirmed by solid state NMR spectroscopy. The adsorption enthalpy of H_2 uptake in Li–MIL–53(Al)–OH is 11.6 kJ mol^{-1}, double the value for MIL–53(Al)–OH (5.8 kJ mol^{-1}) [185]. This value is close to the value of 13 kJ mol^{-1} estimated from theoretical calculations [172], again supporting the strategy of Li doping to enhance H_2 adsorption.

The material DO-MOF has a pillared framework structure, in which 4,4′bipyridine pillars bridge 2-D square 4,4-nets comprising binuclear Zn(II) nodes and 4,4′,4″,4‴-benzene-1,2,4,5-tetrayltetrabenzoate. Addition of *t*-BuOLi dopes the framework with Li^+ [186] and, similarly, Mg^{2+} can be introduced by

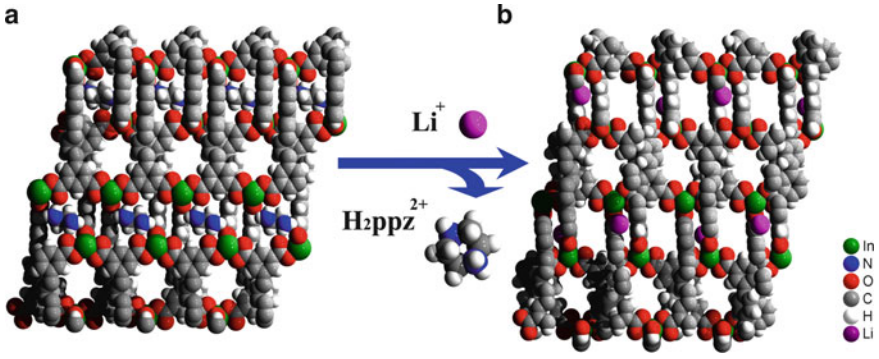

Fig. 18 Views of framework structures of (**a**) $H_2PPZ[In(QPTC)]$ and (**b**) Li[In(QPTC)] (indium *green*, nitrogen *blue*, oxygen *red*, carbon *grey*, hydrogen *white*, lithium *purple*) [183]. Reproduced by kind permission of the authors

using $Mg(OMe)_2$. Interestingly, the H_2 adsorption capacities of Li^+ or Mg^{2+} doped samples at 77 K and 1 bar show no significant difference to the corresponding undoped samples, and their adsorption enthalpies are the same at zero loading. However, the H_2 adsorption enthalpies of Li and Mg doped DO-MOF do not decrease with increasing H_2 loading. This is extremely unusual, suggesting a strong H_2-framework binding site which is not saturated in the measurement range.

2.10 H_2 Adsorption and Kinetic Trapping

Materials based on 4,4′-bipyridine are one of most extensively explored coordination polymer systems. Reaction of $Ni(NO_3)_2$ and 4,4′-bipyridine affords two products $[Ni_2(NO_3)_4(4,4'\text{-bipyridine})_3]_\infty$ depending upon whether the reaction is conducted in methanol or ethanol solution[187]. In both materials the charge on Ni(II) is neutralised by coordinated nitrate anions, and the resultant $Ni(NO_3)_2$ centre is connected by three ditopic 4,4-bipy linkers to form a T-shaped node (Fig. 19a). In the product obtained from methanol solution, T-shaped units form a 1-D ladder structure, and these ladders run parallel (material M). In the case of the product isolated from ethanol, T-shaped units give an interlocked 2-D bilayer product (material E). The common characteristics for these two materials are that the interactions between the ladders or the layers are relatively weak and this results in dynamic structures in which the interactions and distances between ladders or layers are modulated as adsorbate molecules enter the framework [187]. Although

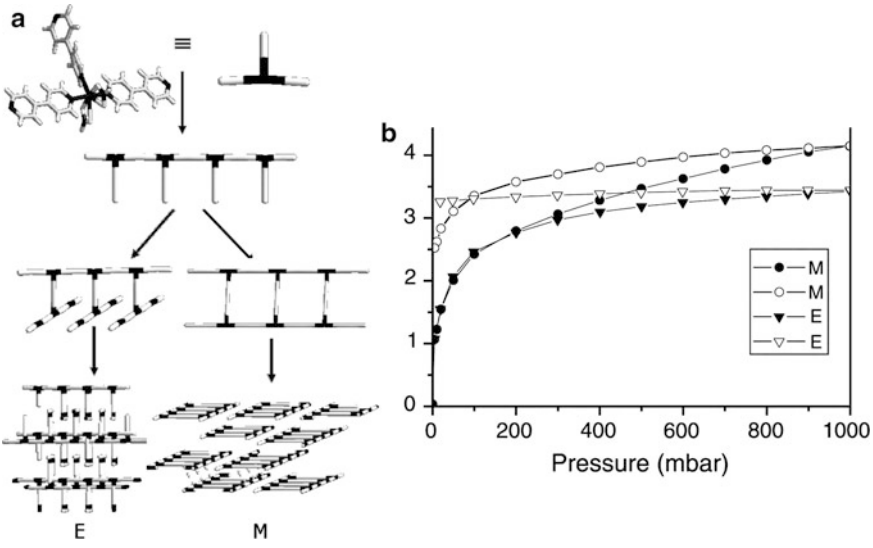

Fig. 19 (a) View of the structures of $[Ni_2(NO_3)_4(4,4'\text{-bipyridine})_3]_\infty$; forms E and M. (b) Hysteretic H_2 adsorption-desorption at 77 K [187]. Reproduced by kind permission of the authors

these materials show only modest H_2 uptake capacity at 77 K (0.82% for M at 1 bar and 0.68% for E for 1 bar) (Fig. 19b), adsorption–desorption hysteresis is observed, particularly for material E. Thus, almost no H_2 is released when the pressure is reduced from 1 bar to 0.1 bar at 77 K with significant release beginning at 110 K. This raises an intriguing idea that H_2 can be loaded under high pressure and stored at low pressure. A range of other Ni(II) porous frameworks have been prepared [188, 189] and these also show modest H_2 uptake.

The above kinetic trap behaviour is also found and studied in the framework of H_2PPZ[In(QPTC)], in which the $[H_2PPZ]^{2+}$ cation was found to act as a kinetic trap to give hysteresis in H_2 uptake; Li^+ exchange eliminates the hysteresis in H_2 adsorption completely. Analysis of the adsorption kinetics at various temperatures revealed that the energy barriers for H_2 diffusion through the small windows is 15 kJ mol^{-1} [183], which is larger than that found in a related material with no adsorption/desorption hysteresis, $[Zn_3(BDC)_3][Cu(Pyen)]$ (Pyen = 5-methyl-4-oxo-1,4-dihydropyridine-3-carboxaldehyde) (M′MOF-1) [190].

2.11 Hydrogen Spillover in MOFs

Although some coordination polymers can adsorb considerable amounts of H_2 at 77 K at relatively low pressures (<100 bar), their H_2 storage capacity at room temperatures can be very low even at very high pressures (>200 bar) [191]. Hydrogen spillover is effective in enhancing H_2 storage capacity at room temperature [191–193]. H_2 spillover in MOFs was first proposed in 2002 [194] although the H_2 spillover effect was confirmed generally many years ago [195]. Creating a carbon bridge between a MOF and Pt particles encourages the diffusion of dissociated H_2. This method can enhance H_2 storage capacities by a factor of 4 for IRMOF-8 to give 4 wt% H_2 uptake at 200 bar [192, 196, 197]. The overall of adsorption enthalpy of Pt doped IRMOF-8 is between 20 and 25 kJ mol^{-1} and the activation energy of H_2 diffusion on a surface is 9.3 kJ mol^{-1} [197]. The studies of H_2 spillover in MOF-5 [196], HKUST-1 and MIL-101 [198] suggest that H_2 storage capacity at 298 K is correlated with the surface area and pore volumes of these materials. Very interestingly, the effectiveness of spillover was found to be related to the defects in MOF crystals. The optimisation of imperfect lattice and pore networks can improve the amount of H_2 adsorbed, but with the drawback of much slower adsorption kinetics [199].

3 Summary and Outlook

MOFs are a class of very promising materials for H_2 storage at 77 K and at moderate pressure (<100 bar). The building-block, node-linker approach [16–18] offers the capability to design and prepare porous framework materials with new

Table 3 Comparison of CO_2 sorption in metal-organic frameworks

Material	S_A, $m^2\ g^{-1}$		V_P,[a] $cm^3\ g^{-1}$	CO_2 uptake[b] ($cm^3\ g^{-1}$)			Q_{st} of CO_2 adsorption, kJ mol^{-1}	Ref.
	BET[a]	Langmuir[a]		195 K[c]	270 K[c]	298 K[d]		
MOF-5	3,800	4,400	1.13		33.5	494[e]		[31, 87, 88, 201, 202]
MOF-177	4,750	5,640	1.75			759[e]		[31, 88, 201]
IRMOF-6	2,800	3,310	0.993			443[e]		[31, 88, 201]
MIL-100	1,900		1.10			403[f]	62	[28]
MIL-101	4,230		2.15			896[f]	44	[28, 201]
MIL-53(Al)		1,500				224[g]	35	[133]
MIL-53(Cr)		1,500				224[g]	32	[133]
MIL-47		1,500					25	[133]
CUK-1	630[b]		0.26[b]	150		86[h]		[203]
UoC-1′		649	0.24		44.8			[202]
HKUST-1	1,507	2,175	0.75			239[e]	35	[28, 86, 204]
ZIF-100	595	780			38.1			[73]
ZIF-69	950	1,070			≈69			[54]
[Co(HL[b,i])]	796 (833)[i]	964 (1,179)[i]	0.33 (0.30)[i]	240	108		40.5	[126]

[a]Calculated from N_2 isotherm at 77 K except where indicated

[b]For comparison, the units of CO_2 absorbed amounts reported previously have been converted into cm^3(STP) g^{-1} [i.e. cm^3(STP) g^{-1} = (mmol g^{-1}) × (gas constant) = (mg g^{-1}/W_F) × (gas constant)]

[c]Amount of CO_2 adsorbed at 1 atm or 1 bar

[d]Amount of CO_2 adsorbed at 55 bar and 298 K, except where indicated[e]Amount of CO_2 adsorbed at 40 bar

[f]Amount of CO_2 adsorbed at 50 bar and 304 K

[g]Amount of CO_2 adsorbed at 30 bar and 304 K

[h]Amount of CO_2 adsorbed at 298 K and 1 atm

[i]Calculated from CO_2 isotherm at 195 K

topologies and concomitant fine-tuning of framework structures and decoration. There are now several materials (MOF-5, MOF-177, Mn-BTT, NOTT-101, 102, 103, 111, 112, 120, SNU-6) that have formally reached the DoE 2010 H_2 storage targets either as gravimetric or as volumetric stores albeit at 77 K and under intermediate pressures. However, the application of these materials in on-board mobile H_2 storage systems requires a further substantial improvement over the current best results with greater than 10% excess uptake potentially needed. Particular consideration will be required regarding the weight and cost of cryogenic systems and high pressure containers [7]. The current strategy of making more porous and light frameworks materials may address these requirements. Simultaneously, utilizing the kinetic trap observed in MOF materials, it might be possible to compress H_2 into a storage tank at low temperatures and store the H_2 at higher temperatures. However, the pore volumes for materials that have been found to function in this way are as yet too small. To achieve H_2 storage at ambient temperature and at low pressures (~30 bar), a material with an adsorption enthalpy for H_2 of 15.1 kJ mol^{-1} is desirable [200]. Although a few materials have H_2 adsorption enthalpies exceeding 10 kJ mol^{-1} at zero loading [190], high adsorption enthalpies are not maintained due to the saturation of strong binding sites. Several routes are being explored to enhance the H_2-framework interactions, including Li^+-doped MOFs, incorporating more unsaturated metal centres, and the introduction of spillover mechanisms.

MOF materials can show excellent CO_2 (Table 3) and CH_4 (Table 4) storage capacities. The best performing material for CH_4 storage, PCN-14, has a storage capacity 28% higher than DoE requirement. MOF materials can also show very high capacity in CO_2 adsorption and the significantly enhanced CO_2 selectivity over other gases (N_2, CO, CH_4) have been observed by generating coordination polymers with free functional groups within the framework surface. The challenge still remains to design new functional and robust materials incorporating higher pore volumes and specific multi-functional groups. The role of design and synthesis has never been more important.

Table 4 Comparison of CH_4 adsorption in metal-organic frameworks

Materials	S_A, m^2 g^{-1}		V_P, cm^3 g^{-1}	CH_4 uptake at 35 bar, 298 K, mg g^{-1} (v(STP)/v)	Ref.
	BET	Langmuir			
MOF-5	3,800	4,400	1.13	120 (135)	[52]
IRMOF-3	2,446	3,062	1.07	104 (120)	[52]
IRMOF-6	2,800	3,310	0.993	171 (155)	[52]
MIL-100	1,900		1.10	121 (119)	[28]
MIL-101	4,230	5,500	2.15	162(100)	[28]
MIL-53(Al, Cr)	1,270	1,580		96 (155) (304 K)	[133]
HKUST-1	1,507	2,175	0.75	78 (109)	[110]
PCN-14	1,750	2,180	0.87	189 (230) (290 K)	[27]
$\{CuSiF_6(4,4'\text{-bipyridine})_2\}_n$	1,337		0.56	104 (133)	[79]

Acknowledgments We thank the EPSRC (Supergen consortium UKSHEC) for support. MS gratefully acknowledges receipt of a Wolfson Royal Society Merit Award and the ERC for an Advanced Grant to MS.

References

1. Energy Information Administration, Offical Energy Statistics from the U.S Government, International Energy Annual 2005. http://www.eia.doe.gov/emeu/iea/
2. Schlapbach L, Züttel A (2001) Nature 414:353
3. Hydrogen Storage: State-of-the-Art and Future Perspective. http://www.jrc.nl/publ/2003_publ.html
4. U.S. Department of Energy, Energy Efficiency and Renewable Energy. http://www.eere.energy.gov/hydrogenandfuelcells/pdfs/freedomcar_targets_explanations.pdf
5. Hydrogen, Fuel Cells, & Infrastructure Technologies Program: Multi-year Research, Development, and Demonstration Plan. http://www.eere.energy.gov/hydrogenandfuelcells/mypp/
6. Basic Research Needs for the Hydrogen Economy, Report of the Basic Energy Sciences Workshop on Hydrogen Production, Storage, and Use. http://www.sc.doe.gov/bes/
7. Eberle U, Felderhoff M, Schüth F (2009) Angew Chem Int Ed 48:6608
8. Lin X, Jia J, Hubberstey P, Schröder M, Champness NR (2007) CrystEngComm 9:438
9. Collins DJ, Zhou H-C (2007) J Mater Chem 17:3154
10. Murray LJ, Dincă M, Long JR (2009) Chem Soc Rev 38:1294

10a. Czaja AU, Trukhan N, Müller U (2009) Chem Soc Rev 38:1284

11. Kubo M, Kishita M, Kuroda Y (1960) J Polym Sci 48:467
12. Block BP, Simkin J, Ocone LR (1962) J Am Chem Soc 84:1749
13. Glick MD, Dahl LF (1966) Inorg Chem 5:289
14. Peard WJ, Pflaum RT (1958) J Am Chem Soc 80:1593
15. Musgrave TR, Mattson CE (1968) Inorg Chem 7:1433
16. Hoskins BF, Robson RJ (1989) Am Chem Soc 111:5962
17. Hoskins BF, Robson R (1990) J Am Chem Soc 112:1546
18. Robson R, Abrahams BF, Batten SR, Gable RW, Hoskins BF, Liu J (1992) ACS Symp Ser 499:256
19. Bowes CL, Ozin GA (1996) Adv Mat 8:13
20. Sauriat-Dorizon N, Maris T, Wuest JD, Enright GD (2003) J Org Chem 68:240
21. Desiraju GR (1995) Angew Chem Int Ed Engl 34:2311
22. Champness NR, Schröder M (1998) Curr Opin Solid State Mater Chem 3:419
23. Khlobystov AN, Brett MT, Blake AJ, Champness NR, Gill PMW, O'Neill DP, Teat SJ, Wilson C, Schröder M (2003) J Am Chem Soc 125:6753
24. Wegrzyn J, Gurevich M (1996) Appl Energy 55:71
25. Burchell T, Rogers M (2000) SAE Technical Paper Series 2000-01-2205
26. Lozano-Castello D, Cazorla-Amoros D, Linares-Solano A (2002) Energy Fuels 16:1321
27. Ma S, Sun D, Simmons JM, Collier CD, Yuan D, Zhou H-C (2008) J Am Chem Soc 130:1012
28. Llewellyn PL, Bourrelly S, Serre C, Vimont A, Daturi M, Hamon L, De Weireld G, Chang J-S, Hong D-Y, Hwang YK, Jhung SH, Férey G (2008) Langmuir 24:7245
29. Johnson J (2004) Chem Eng News 82:36
30. Yong Z, Mata V, Rodrigues AE (2002) Sep Purif Technol 26:195
31. Millward AR, Yaghi OM (2005) J Am Chem Soc 127:17998
32. Couck S, Denayer JFM, Baron GV, Rémy T, Gascon J, Kapteijn F (2009) J Am Chem Soc 131:6326
33. Ahnfeldt T, Gunzelmann D, Loiseau T, Hirsemann D, Senker J, Férey G, Stock N (2009) Inorg Chem 48:3057

34. Gascon J, Aktay U, Hernandez-Alonso MD, van Klink GPM, Kapteijn F (2009) J Catal 261:75
35. Davis ME (1995) Stud Surf Sci Catal 97:35
36. Lobo RF, Zones SI, Davis ME (1995) J Incl Phen Mol Rec Chem 21:47
37. Burkett SL, Davis ME (1996) Compr Supramol Chem 7:465
38. Raman NK, Anderson MT, Brinker CJ (1996) Chem Mater 8:1682
39. Barton TJ, Bull LM, Klemperer WG, Loy DA, McEnaney B, Misono M, Monson PA, Pez G, Scherer GW, Vartuli JC, Yaghi OM (1999) Chem Mater 11:2633
40. Yaghi OM, Li H, Davis C, Richardson D, Groy TL (1998) Acc Chem Res 31:474
41. Blake AJ, Champness NR, Hubberstey P, Li W-S, Withersby MA, Schröder M (1999) Coord Chem Rev 183:117
42. Moulton B, Zaworotko MJ (2001) Chem Rev 101:1629
43. Evans OR, Lin W (2002) Acc Chem Res 35:511
44. Férey G, Mellot-Draznieks C, Serre C, Millange F (2005) Acc Chem Res 38:217
45. Tranchemontagne DJ, Mendoza-Cortes JL, O'Keeffe M, Yaghi OM (2009) Chem Soc Rev 38:1257
46. Rosi NL, Eddaoudi M, Kim J, O'Keeffe M, Yaghi OM (2002) CrystEngComm 4:401
47. James SL (2003) Chem Soc Rev 32:276
48. Braga D, Brammer L, Champness NR (2005) CrystEngComm 7:1
49. Hill RJ, Long D-L, Champness NR, Hubberstey P, Schröder M (2005) Acc Chem Res 38:335
50. Deiters E, Bulach V, Hosseini MW (2005) Chem Commun 3906
51. Ockwig NW, Delgado-Friedrichs O, O'Keeffe M, Yaghi OM (2005) Acc Chem Res 38:176
52. Eddaoudi M, Kim J, Rosi N, Vodak D, Wachter J, O'Keeffe M, Yaghi OM (2002) Science 295:469
53. Chun H, Dybtsev DN, Kim H, Kim K (2005) Chem Eur J 11:3521
54. Banerjee R, Phan A, Wang B, Knobler C, Furukawa H, O'Keeffe M, Yaghi OM (2008) Science 319:939
55. Park KS, Ni Z, Côté AP, Choi JY, Huang R, Uribe-Romo FJ, Chae HK, O'Keeffe M, Yaghi OM (2006) Proc Natl Acad Sci USA 103:10186
56. Lin X, Telepeni I, Blake AJ, Dailly A, Brown CM, Simmons JM, Zoppi M, Walker GS, Thomas KM, Mays TJ, Hubberstey P, Champness NR, Schröder M (2009) J Am Chem Soc 131:2159
57. Lin X, Jia J, Zhao X, Thomas KM, Blake AJ, Walker GS, Champness NR, Hubberstey P, Schröder M (2006) Angew Chem Int Ed 45:7358
58. O'Keeffe M, Eddaoudi M, Li HL, Reineke T, Yaghi OM (2000) J Solid State Chem 152:3
59. Eddaoudi M, Moler DB, Li H, Chen B, Reineke TM, O'Keeffe M, Yaghi OM (2001) Acc Chem Res 34:319
60. Yaghi OM, O'Keeffe M, Ockwig NW, Chae HK, Eddaoudi M, Kim J (2003) Nature 423:705
61. Rowsell JLC, Yaghi OM (2004) Microporous Mesoporous Mater 73:3
62. Kitagawa S, Kitaura R, S-i N (2004) Angew Chem Int Ed 43:2334
63. Rao CNR, Natarajan S, Vaidhyanathan R (2004) Angew Chem Int Ed 43:1466
64. Champness NR (2006) Dalton Transactions 877
65. O'Keeffe M, Peskov MA, Ramsden SJ, Yaghi OM (2008) Acc Chem Res 41:1782
66. Macgillivray LR, Subramanian S, Zaworotko MJ (1994) Chem Commun 1325
67. Blake AJ, Champness NR, Chung SSM, Li W-S, Schröder M (1997) Chem Commun 1473
68. Blake AJ, Champness NR, Khlobystov AN, Lemenovskii DA, Li W-S, Schröder M (1997) Chem Commun 1339
69. Long D-L, Hill RJ, Blake AJ, Champness NR, Hubberstey P, Proserpio DM, Wilson C, Schröder M (2004) Angew Chem Int Ed 43:1851
70. Hill RJ, Long D-L, Hubberstey P, Schröder M, Champness NR (2005) J Solid State Chem 178:2414
71. Blake AJ, Brooks NR, Champness NR, Crew M, Hanton LR, Hubberstey P, Parsons S, Schröder M (1999) J Chem Soc Dalton Trans 2813

72. Banerjee R, Furukawa H, Britt D, Knobler C, O'Keeffe M, Yaghi OM (2009) J Am Chem Soc 131:3875
73. Wang B, Côté AP, Furukawa H, O'Keeffe M, Yaghi OM (2008) Nature 453:207
74. Hayashi H, Côté AP, Furukawa H, O'Keeffe M, Yaghi OM (2007) Nat Mater 6:501
75. Tian Y-Q, Cai C-X, Ji Y, You X-Z, Peng SM, Lee GH (2002) Angew Chem Int Ed 41:1384
76. Tian Y-Q, Cai C-X, Ren X-M, Duan C-Y, Xu Y, Gao S, You X-Z (2003) Chemistry Eur J 9:5673
77. Tian Y-Q, Chen Z-X, Weng LH, Guo HB, Gao S, Zhao DY (2004) Inorg Chem 43:4631
78. Tian YQ, Zhao YM, Chen ZX, Zhang GN, Weng LH, Zhao DY (2007) Chem Eur J 13:4146
79. S-i N, Kitagawa S, Kondo M, Seki K (2000) Angew Chem Int Ed 39:2082
80. Rosi NL, Eckert J, Eddaoudi M, Vodak DT, Kim J, O'Keeffe M, Yaghi OM (2003) Science 300:1127
81. Buser HJ, Schwarzenbach D, Petter W, Ludi A (1977) Inorg Chem 16:2704
82. Kaye SS, Long JR (2005) J Am Chem Soc 127:6506
83. Chapman KW, Chupas PJ, Maxey ER, Richardson JW (2006) Chem Commun 4013
84. Hartman MR, Peterson VK, Liu Y, Kaye SS, Long JR (2006) Chem Mater 18:3221
85. Rowsell JLC, Millward AR, Park KS, Yaghi OM (2004) J Am Chem Soc 126:5666
86. Rowsell JLC, Yaghi OM (2006) J Am Chem Soc 128:1304
87. Kaye SS, Dailly A, Yaghi OM, Long JR (2007) J Am Chem Soc 129:14176
88. Wong-Foy AG, Matzger AJ, Yaghi OM (2006) J Am Chem Soc 128:3494
89. Mueller U, Schubert M, Teich F, Puetter H, Schierle-Arndt K, Pastre J (2006) J Mater Chem 16:626
90. Choi JY, Kim J, Jhung SH, Kim HK, Chang JS, Chae HK (2006) Bull Korean Chem Soc 27:1523
91. Everett DH, Powl JC (1976) J Chem Soc Faraday Trans I 72:619
92. Batten SR, Robson R (1998) Angew Chem Int Ed 37:1461
93. Withersby MA, Blake AJ, Champness NR, Cooke PA, Hubberstey P, Realf AL, Teat SJ, Schröder M (2000) Dalton Trans 3261
94. Evans OR, Lin W (2001) Chem Mater 13:2705
95. Kesanli B, Cui Y, Smith MR, Bittner EW, Bockrath BC, Lin WB (2005) Angew Chem Int Ed 44:72
96. Kaye SS, Long JR (2008) J Am Chem Soc 130:806
97. Howdle SM, Healy MA, Poliakoff M (1990) J Am Chem Soc 112:4804
98. Walton KS, Millward AR, Dubbeldam D, Frost H, Low JJ, Yaghi OM, Snurr RQ (2008) J Am Chem Soc 130:406
99. Liu Y, Kabbour H, Brown CM, Neumann DA, Ahn CC (2008) Langmuir 24:4772
100. Chae HK, Siberio-Perez DY, Kim J, Go YB, Eddaoudi M, Matzger AJ, O'Keeffe M, Yaghi OM (2004) Nature 427:523
101. Cotton FA, Mester ZC, Webb TR (1974) Acta Cryst Sec B 30:2768
102. Ceccherelli P, Curini M, Marcotullio MC, Rosati O (1991) Tetrahedron 47:7403
103. Chui SSY, Lo SMF, Charmant JPH, Orpen AG, Williams ID (1999) Science 283:1148
104. Panella B, Hirscher M (2005) Adv Mater 17:538
105. Prestipino C, Regli L, Vitillo JG, Bonino F, Damin A, Lamberti C, Zecchina A, Solari PL, Kongshaug KO, Bordiga S (2006) Chem Mater 18:1337
106. Kramer M, Schwarz U, Kaskel S (2006) J Mater Chem 16:2245
107. Peterson VK, Liu Y, Brown CM, Kepert CJ (2006) J Am Chem Soc 128:15578
108. Brown CM, Liu Y, Yildirim T, Peterson VK, Kepert CJ (2009) Nanotechnology 20:204025
109. Liu Y, Brown CM, Neumann DA, Peterson VK, Kepert CJ (2007) J Alloys Compd 446–447:385
110. Senkovska I, Kaskel S (2008) Microporous Mesoporous Mater 112:108
111. Ma S, Sun D, Ambrogio M, Fillinger JA, Parkin S, Zhou H-C (2007) J Am Chem Soc 129:1858
112. Sun D, Ma S, Ke Y, Collins DJ, Zhou H-C (2006) J Am Chem Soc 128:3896

113. Chen B, Ockwig NW, Millward AR, Contreras DS, Yaghi OM (2005) Angew Chem Int Ed 44:4745
114. Ma S, Simmons JM, Sun D, Yuan D, Zhou H-C (2009) Inorg Chem 48:5263
115. Yang S, Lin X, Dailly A, Blake AJ, Champness NR, Hubberstey P, Schröder M (2009) Chem Eur J 15:4829
116. Kim H, Samsonenko DG, Das S, Kim G-H, Lee H-S, Dybtsev DN, Berdonosova EA, Kim K (2009) Chem Asian J 4:886
117. Chun H, Moon J (2007) Inorg Chem 46:4371
118. Yan Y, Lin X, Yang S, Blake AJ, Dailly A, Champness NR, Hubberstey P, Schröder M (2009) Chem Commun 1025
119. Nouar F, Eubank JF, Bousquet T, Wojtas L, Zaworotko MJ, Eddaoudi M (2008) J Am Chem Soc 130:1833
120. Chun H (2008) J Am Chem Soc 130:800
121. Furukawa H, Miller MA, Yaghi OM (2007) J Mater Chem 17:3197
122. Latroche M, Surblé S, Serre C, Mellot-Draznieks C, Llewellyn PL, Lee J-H, Chang J-S, Jhung SH, Férey G (2006) Angew Chem Int Ed 45:8227
123. Férey G, Mellot-Draznieks C, Serre C, Millange F, Dutour J, Surblé S, Margiolaki I (2005) Science 309:2040
124. Wang X-S, Ma S, Forster PM, Yuan D, Eckert J, López JJ, Murphy BJ, Parise JB, Zhou H-C (2008) Angew Chem Int Ed 47:7263
125. Yang W, Lin X, Jia J, Blake AJ, Wilson C, Hubberstey P, Champness NR, Schröder M (2008) Chem Commun 359
126. Yang W, Lin X, Matsuda R, Blake AJ, Wilson C, Lewis W, Hubberstey P, Kitagawa S, Sakamoto H, Champness NR, Schröder M (2009) unpublished work
127. Férey G (2005) Science 310:1119
128. Surblé S, Millange F, Serre C, Düren T, Latroche M, Bourrelly S, Llewellyn PL, Férey G (2006) J Am Chem Soc 128:14889
129. Sonnauer A, Hoffmann F, Froeba M, Kienle L, Duppel V, Thommes M, Serre C, Férey G, Stock N (2009) Angew Chem Int Ed 48:3791
130. Millange F, Guillou N, Walton RI, Greneche J-M, Margiolaki I, Férey G (2008) Chem Commun 4732
131. Férey G, Latroche M, Serre C, Millange F, Loiseau T, Percheron-Guegan A (2003) Chem Commun 2976
132. Millange F, Serre C, Férey G (2002) Chem Commun 822
133. Bourrelly S, Llewellyn PL, Serre C, Millange F, Loiseau T, Férey G (2005) J Am Chem Soc 127:13519
134. Loiseau T, Serre C, Huguenard C, Fink G, Taulelle F, Henry M, Bataille T, Férey G (2004) Chem Eur J 10:1373
135. Llewellyn PL, Bourrelly S, Serre C, Filinchuk Y, Férey G (2006) Angew Chem Int Ed 45:7751
136. Llewellyn PL, Maurin G, Devic T, Loera-Serna S, Rosenbach N, Serre C, Bourrelly S, Horcajada P, Filinchuk Y, Férey G (2008) J Am Chem Soc 130:12808
137. Alaerts L, Maes M, Giebeler L, Jacobs PA, Martens JA, Denayer JFM, Kirschhock CEA, De Vos DE (2008) J Am Chem Soc 130:14170
138. Liu Y, Her J-H, Dailly A, Ramirez-Cuesta AJ, Neumann DA, Brown CM (2008) J Am Chem Soc 130:11813
139. Bourrelly S, Llewellyn PL, Serre C, Millange F, Loiseau T, Férey G (2005) J Am Chem Soc 127:13519
140. Liu Y, Eubank JF, Cairns AJ, Eckert J, Kravtsov VC, Luebke R, Eddaoudi M (2007) Angew Chem Int Ed 46:3278
141. Dincă M, Long JR (2005) J Am Chem Soc 127:9376
142. Senkovska I, Fritsch J, Kaskel S (2007) Eur J Inorg Chem 5475
143. Senkovska I, Kaskel S (2006) Eur J Inorg Chem 4564

144. Rood JA, Noll BC, Henderson KW (2007) Inorg Chem 46:7259
145. Rood JA, Noll BC, Henderson KW (2006) Inorg Chem 45:5521
146. Loiseau T, Lecroq L, Volkringer C, Marrot J, Férey G, Haouas M, Taulelle F, Bourrelly S, Llewellyn PL, Latroche M (2006) J Am Chem Soc 128:10223
147. Loiseau T, Beitone L, Taulelle F, Férey G (2006) Solid State Sci 8:346
148. Ahnfeldt T, Guillou N, Gunzelmann D, Margiolaki I, Loiseau T, Férey G, Senker J, Stock N (2009) Angew Chem Int Ed 48:5163
149. Dincă M, Dailly A, Liu Y, Brown CM, Neumann DA, Long JR (2006) J Am Chem Soc 128:16876
150. Dincă M, Han WS, Liu Y, Dailly A, Brown CM, Long JR (2007) Angew Chem Int Ed 46:1419
151. Dincă M, Long JR (2007) J Am Chem Soc 129:11172
152. Demessence A, D'Alessandro DM, Foo ML, Long JR (2009) J Am Chem Soc 131:8784
153. Choi HJ, Dincă M, Long JR (2008) J Am Chem Soc 130:7848
154. Dybtsev DN, Chun H, Yoon SH, Kim D, Kim K (2004) J Am Chem Soc 126:32
155. Ma S, Zhou H-C (2006) J Am Chem Soc 128:11734
156. Navarro JAR, Barea E, Salas JM, Masciocchi N, Galli S, Sironi A, Ania CO, Parra JB (2006) Inorg Chem 45:2397
157. Chen B, Ma S, Zapata F, Lobkovsky EB, Yang J (2006) Inorg Chem 45:5718
158. Park HJ, Suh MP (2007) Chem Eur J 14:8812
159. Lin X, Blake Alexander J, Wilson C, Sun XZ, Champness NR, George MW, Hubberstey P, Mokaya R, Schröder M (2006) J Am Chem Soc 128:10745
160. Jia J, Lin X, Blake AJ, Champness NR, Hubberstey P, Shao L, Walker G, Wilson C, Schröder M (2006) Inorg Chem 45:8838
161. Humphrey SM, Chang JS, Jhung SH, Yoon JW, Wood PT (2007) Angew Chem Int Ed 46:272
162. Horike S, Matsuda R, Tanaka D, Matsubara S, Mizuno M, Endo K, Kitagawa S (2006) Angew Chem Int Ed 45:7226
163. Chen CL, Goforth AM, Smith MD, Su CY, zur Loye HC (2005) Inorg Chem 44:8762
164. Ma BQ, Mulfort KL, Hupp JT (2005) Inorg Chem 44:4912
165. Jia J, Lin X, Wilson C, Blake AJ, Champness NR, Hubberstey P, Walker G, Cussen EJ, Schröder M (2007) Chem Commun 840
166. Lee EY, Suh MP (2004) Angew Chem Int Ed 43:2798
167. Koh K, Wong-Foy AG, Matzger AJ (2008) Angew Chem Int Ed 47:677
168. Koh K, Wong-Foy AG, Matzger AJ (2009) J Am Chem Soc 131:4184
169. Doonan CJ, Morris W, Furukawa H, Yaghi OM (2009) J Am Chem Soc 131:9492
170. Han SS, Goddard WA III (2007) J Am Chem Soc 129:8422
171. Han SS, Furukawa H, Yaghi OM, Goddard WA (2008) J Am Chem Soc 130:11580
172. Klontzas E, Mavrandonakis A, Tylianakis E, Froudakis GE (2008) Nano Lett 8:1572
173. Lochan RC, Head-Gordon M (2006) Phys Chem Chem Phys 8:1357
174. Barbatti M, Jalbert G, Nascimento MAC (2002) J Phys Chem A 106:551
175. Blomqvist A, Araújo CM, Srepusharawoot P, Ahuja R (2007) Proc Natl Acad Sci USA 104:20173
176. Mavrandonakis A, Tylianakis E, Stubos AK, Froudakis GE (2008) J Phys Chem C 112:7290
177. Dalach P, Frost H, Snurr RQ, Ellis DE (2008) J Phys Chem C 112:9278
178. Yang S, Lin X, Blake AJ, Thomas KM, Hubberstey P, Champness NR, Schröder M (2008) Chem Commun 6108
179. Nouar F, Eckert J, Eubank JF, Forster P, Eddaoudi M (2009) J Am Chem Soc 131:2864
180. Mulfort KL, Hupp JT (2008) Inorg Chem 47:7936
181. Mulfort KL, Hupp JT (2007) J Am Chem Soc 129:9604
182. Mulfort KL, Wilson TM, Wasielewski MR, Hupp JT (2009) Langmuir 25:503
183. Yang S, Lin X, Blake AJ, Walker GS, Hubberstey P, Champness NR, Schröder M (2009) Nat Chem 1:487

184. Snurr R (2009) Nat Chem 1:426
185. Himsl D, Wallacher D, Hartmann M (2009) Angew Chem Int Ed 48:4639
186. Mulfort KL, Farha OK, Stern CL, Sarjeant AA, Hupp JT (2009) J Am Chem Soc 131:3866
187. Zhao X, Xiao B, Fletcher AJ, Thomas KM, Bradshaw D, Rosseinsky MJ (2004) Science 306:1012
188. Dietzel PDC, Panella B, Hirscher M, Blom R, Fjellvag H (2006) Chem Commun 959
189. Forster PM, Eckert J, Heiken BD, Parise JB, Yoon JW, Jhung SH, Chang J-S, Cheetham AK (2006) J Am Chem Soc 128:16846
190. Chen B, Zhao X, Putkham A, Hong K, Lobkovsky EB, Hurtado EJ, Fletcher AJ, Thomas KM (2008) J Am Chem Soc 130:6411
191. Li Y, Yang RT (2007) Langmuir 23:12937
192. Li Y, Yang RT (2006) J Am Chem Soc 128:8136
193. Li Y, Yang RT (2006) J Am Chem Soc 128:726
194. Lueking A, Yang RT (2002) J Catal 206:165
195. King TS, Wu X, Gerstein BC (1986) J Am Chem Soc 108:6056
196. Lachawiec AJ Jr, Yang RT (2008) Langmuir 24:6159
197. Li Y, Yang FH, Yang RT (2007) J Phys Chem C 111:3405
198. Li Y, Yang RT (2008) AIChE J 54:269
199. Tsao C-S, Yu M-S, Wang C-Y, Liao P-Y, Chen H-L, Jeng US, Tzeng Y-R, Chung T-Y, Wu H-C (2009) J Am Chem Soc 131:1404
200. Bhatia SK, Myers AL (2006) Langmuir 22:1688
201. Furukawa H, Yaghi OM (2009) J Am Chem Soc 131:8875
202. Neofotistou E, Malliakas CD, Trikalitis PN (2009) Chem Eur J 15:4523
203. Jhung JWYSH, Hwang YK, Humphrey SM, Wood PT, Chang J-S (2007) Adv Mater 19:1830
204. Plant DF, Maurin G, Deroche I, Llewellyn PL (2007) Microporous Mesoporous Mater 99:70

Top Curr Chem (2010) 293: 77–113
DOI 10.1007/128_2009_4

Published online: 03 October 2009

Doping of Metal-Organic Frameworks with Functional Guest Molecules and Nanoparticles

Felicitas Schröder and Roland A. Fischer

Abstract Nanoparticle synthesis within metal-organic frameworks (MOFs) is performed by the adsorption of suitable precursor molecules for the metal component and subsequent decomposition to the composite materials nanoparticles@MOF. This chapter will review different approaches of loading MOFs with more complex organic molecules and metal-organic precursor molecules. The related reactions inside MOFs are discussed with a focus on stabilizing reactive intermediates in the corresponding cavities. The syntheses of metal and metal oxide nanoparticles inside MOFs are reviewed, and different synthetic routes compared. Emphasis is placed on the micro structural characterization of the materials nanoparticles@MOF with a particular focus on the location of embedded nanoparticles using TEM methods. Some first examples of applications of the doped MOFs in heterogeneous catalysis and hydrogen storage are described.

Keywords Catalysis • Hydrogen storage • Metal oxides • Metal-organic frameworks • Nanoparticles

Contents

F. Schröder and R.A. Fischer (✉)
Lehrstuhl für Anorganische Chemie II-Organometallics and Materials,
Ruhr Universität Bochum, Germany
e-mail: roland.fischer@rub.de

Abbreviations

bdc	1,4-Benzene-dicarboxylate
bpdc	4,4′,-Biphenyldicarboxylate
BPTC	1,1´-Biphenyl-2,2´,6,6´-tetracarboxylate
CN^{t}Bu	Tertiary-butyl isonitrile
cod	*cis*,*cis*-1,5-Cyclooctane
COF	Covalent organic framework
cot	*cis*,*cis*,*cis*-1,3,5-Cyclooctatriene
Cp	Cyclopentadienyl-anion (C_5H_5)
cyclam	1,4,8,11-Tetraaza-cyclotetradecane
dabco	1,4-Diazabicyclo[2.2.2]octane
DMA	*N*,*N*-Dimethylacetamide
dmf	Dimethylformamide
EXAFS	Extended X-ray absorption fine structure
FT-IR	Fourier transform infrared spectroscopy
FWHM	Full width at half maximum
HAADF	High-angle annular dark field
HKUST	Hong Kong University of Science and Technology
JUC	Jilin University China
Me	Methyl
MIL	Matérial Institute Lavoisier
MOCVD	Metal-organic vapor deposition
MOF	Metal-organic framework
mtb	methanetetra-benzoate
O*i*Pr	Iso-propoxide
pyz	Pyrazine
SAED	Selected area electron diffraction
STEM	Scanning transmission electron microscopy
TATB	triazine-1,3,5-tribenzoate
TEM	Transmission electron microscopy
THF	Tetrahydrofuran
wt%	Weight percent
XANES	X-ray absorption near edge structure
XAS	X-ray absorption spectroscopy
XRD	X-ray powder diffraction
ZIF	Zeolite A imidazolate framework

1 Introduction

Metal-organic frameworks (MOFs) allow reversible adsorption of guest molecules and are thus characterized by a permanent porosity. This novel class of hybrid inorganic–organic soft solid state materials is largely based on Werner-type coordination chemistry. Specifically, the research on porous coordination polymers has become a major field of research during the past decade [1–8]. For example, the concepts of "reticular synthesis," along with the basic zinc and copper carboxylates based so-called MOFs [9,10] were established; likewise boronic ester based frameworks (COFs) [7] and zinc imidazolate based MOFs (ZIFs) [13–15] were also introduced. The responsive and adaptive properties of soft porous coordination polymers with applications in gas storage, sensing and catalysis have been investigated as well [16–19]. The so-called Materials of Institute Lavoisier (MILs) [20,21], were introduced, with MIL-53 and MIL-88 demonstrating large and reversible structural changes upon guest exchange and MIL-101 being the most porous material known to date, with an equivalent Langmuir surface area of 5,900 $m^2 g^{-1}$ [22]. Chiral MOFs, e.g., with an amino acid backbone, exhibiting interesting properties in selective solvent sorption have been studied [23]. A wide range of studies on the applications of all these materials in gas storage and separation as well as solvent separation have been performed [15,25–33]. Furthermore the controlled growth of MOF thin films at surfaces ("SURMOFs") has been demonstrated by a few groups recently [34–38]. This paves the way for integration of MOF materials into more complex functional devices such as smart membranes and chemical sensors. Herein we will focus on the doping of MOFs with nanoparticles. Similar to zeolites, mesoporous silica and other inorganic porous materials, the grafting of functional molecular species at the internal surface of MOFs and the loading of the pores, cavities or channels of MOFs with functional nanoparticles is relevant for a number of potential applications including catalysis, hydrogen storage and sensing [39–44]. In addition, the use of MOFs as host materials for the formation of nanosized metals or metal oxides is of considerable interest as it helps to study the resulting specific properties and host-synergetic functions [45–47]. In this chapter we will cover the current literature related to the doping of MOFs with nanoparticles with some emphasis on the involved precursor concepts. The discussion will include relevant aspects of the loading of MOFs and loading-related properties in general. This appears to be very important since the loading of MOFs, using molecular precursors to provide the components for the nanoparticle growth inside the framework, clearly relies on the supramolecular host–guest chemistry of MOFs in general.

2 Loading of Metal-Organic Frameworks with Guest Molecules

The synthesis of MOFs usually requires the pores or channels to be occupied with solvent molecules and sometimes also with unreacted, excess linkers. These molecules should be removable or exchangeable by other solvent or gas molecules

without any structural change of the parent framework in order to load MOFs with more complex functional molecules. This is apparently mandatory, since in some cases structural changes of the host or even complete collapse of the framework structure can occur upon solvent removal [17,18]. MOFs are typically studied in the context of their gas storage and/or separation properties, mainly focusing on rather nonpolar hydrocarbons [25–33]. Most MOFs exhibit nonpolar, i.e., hydrophobic, inner surfaces and we will largely restrict our discussion to these types of MOFs.

2.1 Large Organic Molecules

Only a few key examples of MOFs have been tested in loading with larger, more complex organic molecules so far. In their first report on the zinc-1,3,5-benzenetribenzoate based MOF-177 in 2004 [10], Yaghi et al. introduced loading of this highly porous framework with dye molecules of Astrazon Orange R, Nile red and Reichardt's dye as well as with C_{60} molecules. The inclusion of these compounds in MOF-177 was followed by UV- and Raman-Spectroscopy (Fig. 1). Quantitative uptake analysis of the materials revealed sixteen molecules of Astrazon Orange R, two molecules of Nile red and one molecule of Reichardt's dye per MOF-177 unit cell, already demonstrating the size dependant sorption properties of MOF-177.

Quiu et al. presented the synthesis of the porous framework $[Cd_3(bpdc)_3(dmf)]\cdot 5\,dmf\bullet 18\,H_2O$ (bpdc = 4,4′-biphenyldicarboxylate, dmf = dimethylformamide, JUC-48, JUC = Jilin University China) and the assembly of Rh6G dye molecules in its pores [48]. The dye molecules were infiltrated by either adding an ethanolic solution of the dye to the mother liquor of the MOF or immersion of the framework in the dye solution. The dye@MOF composite showed temperature dependent fluorescence properties. Férey et al. studied the loading of the chromium terephthalate based MIL-101 with the Keggin anion $[PW_{11}O_{40}]^{7-}$ in order to show the selective inclusion of very large guest molecules into the spacious cages of the MIL-101 (Fig. 2) [22]. The loading was followed by powder X-ray diffraction (PXRD), N_2 adsorption and ^{31}P-NMR. From elemental analysis 0.05 Keggin anions per chromium were found, corresponding to a loading of five Keggin moieties per large cage of MIL-101. The volume of five Keggin anions represents 10,100 Å^3 in volume, the volume of the large cage of MIL-101 however is 20,600 Å^3, and the authors therefore assume that the remaining space is filled with cations and water molecules. The Férey group also introduced the first drug (Ibuprofen) release study of a MOF [49,50]. The Ibuprofen uptake of the frameworks as well as the subsequent release were investigated.

Leaving the well known toxicity of chromium aside, the drug release study of MIL-101 and MIL-100 shows the potential of MOFs for not only the loading but also the controlled release of an imbedded compound [49]. MIL-101 is able to take up four times as much Ibuprofen as MCM-41, which has comparable cage sizes. It also shows a slower delivery rate, which presents advantages for larger

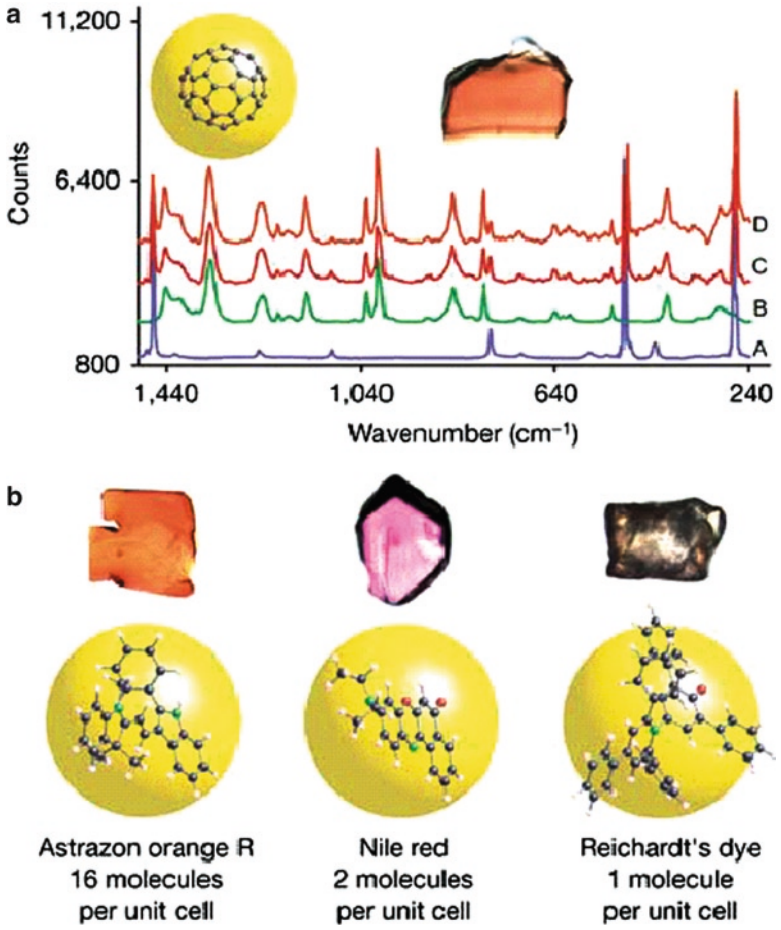

Fig. 1 Loading of MOF-177: (**a**) Raman spectra of (A) bulk C_{60}, (B) evacuated MOF-177 crystal, (C) whole MOF-177 crystals loaded with C_{60} and (D) sliced MOF-177 crystals loaded with C_{60}. (**b**) MOF-177 crystal loaded with dye molecules.[10] Reprinted by permission from Macmillian Publishers Ltd: [Nature] [10] copyright 2004

pharmacological molecules. Very recently, the "breathing" chromium and iron based MIL-53 materials have also been used as matrices for the delivery of Ibuprofen [50]. Very slow, controlled and complete delivery was achieved under physiological conditions which are due to the ability of the framework to adapt to the dimensions of the drug.

These and similar studies employing more complex organic molecules as guests prove distinct features of the corresponding framework, like extraordinary cavity size or adsorption properties. The loading of MOFs with metal-organic precursor molecules is effected by the combination of the functionality of the precursors to

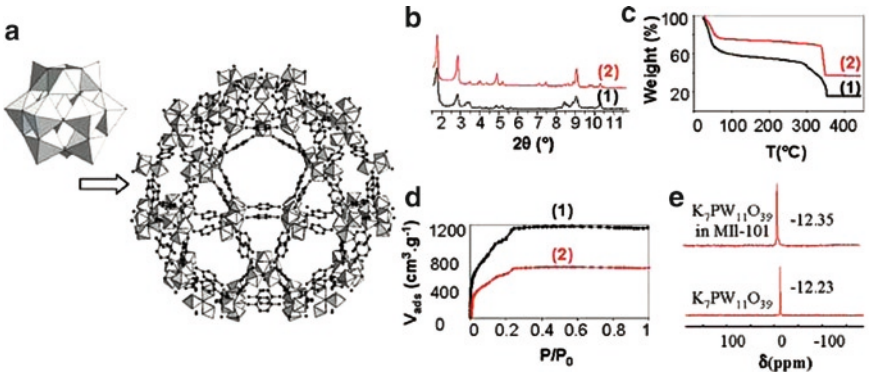

Fig. 2 (**a**) Schematic view of the insertion of Keggin anions within the largest pore of MIL-101. (**b**) XRD of MIL-101 (1) and MIL-101(Keggin) (2). θ, in degrees. (**c**) TGA of MIL-101 (1) and MIL-101(Keggin) (2). *T*, temperature (K). (**d**) Nitrogen sorption–desorption isotherms at 78 K of MIL-101 (1) and MIL-101(Keggin) (2). V_{ads}, volume adsorbed in cm^3g^{-1}. (**e**)^{31}P solid state NMR spectra of the Keggin salt and MIL-101(Keggin). δ, chemical shift in ppm. From [22]. Reprinted with permission from AAAS

serve as sources for nanoparticles, with the property of the MOF to restrict the growth and the aggregation of the particles by caging effects. Interestingly, the characteristic sizes of cavities, channels and pores of MOFs cover a size regime between classical zeolites ≤1 nm and mesoporous materials ≥2–3 nm. In contrast to these latter materials however, MOFs are expected to show a much weaker particle/host interaction.

3 Towards Nanoparticles in Metal-Organic Frameworks

Metal doping of MOFs seems to be a promising field of research not only for catalytic applications but also for enhanced capacity in gas storage as compared to the pure MOF [51]. In general one could think of two different approaches for the synthesis of metal nanoparticles inside MOFs: the infiltration of preformed nanoparticles stabilized by organic molecules (surfactants) in solution or the stepwise infiltration of suitable precursors and their conversion into nanoparticles inside the framework cavity. For other porous host materials, such as silica and alumina, several approaches for embedding nanoparticles in their cavities via immersion in colloidal solutions are known in the literature [52,53]. However, the typical cavity sizes of MOFs are too small to match the size of surfactant stabilized nanoparticles with hydrodynamic radii typically larger than 3 nm. In order to utilize the MOF as a stabilizing agent and host material at the same time, stepwise precursor infiltration and subsequent decomposition appear to constitute the most suitable approach. In this way, the size and shape of the nanoparticles, synthesized directly in the pores

of the framework, should be controlled by the pore size, shape and channel structure of the host material. Suitable precursors for the synthesis of metal nanoparticles in MOFs can in general be molecules that are also commonly used in the synthesis of colloidal metal nanoparticles in solution or metal nanoparticles in the solid state. These molecules are often also known from thin film formation processes such as metal-organic vapor deposition (MOCVD) or atomic layer deposition (ALD) and are basically metal-organic coordination compounds, the so-called organometallic compounds, often with entirely hydrocarbon ligand molecules, featuring metal carbon bonds. Upon decomposition, the ligands of these molecules are cleaved from the metal center, leaving "free" metal atoms that will then fuse together to form metal clusters [54,55]. Spatial confinement of the MOF cavities should limit the growth of the particles to the size of the corresponding pore diameter. Note, that the host framework should be inert towards the embedded precursor as well as to decomposition products or free ligands of the precursor molecules. Here, common approaches known from colloid and nanoparticle chemistry in general, like the "polyol process" for coinage and noble metal colloids seem to have a somewhat lower importance due to the reactivity of many MOFs toward acidic conditions (protons) and halides, especially at elevated temperatures. That typical metal-organic precursor molecules often exhibit an intrinsic reactivity toward protic solvent residues, hydroxyl groups or other reactive groups inside the host material, should not also be overlooked. Thus, a careful choice of the MOF and the precursor is mandatory for a controlled nanoparticle synthesis inside a MOF. We will now discuss the loading of MOFs with metal-organic coordination complexes and related precursors for metal nanoparticles.

3.1 Loading with MOCVD Precursors

Loading of metal-organic frameworks with MOCVD precursor molecules can be seen as an extension of the loading with larger nontrivial organic molecules as mentioned above. Some of these coordination compounds are highly volatile already at room temperature; others are sublimable at elevated temperature and pressure. Loading of MOFs with these compounds can therefore be compared to loading with gases or volatile solvents and is usually performed in vacuum. With respect to the subsequent controlled decomposition of the included molecules to nanoparticles, MOCVD precursors are a suitable class of compounds for the loading of MOFs. For a controlled loading, the characterization of the primary inclusion compounds precursor@MOF is required to afford a well-defined metal@MOF composite in a second step. In addition, studying the loading process of the MOF with precursor molecules also offers interesting insights into the host–guest interactions of this composite which may help to elucidate the interactions between imbedded metal nanoparticles and the MOF. This is highly relevant since catalytic processes, for example, often demand well-defined host–guest interactions to enable stabilization of free adsorption sites for molecules in the catalytic reaction.

Depending on the guest molecules, loading of MOFs can be generally performed via the gas phase under vacuum or via solution. In all studies discussed above, loading of MOFs with dye molecules [10,48], C_{60} [10], Keggin anions [22] and Ibuprofen [49,50] was performed via solution impregnation of the MOF powders. The MOF materials were immersed in saturated solutions of the compounds, allowing the guest molecules to diffuse slowly into the MOF cavities. When loading via solution, the competition in diffusion between the guest and the solvent molecules has to be taken into account. A uniform distribution of the guest molecules throughout the framework is not easy to achieve due to the inclusion of solvent molecules at the same time [10]. Kaskel et al. have used the "incipient wetness technique" to load MOF-5 with the Pd precursor [$Pd(acac)_2$] (acac = acetylacetonate) [51]. The advantage of this technique is the rather precise control of the loading just by choosing a certain concentration of the precursor in the solution. With this technique however, the loading with precursors is limited to the solubility of the precursor molecule in the solvent used. Note that, Kaskel et al. introduced only 1 wt% Pd into MOF-5, which is however, fine for many catalytic applications. Due to its facile synthesis even in larger scales, temperature stability up to 400°C in argon, high Langmuir surface area of up to 4,400 $m^2 g^{-1}$ [56] and the relatively large pore opening of 7.8 Å [6], MOF-5 is quite a nice test system for various types of loading studies. However, the reactivity of MOF-5 towards water and humid air [57,58] limits its application in technical processes to some extent. The first studies on the loading of MOFs with MOCVD precursor molecules and the subsequent synthesis of metal nanoparticles in MOF (which we will discuss later), have been performed by infiltration of [$CpPd(\eta^3\text{-}C_3H_5)$], [$CpCu(PMe_3)$] and [$Au(CH_3)(PMe_3)$] in MOF-5 ($Zn_4O(bdc)_3$, bdc = benzene-1,4-dicarboxylate) in vacuum [59].

Thus, freshly prepared [$Zn_4O(bdc)_3$] was activated in vacuum and then exposed to the vapors of the different metal-organic molecules. The loading was followed by ^1H and ^{13}C MAS-NMR, FT-IR, PXRD and elemental analysis. It was shown that similar to the loading with the large organic molecules, the structure of the host framework remains intact after inclusion of the MOCVD precursor compounds. The presence of the unchanged guest molecules inside the MOF cavities was shown by the corresponding solid state ^1H and ^{13}C MAS-NMR signals and elemental analyzes. In a second, more detailed study, the loading of MOF-5 was extended to a variety of metal and metal oxide precursors, here different aspects of the loading were investigated [61]. The metal loading was in a range of 10–40 wt% (see Table 1). The reversible loading of MOF-5 was presented, without changing the chemical properties of the precursors or the host framework.

Ferrocene, as a representative example for many organometallic compounds of interest here, can be first infiltrated into the MOF-5 cavities (see Fig. 3) and can then be removed without any change of the host material. Also, the dependence of the size of the precursor molecules on the loading was shown. MOF-5 cavities exhibit an opening diameter of 7.8 Å. Ideally, only one of the three principal axes (x, y, z; see Table 2) of the enveloping ellipsoid representing the van der Waals volume of the respective precursor molecule should exceed this diameter in order to allow diffusion into the MOF cavities. For that reason, [$Cu(OCHMeCH_2NMe_2)_2$]

Table 1 Loading parameters of various precursors in MOF-5 and MOF-177

MOF-5				
	Elemental analysis (measured/calculated)			
Precursor	M (%)	C (%)	H (%)	Calculated number of molecules
$[CpPd(\eta^3\text{-}C_3H_5)]$	26.4/26.3	41.5/41.5	3.14/3.2	4
$[CpPtMe_3]$	34.5/34.7	34.2/34.2	3.0/3.2	3
$[FeCp_2]$[a]	–	54.22/54.49	3.98/3.99	7
$[CpCu(CN^tBu)]$	6.4/6.5	41.2/41.6	2.6/2.6	1
$[CpCu(PMe_3)]$	10.7/10.8	40.4/40.7	3.4/3.4	3
$[Au(CH_3)(PMe_3)]$	40.8/41.0	23.4/24.9	3.4/3.1	3
$[Sn(C_4H_9)_2(OOC_2H_3)_2]$	8.7/–	38.5/–	2.8/–	0.75
$[Zn(C_2H_5)_2]$	41.8/42.0	31.1/30.9	1.3/1.29	2
$[CpPd(\eta^3\text{-}C_3H_5)]/[CpPtMe_3]$	12.2/–; 16.7	38.1/–	3.75/–	1.70;1.76
MOF-177				
$[CpPd(\eta^3\text{-}C_3H_5)]$	31.9/32.4	47.7/48.9	3.8/4.3	11
$[CpCu(PMe_3)]$	8.3/8.2	49.6/53.9	3.8/3.8	10
$[CpCu(CN^tBu)]$	8.3/8.2	50.9/56.5	3.8/3.7	2
$[FeCp_2]$	19.4/19.1	60.3/61.2	4.5/4.4	2
$[ZnCp^*_2]$	19.1/21.4	63.5/62.2	8.1/3.3	2

[a]Loading parameters for $[FeCp_2]$@MOF-5 were taken from Kim et al. [60]

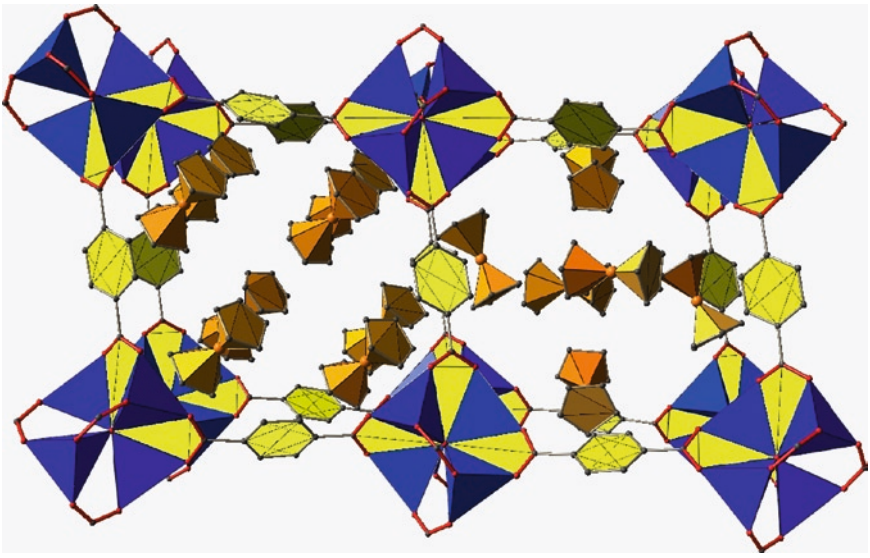

Fig. 3 Cut-out of the crystal structure [60] of the inclusion compound ferrocene$_7$@MOF-5

Table 2 Characteristic molecular dimensions of organometallic precursors absorbed by MOF-5 and MOF-177

Precursor	*x*	*y*	*z*	Max.
[CpPd(η^3-C_3H_5)]	4.5	4.5	4.5	5.5
[CpPtMe_3]	4.3	4.7	4.7	6.5
[$FeCp_2$][a]	3.5	4.5	4.5	5.2
[CpCu(CN^{t}Bu)]	4.5	4.5	7.6	8.2
[CpCu(PMe_3)]	5.0	5.0	7.5	7.5
[Au(CH_3)(PMe_3)]	4.5	4.5	7.0	7.0
[Sn(C_4H_9)$_2$(OOC_2H_3)$_2$]	6.5	7.8	10.0	10.0
[Zn(C_2H_5)$_2$]	1.8	3.0	8.0	8.0
[$Fe(CO)_5$]	4.2	4.2	5.9	5.9
[Cu($OCHMeCH_2NMe_2$)$_2$]	6.5	7.9	8.7	8.7

[a]*x*, *y*, *z* in Å

is not adsorbed by the MOF-5 matrix since its characteristic dimensions exceed the pore opening in all three dimensions (see Table 2). Not surprisingly, the loading is also dependent on the vapor pressure of the precursor molecule. Rapid desorption is observed for small, comparably volatile compounds such as [$Fe(CO)_5$] or [Zn(C_2H_5)$_2$]. Cyclopentadienyl complexes such as [$FeCp_2$] form more stable inclusion compounds with the MOF-5 matrix. More or less stoichiometric inclusion compounds of the formula precursor$_n$@MOF-5 (where n is the average number of precursor molecules per MOF-5 cavity) are obtained in all cases according to elemental analytical data (see Table 1). In addition to this, the loading of MOF-177, another member of the zinc(II) carboxylate based MOFs, with MOCVD precursor molecules has been studied [62,63]. The larger pore opening and pore volume of MOF-177 (10.8 Å and 1.59 $m^2 g^{-1}$ [10]) in comparison to MOF-5 (7.8 Å and 1.04 $m^2 g^{-1}$ [6]), allows the diffusion of larger molecules like [Cu($OCHMeCH_2NMe_2$)$_2$] into the cavities, and the overall absorption of more molecules per cavity than in MOF-5 [63]. Typically the included precursor molecules are very mobile and behave as in solution. This was concluded from the comparison of the solid state NMR of the samples precursor@MOF with the respective high resolution NMR data of the precursors in solution [61]. When the precursors are intercalated in MOF-5, they exhibit the same number of signals with almost the same chemical shift as in solution. This indicates a low interaction with the host framework and the high mobility of the precursor molecules. For example, the solid state ^{13}C MAS-NMR of [Ru(cod)(cot)]@MOF-5 (cod = 1,5-cyclooctadienyl, cot = 1,3,5-cyclooctatrienyl) exhibits six signals for the carbon centers of the intercalated precursor, corresponding to the number of signals of [Ru(cod)(cot)] in C_6D_6 solution [64]. In contrast, the solid state ^{13}C MAS-NMR of the pure, crystalline Ru precursor exhibits 16 signals, i.e., each carbon center of the ligands is different. MAS-NMR and FT-IR spectroscopy and PXRD are very powerful techniques to follow guest inclusion in porous materials. The loading of MOF-5 with [Ru(cod)(cot)] was also followed by means of the change of MOF-5 PXRD reflection intensities below 10° 2θ.

In general, the overall intensity of the host XRD reflections will decrease upon inclusion of guest molecules due to the enhancement of the X-ray scattering contrast [65]. In MOF-5, the intensity ratio of the reflections at especially $2\theta = 6.9°$ and 9.7° will change upon loading [66]. This is also observed when the powder X-ray data of pure, empty MOF-5 and [Ru(cod)(cot)]@MOF-5 are compared (see Fig. 4); the intensities of these peaks are inverted. Most noteworthy, the PXRD of [Ru(cod)(cot)]@MOF-5 displays many additional reflections which originate from the ordering of the guest molecules in the MOF-5 with new reflections observed at $2\theta = 10–20°$, with the most prominent new reflection at 13.8°. However, the exact structure of the material [Ru(cod)(cot)]@MOF-5 could not be fully elucidated with Rietveld analysis. Usually the embedded precursor molecules are randomly distributed which is deduced from the almost unchanged PXRD of the host matrix, i.e., lacking new extra diffraction peaks and only showing some more or less pronounced intensity deviations. However, investigating the ordering of organometallic molecules in the MOF cavities is clearly an interesting aspect of loading of MOFs in general. Only in a few cases can a crystal structure of the host–guest composite be obtained. The first example of such a substructure was investigated by Kim et al. [60]. Similar to the first reports by us, MOF-5 was loaded with ferrocene via gas phase in vacuum. Interestingly, the authors attempted loading of MOF-5 in dimethylformamide (DMF) solution as well. However in this case, inclusion of the guest molecules was not successful as shown by UV/VIS spectroscopy (see our above comments regarding solution impregnation). By applying synchrotron radiation at 100 K, a single crystal structure of the compound $[FeCp_2]_7$@MOF-5 was obtained. Shrinkage of the unit cell volume of 3.7% is observed compared to the evacuated host.

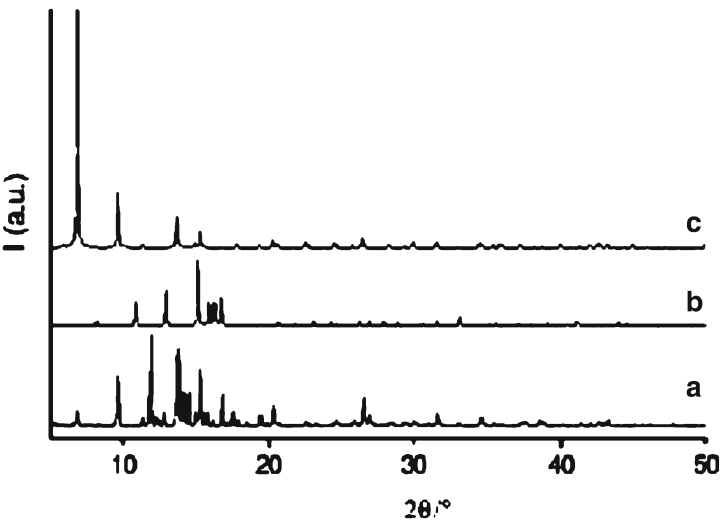

Fig. 4 Powder X-ray diffractogramms of (**a**) [Ru(cod)(cot)]@MOF-5, (**b**) [Ru(cod)(cot)] and (**c**) MOF-5. Reproduced with permission from [64]. Copyright 2008 American Chemical Society

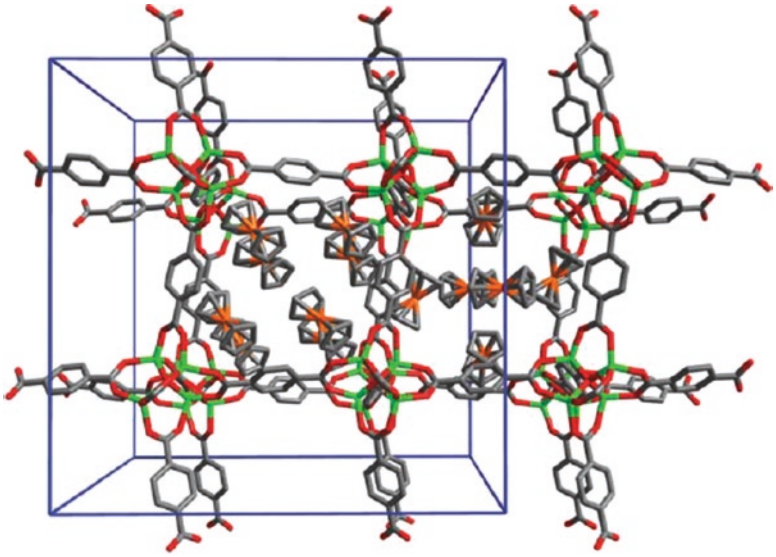

Fig. 5 Single crystal structure of $[FeCp_2]_7$@MOF-5 [60]. Reproduced by permission of the Royal Society of Chemistry

The unit cell is defined by the space group *Pa-3*. The smaller pores of MOF-5 are filled with six ferrocene molecules; the larger pores with eight (see Fig. 5) [60]. Depending on the tilting of the *bdc* linkers, MOF-5 exhibits two kinds of pore diameters with 11.0 and 15.1 Å [6]. From elemental analysis the results of the crystal structure were confirmed, giving seven ferrocene molecules per formula unit of MOF-5, which corresponds to 56 ferrocene molecules per elementary cell of the MOF-5 structure. The six ferrocene molecules in the smaller pore adopt an octahedral arrangement with the ferrocene molecules close to the faces of the cube shaped cavity. The eight molecules in the larger pore are positioned near the corners of the MOF-5 pores (see Fig. 6). Here extensive π–π interactions exist between the guest molecules as well as between the guests and the framework itself. The packing of the ferrocene molecules in the pores leaves only 1.6% of the crystal volume accessible to other guest molecules.

In another study, Kim et al. have shown the loading of porous $[Tb_{16}(TATB)_{16}(DMA)_{24}](DMA)_{91}(H_2O)_{108}$ (TATB = triazine-1,3,5-tribenzoate, DMA = *N,N*-dimethylacetamide) with ferrocene [67]. In this case, a crystal structure of the composite was not obtained. Loading was followed by emission spectroscopy and ^{1}H-NMR spectroscopy with elemental analytical data suggesting 65 ferrocene molecules per formula unit. It is important to mention that it is not at all straightforward to obtain the superstructure of the guest molecules inside MOFs. As discussed above, at least in MOF-5, which exhibits no additional functional groups at the *bdc* linkers, the interaction between intercalated guests and the host is comparatively low with the intercalated guest molecule behaving almost as in a solid solvent cage. Therefore, X-ray diffraction

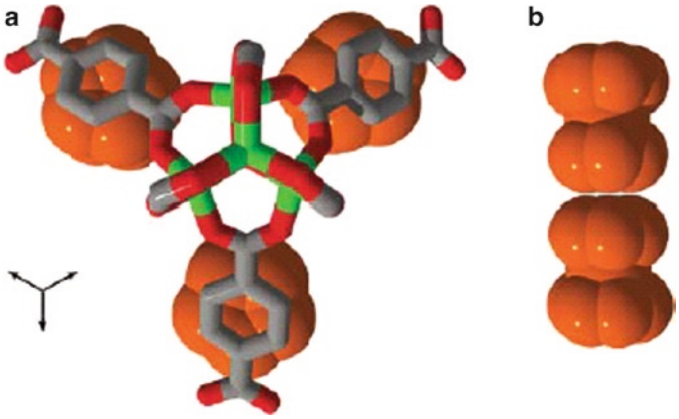

Fig. 6 The orientation of the ferrocene molecules in the larger pore of MOF-5 [60]. Reproduced by permission of the Royal Society of Chemistry

measurements should be performed at low temperatures, thus reducing mobility in order to obtain a high quality data set. In addition, the reflections of the guest structure are often rather weak, which demands the use of high intensity X-rays, e. g. synchrotron radiation for collecting diffraction data. However, the crystal structure of ferrocene@MOF-5 nicely shows the influence of the space limitation of the MOF cavities on the ferrocene arrangement and conversely, the subtle effects of the loading on the MOF-5 framework itself. This leads to another aspect of loading MOFs. The space confinement of the MOF cavities may also support and stabilize reactive species as intermediates of organometallic or organic reactions.

3.2 Reactions Inside MOFs

The interior of porous hosts may be very different from that of the exterior surroundings, leading to a novel kind of reactive species in these pores. For example, reactive intermediates from metal-organic or organic reactions could possibly be stabilized in the cavities of the host material.

At this point, it is noteworthy, that detailed studies on the stabilization of reactive species inside metal-organic polyhedrons have already been performed. Here, the group of Raymond et al. has given interesting insights into the rich host–guest chemistry of the assemblies of the type M_4L_6 (see Fig. 7) [68,69]. For instance, it was shown that the ionic $[(Cp)Ru(cod)]^+$ and $[(Cp^*)Ru(\textit{cis}\text{-}1,3,7\text{-octatriene})]^+$ species, which usually rapidly decompose in water, are stabilized inside the cluster $[Ga_4L_6]^{12-}$ in aqueous solution [70]. Despite their stabilization within the host, the guest molecules are still able to react stoichiometrically with CO. In addition, the ability of the tetrahedral assemblies to act as nanoenzymes, catalyzing the hydrolysis of acetals and ketals in basic solution has been presented [71]. In a similar metal-organic

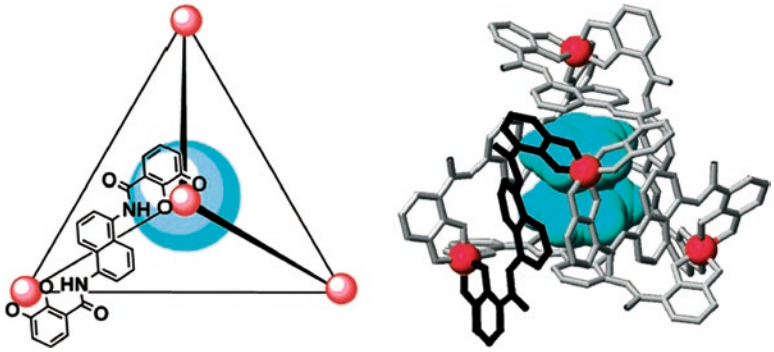

Fig. 7 Schematic presentation of the supramolecular tetrahedral assembly Ga_4L_6 a guest molecule included in the nanocage [57,58]. Copyright Wiley-VCH Verlag GmbH & Co. KGaA. Reproduced with permission

polyhedron even the observation of a reactive intermediate of the photodissociation of [Cp´Mn(CO)$_3$] by crystal structure was shown by Fujita et al. [72] with the in situ generated pyramidal [Cp´Mn(CO)$_2$] observed directly by X-ray diffraction.

These results suggest that MOFs as "extended" metal-organic assemblies could show a similar host–guest chemistry. In uncharged MOFs however, space confinement should be the most effective stabilizing effect on these species.

So far only few reports on reactions inside MOF and the trapping of reactive intermediates have been published. The first example was reported by Long et al. who showed functionalization of MOF-5 *bdc* linkers with {Cr(CO)$_3$} fragments and subsequent photoreactions [73]. The fragments were introduced by heating the MOF-5 powder in a solution of Cr(CO)$_6$ in THF/Bu$_2$O. Photoreactions of the {Cr(CO)$_3$} fragment with N_2 and H_2 lead to stable (η^6-arene)Cr(CO)$_2$(N_2) and (η^6-arene)Cr(CO)$_2$(H_2) species which are usually only accessible in frozen gas matrices or supercritical fluids (Fig. 8). Thus, the MOF framework shows a remarkably stabilizing effect on the reactive fragments. Another example of reactions inside a MOF was presented by us. The hydrogenolysis of [Ru(cod)(cot)] inside MOF-5 at atmospheric H_2 pressure led to the formation of (η^6-arene)Ru(cod) species with the *bdc* linkers of MOF-5 as a side- product of Ru nanoparticle formation in the framework [64]. This is in full agreement with known arene/cot exchange reactions of [Ru(cod)(cot)] taking place when the precursor is treated with 1 bar H_2 in the presence of arenes in solution. In contrast to the work of Long et al., not all *bdc* linkers were coordinated by {Ru(cod)}, and ^{13}C MAS-NMR showed signals of "free" *bdc* linkers. Here, obviously diffusion limitation inside the framework causes incomplete splitting of the alkene ligands of the Ru precursor by hydrogenolysis, and this enables coordination of {Ru(cod)} fragments to a fraction of the aromatic moiety of the *bdc* linkers. So far, there are no reports in the literature on molecular complexes of the {Ru(cod)} fragment and terephthalic acid or its derivatives. Evidently, the caging effect of MOF-5 has an influence on the kinetics of the hydrogenolysis of [Ru(cod)(cot)] leading to partial functionalization of *bdc* linkers with {Ru(cod)} fragments.

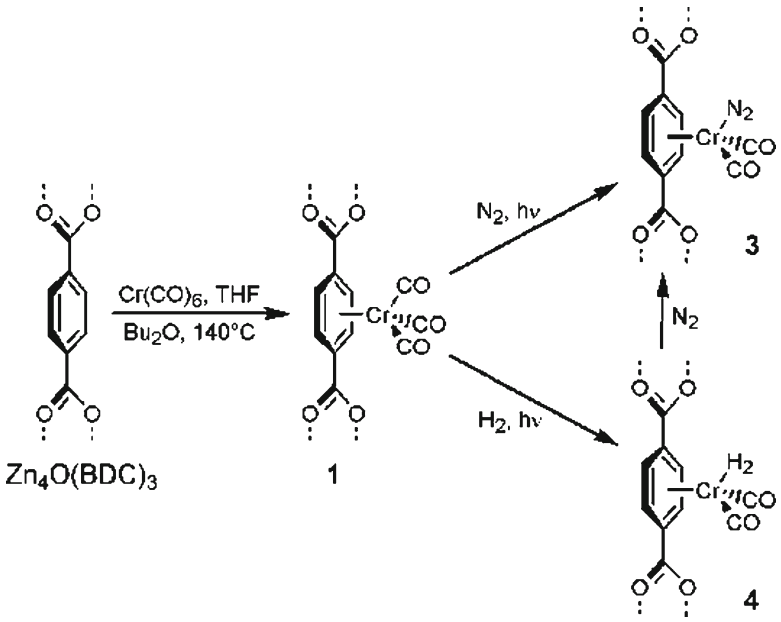

Fig. 8 Reaction of $[Zn_4O(bdc)_3]$ with $Cr(CO)_6$. Reproduced with permission from [73]. Copyright 2008 American Chemical Society

From these first examples it can be concluded that MOFs, especially MOF-5, show potential as stabilizing matrices for reactive intermediates in metal-organic reactions. In the future this will definitely be studied in more detail.

4 Nanoparticles Inside Metal-Organic Frameworks

The synthesis of nanoparticles inside MOFs is another, still more special example of reactions inside the framework. Nanoparticles "trapped" inside MOF cavities, with a high number of reactive surface atoms, are indeed reactive species as well. Their synthesis inside the porous hosts, starting from molecular precursors, anticipates the caging effect of the framework. To prevent the clusters from growing to larger, bulk agglomerates, the space confinement of the framework pores is utilized naturally.

4.1 General Synthesis

In the few reports of the synthesis of nanoparticles inside MOFs, the formation of nanoparticles is obtained in two steps: loading of the porous host with precursor molecules followed by decomposition of the precursors inside the porous host.

Depending on the properties of the intercalated precursor, the decomposition conditions have to be chosen carefully. In general, decomposition of MOCVD precursors can be achieved by treatment with reactive gases such as H_2 at a suitable temperature, by treatment at an elevated temperature or by photolysis. The formation of nanoparticles from metal salts, i.e., loading the MOFs with metal cations or inorganic metal complexes, e.g., $[PdCl_4]^{2-}$ as precursors, will be addressed as a special case later. It is mandatory to choose precursors with decomposition conditions that will be tolerated by the host framework. Therefore, the thermal stability of the framework should match the corresponding decomposition temperature of the precursor in order to obtain nanoparticles in an unchanged host matrix. Also, the stability of the MOF towards possible additional reactive gases or UV radiation has to be confirmed. For different precursors, different decomposition protocols have to be applied. The obtained nanoparticle@MOF composites can subsequently be investigated by analytical techniques such as PXRD, X-ray absorption spectroscopy (XAS), N_2 sorption measurements and transmission electron microscopy (TEM). As for related research on nanoparticles hosted by zeolites or mesoporous silica, the challenge is to determine whether the nanoparticles are located inside or outside the framework and to investigate and control the distribution of the particles inside the matrix. Beside TEM, routine analytical methods only give indirect proof for the existence of embedded particles. The few reports on the synthesis of either metallic or oxidic nanoparticles in MOFs have mostly been performed with MOF-5; however some other MOFs have been studied as well. We shall therefore, now discuss the synthesis of nanoparticles in MOF-5 followed by their synthesis in other MOFs.

4.2 Metal Nanoparticles Inside MOF-5

In the first report on the synthesis of metal nanoparticles inside MOF-5, the formation of Pd, Cu and Au nanoparticles inside this framework was presented [59]. After loading with the corresponding precursors $[CpPd(\eta^3\text{-}C_3H_5)]$, $[CpCu(PMe_3)]$ or $[Au(CH_3)(PMe_3)]$, (see above) decomposition of the precursor to nanoparticles was achieved by either photolysis (UV radiation) or hydrogenolysis. Both, UV radiation and H_2 treatment, even at elevated temperatures, left MOF-5 unchanged, with controlled decomposition of precursor molecules *only*.

4.2.1 Pd@MOF-5

Palladium nanoparticles with a dimension of 1.4 nm were obtained by photolysis of $[CpPd(\eta^3\text{-}C_3H_5)]$ in MOF-5 at room temperature or below (with cooling) in the absence of additional hydrogen, leaving a perfectly intact MOF-5 matrix as confirmed by powder X-ray analysis and N_2 sorption measurements (see Fig. 9) [59]. The powder XRD of the corresponding sample shows an additional broad

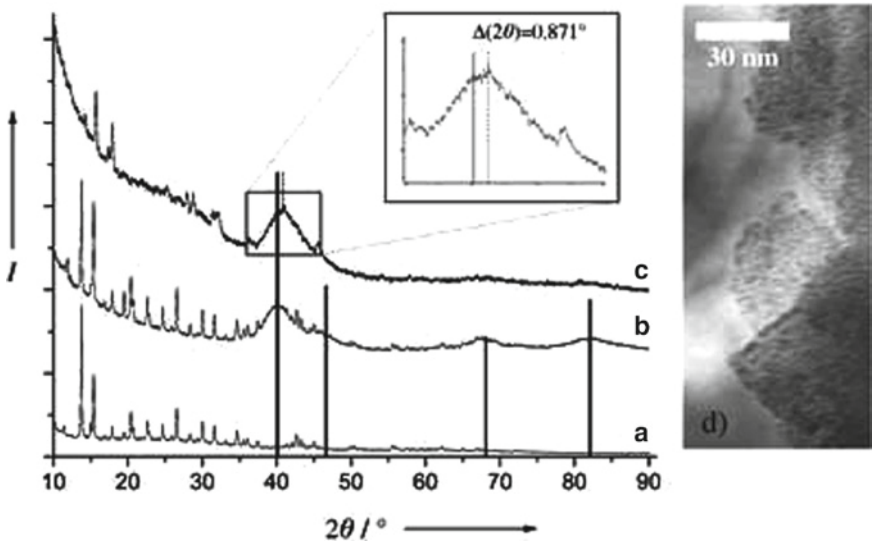

Fig. 9 Powder X-ray diffraction patterns of (**a**) MOF-5, (**b**) photolytically generated Pd@MOF-5, (**c**) Pd@MOF-5 generated by hydrogenolysis and (**d**) TEM picture of photolytically generated Pd@MOF-5 [59]. Copyright Wiley-VCH Verlag GmbH & Co. KGaA. Reproduced with permission

reflection (FWHM = 5.4°) at 2θ = 40.99° typical for nanocrystalline Pd particles. The size of the nanoparticles derived from TEM and PXRD data (Scherrer equation) is in good agreement with the diameter of the MOF-5 cavities (see above) hinting at nanoparticles embedded in the porous host. Treatment of the same precursor@MOF-5 composite with H_2 gas at −35°C led to Pd nanoparticles in the same size regime, here, however, the MOF-5 matrix appears to have lost its 2D long range order (see Fig. 9) Elemental analysis in both cases gave a metal loading of 35.6 wt% Pd.

In order to gain a more thorough insight into the particle distribution throughout the framework, a more detailed analysis of the photolytically synthesized Pd@MOF-5 was performed [74]. These results are illustrated in Figs. 10 and 11. Figure 10a shows a bright field TEM picture of a MOF-5 nanocrystallite with embedded Pd nanoparticles. The enlargement (Fig. 10b) clearly shows the Pd nanoparticles in a size range of 1–3 nm as darker spots, with the larger nanoparticles most probably located either close to the surface of the nanocrystallite or in a locally distorted environment in the inner core of the crystallite. From nanoparticle formation inside zeolitic materials it is known, that particles with a bigger size than the pore diameter can be formed inside the bulk of the matrix [75]. Note that, from the full width at half maximum (FWHM) of the Pd reflection in the PXRD of Pd@MOF-5 (Fig. 9) the particle size was calculated to be well below 3 nm. Evidently, the growth of the particles might cause a local distortion of the framework, allowing larger particles to grow. The selected area electron diffraction

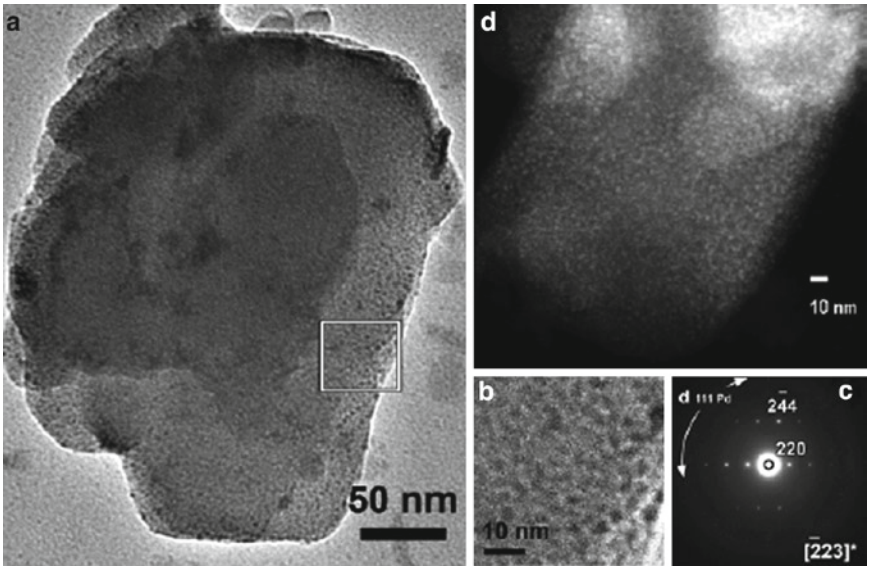

Fig. 10 Pd@MOF-5; (**a**) Bright field TEM image showing the Pd loaded framework. The crystal is faceted, indicating that the framework is still intact after loading; (**b**) Enlarged image of the region indicated (**a**) the particles have sizes ranging from 1 to 3 nm; (**c**) Diffraction pattern taken from a cubic Pd@MOF-5 crystal in [−223]* zone axis. A *weak ring* corresponding to the 111 planes of cubic Pd is also visible; (**d**) HAADF image of the Pd@MOF-5 material showing the Pd particles as *white spots*. Reproduced with permission from [74]. Copyright 2008 American Chemical Society

(SAED) pattern of the corresponding sample is given in Fig. 10c and confirms the intact structure of MOF-5 (sharp reflections) indicating that the crystallite is shown along the [−223] zone axis. In addition to the relatively sharp reflections of the host structure, a faint ring at 2.25 Å is also visible in the SAED pattern which is typical for the cubic spacing of Pd(111). This shows that the embedded particles exhibit the cubic Pd structure which is in agreement with the results from the PXRD analysis of the composite (Fig. 9). Figure 10d presents the result of a high-angle annular dark field scanning transmission electron microscopy (HAADF-STEM) measurement of the same material. The contrast in this type of image depends on both the thickness and the atomic number Z of the sample. Here, the heavier Pd nanoparticles appear as white dots within the MOF-5 framework. From this picture a close packing of the particles can be deduced. The 3D distribution of the Pd nanoparticles inside MOF-5 was examined by tomographical TEM measurements (Fig. 11), for which a 3D reconstruction of several TEM images of Pd@MOF-5 was performed. The TEM image of Pd@MOF-5 in Fig. 11a exhibits Pd nanoparticles in a range of 1–5 nm, however the larger particles here seem to be agglomerates of several smaller particles.

In tomographical TEM measurements, the resolution is usually rather low in order to avoid beam damage of the sample, and, therefore, smaller particles within the

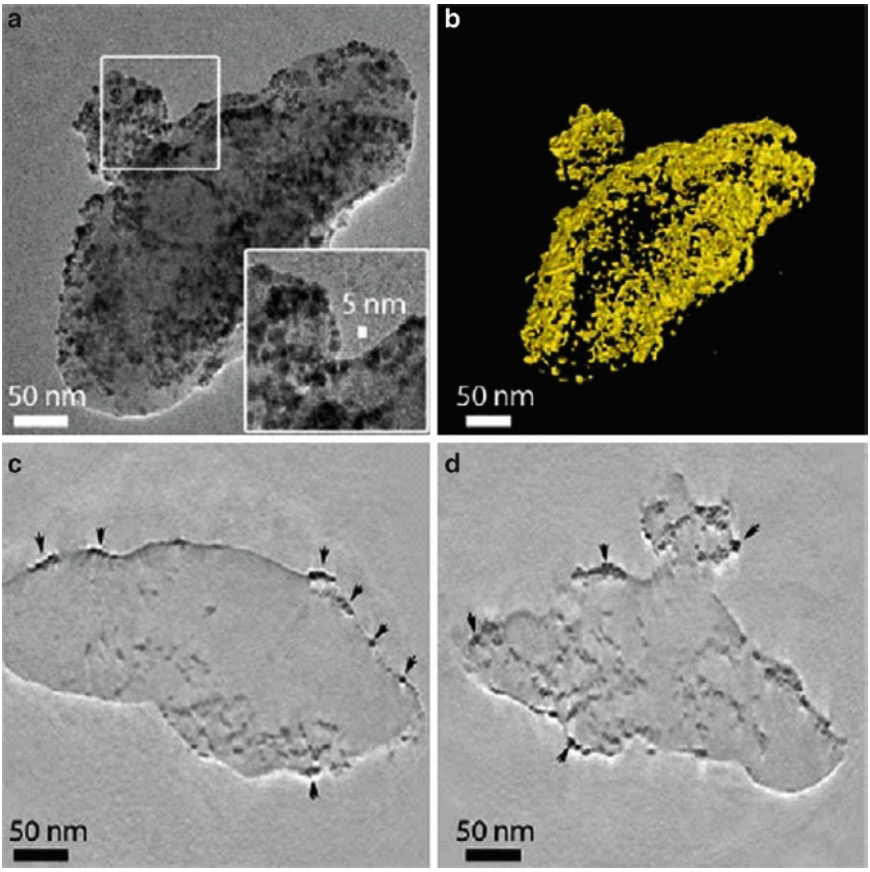

Fig. 11 (**a**) Bright field TEM image of a Pd@MOF-5. Inset; particles from 1 to 5 nm in diameter are present, some particles appear to have agglomerated; (**b**) Tomographically reconstructed Pd particles (matrix not imaged); (**c**) and (**d**) Slices through the tomographically reconstructed volume: the metallic particles are mostly imbedded inside the MOF-5 matrix. Reproduced with permission from [74]. Copyright 2008 American Chemical Society

areas of agglomerates cannot be resolved. The 3D tomographical reconstruction, however, clearly shows the rather uniform particle distribution throughout the framework (Fig. 11b). Inside the imaged MOF-5 matrix (specimen), the particles are in a size range of 1–3 nm (see above). At the surface of the specimen larger agglomerates are observed. Thus, the tomographical measurements provide a direct measure of the particle distribution throughout the framework. In the photolytically synthesized Pd@MOF-5, the particle distribution appears to be rather uniform, although some larger particle agglomerates at the surface of the MOF-5 crystallites can be detected. Another route to introducing Pd nanoparticles into MOF-5 was presented by Kaskel et al. [39–44]. Here, MOF-5 powder was loaded

with a solution of [$Pd(acac)_2$] in $CHCl_3$ following standard recipes of the "incipient wetness technique." For this technique the volume of the solvent applied in the loading procedure is estimated from the free volume of the porous material used. The corresponding precursor molecules are then dissolved in this restricted amount of solvent and infiltrated into the porous material. Decomposition of the precursor was achieved by thermal treatment at 150–200°C or hydrogenolysis at 150–200°C. The metal loading was determined to be 1 wt% by elemental analysis and no additional reflections for Pd were observed in the PXRD of the composite. Due to the low metal loading, detection of the embedded Pd species and its chemical nature, whether fully reduced to Pd^0 nanoparticles or still some remaining Pd^{2+} species, was difficult. These aspects were not reported and discussed in detail by the authors. The BET surface area of the composite material was however reduced in comparison to the starting material, from 2,885 to 958 $g\,m^{-2}$ which is most probably due to the embedding of Pd nanoparticles. In another approach, Kaskel et al. also applied coprecipitation for the preparation of Pd in MOF-5 [76]. In this case, $Pd(NO_3)_2$ was directly added during the synthesis of the MOF, leading to Pd contents of 0.43–0.64 wt%. Again, no Pd reflections were observed in the corresponding PXRD data, although a slightly reduced surface area was observed. The detection of the location and the nature of imbedded metal species in MOF-5 remains a particular challenge, especially when the corresponding metal content is rather low. Here the detection limit of most analytic techniques obviously anticipates a detailed examination. However, our study on Pd@MOF-5 at a high metal loading of 35.6 wt% shows the general ability of MOF-5 to host metal nanoparticles.

4.2.2 Ru@MOF-5

In order to study the stabilizing property of MOF-5 in comparison to the surfactant approach in non aqueous colloid chemistry of metal particles, the system Ru@MOF-5 was selected as a target [64]. The synthesis and characterization of Ru colloids starting from [Ru(cod)(cot)] in solution is well reported in the literature [77–79].

Therefore, this species is a well suited model system for investigation inside MOFs. With a preparation method similar to the one described above, Ru nanoparticles in MOF-5 were obtained. Thus, [Ru(cod)(cot)] can be introduced into the porous [$Zn_4O(bdc)_3$] and hydrogenolysis at lower temperatures and H_2 pressure lead to coordination of {Ru(cod)} species to part of the *bdc* linkers as a side reaction to Ru nanoparticle formation. "Pure" Ru@MOF-5 was obtained by hydrogenolysis at 150°C, 3 bar H_2, 48 h, with an Ru content of 31.5 wt%. As in the case of higher Pd loadings in MOF-5, an additional reflection for Ru is observed in the PXRD of the composite. Here also the low angle region of the PXRD was investigated. The change of the reflection intensities was not as pronounced as in the case of the intact precursor due to only a fraction of all MOF cavities occupied by Ru particles [64]. Given an Ru content of 31.5 wt% and based on the fact

that Ru nanoparticles in the size regime of the MOF-5 cavities are likely to consist of~140–150 atoms, only 2% of all MOF-5 cavities would be filled with Ru particles. The corresponding TEM micrographs reveal small Ru nanoparticles of 1.5–1.7 nm, matching the typical MOF-5 pore diameter, distributed over the porous matrix without any bigger agglomerates at the surface (Fig. 12). The SAED pattern of hexagonal Ru could be detected, and the distribution of the Ru nanoparticles was examined with tomographical TEM measurements which are illustrated in Fig. 13 [74]. Figure 13a shows a more or less uniform particle distribution of the Ru nanoparticles throughout the MOF-5 nanocrystallite. In contrast to this, the tomographical

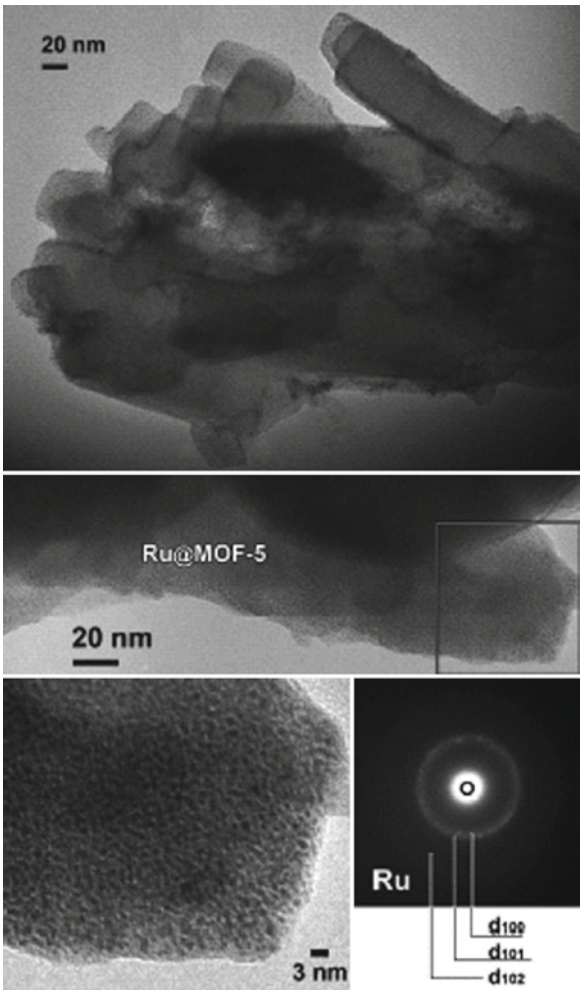

Fig. 12 TEM pictures of Ru@MOF-5 with a corresponding SAED pattern for the embedded Ru nanoparticles. Reproduced with permission from [64]. Copyright 2008 American Chemical Society

3D reconstruction (Fig. 13b) shows that most of the particles are in fact located at the outer domains of the investigated MOF-5 specimens with a maximum penetration of 20 nm, and only some particles are located in the core of the MOF-5 crystallites. This is in contrast to the results from the tomographical TEM measurements of Pd@MOF-5 (Fig. 11), where a more or less uniform particle distribution was observed. Obviously, the preparation technique has a great impact on the particles distribution. The photolytically synthesized Pd@MOF-5 shows a more uniform particle distribution than the material Ru@MOF-5, which was obtained by thermally activated hydrogenolysis over a long period of time. In the case of Ru@MOF-5,

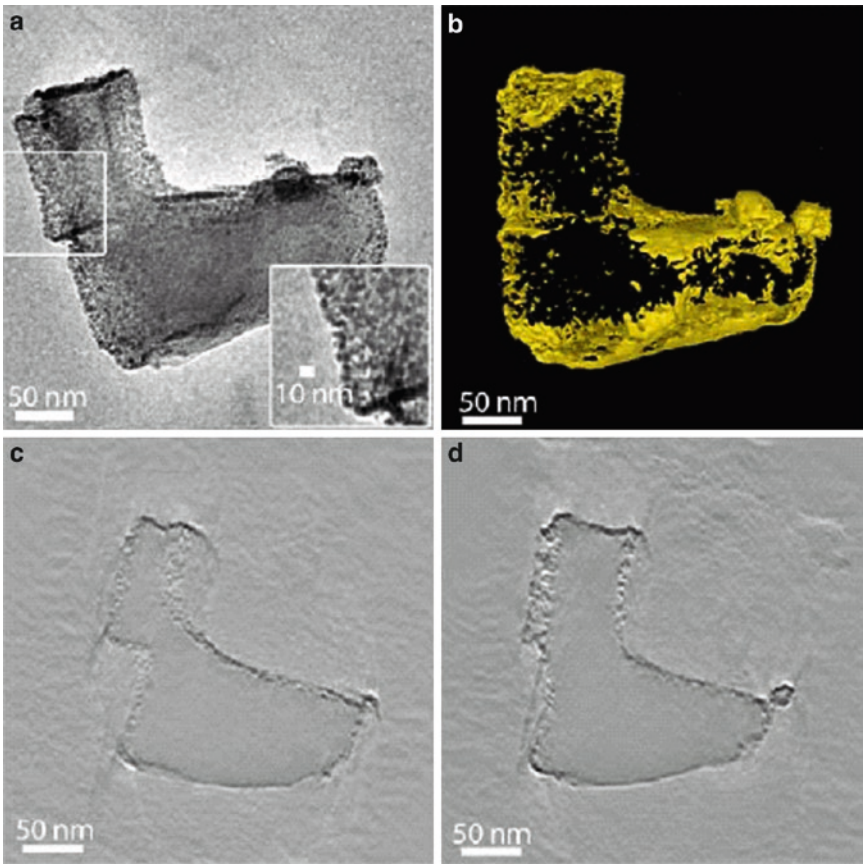

Fig. 13 (**a**) Bright field TEM image of a Ru loaded MOF. Inset; particles from 1 to 5 nm in diameter are present, the matrix appears to be densely packed; (**b**) Tomographically reconstructed Ru particles (matrix not imaged) Some overlapping of the particles is present due to diffraction contrast; (**c**) and (**d**) Slices through the tomographically reconstructed volume: the metallic particles are not completely imbedded in the inner core of the MOF-5 matrix. Most particles are positioned at the surface of the matrix, or close to the surface (up to approximately 20 nm deep). Reproduced with permission from [74]. Copyright 2008 American Chemical Society

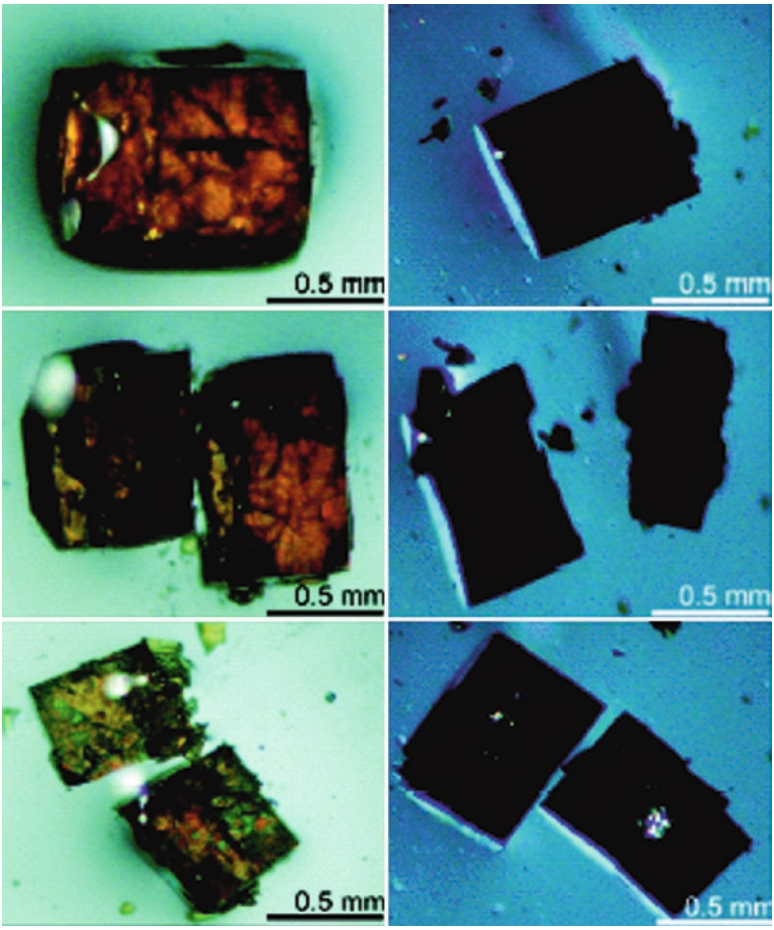

Fig. 14 Images of millimeter-sized MOF-5 crystals after loading with [Ru(cod)(cot)] before (*left*) and after (*right*) treatment with H_2. The presented crystals on the *left* and the *right* side stem from the same loading experiment. One of them (*right*) was then treated with H_2. In order to show the macroscopically uniform distribution of the precursor and the Ru nanoparticles after hydrogenolysis, the crystals were cut (*middle*) and turned to examine the cross section (*bottom*). Reproduced with permission from [64]. Copyright 2008 American Chemical Society

presumably an autocatalytical process starting at the surface of the MOF-5 crystallites leads to a segregation of the particles to the interfaces of the MOF-5 microcrystals in a powder sample. Loading a MOF-5 single crystal however, the distribution of [Ru(cod)(cot] precursor molecules is rather uniform as can be observed by the light microscopic image in Fig. 14. Also the Ru nanoparticle distribution on the macroscopic scale appears to be uniform, when such a single crystal is exposed to the hydrogenolysis. However, the detailed investigation by TEM on the nanoscale

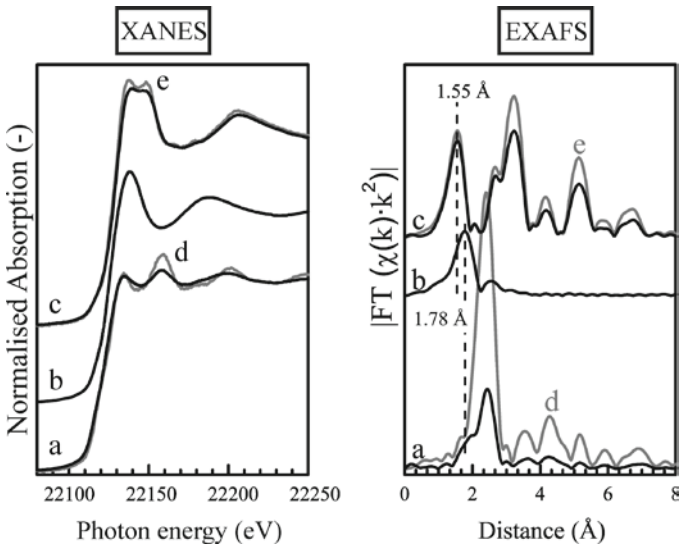

Fig. 15 XANES (*left*) and EXAFS (*right*) of (**a**) Ru@MOF-5, (**b**) [Ru(cod)(cot)@MOF-5, (**c**) Ru–ox@MOF-5, (**d**) Ru foil and (**e**) RuO_2. All data were recorded at liquid nitrogen temperature. Reproduced with permission [64]. Copyright 2008 American Chemical Society

reveals quite the opposite, with Ru nanoparticles mostly located close to the outer surface of the imaged specimen.

XAS measurements were performed on the Ru@MOF-5 powder material to give additional insights into host–particle interactions. The X-ray absorption near edge structure (XANES) of Ru@MOF-5 is indicative of metallic ruthenium. The curves of Ru@MOF-5 and the reference Ru foil overlap to a large degree and the edge shift excludes oxidation of the Ru nanoparticles (Fig. 15a). The EXAFS of Ru@MOF-5 is typical for small Ru nanoparticles with a small amplitude in the FT curve for the first Ru shell when compared to the Ru foil (Fig. 15b). Interestingly, a small shoulder is visible in the EXAFS of Ru@MOF-5 at 1.78 Å which can be assigned to a Ru–C interaction most probably from interaction of the Ru nanoparticles and the *bdc* linkers. This is indirect proof for the Ru nanoparticles being indeed located *inside* the MOF-5 matrix. This example nicely shows the combination of different methods in order to investigate the location of nanoparticles inside MOFs. The framework–particle interaction was studied also by static ^2H solid state NMR of surface-bound hydrides on Ru nanoparticles inside MOF-5. A remarkably high mobility was found, even exceeding the one of surface hydrides on Ru colloids. This suggests a rather weak framework–particle interaction superior to that of other common porous solids which also explains the particle distribution within the framework observed by tomographical TEM measurements. Presumably, the surface of nanoparticles embedded in MOF-5 is readily accessible to reagents, e.g., in catalytic applications.

4.2.3 Cu@MOF-5 and Au@MOF-5

In addition to the already discussed metal@MOF-5 composites Pd@MOF-5 and Ru@MOF-5, the synthesis of copper and gold nanoparticles in MOF-5 has also been investigated. As for the synthesis protocols discussed above, these materials were obtained by hydrogenolysis of [$CpCuPMe_3$)] [51,72] or [$CpCu(CN^tBu)$] [80] and [$Au(CH_3)(PMe_3)$] [59] as precursors in MOF-5 at elevated temperatures. Figure 16 shows the PXRD patterns of the parent MOF-5 as well as the ones of the Cu precursors in MOF and Cu@MOF-5 synthesized from these composites. The characteristic reflections of the MOF-5 host are retained in all cases. The structural quality of the Cu@MOF-5 composite derived from [$CpCu(CN^tBu)$]@MOF-5 appears to be better than the one of the material derived from [$CpCu(PMe_3)$]@MOF-5. This effect may be due to the interaction of the PMe_3 ligand with the MOF-5 matrix [80]. From PXRD and TEM measurements, the size of the Cu nanoparticles was determined to be in a range of 1–3 nm (see discussion above) with a metal loading of 10–11 wt%. In this case tomographical TEM measurements to determine the particle distribution inside the MOF-5 host were not performed.

In contrast, TEM and PXRD data of Au@MOF-5 show polydispersed Au particles in a size range of 5–20 nm (see Fig. 17), with a metal loading in Au@MOF-5 determined to be 48 wt%. The gold particles appear to interact more weakly with the host matrix than the Pd, Ru and Cu particles and thus larger agglomerates are formed possibly by diffusion of the particles to the outer surface.

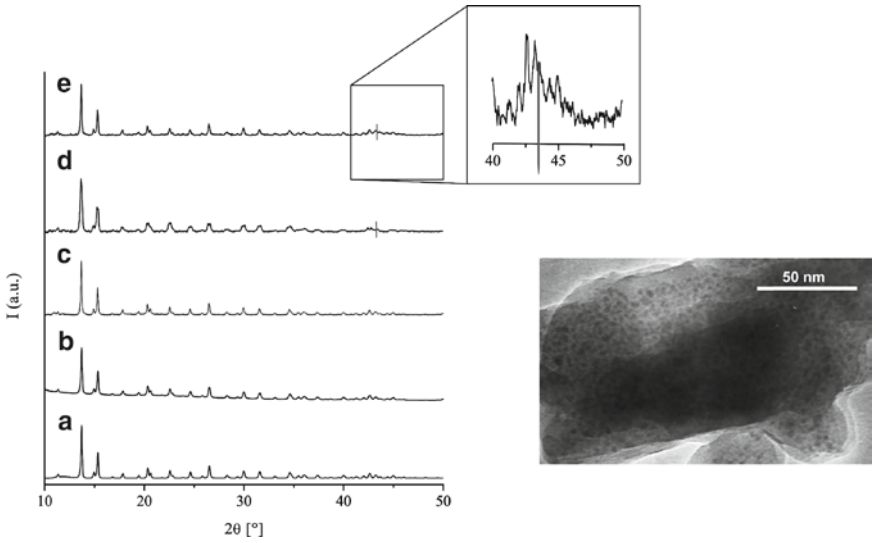

Fig. 16 Powder X-ray diffraction patterns of (**a**) pure, activated MOF-5, (**b**) [$CpCu(PMe_3)$]@MOF-5, (**c**) [$CpCu(CN^tBu)$]@MOF-5, (**d**) Cu@MOF-5 (derived from [$CpCu(PMe_3)$]@MOF-5) (**e**) Cu@MOF-5 (derived from [$CpCu(CN^tBu)$]@MOF-5). TEM image of Cu@MOF-5 (derived from [$CpCu(PMe_3)$]@MOF-5). Reproduced with permission [80]. Copyright 2008 American Chemical Society

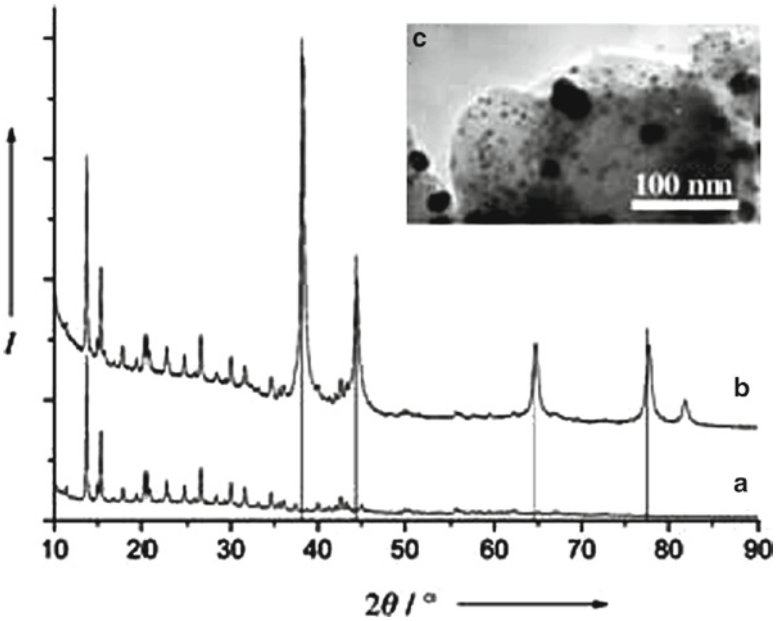

Fig. 17 Powder X-ray diffraction patterns of (**a**) MOF-5, (**b**) Au@MOF-5 and (**c**) TEM picture of Au@MOF-5 [59]. Copyright Wiley-VCH Verlag GmbH & Co. KGaA. Reproduced with permission

Similar observations have been made for the loading of mesoporous silica in which Au and Ag nanoparticles grow larger than the pore diameter of the host, presumably due to a destructive growth mechanism of the embedded particles [81–83]. We have already discussed the rather weak interaction between the particles and the host framework for Ru@MOF-5. From the TEM pictures of the Pd, Ru and Cu nanoparticles in MOF-5 it can be deduced that they are mostly located inside the framework even though few nanoparticles exhibit a size larger than the MOF-5 pore diameter. In this case a local distortion of the porous host allows particles to grow slightly larger than the actual pore size. In order to create a stronger interaction between the host and the embedded particles, several approaches appear possible. The functionalization of the MOF-5 linkers with –OH, –OR, –SH or $–NH_2$ groups is one possible strategy to bind the embedded particles to the framework. Another approach is the embedding of metal oxide species in the MOF matrix prior to the embedding of the nanoparticles to increase the interaction between the host and the metal nanoparticles. In combination with metal nanoparticles, metal oxide species in MOFs are known to have a promoting effect on catalytical properties of the embedded metal nanoparticles as seen in Cu/ZnO composites in methanol catalysis [84–87]. In addition, nanosized metal oxide species such as ZnO or TiO_2 embedded in MOF could enhance the semiconducting properties of MOF-5 [20,21].

4.3 Metaloxide@MOF and Metal/Metaloxide@MOF

In this section we will refer to the formation of metal oxide and metal/metal oxide species in MOF-5 similar to the formation of metal nanoparticles@MOF-5. After infiltration of precursor molecules, oxidation of the precursor molecules to oxide species by O_2 gas is performed. However classical sol–gel chemistry might be another synthetic strategy to yield oxide species inside MOFs and will surely be investigated in the future. Due to the sensitivity of MOF-5 towards moisture however, a sol–gel approach is not feasible. The sol–gel chemistry inside MOFs requires water stable structures. We have reported the synthesis of Cu/ZnO species in MOF-5, the preparation of nanometer sized ZnO species in MOF-5 and the subsequent introduction of Cu nanoparticles [80]. $ZnEt_2$ was used as a ZnO precursor and was adsorbed inside MOF-5 and then converted to ZnO species by either exposure to O_2 gas (dry method) or by very careful hydrolysis (wet method), followed by annealing at 250°C. ^{17}O labeling studies using $H_2{}^{17}O$ revealed that neither the *bdc* linkers nor the central oxide ion of the Zn_4O unit exchange oxygen atoms/ions with the imbedded ZnO species [80]. Depending on the preparation conditions, Zn contents from 10 to 35 wt% were introduced in MOF-5. Results from PXRD, TEM, UV–VIS and ^{17}O MAS-NMR spectroscopy gave evidence for a largely intact MOF-5 matrix with imbedded ZnO nanoparticles <4 nm (see Fig. 18).

Langmuir surface areas of the composite gave values of 900 $m^2 g^{-1}$ (wet method) and 1,750 $m^2 g^{-1}$ (dry method) which shows the advantage of the dry method, leaving a remarkably high surface area at a Zn loading of 35.5 wt%. The corresponding TEM micrographs reveal the typical faceted MOF-5 nanocrystallites. However, due to the low contrast of the ZnO in the Zn-based MOF matrix, the single particles could not be detected. In addition to the synthesis of ZnO@MOF-5, TiO_2@MOF-5 was obtained by the oxidation of $Ti(OiPr)_4$ inside the MOF cavities [88]. The resulting metal oxide aggregates are presumably quite small and neither showed reflections in the PXRD nor in the SAED. Attempts to synthesize CuO or Cu_2O species in MOF-5 by oxidizing the composite Cu@MOF-5 with O_2 led to a complete collapse of the framework as indicated by PXRD [80]. Yet, soft oxidation of the embedded Cu nanoparticles with N_2O yields core-shell Cu_2O/Cu nanoparticles inside the framework with the host matrix remaining completely unchanged. The oxidation is completely reversible and upon treatment with H_2 gas Cu_2O/Cu@MOF-5 is fully re-reduced to Cu@MOF-5 [80]. Cu/ZnO@MOF-5 was obtained by gas phase loading of ZnO@MOF-5 with [CpCuL] (L = PMe_3, CN^tBu) followed by hydrogenolysis. Here, a Cu loading of 1.4 wt% together with a ZnO loading of 9.9 wt% was obtained. The composite exhibited a surface area of 920 $m^2 g^{-1}$ indicating an intact host matrix. In this case, the order of introduction of the different nano species is a crucial point. Although both precursors of ZnO and Cu nanoparticles were infiltrated in the MOF simultaneously as unchanged molecules, the simultaneous conversion by pyrolysis, photolysis or hydrogenolysis of both to Cu/ZnO@MOF-5 failed and

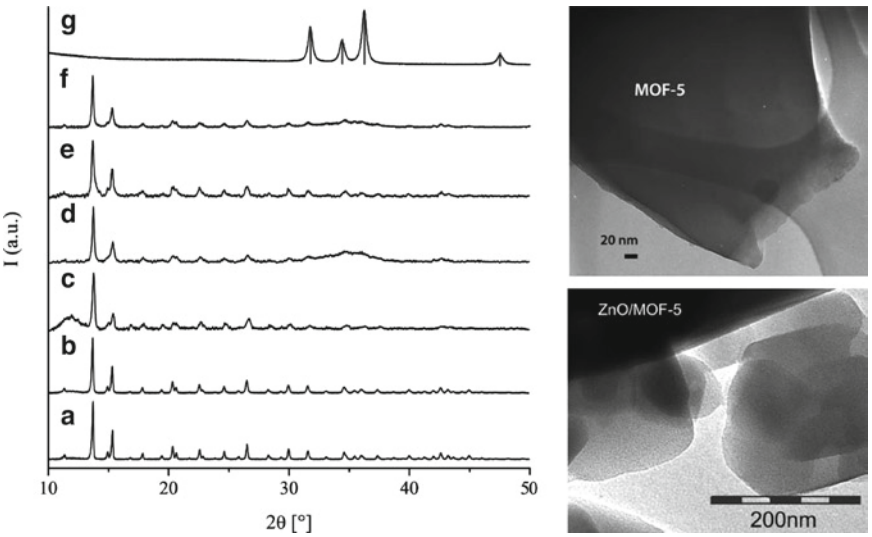

Fig. 18 *Left*: Powder X-ray diffraction patterns of MOF-5 (**a**), [$ZnEt_2$]@MOF-5 (**b**), as ZnO@MOF-5 (as synthesized by the wet method) (**c**), ZnO@MOF-5 (after annealing and derived by the wet method) (**d**), as ZnO@MOF-5 (as synthesized by the dry method) (**e**), ZnO@MOF-5 (after annealing and derived by the dry method) (**f**) and ZnO-reference sample obtained from controlled hydrolysis of $ZnEt_2$ and annealing in air (**g**). The positions of the characteristic reflections of hexagonal ZnO are marked. *Right*: TEM images of unloaded MOF-5 (a) and ZnO@MOF-5 (f, after annealing and derived by the dry method). Reproduced with permission [80]. Copyright 2008 American Chemical Society

led to the collapse of the host matrix. Therefore, the Cu precursor had to be introduced after the formation of the ZnO species in MOF-5. Below we will discuss the catalytic properties of the obtained composite Cu/ZnO@MOF-5.

4.4 Other Frameworks and Other Loading Techniques

Due to its easy accessibility and photochemical as well as thermal stability MOF-5 has been the typical study case for nanoparticle@MOF synthesis and characterization. However, a few studies of other frameworks are known as well and are summarized in the following.

4.4.1 Noble Metal Particle Formation at Redox-Active Frameworks

Suh et al. studied the nanoparticle formation in MOFs using metal salts as precursors which are reduced to form metal clusters by a special redox-active framework

[89–91]. Silver nanoparticles of ~3 nm are formed when the MOF $[\{Ni(C_{10}H_{26}N_6)\}_3(bpdc)_3]\cdot 2C_5H_5N\cdot 6H_2O$ (bpdc = 4,4′-biphenyldicarboxylate; Fig. 19) is immersed in a methanolic solution of $Ag(NO_3)$. The reaction proceeds stoichiometrically with a relation of a ration of Ni^{2+}(in the host): Ag^+ of 1:1. The host framework remains unchanged upon oxidation of its Ni-centers from Ni^{2+} to Ni^{3+}. Due to the positive charge of the MOF during the redox reaction, however, NO_3^- ions are adsorbed in the framework channels as well. The size of the Ag nanoparticles (3 nm) exceeds the window size of the host framework of 7.3 Å (Fig. 20), which might be due to diffusion of the particles to the framework's surface [89]. Similarly, in a second report Suh et al. presented the synthesis of Ag and Au nanoparticles by the redox reaction of $Ag(NO_3)$ or $HAuCl_4$ with the 2D framework $\{[Ni(cyclam)]_2[BPTC]\}_n\cdot 2nH_2O$

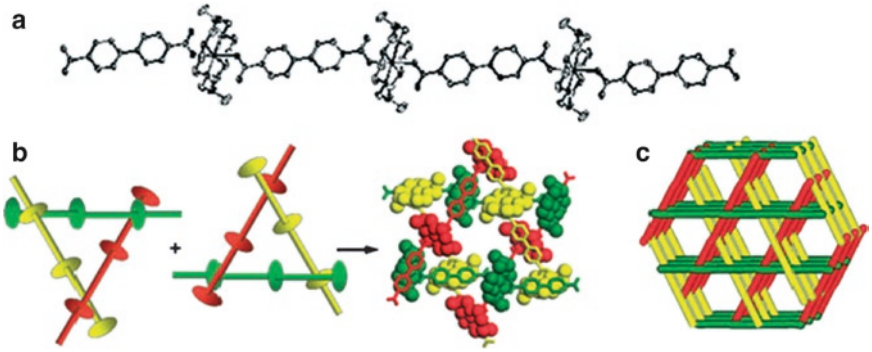

Fig. 19 X-ray structure of $[\{Ni(C_{10}H_{26}N_6)\}_3(bpdc)_3]\cdot 2\ C_5H_5N\cdot 6\ H_2O$. (**a**) Structure of the linear coordination polymer. (**b**) Double network of threefold braids where macrocycle grooves are created by $bpdc^{2-}$ ligands. (**c**) View showing the stacking of the linear chains to generate 1D channels [89]. Copyright Wiley-VCH Verlag GmbH & Co. KGaA. Reproduced with permission

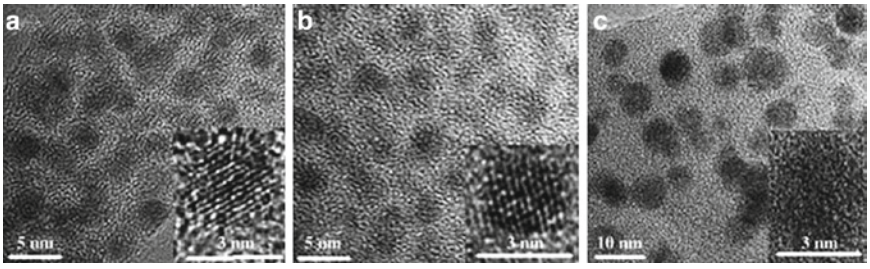

Fig. 20 HRTEM images of $[\{Ni(C_{10}H_{26}N_6)\}_3(bpdc)_3]$ after immersion in methanolic $Ag(NO_3)$ solution at room temperature for (**a**) 10 min, (**b**) 18 h and (**c**) after removal of the host by heating the solid of (**b**) in dioctylether solution [89]. Copyright Wiley-VCH Verlag GmbH & Co. KGaA. Reproduced with permission

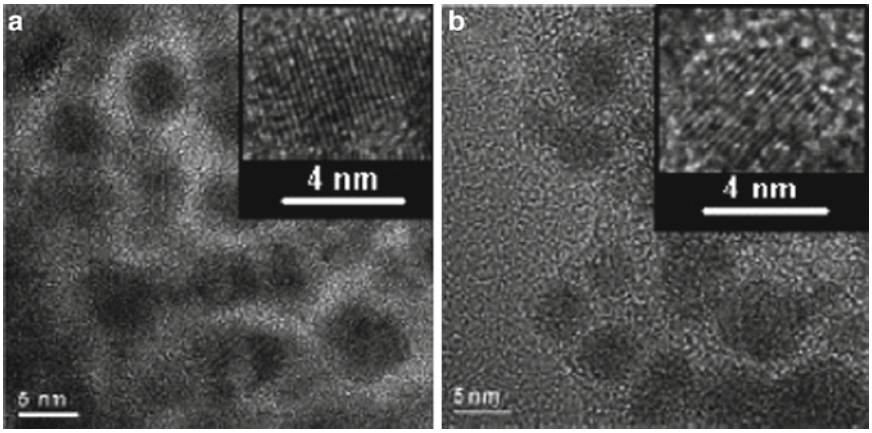

Fig. 21 HRTEM images of Ag nanoparticles formed by immersion of $[Ni(cyclam)]_2[BPTC]\}_n \cdot 2_n H_2O$ in the EtOH solution of $AgNO_3$ (1.3×10^{-1} M) at room temperature (**a**) for 5 min and (**b**) for 16 h [90]. Copyright Wiley-VCH Verlag GmbH & Co. KGaA. Reproduced with permission

(cyclam = 1,4,8,11-tetraaza-cyclotetradecane and BPTC = 1,1´-biphenyl-2,2´,6,6´-tetracarboxylate) [90].

Ag nanoparticles of 4 nm and Au nanoparticles (Fig. 21) of 2 nm are obtained which exceed the void size between two layers in the framework. As in the case above, the authors assume particle diffusion to the surface of the framework as a reason for this finding. In addition, Suh et al. reported Pd nanoparticle synthesis in the MOF $[\{Ni(cyclam)]_2(mtb)\}_n]\cdot 8n\ H_2O \cdot 4n$ DMF (mtb = methanetetra-benzoate) from $Pd(NO_3)_2$ solution in acetonitrile [91]. The presumably stoichiometric reaction between the Ni^{II} centers of the framework and the Pd salt, gives Pd^0 and Pd^{II} coexisting in the framework as determined by XPS measurements. TEM analysis reveals that again the size of the obtained Pd nanoparticles exceeds the size of the MOF channels. In this case, the authors state that Pd nanoparticles were already spontaneously formed from the solution of $Pd(NO_3)_2$ in MeCN [91]. In all examples of metal nanoparticles formed at the redox-active MOFs, the sizes of the obtained nanoparticles largely exceed those of the host channels (i.e., 3 nm particles in a framework with 7.3 Å pore diameter). No TEM tomographical measurements have been reported for these composites. Also, it is not clear whether the redox reaction requires a penetration of the noble metal salt into the MOF or whether these reactions occur only at the surface. It is not really clear whether the particles are actually still located in the framework ("outer surface") or indeed outside. From the presented TEM pictures it cannot really be ruled out that at least some of the larger particles are located outside the framework. For MOF-5 we have already discussed the rather low interaction between the framework and embedded particles which might allow the diffusion of the particles out of the host matrix. This might also be the case for the redox-active MOFs.

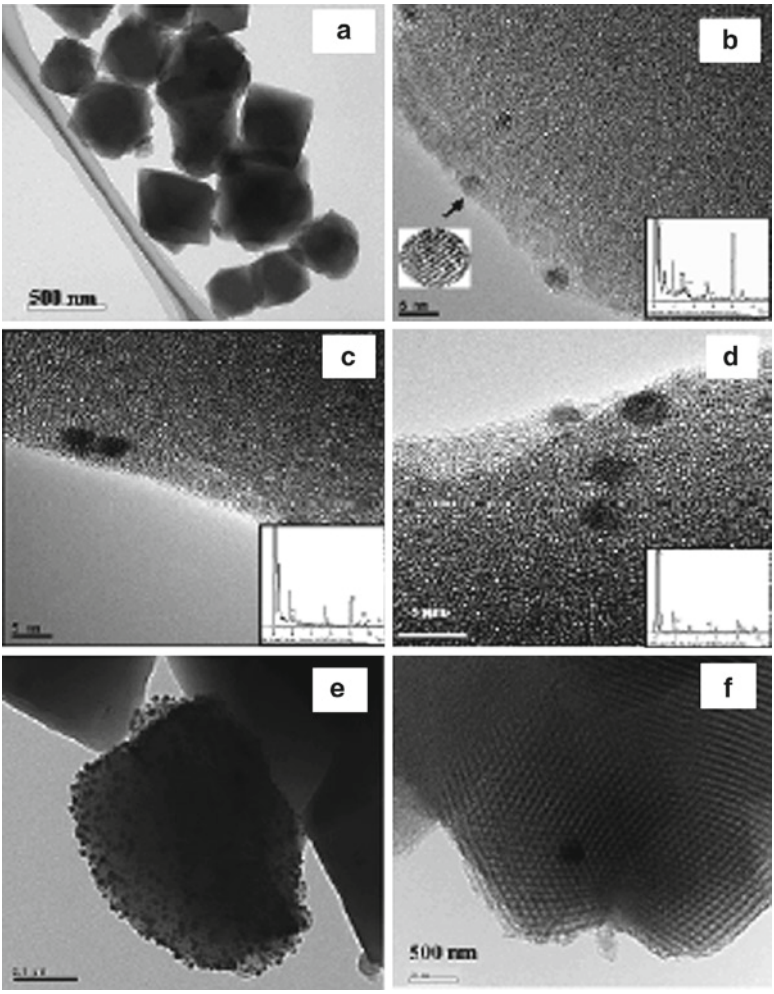

Fig. 22 TEM images of as synthesized MIL-101 and precious metal immobilized EDMIL-101. (**a**) as synthesized MIL-101, (**b**) Pd/ED-MIL-101, (**c**) Au/ED-MIL-101, (**d**) Pt/EDMIL-101, (**e**) Pd- impregnated MIL-101 and (**f**) Pd/APS-SBA-15. Insets are EDX profiles of impregnated precious metal nanoparticles [92]. Copyright Wiley-VCH Verlag GmbH & Co. KGaA. Reproduced with permission

4.4.2 Grafting of Metal Nanoparticles Inside MOFs

A method known from nanoparticle synthesis in silica materials was introduced very recently to direct the loading with metal precursors and in parallel to reduce the problems resulting from the rather low interaction of the host materials with

embedded particles. The synthesis of Pd, Pt and Au nanoparticles inside chromium based MIL-101 was reported by Férey et al. [92].

A subsequent treatment with HCl resulted in the formation of ammonium groups inside the cavities in order to facilitate ionic interactions with $[PdCl_4]^{2-}$, $[PtCl_6]^{4-}$ or $[AuCl_4]^-$ as carrier species for the noble metal component. Finally, the adsorbed anionic noble metal complex was reduced with $NaBH_4$. Again, the particle formation has no influence on the crystallinity of the host framework and no additional Bragg peaks are visible in the PXRD patterns. This is possibly due to the surprisingly low metal loading of about 1 wt%. TEM analysis reveals particle sizes of 2–4 nm matching the pore dimensions of MIL-101 (2.4 and 3.9 nm). However, larger particles outside the framework were also detected by TEM which might be due to a leaching process during the reduction step of the metal salt (Fig. 23). The grafting of the MIL-101 frameworks has a great effect on the interaction between the framework and the embedded particles. Through grafting of the framework with functional amine groups, it was possible to obtain Au nanoparticles embedded inside the framework. As discussed above, Au nanoparticles might otherwise readily diffuse out of the framework to form larger agglomerates. The overall metal content of Pd, Pt and Au in MIl-101 is rather low, so it will be interesting to see in future whether an increased loading can be obtained and what effect it will have on the particle sizes in the MIL materials. In addition, synthesis of Pd@MIL-101 was also performed using the "incipient wetness technique" by Kaskel et al. [93]. Using a similar procedure to that published previously on the loading of MOF-5 [51], Pd nanospecies in MIL-101 at rather low Pd content (1 wt%) were obtained. As in the previous work of the same group [51], no additional Bragg reflections for palladium were observed in the corresponding PXRD

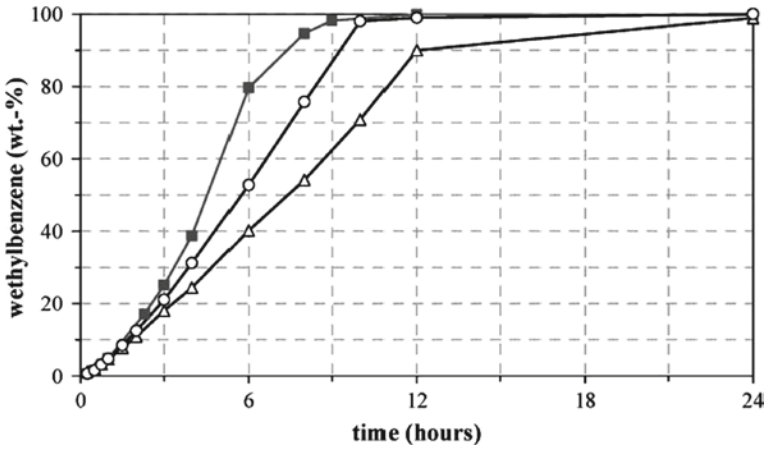

Fig. 23 Ethylbenzene formation with different Pd supported catalysts. *Filled square* represents Pd@MOF-5 (1 wt%), *open circle* represents Pd/Norit A (1 wt%) and open *triangle* represents Pd/C (purchased from Aldrich,1 wt%[51]. Reproduced with permission of The Royal Society of Chemistry

of Pd@MIL-101. The results from N_2 and H_2 sorption measurements, however, indicate the loading of the pores in MIL-101.

4.5 Applications of Nanoparticles Loaded MOFs in Catalysis

Most of the examples of metal@MOFs and metaloxides@MOFs discussed up to now have been synthesized in order to obtain novel kinds of supported nanoparticles with potentially advantageous properties for applications in catalysis. The catalytic properties of the composite materials Pd@MOF-5 and Cu@MOF-5 were among the first to be tested. The Pd@MOF-5 composite that was obtained by the gas phase loading/photolysis synthetic protocol (35.6 wt% Pd) showed moderate activity in catalysis of hydrogenation of cyclooctene [59]. The Pd@MOF-5 (1 wt%) synthesized by the "incipient wetness technique" from [$Pd(acac)_2$] was tested as catalyst in hydrogenation of styrene, 1-octene and *cis*-cyclooctene, and exhibited a slightly higher catalytic activity than Pd supported on activated carbon (Pd/Norit A; Fig. 23) [51].

The observed enhanced catalytic performance of Pd@MOF-5 (1 wt%) in comparison to Pd/Norit A (1 wt%) and Pd@MOF-5 (35.6 wt%) [59] is due possibly to the higher dispersion and accessibility of the active Pd sites in this sample. Also, Pd@MOF-5 was tested in hydrogen adsorption revealing a capacity of up to 1.86 wt% (at 77 K, 1 bar) clearly exceeding the value of Pd-free MOF-5 (1.32 wt% at 77 K, 1 bar) by about 40%. The material Pd@MOF-5 material obtained from coprecipitation [76] was also tested in hydrogenation catalysis of ethyl cinnamate, revealing an activity twice as high as the one of Pd supported on activated carbon. Again, the higher performance was attributed to the higher dispersion and better accessibility of the palladium; however, the actual microstructure of the catalyst is still unknown. From N_2 measurements of the composite material after subsequent catalytic test reactions, however, it was found that the Pd is most probably bound to the outer surface of the MOF-5 crystals. Therefore the as prepared composite might be less stable in prolonged catalytic runs than a sample with the Pd located in the MOF-5 pores. The Pd loaded MIL-101 composite was tested in catalysis of the Heck reaction of acrylic acid with iodobenzene. Its activity is comparable to that of commercially available Pd/C catalysts [92]. Kaskel et al. also performed catalytic test reactions of the composite Pd@MIL-101 [93]. The material exhibited a higher catalytic activity in the hydrogenation of styrene and octane than Pd@MOF-5. Furthermore, sustained activity in gas phase hydrogenation of acetylene/ethylene mixtures was found. The work of Kaskel et al. and Férey et al. show that for distinct catalytic applications, "incipient wetness" loading or solution loading in general might be more suitable than gas phase loading, since the metal content of the resulting metal@MOF composite can be controlled more readily. However other applications, e.g., methanol synthesis, demand a high metal (Cu) content of a catalyst sample. Here, the gas phase loading may be more advantageous, since comparably high metal loadings can be obtained rather straightforwardly. Accordingly,

the composite Cu@MOF-5 [59] was tested in methanol catalysis from synthesis gas (H_2/CO/CO_2) and showed some catalytic activity, matching the performance of Cu/ZnO@MCM-41 [94]. This is surprising since the promotion of Cu by ZnO_x species is usually essential for catalytic activity in methanol synthesis [80]. Apparently, in Cu@MOF-5 this is not necessary or provided in a novel form by the zinc carboxylate based host material MOF-5. A significant decomposition of Cu@MOF-5 during the catalytic test reactions to yield promoting ZnO has been ruled out by characterization of the used catalyst. In order to study the influence of additional ZnO species as a promoter for Cu@MOF-5, the Cu/ZnO@MOF-5 system discussed above was also tested as a catalyst for methanol synthesis. The material expectedly showed enhanced catalytic activity peaking at about 60% of an industrial reference catalyst [80]. With a comparably very low Cu loading of only 1.4 wt%, obviously a superior interfacial contact between the Cu and ZnO nano species must exist. However, the MOF-5 host material collapsed after several hours under catalytic conditions, leading to poor final activities. The same effect was found for the catalytic test reaction of Ru@MOF-5 (oxidized) in alcohol oxidation, although at the beginning of the test run, some conversion is observed [64]. Upon prolonged reaction time, the framework collapsed. These observations are attributed to the instability of MOF-5 against water, and water is a by-product in many oxidation reactions. Due to its sensitivity to water, MOF-5 appears to be less suitable as a support material in catalytic reactions that demand or release water. Yet, the presented results are encouraging and show the general potential of MOFs as support matrices in catalytic reactions. Beside the zinc carboxylate MOFs, other, more stable structures will be surely investigated in more detail in the future.

5 Conclusion

Different preparative approaches to forming nanoparticles inside MOFs have been reviewed herein. As for other porous materials, the characterization of the embedded particle and its location *in* or *outside* the framework is always a challenge. To date, nanoparticles with MOF-5 are still the most investigated systems. However, these results have been transferred to MOF-177, [62,63] HKUST-1 [38] and [Zn(bdc)(dabco)]. [38] It was found that the embedded particles interact very weakly with the host matrix such that, in the case of Au@MOF-5 large nanoparticles are formed outside the framework. The sizes of embedded Pd, Ru and Cu particles have been found to be in the range between 1–3 nm, which accounts for at least a fraction of the nanoparticles, exhibiting sizes that exceed those of the MOF-5 cavities (1.5 nm). Nevertheless, even the larger nanoparticles (>1.5 nm) are located inside the MOF-5 host matrix, most probably in a locally distorted environment, as seen in the case of Pd@MOF-5, in particular. Furthermore, nanoparticle distribution is obviously dependent on the synthesis procedure applied. Autocatalytic hydrogenolysis can lead to an agglomeration of particles at the outer surface of MOF-5 due to diffusion limitations of the reactive gas and the mobility of the included organometallic precursors.

In all examples, tomographical TEM measurements are clearly the most potent tool for the direct imaging of the embedded particles and for studying their location inside the host matrix. The usual 2D TEM pictures can present misleading results. Catalytic tests of the embedded Cu and Pd nanoparticles (and Ru nanoparticles) show the potential of MOFs to act as host materials for functional nanoparticles. Enhanced hydrogen storage capacity was measured for Pd@MOF-5 (1 wt%). However, MOF-5 is rather sensitive to water and moist air which limits its application as a host matrix. The results can, however, be clearly transferred to other nanoparticle@MOF composites that are more promising for industrial applications. Studies on nanoparticle synthesis in other MOFs have already been published and are very likely to be extended in the future. Host frameworks with a high temperature and chemical stability will surely be addressed in upcoming investigations.

References

1. Hoskins BF, Robson R (1989) J Am Chem Soc 111:5962
2. Hoskins BF, Robson R (1990) J Am Chem Soc 112:1546
3. Abrahams BF, Hoskins BF, Michail DM, Robson R (1994) Nature 369:727
4. Venkataraman D, Gardner GB, Lee S, Moore JS (1995) J Am Chem Soc 117:11600
5. Gardner GB, Venkataraman D, Moore JS, Lee S (1995) Nature 374:792
6. Li H, Eddaoudi M, O'Keeffe M, Yaghi OM (1999) Nature 402:276
7. Subramanian S, Zaworotko MJ (1995) Angew Chem Int Ed 34:2127
8. James SL (2003) Chem Soc Rev 32:276
9. Yaghi OM, O'Keeffe M, Ockwig NW, Chae HK, Eddaoudi M, Kim J (2003) Nature 423:705
10. Chae HK, Siberio-Pérez DY, Kim J, Go Y, Eddaoudi M, Matzger AJ, O'Keeffe M, Yaghi OM (2004) Nature 427:523
11. Côté AP, Benin AL, Ockwig NW, O'Keeffe M, Matzger AJ, Yaghi OM (2005) Science 310:1166
12. El-Kaderi HM, Hunt JR, Medosa-Cortés JL, Côté AP, Taylor RE, O'Keeffe M, Yaghi OM (2007) Science 316:268
13. Park KS, Ni Z, Côté AP, Choi JY, Huang R, Uribe-Romo FJ, Chae HK, O'Keeffe M, Yaghi OM (2006) Proc Natl Acad Sci USA 103:10186
14. Hayashi H, Côté AP, Furukawa H, O'Keeffe M, Yaghi OM (2007) Nature 6:501
15. Banerjee R, Phan A, Wang B, Knobler C, Furukawa H, O'Keeffe M, Yaghi OM (2008) Science 319:939
16. Kitagawa S, Kitaura R, Noro S (2004) Angew Chem Int Ed 43:2334
17. Kitagawa S, Uemura K (2005) Chem Soc Rev 34:109
18. Tanaka D, Kitagawa S (2008) Chem Mater 20:922
19. Uemura T, Kitaura R, Ohta Y, Nagaoka M, Kitagawa S (2006) Angew Chem Int Ed 44:4112
20. Férey G, Mellot-Draznieks C, Serre C, Millange F (2005) Acc Chem Res 38:217
21. Férey G (2008) Chem Soc Rev 37:191
22. Férey G, Mellot-Draznieks C, Serre C, Millange F, Dutour J, Surble S, Margiolaki I (2005) Science 309:2040
23. Seo JS, Whang D, Lee H, Jun SI, Oh J, Jeon YJ, Kim K (2000) Nature 404:982
24. Vaidhyanathan R, Bradshaw D, Rebilly JN, Barrio JP, Gould JA, Berry NG, Rosseinsky MJ (2006) Angew Chem Int Ed 118:1
25. Eddaoudi M, Kim J, Rosi N, Vodak D, Wachter J, O'Keeffe M, Yaghi OM (2002) Science 295:469

26. Serre C, Millange F, Thouvenot C, Noguès M, Marsolier G, Louër D, Férey G (2002) J Am Chem Soc 124:13519
27. Rowsell JL, Millward CAR, Park KS, Yaghi OM (2004) J Am Chem Soc 126:5666
28. Millward AR, Yaghi OM (2005) J Am Chem Soc 127:17998
29. Matsuda R, Kitaura R, Kitagawa S, Kubota Y, Belosludov RV, Kobayashi TC, Sakamoto H, Chiba T, Takata M, Kawazoe Y, Mita Y (2005) Nature 436:238
30. Rowsell JLC, Yaghi OM (2005) Angew Chem Int Ed 44:4670
31. Surblé S, Millange F, Serre C, Düren T, Latroche M, Bourrelly S, Llewellyn PL, Férey G (2006) J Am Chem Soc 128:14889
32. Maji TK, Matsuda R, Kitagawa S (2007) Nat Mater 6:142
33. Alaerts L, Kirschhock CEA, Maes M, van der Veen MA, Finsy V, Depla A, Martens JA, Baron GV, Jacobs PA, Denayer JFM, De Vos DE (2007) Angew Chem Int Ed 119:1
34. Hermes S, Schröder F, Chelmowski R, Wöll C, Fischer RA (2005) J Am Chem Soc 127:13744
35. Hermes S, Zacher D, Baunemann A, Wöll C, Fischer RA (2007) Chem Mater 19:2168
36. Shekhah O, Wang H, Kowarik S, Schreiber F, Paulus M, Tolan M, Sternemann C, Evers F, Zacher D, Fischer RA, Wöll C (2007) J Am Chem Soc 129:15118
37. Biemmi E, Scherb C, Bein T (2007) J Am Chem Soc 129:8054
38. Zacher D, Baunemann A, Hermes S, Fischer RA (2007) J Mater Chem 17:2785
39. Wu CD, Hu A, Zhang L, Lin W (2005) J Am Chem Soc 127:8940
40. Cho SH, Ma B, Nguyen ST, Hupp JT, Albrecht-Schmitt TE (2006) Chem Commun 24:2563
41. Bauer CA, Timofeeva TV, Settersten TB, Patterson BD, Liu VH, Simmons BA, Allendorf MD (2007) J Am Chem Soc 129:7136
42. Chen B, Yang Y, Zapata F, Lin G, Qian G, Lobkovsky EB (2007) Adv Mater 19:1693
43. Llabres i Xamena FX, Corma A, Garcia H (2007) J Phys Chem C 111:80
44. Alvaro M, Carbonell E, Ferrer B, Llabres i Xamena FX, Garcia H (2007) Chem Eur J 13:5106
45. Hulteen JC, Martin CR (1997) J Mater Chem 7:1075
46. Joo SH, Choi SJ, Oh I, Kwak J, Liu Z, Terasaki O, Ryoo R (2001) Nature 412:169
47. Gray DH, Hu S, Juang E, Gin DL (1997) Adv Mater 9:731
48. Fang QR, Zhu GS, Jin Z, Ji YY, Ye JW, Xue M, Yang H, Wang Y, Qiu SL (2007) Angew Chem Int Ed 46:6638
49. Horcajada P, Serre C, Vallet-Regí M, Sebban M, Taulelle F, Férey G (2006) Angew Chem Int Ed 118:6120
50. Horcajada P, Serre C, Maurin G, Ramsahye NA, Balas F, Vallet-Regí M, Sebban M, Taulelle F, Férey G (2008) J Am Chem Soc 130:6774
51. Sabo M, Henschel A, Fröde H, Klemm E, Kaskel S (2007) J Mater Chem 17:3827
52. Schmid G (1992) Chem Rev 92:1709
53. Bradley JS (1994) The Chemistry of Transition Metal Colloids. In: Schmid G (ed) Clusters and Colloids: from Theory to Applications. VCH, Weinheim, pp 459–544
54. Hitchman ML, Jensen KF (1993) Chemical Vapor Deposition. Academic Press, Principles and Applications. London
55. Sherman A (1987) Chemical vapor deposition for microelectronics. Principles, technology and applications. Noyes Publications, Park Ridge
56. Kaye SS, Dailly A, Yaghi OM, Long JR (2007) J Am Chem Soc 129:14176
57. Huang L, Wang H, Chen J, Wang Z, Sun J, Zhao D, Yan Y (2003) Microporous Mesoporous Mater 58:105
58. Greathouse JA, Allendorf MD (2006) J Am Chem Soc 128:10678
59. Hermes S, Schröter MK, Schmid R, Khodeir L, Muhler M, Tissler A, Fischer RW (2005) Angew Chem Int Ed 44:6237
60. Kim H, Chun H, Kim GH, Leeb HS, Kim K (2005) Chem Commun:2759
61. Hermes S, Schröder F, Amirjalayer S, Schmid R, Fischer RA (2006) J Mater Chem 16:2464
62. Proch S, Hermannsdörfer J, Kempe R, Kern C, Jess A, Seyfahrt L, Senker J (2008) Chem Eur J 14:8204

63. Müller M, Lebedev OI, Fischer RA (2008) J Mater Chem 18:5274
64. Schröder F, Esken D, Cokoja M, van den Berg MWE, Lebedev OI, Van Tendeloo G, Walaszek B, Buntkowsky G, Limbach HH, Chaudret B, Fischer RA (2008) J Am Chem Soc 130:6119
65. Sauer J, Marlow F, Spliethoff B, Schüth F (2002) Chem Mater 14:217
66. Hafizovic J, Bjorgen M, Olsbye U, Dietzel PDC, Bordiga S, Prestipino C, Lamberti C, Lillerud KP (2007) J Am Chem Soc 129:3612
67. Park YK, Choi SB, Kim H, Kim K, Won BH, Choi K, Choi JS, Ahn WS, Won N, Kim S, Jung DH, Choi SH, Kim GH, Cha SS, Jhon YH, Yang JK, Kim J (2007) Angew Chem Int Ed 46:8230
68. Caulder DL, Brückner C, Powers RE, König S, Parac TN, Leary JA, Raymond KN (2001) J Am Chem Soc 123:8923
69. Leary JA, Pluth MD, Raymond KN (2006) Chem Soc Rev 36:161
70. Fiedler D, Bergman RG, Raymond KN (2006) Angew Chem Int Ed 45:745
71. Pluth MD, Bergman RG, Raymond KN (2007) Angew Chem Int Ed 46:8587
72. Kawano M, Kobayashi Y, Ozeki T, Fujita M (2006) J Am Chem Soc 128:6558
73. Kaye SS, Long JR (2008) J Am Chem Soc 130:806
74. Turner S, Lebedev OI, Schröder F, Esken D, Fischer RA, Van Tendeloo G (2008) Chem Mater 20:5622
75. Kampers FWH, Engelein CWR, van Hoff JHC, Koningsberger DC (1990) J Phys Chem 94:8574
76. Opelt S, Türk S, Dietzsch E, Henschel A, Kaskel S, Klemm E (2008) Catal Commun 9:1286
77. Pan C, Pelzer K, Philippot K, Chaudret B, Dassenoy F, Lecante P, Casanove MJ (2001) J Am Chem Soc 123:7584
78. Pelzer K, Laleu B, Lefebvre F, Philippot K, Chaudret B, Candy JP, Basset JM (2004) Chem Mater 16:4937
79. Pelzer K, Vidoni O, Philippot K, Chaudret B, Colliere V (2003) Adv Funct Mater 13:118
80. Müller M, Hermes S, Kähler K, Muhler M, Fischer RA (2008) Chem Mater 20:4576
81. Sung CK, Hong W, Shi Q, Kou X, Yeung MH, Wang J, Stucky GD (2006) Adv Funct Mater 16:2225
82. Besson S, Gacoin T, Ricolleau Boilot JP (2003) Chem Commun 3:360
83. Plyuto Y, Berquier JM, Jacquiod C, Ricolleau C (1999) Chem Commun 17:1653
84. Hansen PL, Wagner JB, Helveg S, Rostrup-Nielsen JR, Clausen BS, Topsøe H (2002) Science 295:2053
85. Günter MM, Ressler T, Bems B, Büscher C, Genger T, Hinrichsen O, Muhler M, Schlögl R (2001) Catal Lett 71:37
86. Fujitani T, Nakamura J (2000) Appl Catal A 191:111
87. Kurtz M, Bauer N, Buscher C, Wilmer H, Hinrichsen O, Becker R, Rabe S, Merz K, Driess M, Fischer RA, Muhler M (2004) Catal Lett 92:49
88. Müller M, Zhang X, Wang Y, Fischer RA (2009) Chem Commun . doi:10.1039/b814241f
89. RiMoon H, Kim JH, Suh MP (2005) Angew Chem Int Ed 44:1261
90. Suh MP, Moon HR, Lee EY, Jang SJ (2006) J Am Chem Soc 128:4710
91. Cheon YE, Suh MP (2008) Chem Eur J 14:3961
92. Hwang YK, Hong DY, Chang JS, Jhung SH, Seo YK, Kim J, Vimont A, Daturi M, Serre C, Férey G (2008) Angew Chem Int Ed 47:4144
93. Henschel A, Gedrich K, Kraehnert R, Kaskel S (2008) Chem Commun:4192
94. Becker R, Parala H, Hipler F, Tkachenko OP, Klementiev KV, Grünert W, Wilmer H, Hinrichsen O, Muhler M, Birkner A, Wöll C, Schäfer S, Fischer RA (2004) Angew Chem Int Ed 43:2839

Top Curr Chem (2010) 293: 115–153
DOI 10.1007/128_2009_7

Published online: 26 August 2009

Chiral Metal-Organic Porous Materials: Synthetic Strategies and Applications in Chiral Separation and Catalysis

Kimoon Kim, Mainak Banerjee, Minyoung Yoon, and Sunirban Das

Abstract In the light of growing demand for chiral purity in biological and chemical processes, the synthesis of chiral metal-organic porous materials (CMOPMs) have become immensely important because of their potential applications in chiral separation and asymmetric catalysis. In this chapter, the synthetic strategies for CMOPMs are discussed briefly keeping the focus on their applications. Two distinct approaches have been taken to synthesize a wide variety of chiral structures with different topologies and accessible cavities. Several CMOPMs have shown catalytic activity and enantioselectivity toward a number of chemical transformations. On many occasions, the chiral pores of the MOPMs have been utilized in order to achieve separation of enantiomers from racemates. Recent applications of homochiral MOPMs in heterogeneous asymmetric catalysis and chiral separations are also presented here.

Keywords Asymmetric catalysis • Chirality • Crystal structure • Enantioselection • Metal-organic porous materials

K. Kim (✉), M. Banerjee, M. Yoon and S. Das
Department of Chemistry, Division of Advanced Materials Science, and
National Creative Research Initiative Center for Smart Supramolecules,
Pohang University of Science and Technology, Pohang, 790-784,
Republic of Korea
e-mail: kkim@postech.ac.kr

Contents

Abbreviations

1,2-pd	1,2-propanediol
asp	aspartate
bdc	1,4-benzenedicarboxylate
BINAP	2,2′-bis(diphenylphosphino)-1,1′-binaphthyl
BINOL	2,2′-dihydroxy-1,1′-binaphthyl
bipy	4,4′-bipyridine
bpdc	4,4′-biphenyldicarboxylate
bpe	1,2-bis(4-pyridyl)ethylene
bpy	2,2′-bipyridine
btc	1,3,5-benzenetricarboxylate
CMOPM	Chiral metal-organic porous material
CSP	Chiral stationary phase
dca	dicyanamide
DPEN	1,2-diphenylethylenediamine
IRMOF	Isoreticular metal organic framework
lac	Lactate
MOF	Metal-organic framework
MOPM	Metal-organic porous material
pic	picoline
QA	6-methoxyl-(8*S*,9*R*)-cinchonan-9-ol-3-carboxylate
sala	*N*-(2-hydroxybenzyl)-L-alanine
salen	1,2-cyclohexanediimino-salicylidene
SBU	Secondary building unit
SHG	Second harmonic generation
TOF	Turn over frequency
TON	Turn over number
UHP	Urea hydroperoxide

1 Introduction

Porous materials are ubiquitous in nature. The earth's crust contains many porous materials e.g., soil, sandstones, carbonates, shales; even biological tissues can be porous. Porous materials have found enormous applications in many traditional scientific fields such as catalysis, adsorption, and environmental technology because of their high surface area coupled with many other unique chemical and physical properties. A classic example of naturally occurring porous materials is zeolites, a class of aluminosilicates with interconnected small cavities of 4–13 Å in dimensions, used as catalysts for oil refining, petrochemistry, and organic synthesis in the production of fine and specialty chemicals [1]. The loosely bound cations present inside the channels and pores of zeolites can be readily exchanged with other cations when in aqueous media; this also make them ideal choices as water softening devices and in detergent and soap industries. In fact, a major part of the global economy (~$350 billion) is currently based on the use of crystalline microporous zeolites in several industrial processes [2], which reflects the importance of such porous materials in the daily life of man.

As the demand for optically pure compounds grows, significant research efforts have been devoted to developing chiral zeolites and related chiral porous solids with the goal of using them for the production of enantiopure materials via asymmetric chemical transformations and/or chiral separations [3]. Despite considerable efforts, however, only a few optically *pure* zeolites have been synthesized to date [4,5]. More importantly, local chirality at the catalytic center would provide more impact than the topological chirality in imparting strong asymmetric induction to the substrate during the reaction. This has prompted exploration of other strategies for the synthesis of similar porous solids with embedded chiral functionalities, which may find practical applications in chirotechnology.

There has been considerable research interest in metal-organic porous materials (MOPMs) or metal-organic frameworks (MOFs) over the last couple of decades because of their potential impact on several technologies, such as gas storage, separation, and heterogeneous catalysis [6–11]. Although not as robust as zeolites, they certainly have some advantages over zeolites. MOPMs are typically synthesized under very mild conditions, which should allow facile construction of homochiral MOPMs by appropriate choice of chiral building blocks. Ideally, they can possess chiral functionalities that are accessible via the open channels or cavities. Such readily accessible, regularly ordered chiral functionalities could be exploited to generate heterogeneous asymmetric catalysts for the economical production of optically pure compounds. The cavities of homochiral MOPMs can also be utilized in separation of enantiomers by selective recognition/sorption. Successful design of homochiral MOPMs may therefore lead to practical applications in the field of chirotechnology. From the beginning of this century, research of great potential in this field has started to flourish. Several review articles on this highly important field of research are available [12–14]. This review aims to provide current status and trends in the development of chiral metal-organic porous materials (CMOPMs)

and indicate their useful and practical applications in the burgeoning field of chirotechnology.

1.1 Chirality in Crystal Structure

In the context of chemistry, the term "*chirality*" usually refers to a pair of molecules that cannot be superimposed onto each other - also referred to as enantiomers or optical isomers. The main characteristic of chirality is the absence of an axis of improper rotation. The existence of such a symmetry element is implied by the presence of either a mirror plane through the central atom or a center of inversion; if either of these elements is present, the molecule is achiral. The chiral sense of a molecule is specified by its absolute configuration (*R/S*, D/L, or Δ/Λ). Molecules may be present as enantiomeric mixtures, of which those with compositions 100:0 and 0:100%, described as enantiomerically pure or homochiral, and the equimolar one of 50:50% described as a racemate or racemic mixture are particularly important.

A total of 230 space groups, which are the combination of 32 crystallographic point groups and 14 Bravais lattices, are used to define the 3D solid-state structure of a molecule. Out of these 230 space groups, 65 are noncentrosymmetric, which contain only pure rotation and screw axes- for example, the two-, three-, four-, or six-fold rotations with screw axis without any plane of symmetry or inversion center. Among these, 22 space groups are pair wise enantiomorphous, and therefore inherently chiral. Within each pair, inversion through a point transforms one space group into the other, e.g., $P6_2$ transforms into $P6_4$ and vice versa. When coordination polymers crystallize, they form well-ordered 1D, 2D or 3D net structures connected through covalent or noncovalent bonds with defined topologies. Coordination polymers with chiral components always crystallize in noncentrosymmetric space groups due to the embedded chirality in the subunits. However, in principle, a crystal with single-handed helical arrangement of the components is chiral. Therefore, a helix may be a good model to transmit chirality to the crystal structure even if it is constructed from achiral components. In this sense, the topology-based approach is much more convenient for the design of noncentrosymmetric coordination networks because of the presence of some inherently chiral nets. The simplest and most common nontrivial regular 3D chiral topologies are 3-connected (10, 3)-a and (12, 3) nets (Fig. 1) [15]. The symbol (10, 3) is used to characterize the topology of a net in which all nodes are 3-connected and the shortest circuits involving all three different pairs of connections radiating from each node are 10-gons. The chirality in (10,3)-a arises from the disposition of the same handed 4-fold helices parallel to each of the three crystallographic cubic axes. Similarly, a (12,3) net can be realized in a completely strain-free manner from alternating T and trigonal nodes. Among 4-connected nets, diamond-like nets with unsymmetrical linkers have the ability to generate noncentrosymmetric crystals. The diamondoid network consisting of alternating adamantane-like cavities can be constructed with alternate tetrahedral metal centers linked together by rigid, linear bridging ligands (Fig. 1c).

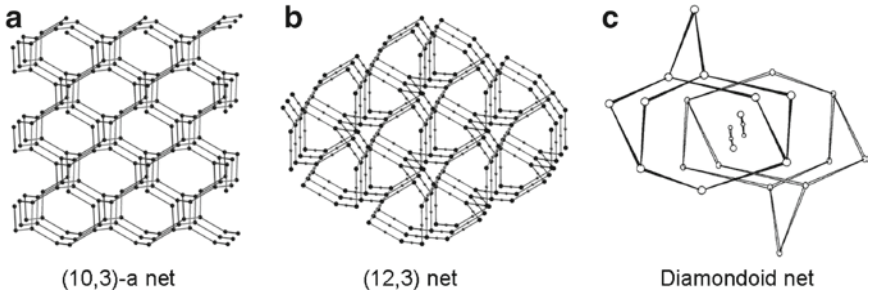

Fig. 1 Representative topologies of (10,3)-a, (12,3), and 2-fold diamondoid nets

1.2 Metal-Organic Porous Materials: Brief History and Key Developments

There are a number of excellent reviews on coordination polymers, MOFs or MOPMs [9–11,16–20]. Here we briefly touch the history and key developments in this area.

The design of extended solids with ordered array of the basic building units has been a subject of intense study in conjunction with developing new solid-state functional materials. Hydrogen bonding has been extensively used in designing organic solids with specific structures, largely because of its strength and directionality [21–23]. The strong and yet reversible nature with high directionality of metal-ligand coordination bond makes it widely exploited in constructing network structures with specific topologies and geometries. In 1990, for the first time, Robson introduced a design concept to the construction of 3D MOFs using appropriate molecular building blocks and metal ions [24]. Following the seminal work, several groups including Zaworotko [25,26], Yaghi and O'Keeffe [27,28] contributed significantly to the developments in this field in terms of establishing designing principles. Particularly, the node (simple metal ions or metal clusters) and spacer (bridging organic ligands) approach has been remarkably successful in producing well-ordered crystalline solids with predictable network architectures [29].

In particular, MOFs with large pores or metal-organic porous materials (MOPMs) have attracted considerable attention due to their potential applications in many areas including gas storage and catalysis. Considerable efforts have thus been made in designing MOPMs with specific pore sizes, shapes, and chemical environments. One of the early issues in this area was to design a stable framework. MOFs are usually produced with guest molecules – typically solvents or templates – in the pores. However, the attempts to remove guest molecules from the pores often result in collapse of the framework. Therefore, rigid and directional building units are the prime choice in controlling the porosity as well as the stability of the frameworks. Yaghi and coworkers demonstrated how the concept of secondary building units (SBUs) could be applied with great success to design highly porous and stable rigid MOFs [30–32]. The clusters of metal-carboxylates have been used

as rigid SBUs that act as vertices in the framework, and the length of the organic linkers can be modulated to vary the pore sizes systematically. With increasing pore size, however, frameworks show a tendency to undergo interpenetration. Although interpenetration may increase the stability of the framework and selectivity in sorption, it substantially decreases the possibility to accommodate larger molecules for separation and catalysis. The use of bulky solvent molecules as a template or bulky ligands at times decreases the possibilities of interpenetration [33].

The primary objectives of the design and synthesis of these open-framework solids are to utilize them as functional materials. Except some applications such as nonlinear optics, many applications including catalysis, ion exchange, and gas sorption rely on the fact that the open cavities allow passage of certain species to the active centers and exclude others [34–36]. The basic functions of these materials, whether two- or three-dimensional, are dependent on the building blocks and topology of the material. With the achievement of permanent porosity and high surface area, these materials are used for gas storage and separation. For example, Kitagawa and Yaghi first demonstrated the use of such materials for methane and hydrogen gas storage, respectively [37,38]. The guest induced structural transformations have also been used for selective sorption and separation [39]. However, one of the most exciting applications of MOPMs is catalysis. Fujita first elegantly demonstrated the use of MOPMs as a heterogeneous catalyst to facilitate chemical transformations, while Kim demonstrated that homochiral MOPMs are useful for enantioselective separation and catalysis [40,41].

1.2.1 Chiral Metal-Organic Porous Materials

A compelling motivation to prepare porous materials with built-in chirality is their potential use in enantioselective separation and in the synthesis of optically pure compounds, beside their second harmonic generation (SHG) properties. Although microporous zeolites show a profound range of applications in heterogeneous catalysis, the dearth of chiral zeolites limits their contribution in heterogeneous asymmetric catalysis or chiral separation. There are sporadic reports on the immobilization of chiral units in zeolites and successful application in asymmetric induction. However, this process does not guarantee a stable well-ordered chiral environment within the pores [42,43]. CMOPMs with well-defined chiral centers and/or reactive sites may thus emerge as a useful substitute to the practically inaccessible chiral zeolites in the realm of chirotechnology. Such chiral porous matrices have some additional advantages over zeolites. First, it is easy to introduce various functional groups into the cavity of CMOPMs. Second, these materials are not only restricted to the rigid tetrahedral network topologies like zeolites, but a variety of topologies can be generated with more internal flexibilities to allow easy access of guest molecules to the cavities. Third, it is also possible to keep hydrophilic and hydrophobic balance in the pores by judicious choice of linkers. During the last 5–10 years, several CMOPMs have been synthesized adopting different strategies, which will be discussed in Sect. 2 in detail.

2 Synthetic Strategies of Chiral MOPMs

To achieve well-ordered chiral catalytic centers in the solid phase, it is necessary to select proper chiral organic building units and metal salts that form periodically ordered porous materials with appropriate void space. The accessibility of the active sites, which depends on the shape and size of the window and cavity in the MOPM, is crucial for the activity and selectivity of the final catalyst. Nanometer sized pores are ideal to access the catalytic centers of the framework, and to achieve strong multidirectional interactions between substrates and the chiral environment of the cavities. Keeping these points in mind, different strategies have emerged for the construction of well-defined metal-organic porous frameworks with chiral environments. In principle, one can construct CMOPMs in two distinct ways, (a) by deliberate design of homochiral frameworks from the building blocks, and (b) introduction of chiral units inside pre-assembled achiral frameworks by post-modification. A large number of chiral MOPMs have been synthesized using the first approach, either from achiral building blocks or from chiral molecular components. In this section, we describe the strategies for the construction of CMOPMs with illustrative examples.

2.1 Direct Synthesis of Chiral MOPMs from Building Blocks

Chiral building blocks are the preferred choice for building homochiral frameworks. However, achiral molecular components are also capable of generating chiral frameworks by adopting chiral net structures. Both approaches are discussed here in separate subsections.

2.1.1 Chiral MOPMs from Achiral Building Blocks

Any MOPM - whether built with achiral or chiral components, may acquire a chiral space group during crystallization by unique spatial disposition of all the building units within the MOPM. There are numerous examples of MOPMs built with simple achiral molecules that crystallize in chiral space groups through self-resolution [44–47]. Although the individual crystals of such systems are chiral, the bulk samples tend to contain both enantiomorphs and thus can be racemic. However, it is not understood how to induce homochirality in the bulk phase in such a way that every crystal is oriented with the same chirality. Therefore, the design of noncentrosymmetric coordination networks requires identification of those nets that are not predisposed to pack in centrosymmetric space groups, and identification of potential nodes and spacers that can lead to the desired noncentrosymmetric topologies. To increase the possibilities of having control over the predicted topology, however, simple systems are better such as 3-connected (10,3)-a net, which is inherently

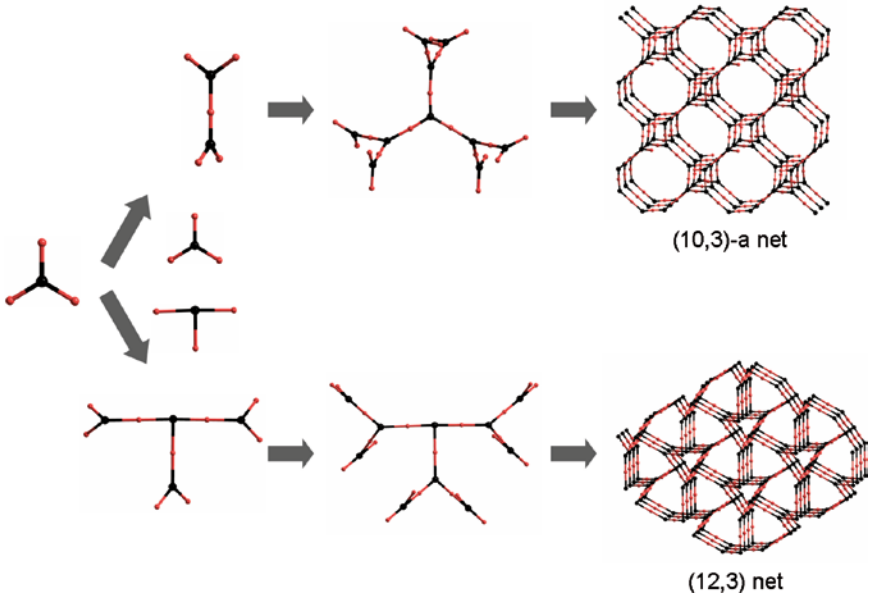

Fig. 2 The course of the assembly of 3D (10,3)-a and (12,3) nets from the 3-connected nodes and liner linkers

chiral (Fig. 2). Many researchers have tried to generate homochiral MOPMs with this topology through self-resolution. Although in some cases individual crystals were enantiomorphic by deliberate design, the bulk sample was still racemic [48,49]. Other networks with applicable porosity include 3-connected (12,3) and 4-connected diamond-like nets. There are several reports of chiral MOFs with these networks through proper selection of linkers, but the high propensity of higher-fold interpenetration often reduces the void space [31].

To generate bulk chirality, the two possible enantiomeric forms must be differentiated. This can be achieved by using chiral templates, such as enantiopure solvents of crystallization, counter cations, or auxiliary ligands. Rosseinsky and coworkers used optically pure coligand, 1,2-propanediol (1,2-pd) as a template to direct the formation of homochiral porous networks of the type $M_3(btc)_2$, where M is a divalent metal ion and btc is 1,3,5-benzenetricarboxylate [50]. In the doubly interpenetrated (10,3)-a network of $[Ni_3(btc)_2(py)_6(1,2\text{-pd})_3]\cdot 11(1,2\text{-pd})\cdot 8(H_2O)$, **1**, the coordinating 1,2-pd acts as a chiral coligand that controls the helical growth of all crystals in the same direction to afford homochiral materials. However, only the *S*-isomer of 1,2-pd binds to the metal center during the formation of the chiral framework. This selectivity was observed even when the crystals were grown from racemic diol, which was ascribed to the steric conflict between the methyl group of diol and btc unit. Recently, Morris and coworkers used a nonligating template to exert chiral purity on a framework [51]. They used chiral ionic liquid, 1-butyl-3-methylimidazolium L-aspartate, as a solvent as well as a template for the synthesis

of homochiral MOPM, $[(BMIm)_2][Ni(Hbtc)_2(H_2O)_2]$, **2**, where the bulky organic counter cations occupied most of the void space. Obviously, a synthetic approach that allows the achiral molecular precursors into extended homochiral frameworks, templated by enantiopure coligands or counter cations will help expanding the diversity of metal-organic homochiral solids. Removal of these extra framework species is, however, much more difficult than that of neutral solvent molecules to access the cavity or channel.

2.1.2 Chiral MOPMs from Homochiral Building Blocks

The most reliable and rational strategy to design homochiral MOPMs is the combination of metal or metal cluster (SBU) containing nodes and chiral organic ligands. The chiral organic ligands ensure the chirality in the final networks. The chiral organic ligands can be used in two ways to construct homochiral MOPMs: (a) using homochiral linkers to connect metal ions or SBUs, or (b) using enantiopure chiral auxiliary ligands to generate chiral SBU, which subsequently connect with rigid achiral linkers. In some cases, it is difficult to classify them into one of the two approaches, but we try to demonstrate the principle with illustrative examples.

From Homochiral Bridging Linkers

The use of well-defined and directional homochiral bridging ligands as building blocks for the synthesis of homochiral MOPMs is without any doubt the most reliable and promising strategy among all available strategies. Before the development of well-known "*reticular synthesis*" or predesigned SBU concept, commercially available, multitopic, homochiral ligands with the propensity to bridge metal centers such as amino acids or hydroxyacids were the most attractive choice for introducing homochirality into a MOF. For example, Randford and coworkers used the amino acid derivative, *N*-(2-hydroxybenzyl)-L-alanine (H_2sala), and metal ions for the synthesis of a homochiral MOF. A honeycomb like framework was formed through the propagation of hydrogen bonded helical chains of discrete dimer, $[\{Zn(sala)(H_2O)_2\}_2]$, **3** [52]. Although thermal dehydration retains the framework integrity, the accessible free space is very small. Subsequently, several other groups tried to generate chiral MOPMs with other cheap and readily available chiral ligands. In some cases, they showed moderate chiral separation; however, their structural prediction was found to be difficult because of the high order flexibility inherent in these building blocks. In addition, these ligands are not always equipped with functional groups required for chiral separation and asymmetric catalysis. Therefore, it is necessary to design rigid, homochiral ligands with proper functionality and connectivity and apply a modular approach to produce the desired framework (Fig. 3).

In 2000, Kim and coworkers reported the first example of a well-defined, crystalline, homochiral MOPM with catalytic activity [41]. They synthesized the

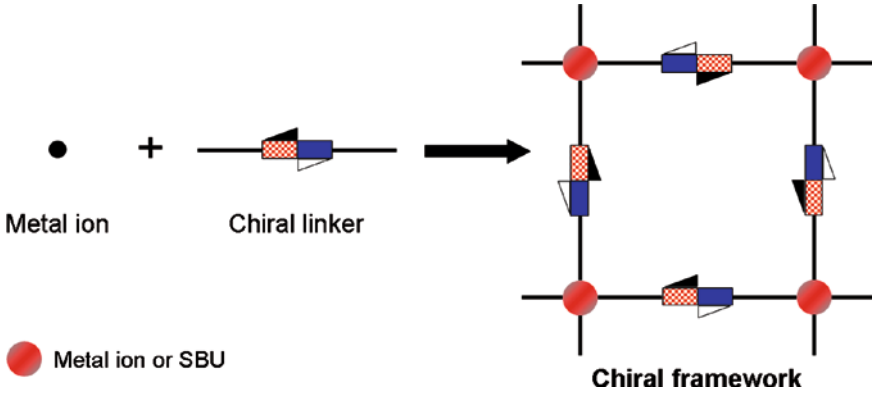

Fig. 3 Schematic representation of the general synthetic strategy of chiral framework by using chiral linker

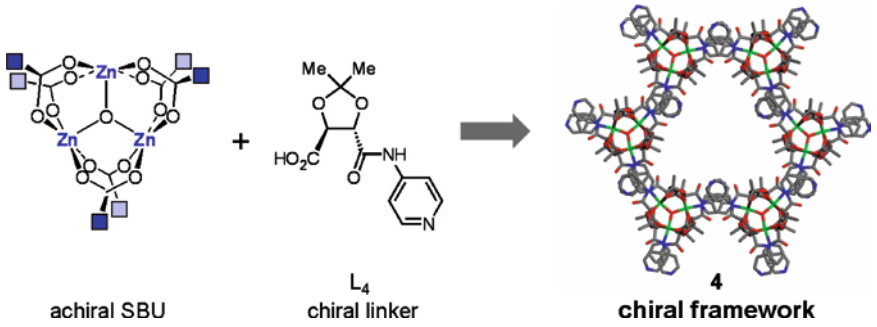

Fig. 4 Schematic representation of the synthesis of POST-1

homochiral open-framework solid, $[Zn_3(\mu^3\text{-}O)(L_4\text{–}H)_6]\cdot 2H_3O\cdot 12H_2O$ (referred to as POST-1 (**4**)) using enantiopure tartaric acid-based unsymmetrical ligand (L_4) (Fig. 4). In POST-1, oxo-bridged trinuclear zinc cluster behaved as an SBU, which in turn was interconnected to generate 2D infinite layers with large 1D channels. The ligand, L_4 can be considered semi-flexible, which leads to an interesting but 2D layered structure. However, more rigid, linear chiral linker, like BINOL or chiral salan based ligands, are expected to produce robust frameworks.

Lin and coworkers used rigid BINOL-based chiral ligands to synthesize several 2D or 3D homochiral MOPMs. The reason behind the selection of BINOL derivatives as chiral linker is their active involvement in several well-known homogeneous catalysts. In order to achieve larger pore size with predictable structure, they designed linear dicarboxylic acid functionalized BINOL derivative (6,6′-dichloro-2,2′-diethoxy-1,1′-binaphthyl-4,4′-dibenzoic acid), L_5, to link with zinc ion. As a result, a chiral framework of cubic topology, $[Zn_4(\mu^4\text{-}O)(L_5)_3(DMF)_2]\cdot 4DMF\cdot 3CH_3OH\cdot 2H_2O$ (**5**), with octahedral zinc-carboxylate unit, $Zn_4O(O_2C^-)_6$, as SBU was obtained [53]

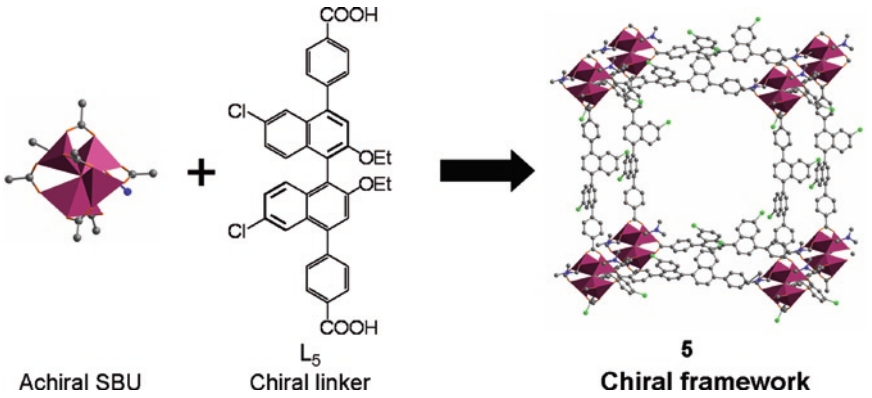

Fig. 5 A typical example of the synthesis of chiral framework by using rigid chiral linker (L_5) and achiral metal cluster SBU

(Fig. 5). Though they could isolate the product with desired network, the interpenetration led to almost closed-pack system. Later, through suitable selection of molecular building blocks and reaction condition, they synthesized a large number of chiral MOPMs with the same strategy.

More recently, Hupp and Nguyen used salen-based chiral Mn-complex as a chiral linker to generate chiral MOPM through pillaring with Zn-carboxylate paddlewheel [54]. Bu et al. also employed the same strategy to construct several homochiral open-framework materials using homochiral camphoric acid as a rigid linker [55].

From Chiral Secondary Building Units

The predesigned synthesis of CMOPMs with readily available chiral building blocks, such as amino acids or sugars, is very difficult as they are flexible in nature. However, these ligands can be utilized as auxiliary units to form clusters, 1D chains, or 2D layers, which function as chiral SBU to generate well-defined networks through proper selection rigid achiral linkers (Fig. 6). Recently, Kim and Fedin have described the synthesis of homochiral framework with permanent porosity by using chiral linear chain as SBU [56]. Homochiral L-lactic acid has been used to form a chiral 1D chain with zinc ion, which is in turn interconnected through 1,4-benzenedicarboxylic acid (H_2bdc) to afford a chiral 3D open-framework [Zn_2(bdc)(L-lac)(dmf)]·(DMF), (**6**·DMF) (Fig. 7). The medium-sized pores (~5 Å) thus formed are essentially chiral by the presence of L-lactate moieties. In a very similar approach, Rosseinsky used chiral 2D layers of Ni-(enantiopure-aspartate) as SBUs, to generate porous 3D homochiral frameworks by pillaring with appropriate neutral achiral bridging linkers [57].

So far, we have discussed several general strategies for constructing homochiral porous frameworks. However, additional requirements are necessary for them to be

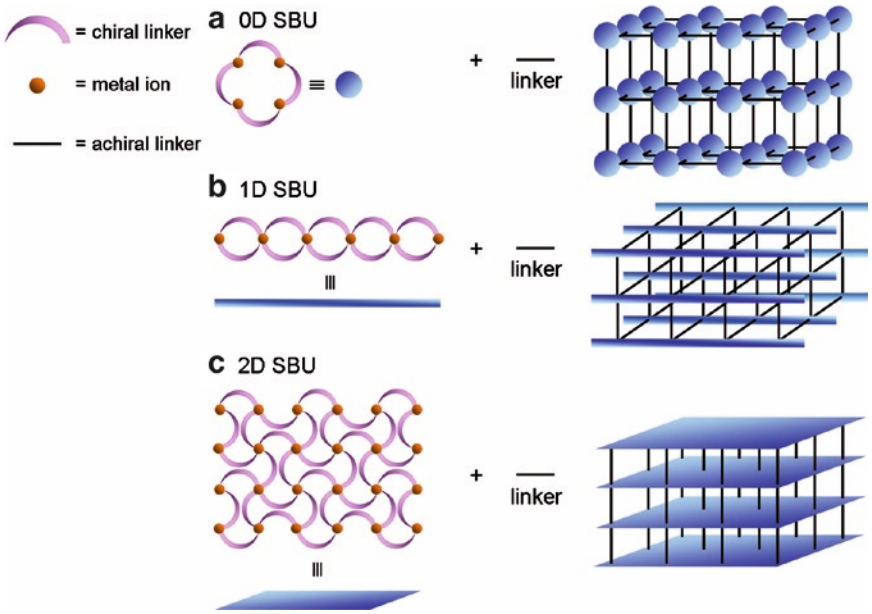

Fig. 6 A synthetic approach toward homochiral metal-organic frameworks through linking chiral secondary building blocks by achiral ligands

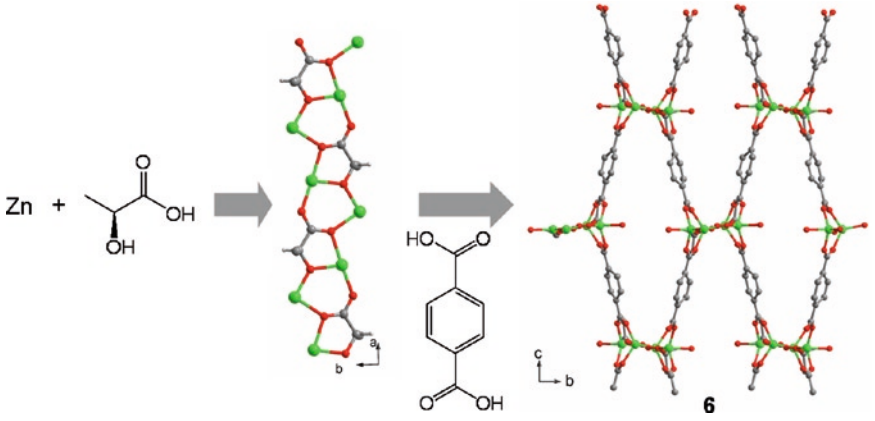

Fig. 7 The formation of 1D chain SBU by zinc ion and L-lactate and the construction of 3D network structure by achiral bridging ligand (viewed along *b* axis)

useful in enantioselective catalysis, including the presence of catalytic centers in the chiral pores.

The simplest system that behaves as a functional material in catalytic processes can be designed with a coordinatively unsaturated metal centers linked to a chiral

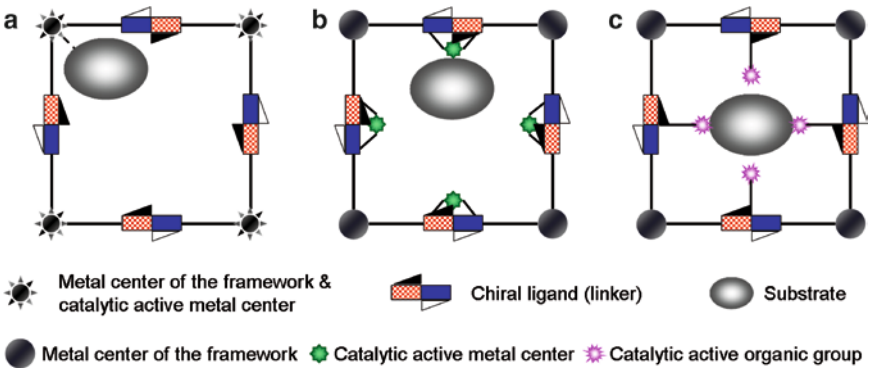

Fig. 8 Schematic representation of the synthetic approaches to possible chiral frameworks for catalysis and separation

ligand to construct a porous metal-organic assembly (Fig. 8a). Here, the metal centers in the homochiral metal-organic assembly should play a dual role as both the structural forming and the catalytically active centers, and the metal center should have an open coordination site or a readily removable ligand. In most cases however, the metal coordination sites are either fully occupied or sterically crowded, which leads to little or no catalytic activity. To avoid such difficulties, one may design a metal-organic assembly with one metal forming the framework, and another catalytically active metal open towards the pore (Fig. 8b).

Pendant organic subunits may also perform catalytic reactions (Fig. 8c) [41,58]. For example, a free basic functional group such as amine can perform a base catalyzed reaction inside the pore. However, for the asymmetric catalysis, the organic catalytic unit should itself be chiral or positioned near a chiral center in the pore.

2.2 Chiral MOPMs Through Postmodification

Unlike previous strategies, the postmodification approach does not require preparation of specific, intricate building blocks for the generation of a targeted functional MOPM. Indeed, MOPMs can be readily modified by subsequent reaction with a variety of organic molecules without changing the framework structure. Kim et al. [41] first successfully demonstrated the postsynthetic covalent modification of MOPMs by *N*-alkylation of the free pyridyl groups present in the cavities of POST-1 without altering the original 3D framework. In recent studies, Cohen and coworkers incorporated various organic subunits to the pendant amino group by postsynthetic covalent modification in IRMOF-3, which is otherwise impossible to introduce inside the framework [59,60]. More recently, Chang and Férey reported the incorporation of primary amine at the coordinatively unsaturated metal center by post-modification, which showed a catalytic activity in Knoevenagel condensation [61].

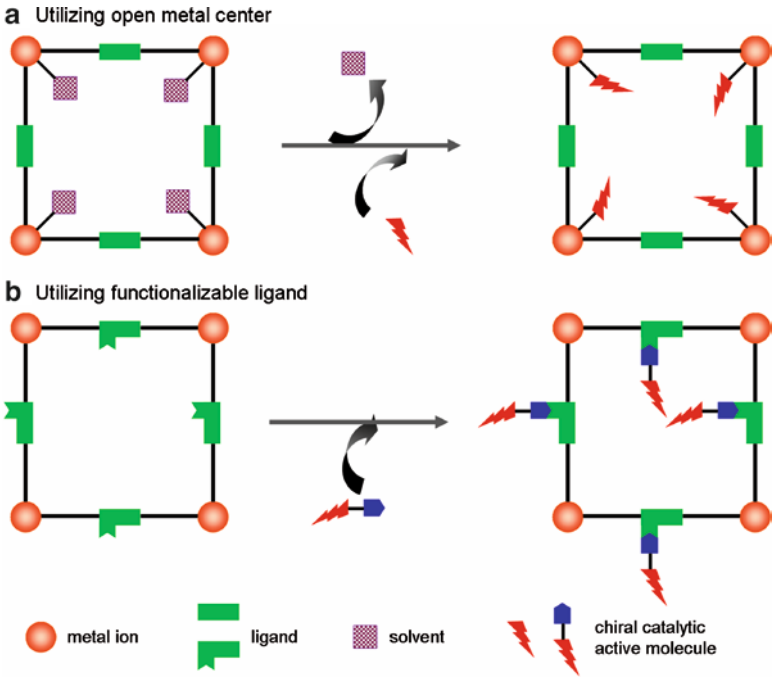

Fig. 9 Schematic representation of the postmodification concepts

Conceptually, a similar strategy may be applied to introduce chiral auxiliary ligands with well-defined binding and catalytic centers to MOPMs that have pendant reactive centers or open metal coordination sites (Fig. 9). Though no CMOPM has been synthesized by this strategy until now, it certainly appears to be quite a feasible and promising strategy.

In Sect. 3, we describe the applications of recently developed, important CMOPMs in chiral separation and heterogeneous asymmetric catalysis with brief structural descriptions.

3 Applications of CMOPMs in Chiral Separation and Catalysis

3.1 Background

For the last few decades, the use of optically pure compounds has significantly increased for economic, environmental, and social reasons. Particularly, pharmaceutical industries desire to produce the active isomer of chiral drugs in optically

pure form to avoid side effects. Among the various methods available to produce selectively single enantiomers, homogeneous chiral catalysis is effective in terms of efficiency and enantioselectivity. However, despite the huge efforts devoted to this field, only few processes (including hydrogenation, epoxidation and reduction) have been applied on an industrial scale [62,63]. One of the main reasons for this unexpected consequence is the difficulty associated with recovery and reuse of highly expensive chiral catalysts. One way to overcome this difficulty is the heterogenization of asymmetric catalysts, which allows facile recovery and reuse of the catalysts [64]. Conventional heterogeneous catalysts are prepared by immobilization of chiral catalysts onto a solid support by covalent bonding or other physical interactions. Mesoporous silica is one of the best choices as solid support for immobilization due to the presence of large well-defined pores with silanol functionality. Organic polymers, ion exchange resins, modified zeolites, and some other materials are also used for immobilization of homogeneous catalysts. This subject has produced several hundred publications and numerous reviews [65–67] to date. In a different immobilization approach, self-supported nonporous coordination polymers with ill-defined structures, but useful for enantioselective catalysis have been prepared by reactions between multitopic chiral ligands and metal ions [68].

All conventional immobilization techniques in chirotechnology suffer from some severe shortcomings. For example, most conventional immobilization methods result in the chiral ligands or catalytically active units randomly anchored onto the solid supports, which often make some of the catalytic sites inaccessible to the substrates. Consequently, the immobilized catalysts display reduced enantioselectivity and lower efficiency in catalysis in comparison with their homogeneous counterparts. As a typical example, the immobilized salen-Mn system of Pini et al. shows only up to 58% ee in epoxydation, which is much lower than that for Jacobsen–Katsuki salen complexes [66,69]. Another major problem is that the bonds between metals and ligands, even if covalent, are often broken under the harsh catalytic reaction conditions and the catalyst breaks away from the solid support and dissolves. This “leaching” process inevitably leads to loss of activity of the catalyst when it is recovered and recycled. Therefore, developing new strategies for the synthesis of more robust metal-ligand conjugates that can sustain harsh conditions is highly desirable.

Chiral separation or sorption is another important technique in chirotechnology. In fact, due to the high cost of chiral catalysts, industries generally prefer chiral separation over asymmetric catalysis to obtain optically pure compounds. As in asymmetric heterogeneous catalysis, a chiral selector (a chiral molecule in optically pure form) can be immobilized on a solid support to make a chiral stationary phase (CSP) of use in direct chiral separation. The basic principle of chiral separation is that the chiral selector interacts differently with the enantiomers of a racemic or enantioenriched mixture to form transient diastereoisomeric species of different stability, and this fine distinction leads to the separation of enantiomers during elution. This topic has also produced a huge number of papers and the readers are referred to the previous reviews for more knowledge on this field [70–73].

3.1.1 Advantages of CMOPMs over Conventional Immobilized Catalysts

In principle, homochiral MOPMs have several advantages over conventional immobilized catalysts: (a) well-ordered structure; (b) high degree of porosity; (c) high density of active catalyst centers; (d) no additional support required. These materials are insoluble in common solvents to fulfill the main prerequisite of a heterogeneous catalyst. Moreover, metals and ligands are strongly bound within the framework to protect "leaching" of the catalyst to the solution and at the same time ensure reusability.

A well-organized chiral pore, large enough for a particular guest molecule to access can induce sufficient enantioselection. The chiral bridging ligands of CMOPMs can provide a chiral environment inside the well-organized cavities/pores, which in principle functions as a chiral selector; therefore, they can be considered to possess a built-in chiral selector. Thus in an ideal situation, CMOPMs also have all the qualities to be efficient CSPs for chiral separation processes.

3.2 Homochiral MOPMs for Enantioselective Separation

Kim and coworkers demonstrated, for the first time, chiral separation in a well-defined microporous cavity utilizing the pores of POST-1 (**4**) (synthesis in Sect. 2.1.2.1) [41]. In POST-1, the carboxylate group of L_5 binds to zinc ions to form an oxo-bridged trinuclear zinc cluster (SBU), which is in turn interconnected via the pyridyl group of L_5 to generate 2D infinite layers consisting of large edge-sharing chair-shaped hexagons with the trinuclear SBU unit at each corner. The chiral 1D channels along the *c* axis have an equilateral triangle-shaped cross section with a side length of ~13.4 Å (Fig. 10). Interestingly, half of six pyridyl groups present in each trinuclear

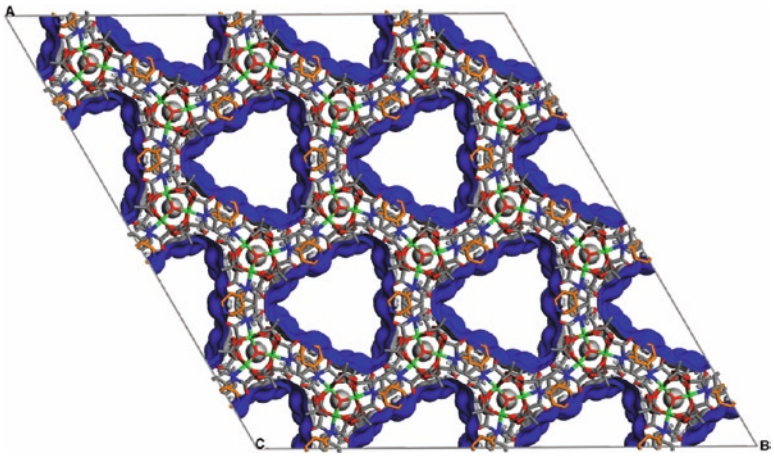

Fig. 10 The Connolly surface of POST-1 showing large chiral channels along the *c* axis. Zn ions (*green*), oxo moieties (*red*) and the pyridyl groups (*orange*) exposed in the channels

unit ($[Zn_3(\mu^3\text{-}O)(L_4\text{–}H)_6]^{2-}$) are coordinated to the zinc ions of three neighboring trinuclear units and the remaining half extrude into the channel without any interactions with the framework, two of which remain protonated.

The presence of large accessible chiral channels in POST-1 (~47%) creates unique opportunity for enantioselective inclusion of chiral molecules. In particular, the large chiral channels of POST-1 were exploited in the separation of racemic $[Ru(bpy)_3]Cl_2$. When L-POST-1 was suspended in a methanolic solution of racemic $[Ru(bpy)_3]Cl_2$, 80% of the exchangeable protons from the dangling pyridine groups were enantioselectively exchanged by $[Ru(bpy)_3]^{2+}$ with 66% enantiomeric excess in favor of the *Δ*-form, which is supported by NMR, UV and CD spectroscopy.

Subsequently, several research groups including Lin, Rosseinsky, Xiong, Fedin and others have designed and synthesized several homochiral porous metal-organic materials capable of enantioselective sorption of chiral organic molecules, which are listed in Table 1.

Xiong and coworkers used an off-the-shelf antimalarial alkaloid, quinine derived enantiopure building block, HQA (6-methoxyl-(8*S*,9*R*)-cinchonan-9-ol-3-carboxylic acid, L_7), to synthesize a homochiral MOPM, $[Cd(QA)_2]$ (**7**, Scheme 1) with an open channel 3D structure, which crystallizes in a distorted octahedral geometry with two

Table 1 List of CMOPMs used for chiral separation

Entry	CMOPMs	Type of Substrate (racemic)	Max. ee (%) achieved	Ref. no.
1	POST-1(**4**)	$[Ru(bpy)_3]Cl_2$	66	[41]
2	$[Cd(QA)_2]$ (**7**)	Small alcohols	98.2	[74]
3	$[Cu_5Cl_6(VB\text{-}N\text{-}ClN)_2]$ (**8**)	2-Butanol	25	[75]
4	$[Cu(PPh_3)(N,N'\text{-}(2\text{-pyridyl-}(4\text{-pyridyl methyl})\text{-amine}))_{1.5}][ClO_4]$ (**9**)	2-Butanol	100	[76]
5	$[Ni_3(btc)_2(3\text{-pic})_6(1,2\text{-pd})_3]$ (**10′**)	Binaphthol	8.3	[77]
6	$[Ni_2(L\text{-asp})_2(bipy)]\cdot CH_3OH\cdot H_2O$ (**11**)	Different diols	53.77	[57]
7	$[Zn_2(bdc)(L\text{-lac})(dmf)]$ (**6**)	Various sulfoxides	60	[56]
8	$[Sm(L_{17e}\text{-}H_2)(L_{17e}\text{-}H_3)(H_2O)_4]\cdot 12H_2O$ (**17e**)	*trans*-1,2-diamino-cyclohexane	13.6	[82]

Ligands: HQA = 6-methoxyl-(8*S*,9*R*)-cinchonan-9-ol-3-carboxylic acid; VB-N-ClN = 4-Vinylbenzyl-cinchonidinium chloride; $L_{17e}\text{–}H_4$ = 2,2′-diethoxy-1,1′-binaphthalene-6,6′-bisphosphonic acid

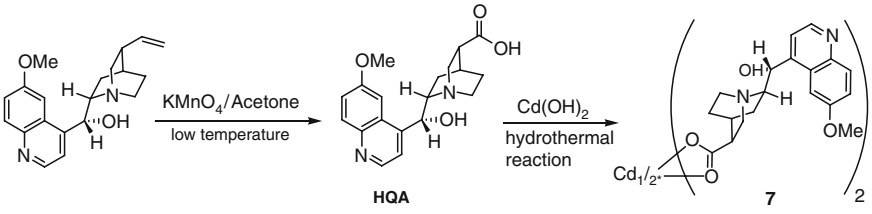

Scheme 1 Synthesis of quitenine (HQA) and the cadmium complex **7**

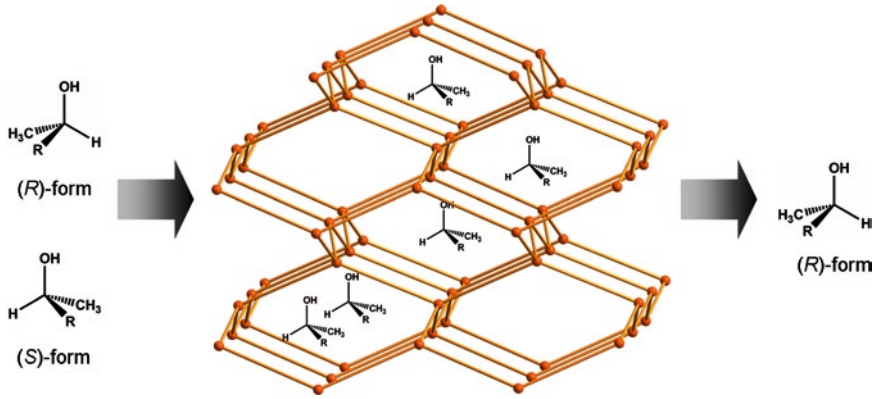

Fig. 11 The diamond-like 3D network of **7**; selective sorption in favor of *S*-alcohol

distinct QA^- ligands bridging the Cd^{2+} ion in different binding modes [74]. From a topological point of view, each Cd^{2+} ion connects with others in a diamond-like fashion, with slight distortion, to form the 3D network (Fig. 11). TGA analysis indicates the robustness of the framework. The adamantane-type cavity within the structure can enantioselectively absorb small organic molecules, such as 2-butanol or 2-methyl-1-butanol. When racemic 2-butanol was mixed with a powdered sample of $[Cd(QA)_2]$ (**7**) under solvothermal conditions, a crystalline sample of (*S*)-2-butanol-$[Cd(QA)_2]$ (**7a**) was obtained. Optical rotation of the desorbed 2-butanol from **7a** matched the standard value of pure (*S*)-2-butanol; the ee value was estimated to be approximately 98.2%. TGA of **7a** shows 8.3% weight loss at 160–204°C corresponding to complete removal of (*S*)-2-butanol, which supports the ability of **7** to include a molecular guest reversibly without changing the framework structure. Relatively larger organic guest, racemic 2-methyl-1-butanol, also gets absorbed in $[Cd(QA)_2]$ (**7b**), but only with 8.4% selectivity in favor of *S*-isomer. Although the homochiral MOPM with a widely used chiral selector in the cavity showed the ability of reversible inclusion of small organic guest molecules, the enantioselectivity drastically decreased with increasing size of the guests. The same group synthesized another 2D homochiral Cu–olefin MOPM (**8**) from a quinine derived ligand, L_8, but its enantioselective sorption ability was rather poor (Table 1) [75].

Xiong et al. also demonstrated that the chiral 2D framework $[Cu(PPh_3)(N,N'$-(2-pyridyl-(4-pyridyl methyl)-amine))$_{1.5}]\cdot ClO_4$ (**9**), with triangular cavities, synthesized from achiral components, $[Cu(MeCN)_2(PPh_3)_2][ClO_4]$ and *N*,*N*′-(2-pyridyl-(4-pyridyl methyl)-amine) can enantioselectively include 2-butanol [76]. Spontaneous resolution produced crystalline inclusion compound **9**·1.5(2-butanol), which was structurally characterized. They manually separated the enantiomorphic forms of **9**·1.5(2-butanol) according to their CD spectra in solid state and evacuated at 100°C to collect enantiopure 2-butanol. Although this work provides an economical route to enantioselective separation of racemic small diols, the separation

process is rather time consuming. The route is also not general, as the framework does not guarantee inclusion of other kind of molecules.

The (10,3)-a net based chiral frameworks developed by Rossenesky et al., showed enantioselective sorption properties [77]. The doubly interpenetrating, distorted (10,3)-a framework, **1**, showed a tendency to collapse upon removal of the guests from its cavity and the resulting nonporous amorphous phase (**1′**) adopted a new 6,3-layered structure upon reexposure to pyridine. Interestingly, the desolvated amorphous phase **1′** can regenerate its original 2 X (10,3)-a network structure upon exposure to 3-picoline, which is found to be stable even after the loss of guest molecules. They separately synthesized the 3-picoline ligated framework, **10**, having a molecular formula $[Ni_3(btc)_2(3\text{-pic})_6(1,2\text{-pd})_3]\cdot 9(1,2\text{-pd})_9\cdot 11(H_2O)$ from enantiopure 1,2-pd. In contrast to **1**, after guest removal at 150°C, **10** retains crystallinity with identical space group symmetry and slightly modified unit cell parameters. Despite the same framework structure, their striking difference in stability is due to unconventional H-bonding between the methyl C–H of the picoline moiety and the noncoordinating oxygen of the btc carboxylate (Fig. 12a).

The estimated 47% void for the desolvated phase **10′** is in good agreement with the Dubinin-Radushkevich micropore volume (0.63(1) mL g^{-1}). In **10′**, two large pores with different diameters (12 Å and 13.6 Å) are available for guest sorption (Fig. 12b). However, the apparent advantage of a larger window goes against enantioselective sorption of small chiral molecules. Although relatively large binaphthol (9 × 9 Å) is enantioselectively sorbed by (*S*)-**10′** (but with only 8.3% ee), smaller guests such as ethyl 3-hydroxybutyrate and fenchone show ready sorption but no enantioselectivity. Thus, a close match of the dimensions of chiral channels and the size of the chiral guests is required for the microporous substances like **10′** to discriminate between the enantiomers. This work requires further investigation of the binding behavior of guest molecules with the chiral pockets of hosts to rationally design and synthesize materials with high enantioselective sorption ability.

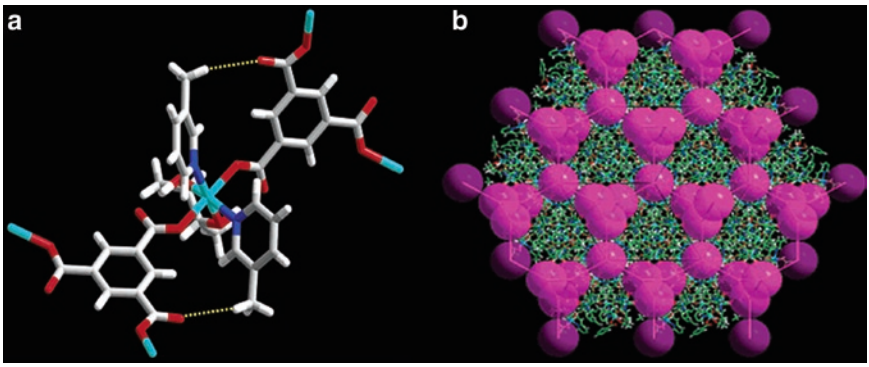

Fig. 12 (**a**) C–H···O interaction (*yellow dotted line*) between the methyl group of the 3-picoline and the nonbonding carboxylate oxygen atom (*red*) of the btc framework forming node in **10**; Ni centers (*light blue*). (**b**) the cavities and interconnecting channels (*purple*) that constitute the chiral porosity of the material. In panels (**c**) and (**d**), the structure is viewed along the 111 direction

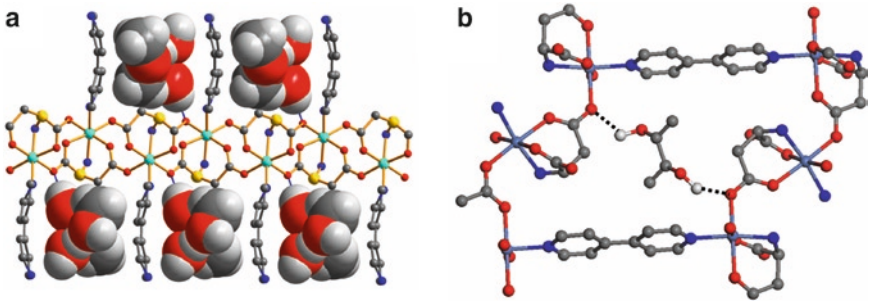

Fig. 13 (**a**) 2D layers of framework **11**; the disordered methanol and water guests that occupy the channels are represented with space filling spheres. (**b**) Location of 1,2-propanediol within the channels of **11**; methyl group is omitted for clarity. Hydrogen bonds are represented by *dashed blue lines*. Ni *cyan*, C *gray*, H *white*, N *blue*, O *red*

Natural amino acids have also been utilized as building blocks to prepare homochiral MOPMs with enantioselective sorption ability [57]. Solvothermal reaction of Ni(L-asp)·3H_2O and 4,4′-bipyridine (bipy) in a water/methanol mixture at 150°C affords the homochiral open-framework material [Ni_2(L-asp)$_2$(bipy)]·CH_3OH·H_2O (**11**). In the crystal structure, an aspartate molecule binds to one nickel center in a tridentate fac mode and two other Ni centers in a monodentate mode to form chiral neutral Ni(L-asp) layers (Fig. 13a). These Ni(L-asp) layers are bridged by bipy ligands to form a pillared structure with 1D channels with a small cross section of 3.8×4.7 Å. The framework is robust and permanently porous as revealed by PXRD and CO_2 measurements, and the estimated guest-accessible volume of the framework is 23.1%. The enantioselective sorption property of **11** examined with different positional isomers of diols starting from propanediol to hexanediol shows ee values up to 53.7%. The host derived from D-aspartate also shows the same degree of enantioenrichment but for the opposite enantiomer in all cases. Several diols of a fixed chain length reveal a large difference in enantioselection. For example, the four carbon chain diols, 1,2-butanediol and 2,3-butanediol show considerably reduced enantioselection (5.0 and 1.5% ee, respectively) with respect to 1,3-butanediol (17.9% ee). The 1,3-disposition of diols seems to be favorable and the highest value of ee was observed for 2-methyl-2,4-pentanediol (53.7%). Although the crystals of the host–guest complexes of **11** could not be grown, the interactions of the diol guests with the internal surface of the porous material can be visualized from their model compound [Ni_2(L,D-asp)$_2$(bipy)]·CH_2(OH)CH(OH)CH_3 (**12**). The crystal structure of **12** showed that the guest located in the pocket while bridging two Ni(asp) layers through hydrogen bonding (Fig. 13b). The docking procedure also proved that the interaction of **13** with the two guest molecules of same alkyl-chain lengths, 1,2-pentanediol and 2-methyl-2,4-pentanediol, sit in exactly identical sorption sites in the pocket (defined by two aspartate and two bipy molecules on opposite sides of the channel), but interact differently with the framework. Both alcoholic groups of (*S*)-2-methyl-2,4-pentanediol participate in hydrogen bonding

with the framework **11** and consequently account for its high ee value. While the tertiary alcohol group forms hydrogen bond with the β-carboxylate group of an aspartate residue (OH···O 2.390 Å), the secondary alcohol group forms an H-bond with the amine group of another aspartate residue (O···HN 2.663 Å). In contrast, only the secondary alcohol group of (*S*)-1,2-pentanediol interacts with the framework of **11** by hydrogen bonding with the β-carboxylate group of an aspartate residue (OH···O 2.667 Å) and the amine group of another aspartate residue (O···HN 2.507 Å). These different modes of interaction account for the observed differences in enantioselection. This descriptive study demonstrates that the surface chemistry of channels is an important factor in addition to their size for an improved enantiosorption of guests by chiral MOPMs.

Permanently porous, homochiral framework, $[Zn_2(bdc)(L\text{-lac})(dmf)]\cdot(DMF)$ (**6**·DMF), was utilized in enantioselective sorption of pharmaceutically important sulfoxides [56]. The material **6** forms medium-sized pores (~5 Å) by the attachment of bdc with 1D chain like chiral SBU containing L-lactates and zinc ions (Fig. 14), which has been exploited in enantiosorption of sulfoxides as well as the enantioselective oxidation of thioethers (see below). The DMF molecules in the pores can be removed by heating at 110–200°C; however, prolonged heating causes partial

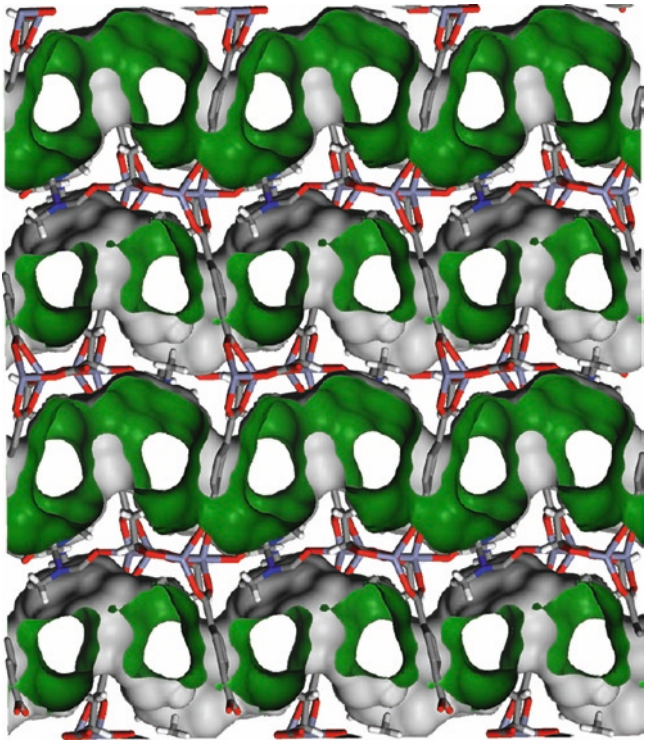

Fig. 14 The Connolly surface of framework **6** showing medium-sized pores (~5 Å) and 1D channels

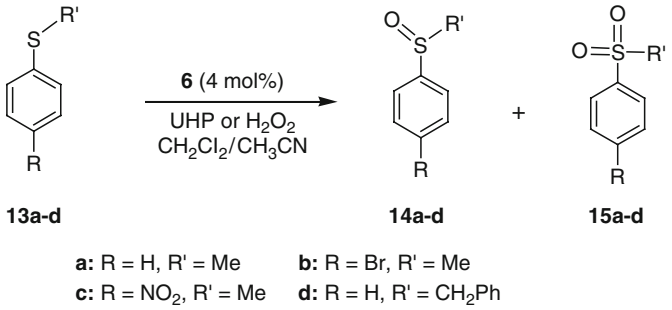

Scheme 2 Oxidation of sulfides catalyzed by **6**

collapse of the framework. The partially evacuated material **6**·$(DMF)_{0.4}$ showed significant sorption ability for the aromatic sulfoxides with small substituents such as **14a** and **14b**: 0.68 and 0.18 molecules, respectively, per formula unit of **6** with moderate ee values (20% for **14a** and 27% for 14b) in favor of *S*-isomer. However, pores of **6** were unable to incorporate larger sulfoxides such as **14c** and **14d**. More interestingly, after extraction of the absorbed molecule, the material **6** can be reused in the next cycle with no appreciable change in its sorption ability.

The material **6** showed a remarkable catalytic activity in the oxidation of thioethers **13** to sulfoxides **14** by urea hydroperoxide (UHP) or H_2O_2 (Scheme 2). Although the conversion and selectivity (for **14** over **15**, >90%) was reasonable with UHP for the substrates with smaller substituents, **13a** and **13b**, the ones with bulkier substrates **13c** and **13d** failed to produce any measurable conversion. The conversion increases to 100% by changing UHP with H_2O_2. The catalytic activity of **6** for selective sulfoxidation remains similar even after 30 cycles. Despite the fact that no asymmetric induction was found in the catalytic sulfoxidations, enantioenriched sulfoxides were obtained by enantioselective sorption of the resulting racemic mixture by the chiral pores of **6**, which occured simultaneously with the catalytic process. Thus, after catalytic oxidation of **13a**, (*S*)-**14a** was preferentially absorbed by the pore of **6** leaving exactly equal amount of the excess *R*-enantiomer in the solution phase (~20% ee). The combination of high catalytic activity and enantioselective sorption property of **6** provides a unique opportunity to device a one-step process to produce enantioenriched products.

Fedin and Bryliakov extended this work to demonstrate the use of **6**·DMF as a CSP for the separation of a racemic mixture of **14a** [78]. The wide difference in the sorption ability between the *S*- and *R*-enantiomers instigates the plan to use **6** as a CSP for liquid column chromatography. Interestingly, both electronic and steric effects of the substituents in the aromatic ring play an important role in determining sorption constant and ee of sorption values. An electron withdrawing substituent at the aromatic ring reduces both sorption constant and ee of sorption by reducing coordination ability of the sorbate (Table 2, entry 1 and 4). Although an electron donating substituent increases the sorption constant value, additional substituent in the aromatic ring results in slower internal diffusion leading to poorer enantioselection (Table 2, entry 3). However,

Table 2 The apparent sorption constants of enantiomerically pure sulfoxides on 6

Entry	Sulfoxide	K_S[a] M^{-1}	K_R[a] M^{-1}	α[b]	ee %[c] (sorption)
1	*p*-BrPhSOMe	11	10	1.1	7 (0.15)
2	PhSOMe	68	15	4.5	60 (0.30)
3	*p*-MePhSOMe	326	129	2.5	38 (0.53)
4	*p*-NO_2PhSOMe	n.m.	n.m.	–	~0 (0.13)
5	PhSOi-Pr	54	12	4.5	55 (0.20)

[a] K_S = sorption constant for *S*-isomer, K_R = sorption constant for *R*-isomer
[b] Stereoselectivity factor, $\alpha = K_S/K_R$
[c] The highest measured ee of the sorbate, and the respective sorption values, in the molecules per formula unit [Zn_2(bdc)(L-lac)(dmf)]

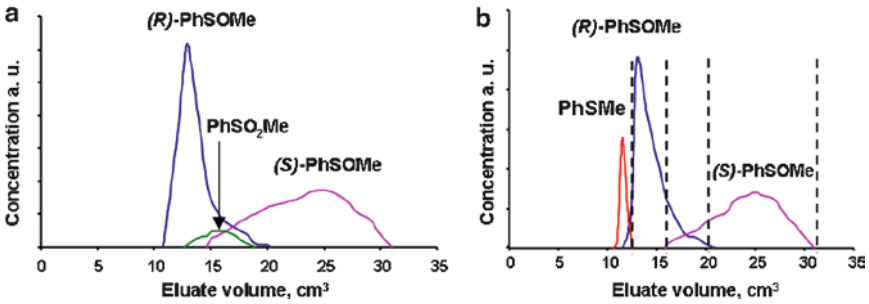

Fig. 15 Catalytic oxidation of PhSMe/enantiomeric separation of PhSOMe over a column with **6**·DMF, using 5-fold (**a**) and 1.5-fold (**b**) excess of the oxidant. Elution rate: 2 $cm^3 h^{-1}$; eluent CH_2Cl_2/CH_3CN:: 85:15

steric crowding at the sulfur atom does not alter the selectivity factor (entry 5), whereas, methyl phenyl sulfoxide (entry 2) with an unsubstituted aromatic ring fits best in the pores of **6**, thus giving best separation of enantiomers.

By taking advantage of both catalytic activity and enantioselective sorption ability of **6** discussed above, a one-step reaction-purification system was developed to synthesize optically pure sulfoxides. In an illustrative example, PhSMe was chosen as a substrate. A mixture of the sulfide and H_2O_2 in 0.01 M of DMF in CH_2Cl_2/CH_3CN was loaded on top of the column packed with **6** and eluted with the same solvent mixture. The *R*-isomer of the corresponding sulfoxide was eluted first as it has low affinity with **6**, followed by *S*-isomer (Fig. 15). Excess amount of H_2O_2 (5-fold) forms about 5% of sulfone (the over-oxidation product), but a little excess (1.5-fold) of the oxidant, even though left out some disulfide in the mixture (conversion = 91%), affords pure enantiomers ca. 35% each based on the starting PhSMe to offer a overall isolated yield of 70% (Fig. 15b). This was the first demonstration of an application of CMOPMs in chiral chromatography. Furthermore, the tandem

procedure to produce optically pure product is attractive in terms of production cost and time consumption, and tempts further studies in this direction.

There are a couple of reports from Pal and coworkers on chiral MOFs capable of enantiospecific inclusion of chiral rotamers [79,80]. Although this type of work is worthwhile from a theoretical point of view, in practical sense the desorbed rotamer will racemize immediately through rotation around the C–C bond, making isolation of optically pure rotamers impossible.

Certainly, a couple of important points can be made from the entire collection of work on chiral separation by CMOPMs: (a) the size of the pore should fit the substrate for proper enantiodifferenciating interactions; (b) different mode of interactions of similar kind of substrates with the surface of the pores/channels alters enantioselection ability. So far, the chiral separation ability of chiral metal-organic assemblies has been studied mostly with small molecules. However, the main goal of designing these materials is to utilize them for the separation of the enantiomers of relatively large molecules (e.g., drugs) and further studies are required in this direction.

3.3 Homochiral MOPMs as Heterogeneous Catalysts

Proper incorporation of suitable catalytic units into CMOPMs with accessible pores for organic substrates can generate potentially useful solid matrices for asymmetric transformations. Fujita et al. first explored the utility of a hybrid organic–inorganic solid as a heterogeneous Lewis acid catalyst [40]. Later, Aoyama and coworkers also demonstrated the catalytic properties of MOPMs for Diels–Alder reactions [81]. In both the cases, however, achiral metal-organic assemblies were used. Despite the huge potential, the use of homochiral metal-organic assemblies for the applications in asymmetric catalysis was not reported until 2000 when Kim and coworkers reported the first asymmetric induction catalyzed by a homochiral MOPM [41]. After this, a number of chiral MOPMs have been synthesized and their heterogeneous, enantioselective catalytic activities studied (Table 3).

The key structural feature of POST-1 - the presence of dangling pyridine groups in the channels - affords a unique opportunity to perform asymmetric heterogeneous catalysis. Thus, potentially, any base catalyzed reactions (e.g., esterification or hydrolysis) can be performed with POST-1. Moreover, chiral pores should induce a degree of enantioselectivity in the final product mixture. The catalytic activity of POST-1 in the transesterification reaction was examined. Although the reaction of **16** and ethanol in the presence of POST-1 in carbon tetrachloride produced ethyl acetate in 77% yield, little or no transesterification occured without POST-1 or with the *N*-methylated POST-1 (Sect. 2.2). The post chemical modification of the pyridine groups in POST-1 proves the role of free pyridine moiety in transesterification reaction. Transesterification of ester **16** with bulkier alcohols such as isobutanol, neopentanol, and 3,3,3-triphenyl-1-propanol occurs at a much slower rate under otherwise identical reaction conditions. Such size selectivity suggests that catalysis mainly occurs in the channels.

Table 3 List of CMOPMs used in heterogeneous asymmetric catalysis

Entry	CMOPMs	Type of reaction[a]	Catalyst loading (mol %)	Yield (%)	ee (%)	Reference number
1	POST-1 (**4**)	Transesterification	10	77	~8	[41]
2	$[Sm(L_{17e}–H_2)(L_{17e}–H_3)(H_2O)_4]\cdot 12H_2O$ (**17e**)	Cyanohdrine formation	10	55–69	<5	[82]
		Ring opening of *meso*-anhydride	10	81	<5	
3	$Zr[Ru(L_{18}$ or $L_{19})(dmf)_2Cl_2]\cdot 2MeOH$ (**18**, **19**)	Hydrogenation of β-keto esters	0.1–1	70–100	65–95	[83]
4	$Zr[Ru(L_{19}–H_4)(DPEN)Cl_2]\cdot 4H_2O$ (**20**) and sameskeleton with L_{18} (**21**)	Hydrogenation of aromatic ketones	0.005–0.1	>99	80–99	[84]
5	$ZrL_{22–24}$ (**22–24**) (active catalyst = (**22–24**)·Ti)	Diethylzinc additions to aromatic aldehydes	20–50	70–99	30–72	[85]
6	$[Cd_3Cl_6(L_{25})_3]\cdot 4DMF\cdot 6MeOH\cdot 3H_2O$ (**25**) (active catalyst = **25**·Ti)	Diethylzinc additions to aromatic aldehydes	13	>99	80–93	[86]
7	$[Cd_3(L_{25})_4(NO_3)_6]\cdot 7MeOH\cdot 5H_2O$, (**26**)(active catalyst = **26**·Ti)	Diethylzinc additions to aromatic aldehydes	12–25	>99	45–90	[87]
8	$[Zn_2(bpdc)_2L_{28}]\cdot 10DMF\cdot 8H_2O$ (**28**)	Epoxidation	0.025	71	82	[54]
9	$[Cu_2(L_{29})_2(H_2O)_2]\cdot MeOH\cdot 2H_2O$ (**29**)	Ring opening of epoxide	5	1–54	0–51	[88]
10	$[Zn_2(bdc)(L\text{-}lac)(dmf)]$ (**6**)	Oxidation of sulfoxides	2	60–100	0[b]	[56]
11	$[Cu_2(D\text{-}/L\text{-}asp)_2bpe]\cdot$(guests)	Methanolysis of *trans*-2,3-epoxybutane	10	30–65[c]	3–17[c]	[89]

[a] Each CMOPM is used as asymmetric catalyst for one (or more) type of reaction on a series of substrates; the range of catalyst loading, yields and ee values are given in the subsequent columns

[b] Although no asymmetric induction was observed, the products enantioselectively absorbed inside the pores with ee ranging from 20 to 27% depending on substrates leaving equal amount of other enantiomer in the solution

[c] Depending on reaction condition both yield and ee vary for a single substrate

Ligands: $L_{17}–H_4$ = 2,2′-diethoxy-1,1′-binaphthalene-6,6′-bisphosphonic acid; $L_{18}–H_4$ = 2,2′-bis(diphenylphosphino)-1,1′-binaphthyl-6,6′-bis(phosphonic acid); $L_{19}–H_4$ = 2,2′-bis(diphenylphosphino)-1,1′-binaphthyl-4,4′-bis(phosphonic acid); $L_{22}–H_4$ = 2,2′-dihydroxy-1,1′-binaphthyl-6,6′-bis(phosphonic acid); $L_{23}–H_4$ = 2,2′-dihydroxy-1,1′-binaphthyl-6,6′-bis(vinylphos-phonic acid); $L_{24}–H_4$ = 2,2′-dihydroxy-1,1′-binaphthyl-6,6′-bis(styrylphosphonic acid); L_{25} = (*R*)-6,6′-dichloro-2,2′-dihydroxy-1,1′-binaphthyl-4,4′-bipyridine; L_{28} = (salen)$Mn^{III}Cl$ (salen = [(*R*,*R*)-(–)-1,2-cyclohexanediamino-*N*,*N*′-bis(3-*tert*-butyl-5-(4-pyridyl)-salicylidene)]); H_2bpdc = biphenyldicarboxylic acid; L_{29} (H_2BDA) = (*R*)-5,5′-(2,20-dihydroxy-1,10-binaphthalene-5,5′-dicarboxylic acid; bpe = 1,2-bis(4-pyridyl)ethylene

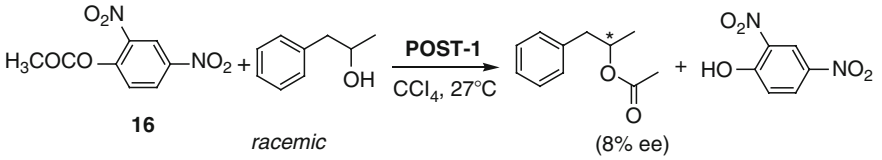

Scheme 3 Catalytic activity of POST-1 in transesterification

Most interestingly, POST-1 showed enantioselective catalytic activity for transesterification of **16**. The reaction of **16** with a large excess of *rac*-1-phenyl-2-propanol in the presence of D-POST-1 or the enantiomorphic L-POST-1 produces corresponding esters with ~8% enantiomeric excess in favor of *S*- or *R*-enantiomer, respectively (Scheme 3). The low enantioselectivity may be the consequence of the fact that the catalytically active units (dangling pyridyl groups) are a bit too far away from the chiral wall of the pores. Even though the ee value is modest, this is the first observation of an asymmetric induction in the catalytic reactions mediated by modular porous materials. This seminal work triggered interest among others to rationally design chiral ligands and synthesize corresponding homochiral metal-organic systems for various heterogeneous catalysis reactions. Later, Gao et al. further explored the utility of POST-1 in supramolecular photochirogenesis [82].

Lin and coworkers adopted a systematic approach toward designing homochiral MOPMs using BINAP units as a building block for chiral separation and asymmetric heterogeneous catalysis [83–88]. They first prepared a series of homochiral porous lamellar lanthanide bisphosphonates of general formula $[Ln(L_{17}–H_2)(L_{17}–H_3)(H_2O)_4]\cdot xH_2O$ ($L_{17}–H_4$ = 2,2′-diethoxy-1,1′-binaphth-alene-6,6′-bisphosphonic acid, Ln = La, Ce, Pr, Nd, Sm, Gd, Tb, x = 9–14, **17a–g**) (Scheme 4) and explored their applications in heterogeneous catalysis and chiral separations [83]. The CMOPMs adopt 2D layered structures with square antiprismatic Ln center that have four H_2O molecules and four oxygen atoms of the phosphonate groups of four different binaphthylbisphosphonates in the coordination sphere (Fig. 16). The space filling model suggested that **17a–g** contain large chiral channels with largest dimension of 12 Å. PXRD pattern of desolvated **17a–g** which

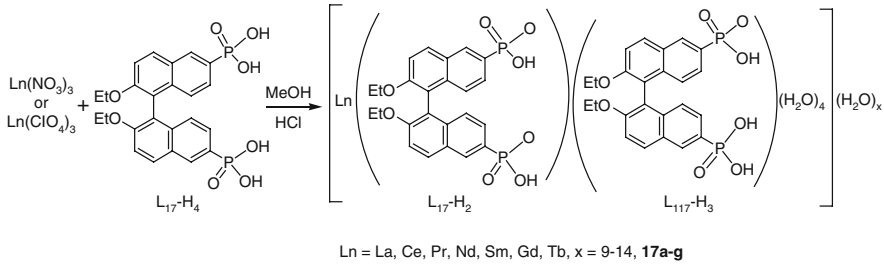

Scheme 4 Preparation of $[Ln(L_{17}–H_2)(L_{17}–H_3)(H_2O)_4]\cdot 12H_2O$ compounds

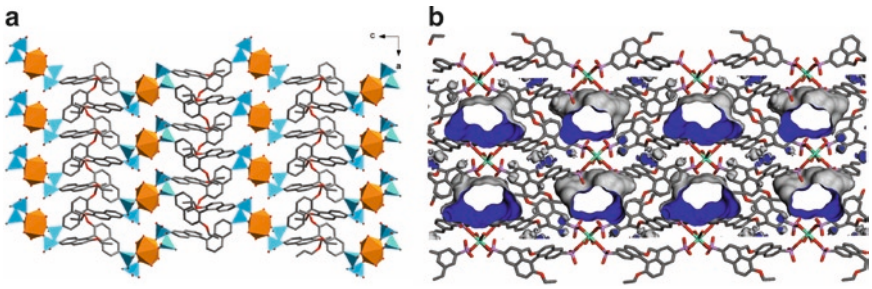

Fig. 16 (**a**) A view of 2D framework of **17f** down the *b* axis; the coordination environments of P atoms and Gd atoms are represented with *blue* and *orange* polyhedra, respectively. (**b**) The Connolly surface of framework **17f** showing 1D channel between 2D layers

suggests that the local coordination environment is retained during desolvation. They exhibit reversible dehydration and framework stability. Compound **17e** was utilized as a chiral Lewis acid catalyst for several organic transformations, including cyanosilylation of aldehydes, ring opening of mesocarboxylic anhydride, and Diels–Alder reactions with high yields but disappointingly low ee (<5%). Such a lack of enantioselectivity was a direct consequence of the highly symmetrical coordination environment around the catalytically active Sm centers and points out the limitations of such simple M-L-M systems.

To improve the enantioselectivity, Lin et al. designed chiral bridging ligands with duel functional groups. While primary functional groups form an extended network structure, chiral secondary functionalities can be used to decorate the porous metal-organic structure and subsequently generate asymmetric catalytic sites, which are accessible to the organic substrates via the open channels or cavities. This strategy was utilized to synthesize porous zirconium phosphonates with pendant chiral chelating bisphosphanes groups [84]. Two new chiral porous Zr-phosphonates with approximate formulae $Zr[Ru(L_{18})(dmf)_2Cl_2]\cdot 2MeOH$ (Zr–Ru–L_{18}, **18**) and $Zr[Ru(L_{19})(dmf)_2Cl_2]\cdot 2MeOH$ (Zr–Ru–L_{19}, **19**) were synthesized by a sequence of reactions starting from BINAP derivatives 2,2′-bis(diphenylphosphino)-1,1′-binaphthyl-6,6′-bis(phosphonic acid) (L_{18}–H_4) and 2,2′-bis(diphenylphosphino)-1,1′-binaphthyl-4,4′-bis(phosphonic acid) (L_{19}–H_4), respectively (Scheme 5). N_2 adsorption measurements indicated that Zr–Ru–L_{18} and Zr–Ru–L_{19} possess high degree of porosity, while powder XRD indicated that both solids are amorphous. Both solids have proved very effective as heterogeneous catalysts for asymmetric hydrogenation of keto esters. Zr–Ru–L_{18} showed better catalytic activity than the other compound for the hydrogenation of a wide range of β-alkyl-substituted β-keto esters with complete conversions and ee values ranging from 91.7 to 95.0% (Table 4). The enantioenrichment of Zr–Ru–L_{18} is the same as the parent homogeneous BINAP–Ru catalyst. The system shows less than 0.01% leaching during the catalytic reactions. The same catalytic activity of Zr–Ru–L_{18} can be retained up to five cycles of hydrogenation with no significant deterioration of enantioselectivity.

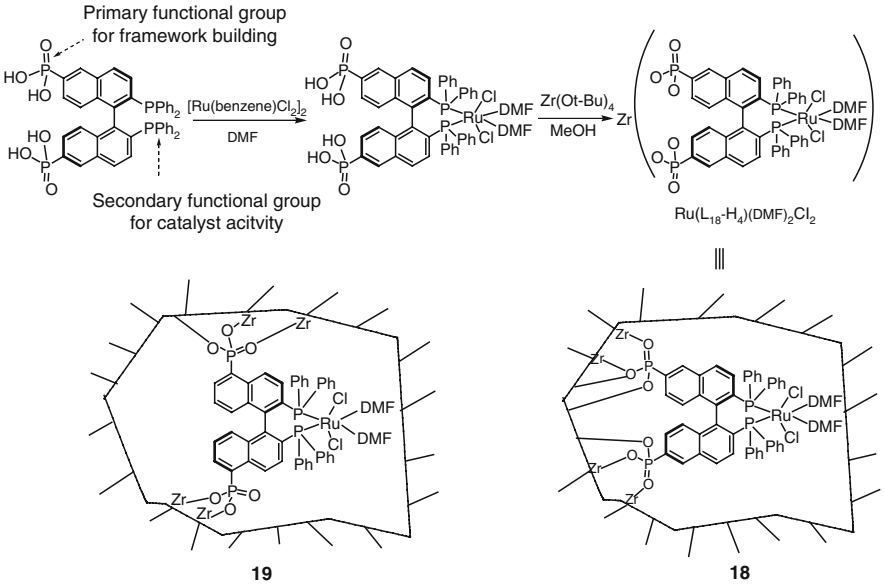

Scheme 5 Synthesis of Zr–Ru–L_{18} and Zr–Ru–L_{19}

Table 4 Heterogeneous asymmetric hydrogenation of β-keto esters with **18** and **19**

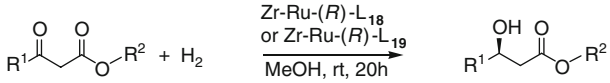

Substrate	Catalyst loading [%]	T (°C)	H_2 Pressure [psi]	Zr-Ru-L_{18} ee (% yield)	Zr-Ru-L_{19} ee (% yield)
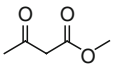	1	60	700	94.0 (100)	73.1 (90)
	1	RT	1400	95.0 (100)	
	0.1	60	700	93.3 (100)	
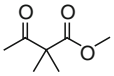	1	RT	1400	93.3 (100)	78.8 (70)
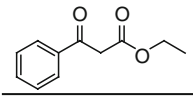	1	RT	1400	69.6 (100)	15.7 (50)

Incorporation of DPEN (1,2-diphenylethylenediamine) in the same skeleton of Zr-phosphonates improves both catalytic activity and enantioselectivity to almost quantitative value [85]. The syntheses involved the same sequence of reactions as in the previous work and TGA and microanalysis suggested their formulae as

Table 5 Heterogeneous asymmetric hydrogenation of aromatic ketones with **20** and **21**

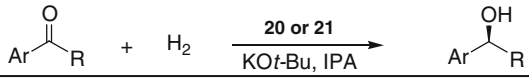

Substrate	Catalyst loading [%]	KO^{t}Bu	**20** ee	**21** ee
Ar: Ph, R: Me	0.1	1	96.3	79.0
Ar: 4?-*t*-Bu-Ph, R: Me	0.1	1	99.2	91.5
Ar: 1-naphthyl, R: Me	0.1	1	99.2	95.8
	0.02	0.4	98.9	
	0.005	0.02	98.8[a]	
	0.005	0.02	98.6[b]	

[a]70% conversion;
[b]40h reaction time

$Zr[Ru(L_{19}–H_4)(DPEN)Cl_2]·4H_2O$ (**20**) and $Zr[Ru(L_{18}–H_4)(DPEN)Cl_2]·4H_2O$ (**21**), respectively. N_2 adsorption measurements indicated that both **20** and **21** are highly porous with rather wide pore size distributions. The enantioselective catalytic activity of **20** and **21** for the hydrogenation of aromatic ketones was studied (Table 5). Only 0.1 mol% loading of catalyst **20** in isopropanol was sufficient to hydrogenate acetophenone with complete conversion and 96.3% ee, which is significantly higher than that observed for the parent Ru–BINAP–DPEN homogeneous catalyst (~80% ee) under similar conditions [89,90].

Although **21** also showed catalytic activity for the same reaction, enantioselectivity is rather modest. A series of substrates was tested with **20,** which showed complete conversion with high ee as illustrated in Table 5. Lowering the amount of catalyst (**20**) to 0.02 mol% does not affect the ee, while a catalyst concentration of 0.005% requires a longer time (40 h) for completion but with the same ee conversion. The TOF is calculated to be 500 h^{-1} at complete conversion and 700 h^{-1} at 70% conversion. Compound **20** can be readily recycled and reused up to eight cycles without any loss of enantioselectivity. High activity and enantioselectivity of these solids thus hold the promise for developing better and practically useful heterogeneous asymmetric catalysts with a similar designing approach.

Lin et al. also used BINOL linkers with phosphonate groups at a proper position to form the main framework with zirconium and explored the presence of the free hydroxyl functional groups as a catalyst holding unit to develop Ti-based catalysts for diethyl zinc addition to aromatic aldehydes [86]. Amorphous chiral porous zirconium phosphonates $Zr–L_{22}$ to $Zr–L_{24}$ (**22**–**24**) when treated with excess $Ti(Oi–Pr)_4$, generate active catalysts, which convert several aromatic aldehydes to corresponding chiral secondary alcohols with high conversion but slightly lowered ee values (up to 72%) (Scheme 6). However, the variable linkers between the BINOL moiety and the phosphonate groups do not show much effect on catalytic activity or enantioselection.

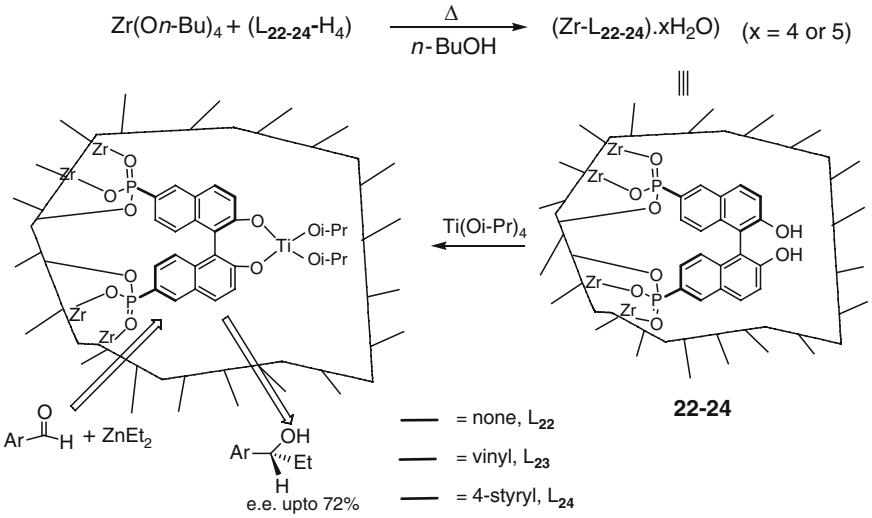

Scheme 6 Synthesis of BINOL derived Ti-based catalysts **22**–**24**

By incorporating a rigid linking arm at the 4 and 4′ positions of BINOL unit, Lin et al. finally succeeded in synthesizing a crystalline homochiral MOPM (**25**) [87]. The BINOL derivative, (*R*)-6,6′-dichloro-2,2′-dihydroxy-1,1′-binaphthyl-4,4′-bipyridine (L_{25}) when reacted with $CdCl_2$, afforded the CMOPM with molecular formula $[Cd_3Cl_6(L_{25})_3]\cdot 4DMF\cdot 6MeOH\cdot 3H_2O$, **25**, which crystallizes in the triclinic P_1 space group. The Cd(II) centers in **25** are doubly bridged by the chlorides to form 1D zigzag $[Cd(\mu^2\text{-}Cl)_2]_n$ chains, which are further connected through the pyridyl groups of L_{25} to form a noninterpenetrating 3D network with large chiral channel with the cross section of 1.6 × 1.8 nm (Fig. 17a). PLATON calculations indicated that **25** contains 54.4% solvent accessible void space. X-ray powder diffraction and CO_2 adsorption measurements of **25** indicated that the porous framework was maintained even after evacuation.

Although two of the three L_{25} ligands in a unit cell are shielded from the open channels, **25** was utilized in asymmetric catalysis by taking advantage of the readily accessible chiral dihydroxy groups of the third ligand (Fig. 17b). Treatment of **25** with excess $Ti(Oi\text{–}Pr)_4$ formed an active catalyst (designated as **25**·Ti) for the diethylzinc addition reactions to a range of aromatic aldehydes with complete conversion and high enantioselectivity (up to 93% ee) (Table 6). The level of enantioselectivity is similar to that of the homogeneous analog under similar conditions (94% ee). Control experiments with a series of larger aldehydes of varying sizes (from 0.8 to 2.0 nm) confirmed that the catalytic activity was dependent on the aldehyde size, and no catalytic activity was observed when the size of the aldehyde became larger than the open channel size. This set of experiments clearly demonstrates that **25**-Ti is a true heterogeneous asymmetric catalyst as both $ZnEt_2$ and

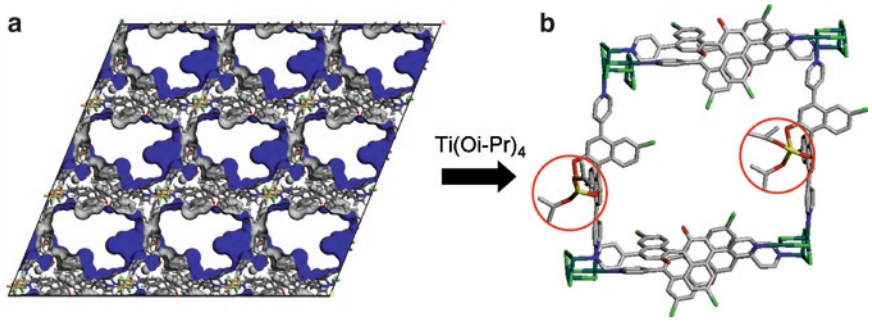

Fig. 17 (**a**) The Connolly surface of **25** clearly showing the large 1D chiral channels; (**b**) Schematic representation of the active (BINOL)Ti(Oi-Pr)$_2$ catalytic sites (marked by *red circle*) in the open channels of **25**

Table 6 Ti(IV)-catalyzed $ZnEt_2$ additions to aromatic aldehydes with (*R*)-**25**

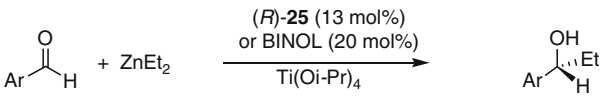

	BINOL		(*R*)-**25**·Ti	
Ar	Conv (%)	ee (%)	Conv (%)	ee (%)
1-Naph	>99	94	>99	93
Ph	>99	88	>99	83
4-Cl-Ph	>99	86	>99	80

All the reactions were conducted at room temperature in presence of excess Ti(Oi-Pr)

aromatic aldehyde accessing the catalytic sites via the open channels generate chiral secondary alcohols.

Very recently, Lin et al. examined the relationship between the framework structure and the catalytic activity of homochiral MOPMs [88]. The same ligand L_{25} was utilized to synthesize two more crystalline chiral MOPMs $[Cd_3(L_{25})_4(NO_3)_6]\cdot 7MeOH\cdot 5H_2O$, **26**, and $[CdL_{25}(H_2O)_2][ClO_4]_2\cdot DMF\cdot 4MeOH\cdot 3H_2O$, **27**. Compound **26** crystallizes in the tetragonal $P4_122$ space group with 1.5 Cd(II) centers in the asymmetric unit. Two independent L_{25} are linked to two different Cd(II) atoms to form 2D square grids and 1D zigzag polymeric chains, respectively. These are further joined to each other by the bridging nitrate groups to form a twofold, interpenetrated, 3D framework with large interconnected channels of 4.9 × 13.1 Å parallel to the a and b axes and 13.5 × 13.5 Å parallel to *c* axis (Fig. 18a); whereas, compound **27** crystallizes in $P4_32_12$ space group, and forms an interlocked 2D rhombic grid and possesses 1D channels ~1.2 × 1.5 nm in dimension (Fig. 18b). PXRD spectrum of

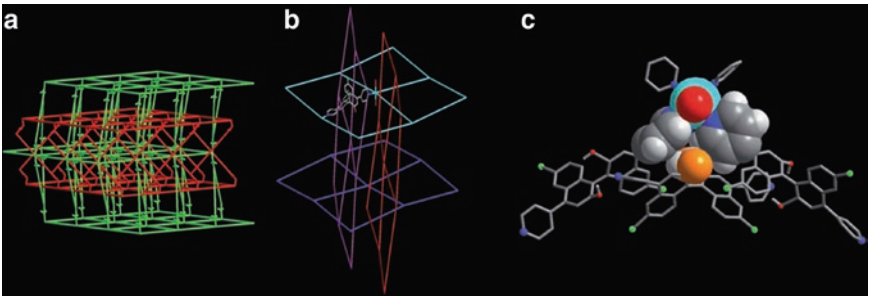

Fig. 18 (**a**) Schematic representation of the twofold interpenetration of **26**; (**b**) schematic representation of the interpenetration of mutually perpendicular 2D rhombic grids in **27**; (**c**) schematic representation of the steric congestion around the chiral dihydroxy groups of L_{25} ligands (*orange spheres*) arising from the interpenetration of 2D rhombic grids through π···π stacking interactions

26 indicated that the crystalline nature was retained after solvent removal. Moreover, CO_2 adsorption measurements showed that both evacuated samples of **26** and **27** possess permanent porosity. While **26** can effectively generate an active catalyst with Ti(Oi–Pr)$_4$ with the addition of diethylzinc to aromatic aldehydes with complete conversion and up to 90% ee, a mixture of **27** and Ti(Oi–Pr)$_4$ was not active in catalyzing the same reaction under identical conditions. The radical difference in catalytic activities of **26** and **27** was rationalized based on their different framework structures. Examination of the structure of **27** shows that the pyridyl and naphthyl rings, from mutually perpendicular interpenetrating 2D rhombic grids, form strong π···π interactions with a nearest C···C separation of 3.273 Å. As a result, all the chiral dihydroxy groups of the L_{25} ligands are tightly held in close proximity to the {Cd(py)$_2$(H$_2$O)$_2$} hinges (Fig. 18c). Due to this steric congestion, Ti(Oi–Pr)$_4$ cannot approach the binolate hydroxyl groups to form the active catalyst [91]. This observation implies that the role of the framework structure is important in determining the catalytic performance of chiral MOPMs, even if they are built from exactly the same building blocks.

A few other interesting reports on enantioselective catalysis of CMOPMs are available. Hupp and Nguyen reported an interesting CMOPM containing chiral Mn(salen) struts (salen = [(*R,R*)-(−)-1,2-cyclohexanediamino-*N,N′*-bis(3-*tert*-butyl-5-(4-pyridyl)-salicylidene)]), which was used as an asymmetric catalyst for olefin epoxidation [54]. The chiral strut, Mn^{III}(salen)Cl with (L_{28}), forms a robust pillared paddlewheel structure, $Zn_2(bpdc)_2L_{28}\cdot 10DMF\cdot 8H_2O$, **28**, which crystallizes in the triclinic P_1 space group with a 2-fold interpenetrating network (Fig. 19). The catalytic efficiency of the crystalline, porous material **28** towards the epoxidation of olefins was studied. In the presence of **28** as a catalyst and 2-(*tert*-butylsulfonyl) iodosylbenzene as an oxidant, 2,2-dimethyl-2H chromene formed the corresponding epoxide in high yield and enantioselectivity (82% ee). Slightly lower enantioselectivity than its homogeneous counterparts (88% ee) was observed, in good agreement

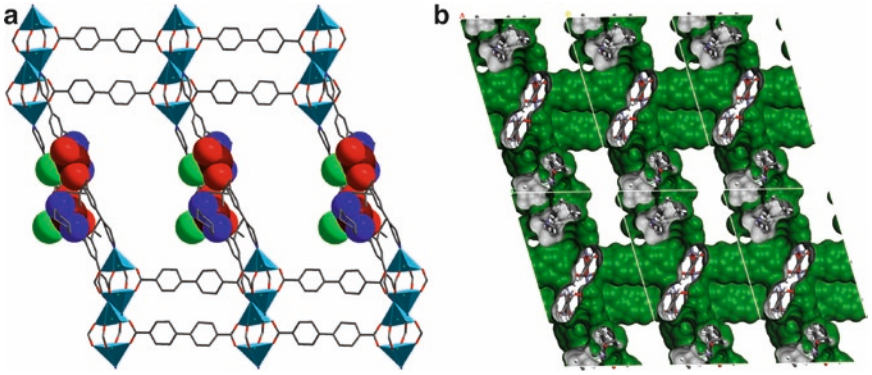

Fig. 19 (**a**) The crystal structure of the framework **28** showing interpenetrated network and framework openings; (**b**) The Connolly surface of the framework showing 2D channel structure

with the electronic effect arising from the bonded pyridyl groups to zinc cations. The compound **28** can be reused, up to third cycle (TON~1,400) with no loss of enantioselectivity and only a small loss of catalytic activity. Competitive size selectivity studies were carried out and they determined that catalysis occurs mainly in the interior and not at the surface of the catalyst. This work demonstrates that well-known salen-based Mn complexes, when confined in a CMOPM, can perform industrially important epoxidation reactions with equal efficiency as their homogeneous counterparts.

Very recently, Tanaka and coworkers have applied a copper–BINAP porous framework in the asymmetric ring opening reaction of epoxides with amines under solvent-free conditions [92]. Slow diffusion of *N,N*-dimethylaniline into a methanolic solution of (*R*)-5,5′-H_2BDA (2,2′-dihydroxy-1,1′-binaphthalene-5,5′-dicarboxylic acid, (*R*)-L_{29}) (or (*S*)-L_{29}) and $Cu(NO_3)_2$ afforded $[Cu_2(5,5'\text{-BDA})_2(H_2O)_2]\cdot MeOH\cdot 2H_2O$, (*R*)-**29**, (or (*S*)-**29**) which crystallized in a $P2_1$ space group and possessed a 2D binuclear square grid coordination network (Fig. 20). TGA of (*R*)-**29** showed 19.5% of mass loss at 25–120°C, while PXRD patterns showed reversible solvent absorption. The porous form of (*R*)-**29** is amorphous and shows catalytic activity toward asymmetric ring opening reactions of epoxides with aromatic amines. While (*S*)-BINOL was totally ineffective in catalytic ring opening reaction of epoxides, (*R*)-**29** catalyzed the reaction to afford corresponding amino alcohols in low to moderate yield with moderate enantioselectivity (40–50% ee). Although this work demonstrates for the first time, the use of Cu-based CMOPMs in epoxide ring opening reactions, the enantioselectivity is rather disappointing. There is a recent report on postsynthetic modification of a homochiral MOPM leading to a Brønsted acidic material. This material can catalyze epoxide ring opening reaction but without any asymmetric induction [93].

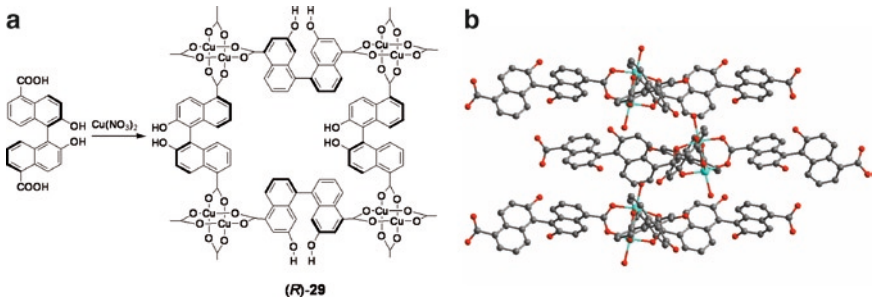

Fig. 20 (**a**) Synthesis of (*R*)-**29**; (**b**) The crystal structure of (*R*)-**29**; 2D layers are stacked in A-B-A type (viewed along the *c* axis)

Although some results described in this section are not highly exciting in terms of catalytic activity and enantioselectivity, they certainly highlight the fact that fine tunability of such a modular approach can lead to other practically useful heterogeneous asymmetric catalysts in the future.

4 Other Applications

A number of chiral coordination polymers show nonlinear optical activity and ferroelectric behavior [94–98]. The essential criterion for a compound to show either nonlinear optical activity or ferroelectric activity is that the material needs to crystallize in a noncentrosymmetric space group belonging to the polar point groups. As a chiral network itself is noncentrosymmetric, chiral coordination polymers are potentially useful as second order NLO-active materials as well as ferroelectric materials. The SHG responses of most reported chiral coordination polymers are same or less than that of urea [94–98]. However, there are a handful of examples, which show stronger SHG response. For example, $[H_2N(CH_3)_2][Zn_3(TATB)_2(HCOO)]$ (**30**) (TATB = 4,4′,4″-*s*-triazine-2,4,6-triyltribenzoate) has three times greater SHG response than urea [98]. A ferroelectric material is one that can be switched rapidly between different states by means of an external electric field. Although most of the reported ferroelectric materials are inorganic materials (e.g., KH_2PO_4, $BaTiO_3$, and $LiNbO_3$) [99], some chiral coordination polymers have also shown promising ferroelectric activity [95]. The chiral copper complex, $[Cu_2(R\text{-hmp})_2(dca)_2]$ (hmp = (*R*)-methyl-2-pyridinemethanol, dca = dicyanamide), **31**, is one such recent example [95]. However, magnetism [100–104] and photoluminescence [105,106] are two other important physical properties, which are often found in chiral coordination polymers but do not intrinsically depend on chirality of the material. It is interesting to note that often more than one of the above mentioned properties coexists in many chiral coordination polymers [94–98,105]. The reader is directed to the [107].

5 Summary and Perspectives

Since the beginning of this century, significant progress has been made in the synthesis of CMOPMs and their applications in chiral separation and catalysis. In this review article, we have discussed the strategies for the synthesis of chiral MOPMs, retaining a focus on their applications. A large number of chiral MOPMs with diverse functionalities and different topologies have been prepared mainly by two distinct approaches. The fine tunability of such approaches allows proper engineering of chiral functionalities within chiral MOPMs. With judicious choice of ligands and metal ions we can construct robust, homochiral open frameworks useful for chiral separation or heterogeneous asymmetric catalysis or both. Although still in a budding stage, CMOPMs have already shown high catalytic activity and enantioselectivity in several organic transformations such as hydrogenation of ketones and β-ketoesters, diethylzinc addition, or epoxidation. It has been established that a chiral catalyst confined inside well-organized pores can produce enantioselectivity comparable to that of its parent homogeneous catalyst. In addition, a study has revealed that the role of the framework structure is important in determining the catalytic performance of chiral MOPMs even if they are built from exactly the same building blocks. In addition, it should be pointed out that the local chirality is essential to achieve high enantioselectivity. Strategically, the synthesis of this new class of metal-organic assemblies is more controllable than the traditional immobilized catalysts and thus, this type of well-ordered, microporous materials with a high density of active catalyst centers on the surface promises to provide a new dimension in heterogeneous asymmetric catalysis. Catalyst loading, recovery, and reusability are among the important factors that determine the efficiency of a heterogeneous catalyst. So far, the preliminary results on these factors are satisfactory, but it is probably too early to raise questions regarding which of these processes have good chances of commercialization. Their ability for enantioselective sorption has been studied mostly with small chiral molecules, but several results cited in this review are still far from satisfactory. In one case, a CMOPM has been efficiently utilized as a CSP in liquid chromatography for the separation of racemates. This could well be the beginning of their potential applications in chirotechnology from a practical point of view. As a whole, the chiral MOPMs show high promise for attracting more financial and intellectual investments for potential breakthroughs in the rapidly increasing field of chirotechnology in the near future.

Note Added in Proof

Since this chapter was prepared, several important papers on the subject have been published. Wang et al. used a modified amino acid as a chiral ligand to synthesize a chiral MOPM with 1D channels (5.12×2.87 Å^2) [108]. The chiral MOPM catalyzes the addition reaction of Grignard reagent to α,β-unsaturated ketones with

excellent conversion and enantioselection. As the size of the pore is too small to accommodate the substrates, however, the catalytic reaction took place mainly on the surface of the material. Lin and coworker illustrated the synthesis of highly porous chiral MOPMs by controlling catenation through both chirality of the bridging ligands and the size of solvent molecules [109]. Bu and coworkers used a small amount of natural alkaloids, (–)-cinchonidine or (+)-cinchonine, to induce the homochiral crystallization of a chiral framework constructed from achiral components [110]. Unlike typical chiral templates, these alkaloids catalytically induced the bulk homochirality without incorporating themselves into the framework. Kim and coworkers have successfully employed the post-modification approach to synthesize catalytically active chiral MOPMs using a pre-assembled robust 3D framework, MIL-101, and chiral catalytic organic units [111]. L-Proline-based chiral organic ligands were incorporated at the unsaturated Cr(III) centers of MIL-101 keeping the parent framework intact. The new chiral MOPMs showed remarkable catalytic activities in asymmetric aldol reactions (yield up to 90% and ee up to 80%), including much higher enantioselectivity than the corresponding chiral catalytic organic units as homogeneous catalysts.

Acknowledgment We gratefully acknowledge the Creative Research Initiatives, Brain Korea 21, and World Class University (WCU) (Project No. R31-2008-000-10059-0) programs of the Korean Ministry of Education, Science and Technology (MOEST), and the Steel Science Programs of POSCO for support of this work.

References

1. Corma A (1997) Chem Rev 97:2373
2. Maesen TLM, Marcus B (2001) In: van Bekkum H, Flanigen EM, Jacobs PA, Jansen JC (eds) Introduction to zeolite science and practice. Elsevier, Amsterdam, p 1
3. Song CE, Lee SG (2002) Chem Rev 102:3495
4. Newsam JM, Treacy MMJ, Koetsier WT, de Gruyter CB (1988) Proc R Soc Lond Ser A 420:375
5. Anderson MW, Terasaki O, Ohsuna T, Philippou A, MacKay SP, Ferreira A, Rocha J, Lidin S (1994) Nature 367:347
6. Janiak C (2003) Dalton Trans:2781
7. James SL (2003) Chem Soc Rev 32:276
8. Rosseinsky MJ (2004) Microporus Mesoporous Mater 73:15
9. Rowsell JLC, Yaghi OM (2005) Angew Chem Int Ed 44:4670
10. Férey G (2008) Chem Soc Rev 37:191
11. Morris RE, Wheatley PS (2008) Angew Chem Int Ed 47:4966
12. Lin W (2005) J Solid State Chem 178:2486
13. Lin W (2005) Top Catal 34:85
14. Lin W (2007) MRS Bull 32:544
15. Wells AF (1977) Three-dimensional nets and polyhedra. Wiley, New York
16. Janiak C (1997) Angew Chem Int Ed Engl 36:1431
17. Kondo M, Okubo T, Asami A, Noro SI, Yoshitomi T, Kitagawa S, Ishii T, Matsuzaka H, Seki K (1999) Angew Chem Int Ed 38:140
18. Moulton B, Zaworotko MJ (2001) Chem Rev 101:1629 and references therein

19. Khlobystov AN, Blake AJ, Champness NR, Lemenovskii DA, Majouga AG, Zyk NV, Schröder M (2001) Coord Chem Rev 222:155
20. Barnett SA, Champness NR (2003) Coord Chem Rev 246:145
21. Desiraju GR (1989) Crystal engineering. The design of organic solids. Elsevier, Amsterdam
22. Desiraju GR (2002) Acc Chem Res 35:565 and references therein
23. Steiner T (2002) Angew Chem Int Ed 41:48
24. Hoskins BF, Robson R (1990) J Am Chem Soc 112:1546
25. Biradha K, Seward C, Zaworotko MJ (1999) Angew Chem Int Ed 38:492
26. Zaworotko MJ (2000) Angew Chem Int Ed 39:3052
27. Yaghi OM, Li H, Davis C, Richardson D, Groy TL (1998) Acc Chem Res 31:474
28. Eddaoudi M, Moler DB, Li H, Chen B, Reineke TM, O'Keeffe M, Yaghi OM (2001) Acc Chem Res 34:319
29. Wang Z, Kravtsov VC, Zaworotko MJ (2005) Angew Chem Int Ed 44:2877
30. Eddaoudi M, Kim J, Rosi N, Vodak D, O'Keeffe M, Yaghi OM (2002) Science 295:469
31. Yaghi OM, O'Keeffe M, Ockwig N, Chae HK, Eddaoudi M, Kim J (2003) Nature 423:705
32. Ockwig N, Friedrichs OD, O'Keeffe M, Yaghi OM (2005) Acc Chem Res 38:176
33. Zhang JP, Lin YY, Huang XC, Chen XM (2005) J Am Chem Soc 127:5495
34. Evans OR, Lin W (2002) Acc Chem Res 35:511
35. Halder GJ, Kepert CJ, Moubaraki B, Murray KS, Cashion JD (2002) Science 298:1762
36. Dincă M, Long JR (2007) J Am Chem Soc 129:11172
37. Noro S, Kitagawa S, Kondo M, Seki K (2000) Angew Chem Int Ed 39:2081
38. Rosi NL, Eckert J, Eddaoidi M, Vodak DT, Kim J, O'Keeffe M, Yaghi OM (2003) Science 300:1127
39. Kitagawa S, Kitaura R, Noro S (2004) Angew Chem Int Ed 43:2334
40. Fujita M, Kwon YJ, Washizu S, Ogura K (1994) J Am Chem Soc 116:1151
41. Seo JS, Whang D, Lee H, Jun SI, Oh J, Jeon Y, Kim K (2000) Nature 404:982
42. Joy A, Ramamurthy V (2000) Chem Eur J 6:1287
43. Sivasubramanian K, Kaanumalle LS, Uppili S, Ramamurthy V (2007) Org Biomol Chem 5:1569
44. Withersby MA, Blake AJ, Champness NR, Hubberstey P, Li WS, Schröder M (1997) Angew Chem Int Ed Engl 36:2327
45. Batten SR, Hoskins BF, Robson R (1997) Angew Chem Int Ed Engl 36:636
46. Krämer R, Lehn JM, De Cian A, Fischer J (1993) Angew Chem Int Ed Engl 32:703
47. Chen XD, Du M, Mak TCW (2005) Chem Commun:4417
48. Abrahams BF, Jackson PA, Robson R (1998) Angew Chem Int Ed 37:2656
49. Kepert CJ, Rosseinsky MJ (1998) Chem Commun:31
50. Kepert CJ, Prior TJ, Rosseinsky MJ (2000) J Am Chem Soc 122:5158
51. Lin Z, Slawin AMZ, Morris RE (2007) J Am Chem Soc 129:4880
52. Ranford JD, Vittal JJ, Wu D (1998) Angew Chem Int Ed 37:1114
53. Kesanli B, Cui Y, Smith MR, Bittner EW, Bockrath BC, Lin W (2005) Angew Chem Int Ed 44:72
54. Cho SH, Ma B, Nguyen ST, Hupp JT, Albrecht-Schmitt TE (2006) Chem Commun:2563
55. Zhang J, Liu R, Feng P, Bu X (2007) Angew Chem Int Ed 46:8388
56. Dybtsev DN, Nuzhdin AL, Chun H, Bryliakov KP, Talsi EP, Fedin VP, Kim K (2006) Angew Chem Int Ed 45:916
57. Vaidhyanathan R, Bradshaw D, Rebilly JN, Barrio JP, Gould JA, Berry NG, Rosseinsky MJ (2006) Angew Chem Int Ed 45:6495
58. Hasegawa S, Horike S, Matsuda R, Furukawa S, Mochizuki K, Kinoshita Y, Kitagawa S (2007) J Am Chem Soc 129:2607
59. Wang Z, Cohen SM (2007) J Am Chem Soc 129:12368
60. Tanabe KK, Wang Z, Cohen SM (2008) J Am Chem Soc 130:8508
61. Hwang YK, Hong DY, Chang JS, Jhung SH, Seo YK, Kim J, Vimont A, Daturi M, Serre C, Férey G (2008) Angew Chem Int Ed 47:4144
62. Collins AN, Sheldrake GN, Crosby J (1996) Chirality in industry. Wiley, NY

63. Blaser HU, Spindler F, Studer M (2001) Appl Catal A Gen 221:119
64. Oehme G (1999) In: Jacobsen EN, Pfaltz A, Yamamoto H (eds) Comprehensive Asymmetric Catalysis. Springer-Verlag, Berlin, Vol 3, p 1378
65. Heitbaum M, Glorius F, Escher I (2006) Angew Chem Int Ed 45:4732
66. McMorn P, Hutchings GJ (2004) Chem Soc Rev 33:108
67. Sherrington DC (2000) Catal Today 57:87
68. Ding K, Wang Z, Wang X, Liang Y, Wang X (2006) Chem Eur J 12:5188
69. Pini D, Mandoli A, Orlandi S, Salvadori P (1999) Tetrahedron Asymmetry 10:3883
70. Ward TJ (2006) Anal Chem 78:3947
71. Maier NM, Lindner W (2007) Anal Bioanal Chem 389:377
72. Gübitz G, Martin G, Schmid MG (2007) Electrophoresis 28:114
73. Cancelliere G, D'Acquarica I, Gasparrini F, Maggini M, Misiti D, Villani C (2006) J Sep Sci 29:770
74. Xiong RG, You XZ, Abrahams BF, Xue ZL, Che CM (2001) Angew Chem Int Ed 40:4422
75. Xie YR, Wang XS, Zhao H, Zhang J, Weng LH, Duan CY, Xiong RG, You XZ, Xue ZL (2003) Organometallics 22:4396
76. Song YM, Zhou T, Wang XS, Li XN, Xiong RG (2006) Cryst Growth Des 6:14
77. Bradshaw D, Prior TJ, Cussen EJ, Claridge JB, Rosseinsky MJ (2004) J Am Chem Soc 126:6106
78. Nuzhdin AL, Dybtsev DN, Bryliakov KP, Talsi EP, Fedin VP (2007) J Am Chem Soc 129:12958
79. Muppidi VK, Zacharias PS, Pal S (2005) Chem Commun:2515
80. Muppidi VK, Zacharias PS, Pal S (2007) J Solid State Chem 180:132
81. Sawaki T, Dewa T, Aoyama Y (1998) J Am Chem Soc 120:8539
82. Gao Y, Wada T, Yang K, Kim K, Inoue Y (2005) Chirality 17:S19
83. Evans OR, Ngo HL, Lin W (2001) J Am Chem Soc 123:10395
84. Hu A, Ngo HL, Lin W (2003) Angew Chem Int Ed 42:6000
85. Hu A, Ngo HL, Lin W (2003) J Am Chem Soc 125:11490
86. Ngo HL, Hu A, Lin W (2004) J Mol Catal A Chem 215:177
87. Wu CD, Hu A, Zhang L, Lin W (2005) J Am Chem Soc 127:8940
88. Wu CD, Lin W (2007) Angew Chem Int Ed 46:1075
89. Ohkuma T, Ooka H, Ikariya T, Noyori R (1995) J Am Chem Soc 117:10417
90. Doucet H, Ohkuma T, Murata K, Yokozawa T, Kozawa M, Katayama E, England AF, Ikariya T, Noyori R (1998) Angew Chem Int Ed 37:1703
91. Jiang H, Lin W (2004) Org Lett 6:861
92. Tanaka K, Oda S, Shiro M (2008) Chem Commun:820
93. Ingleson MJ, Barrio JP, Bacsa J, Dickinson C, Park H, Rosseinsky MJ (2008) Chem Commun:1287
94. Gu ZG, Zhou XH, Jin YB, Xiong RG, Zuo JL, You XZ (2007) Inorg Chem 46:5462
95. Zang S, Su Y, Li Y, Ni Z, Meng Q (2006) Inorg Chem 45:174
96. Xie YR, Zhao H, Wang XS, Qu ZR, Xiong RG, Xue X, Xue Z, You XZ (2003) Eur J Inorg Chem 3712
97. Zang S, Su Y, Li Y, Zhu H, Meng Q (2006) Inorg Chem 45:2972
98. Sun D, Ke Y, Collins DJ, Lorigan GA, Zhou HC (2007) Inorg Chem 46:2725
99. Lee HN, Christen HM, Chisholm MF, Rouleau CM, Lowndes DH (2005) Nature 433:395
100. Gao EQ, Yue YF, Bai SQ, He Z, Yan CH (2004) J Am Chem Soc 126:1419
101. Inoue K, Kikuchi K, Ohba M, Okawa H (2003) Angew Chem Int Ed 42:4810
102. Imai H, Inoue K, Kikuchi K, Yoshida Y, Ito M, Sunahara T, Onaka S (2004) Angew Chem Int Ed 43:5618
103. Wen HR, Wang CF, Song Y, Zuo JL, You XZ (2005) Inorg Chem 44:9039
104. Liu WL, Song Y, Li YZ, Zou Y, Dang DB, Ni CL, Meng QJ (2004) Chem Commun:2348
105. Wang L, Yang M, Li G, Shi Z, Feng S (2006) Inorg Chem 45:2474
106. Yue Q, Yang J, Li GH, Li GD, Chen JS (2006) Inorg Chem 45:4431

107. Roques N, Mugnaini V, Veciana J (2009) Magnetic and porous molecule-based materials. Top Curr Chem . doi:10.1007/128_2009_8
108. Wang M, Xie MH, Wu CD, Wang YG (2009) Chem Commun:2396
109. Ma L, Lin W (2008) J Am Chem Soc 130:13834
110. Zhang J, Chen S, Wu T, Feng P, Bu X (2008) J Am Chem Soc 130:12882
111. Banerjee M, Das S, Yoon M, Choi HJ, Hyun MH, Park SM, Seo G, Kim K (2009) J Am Chem Soc 131:7524

Top Curr Chem (2010) 293: 155–173
DOI 10.1007/128_2009_6

Published online: 26 August 2009

Controlled Polymerization by Incarceration of Monomers in Nanochannels

Takashi Uemura and Susumu Kitagawa

Abstract Porous Coordination Polymers (PCPs) composed of transition metal ions and bridging organic ligands have been extensively studied. The characteristic features of PCPs are highly regular channel structures, controllable channel sizes approximating molecular dimensions, designable surface potentials and functionality, and flexible frameworks responsive to guest molecules. Owing to these advantages, successful applications of PCPs range from molecular storage and separation to heterogeneous catalysts. In particular, use of their regulated and tunable nanochannels in the field of polymerization has allowed multi-level control of polymerization via control of stereoregularlity, molecular weight, etc. In this chapter, we focus on recent progress in polymerization utilizing the nanochannels of PCPs, and demonstrate why this polymerization system is attractive and promising from the viewpoint of precision control of polymeric structures.

Keywords Nanochannel • PCP • Polymer structure • Polymerization

Contents

T. Uemura and S. Kitagawa (✉)
Department of Synthetic Chemistry and Biological Chemistry, Graduate School of Engineering, Kyoto University, Katsura, Nishikyo-ku, Kyoto, 615-8510, Japan
e-mail: uemura@sbchem.kyoto-u.ac.jp

S. Kitagawa
Institute for Integrated Cell-Material Science (iCeMS), Kyoto University, Yoshida, Sakyo-ku, Kyoto, 606-8501, Japan
e-mail: kitagawa@sbchem.kyoto-u.ac.jp

Abbreviations

adc	9,10-Anthracenedicarboxylate
bdc	1,4-Benzenedicarboxylate
bpd	Biphenyl-4,4′-dicarboxylate
bpy	4,4′-Bipyridine
DVB	Divinylbenzene
GPC	Gel permeation chromatography
M_n	Number-average molecular weight
M_w	Weight-average molecular weight
MMA	Methyl methacrylate
ndc	1,4-Naphthalenedicarboxylate
PCP	Porous coordination polymer
PMMA	Poly(methyl methacrylate)
PSt	Polystyrene
PVAc	Poly(vinyl acetate)
pzdc	Pyrazine-2,3-dicarboxylate
St	Styrene
ted	Triethylenediamine
VAc	Vinyl acetate

1 Introduction

All naturally occurring polymers are produced by enzymatic catalysis, where stereoselective, regioselective, and chemoselective polymerizations proceed effectively within regulated and well-organized molecular-scale spaces. Inspired by the elegant operations in these biological events, many synthetic chemists have focused their research interests on polymer synthesis in confined and designed nanospaces to attain precise structural controls of artificial polymers [1–8]. In particular, microporous materials such as porous organic crystals and zeolites of pore size <2 nm with regular channel structures have imposed specific size and shape effects of the nanochannels on reaction kinetics and selectivity in solid-state inclusion polymerization processes. For example, extensive studies on polymerization in organic hosts have been reported from the 1960s–1980s, focusing on radical polymerization of

conjugated diene and triene monomers irradiated with γ-rays [9–18]. Highly stereoregular and sometimes optically active chiral polymers were obtained in the inclusion polymerizations utilizing the organic hosts. On the other hand, impregnation of transition metal ions such as Cu(II), Fe(III), Ni(II), and Co(II) into the nanochannels of microporous zeolites is effective for oxidative polymerizations to produce many conjugated (semi)conducting polymers [6, 19–22]. Mesoporous materials with pore size >2 nm are also attractive from the viewpoints of polymerization as well as fabrications of nanocomposite materials [23–28].

Since the early 1990s, the quest for Porous coordination polymer (PCPs) composed of transition metal ions and bridging organic ligands has been the subject of intense research because of their potential applications in many areas including molecular storage, separation, and exchange [29–36]. Much research effort has been devoted to developing characteristic features of PCPs that differ from those of conventional microporous materials, such as organic hosts, zeolites, and activated carbons: (1) highly regular channel structures; (2) controllable channel size approximating molecular dimensions; (3) designable surface potentials and functionality; and, (4) flexible frameworks responsive to guest molecules. These features are of key importance for the creation of unique nanosize reaction fields based on the PCP materials. Thus control of molecular reactions and transformations within confined environments, utilizing the functional channels of PCPs is currently an important topic in this area, prompting vigorous efforts in the development of PCPs for applications in heterogeneous catalysis, asymmetric reaction, and ship-in-bottle synthesis [37–46]. In particular, employing the PCP nanochannels as a field of polymerization is an attractive idea, which would allow multi-level controls of polymerization (controls of stereo- and regioregularity, molecular weight, polymer topology, etc.) by efficient through-space inductions and specific host-monomer interactions [47]. Because of the highly designable features of PCPs, these functional nanochannels can be applied to a tailor-made polymerization system to obtain preferred polymer structures; such a system is nano-information transcription polymerization.

In this chapter, we will describe how the host frameworks based on PCPs can be designed for the fields of polymerizations in Sect. 2. Later in the following section, details of inclusion polymerization in PCPs such as radical and catalytic polymerization processes are considered. Finally, in Sect. 4, the significant effects of host framework structures on polymer primary structure are discussed.

2 Design of Host Frameworks

2.1 Regularity

Regular nanosize pores are suitable for confining guest molecules even when the intermolecular interaction between guest and host molecules is governed only by the dispersion force, the so-called van der Waals force. Self-assembly processes

from building blocks of metal ions and organic ligands afford microporous structures of PCPs with their particle dimensions of approximately 1 μm^3. Considering that the cross sections of channels of PCPs are mostly ranged from 0.4 to 2.0 nm, one can obtain several millions of regular channels in a particle of size 1 μm^3 [48]. Such regular channels, with their sharp distribution of pore size due to their high crystallinity, provide advantages for controlled polymerization. Densely adsorbed monomers inside the channels are favorable for highly reactive regulated polymerization because all of the channels can be utilized as a reaction field. If we prepare an assembled guest structure with one-directional orientation or hetero-guests accommodation (e.g., AAABBB, ABABAB…) by employing specific regular micropores, we can potentially achieve block or alternating copolymerization and sequence-controlled polymerization. By tuning the regularity of the potential field of the channels, we can create well-ordered monomer assemblies inside the PCP channels towards the target polymerization.

2.2 Pore Size and Shape

The reactivity of guest molecules in confined nanospaces is strongly dependent on the molecular states and behaviors. Generally, the pore sizes of PCPs range from 0.4 to 2.0 nm [48]. In addition, a variety of the pore shapes of PCPs, such as triangles, rectangles, and hexagons has been prepared by the possible combinations of directional organic ligands and geometric metal ions. From the viewpoint of channel dimension, not only one-dimensional but also layered or three-dimensional intersecting channel structures can be synthesized in the PCP materials [48–50]. By tuning the pore size and shape of PCPs, we can create a nanospace with strong confinement capability for a wide range of monomers from gas molecules (e.g., acetylene, ethylene) to larger molecules (e.g., Methyl methacrylate (MMA), Styrene (St)) even at room temperature. With the aid of this confinement, we can control the mobility, alignment, and density of adsorbed molecules in the pore, which is often advantageous for controlled polymerizations.

2.3 Pore Surface Functionality

If one can prepare PCP nanochannels with surface functional Lewis acidic or basic moiety [51], they can be applied to catalytic pores for a variety of polymerization reactions. In this regard, most PCPs have pore surfaces with coordinatively saturated functional groups. The introduction of Lewis-acidic sites into the pore however, requires coordinatively unsaturated metal cation(s) (open metal site(s)) in the pore surface [35, 36, 52–54]. Taking into account that the coordinative saturation of metal ions in PCPs tends to occur in usual frameworks, a clue to create open

metal sites is to use volatile solvent molecules bound to metal ions, such as a water molecule, functionalizing the surface towards guest molecules. The removal of the volatile molecules by heating under vacuum results in Lewis-acidic pore surfaces.

Basic functional sites contribute to superior characteristics of metal-organic frameworks. In spite of their great importance, reports on PCPs with basic porous surfaces have been rare because basic groups are preferentially bound by metal ions as connectors during the assembly [46, 55, 56]. The most quoted examples of robust PCPs are constructed using transition metal cations with either an anionic multi-carboxylate or a neutral bipyridyl linker, whose coordination sites are used to form available pore structures. On the other hand, the creation of free base-functionalized channels is a difficult target as the coordination strength of these ligands increases.

Introduction of relatively weak functional groups, such as carbonyl, hydroxyl, nitro, amide, etc., in the nanochannels of PCPs would affect the monomer alignment, which may lead to precision control of stereoselectivity and regioselectivity of the resulting polymers. In particular, PCPs with either helical or chiral structures on the pore surface are of intense interest in chemistry and such porous solids are potentially useful to find applications in enantioselective sorption/separation and catalysis [34, 38–40, 42, 45]. Of considerable interest is the use of the chiral channels to affect asymmetric polymerizations such as asymmetric selective polymerization of racemic monomers as well as asymmetric polymerization of prochiral monomers, which may give helical polymer conformations.

2.4 Host Flexibility

Dynamic structural transformation based on flexible frameworks is one of the most interesting and presumably characteristic phenomena of PCPs, which cannot be attained by conventional microporous materials such as zeolites and activated carbons [57–61]. Creation of flexible host frameworks that interact with exchangeable guest species in a switchable fashion has implications for the generation of previously undeveloped advanced materials with applications in areas such as molecular sensing. From the viewpoint of inclusion polymerization, utilization of such flexible frameworks based on PCPs would be key principles for highly selective recognition, alignment, and reaction of the accommodated monomers, which is similar to the induced fit theory illustrated by enzymes in biological systems.

The key to creating a flexible framework is to utilize weak molecular interactions in addition to the strong covalent and coordination bonds. Actually, coordination bonds in PCPs are frequently supported by hydrogen bonds, π–π stacking, van der Waals forces and other weak interactions. Intermolecular links with these weaker interactions produce flexible parts in a framework, so that the system can exist in two or more solid phases. Depending on the external perturbations and guest molecules, the system will be in one of the multiple solid phases.

3 Inclusion Polymerizations

3.1 Radical Polymerization

Radical polymerization is the most widely employed process for obtaining organic polymeric materials, not only in industry, but also in the laboratory, because of its versatility in polymerizing a variety of monomers [62, 63]. The industrial significance of radical polymerization is evident in the fact that it accounts for about 50% of all commercial polymers. Recently, radical polymerization of various common vinyl monomers, such as St, MMA, and Vinyl acetate (VAc), has been performed in the PCP nanochannels of $[M_2(L)_2ted]_n$ ($M = Cu^{2+}$ or Zn^{2+}), the channel size of which can be systematically controlled from 4.3 to 10.8 Å by changing the bridging dicarboxylate ligands L (Fig. 1 and 2) [64, 65]. In the polymerization of St and MMA, a strong correlation between the pore size of the PCPs and polymer yield is clearly observed with the conversions for polymerizations decreasing as the size of the nanochannels narrows (Tables 1 and 2). No polymeric product was obtained for the narrowest channels of $[Cu_2(adc)_2ted]_n$ and $[Zn_2(adc)_2ted]_n$ (pore size = 4.8×4.3 Å^2). Solid-state NMR measurements have been used to explain this pore-size-dependent polymerizability of the encapsulated monomers (Fig. 3). The line shapes of the ^{2}H NMR spectra for St-d_8 adsorbed into the larger nanochannels of $[Cu_2(bpd)_2ted]_n$ (pore size = 10.8×10.8 Å^2) and $[Cu_2(bdc)_2ted]_n$ (pore size = 7.5×7.5 Å^2), revealed that the guest St has high mobility with fast rotation in the nanochannels. In contrast, the spectrum for St-d_8 in $[Cu_2(adc)_2ted]_n$ showed completely solid-like behavior, even at polymerization temperatures, indicating that the mobility of St in this narrow channel is highly restricted. This restricted arrangement of St in the nanochannel led to poor reactivity. Compared with the polymerizations of St and MMA, the polymer yields in the VAc system were relatively low (Table 3); in particular, no trace of polymeric product was observed in the polymerizations utilizing even the nanochannels of $[M_2(ndc)_2ted]_n$ (pore size = 5.7×5.7 Å^2). This inhibited conversion of VAc in the nanochannels was ascribed to its low reactivity towards carbon radicals derived from an initiator due to the lack of a conjugated substituent in the VAc monomer unlike St and MMA.

It has been reported that the framework flexibility of PCPs is also of key importance to polymerizability of included monomers [66]. The polymerization of 1,4-disubstituted Divinylbenzene (DVB) (*p*-DVB; molecular dimension = 8.5×4.4 Å) was carried out in the nanochannels of $[Zn_2(bdc)_2ted]_n$ and an isostructural copper complex $[Cu_2(bdc)_2ted]_n$ under the same conditions. In this experiment, polymeric product was obtained in the nanochannels of the Zn compound; in contrast, no trace of polymer was observed by using the Cu complex. In addition, the thermogravimetric analysis showed that the amount of adsorbed monomer in $[Zn_2(bdc)_2ted]_n$ was much larger than that in $[Cu_2(bdc)_2ted]_n$. XRPD measurements gave an important clue to the different adsorption/polymerization properties of $[M_2(bdc)_2ted]_n$ (Fig. 4). In the series of XRPD patterns, small changes of peak

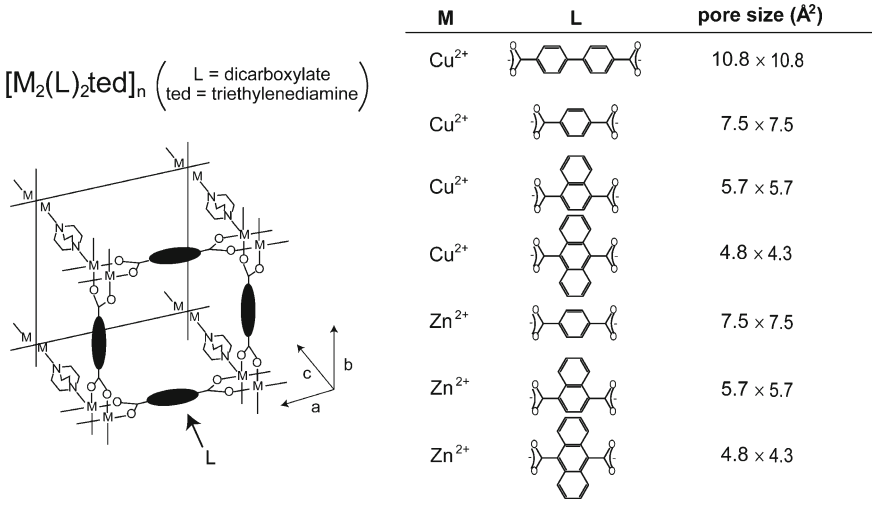

Fig. 1 Schematic illustration of $[M_2(L)_2ted]_n$ ($M = Cu^{2+}$ or Zn^{2+})

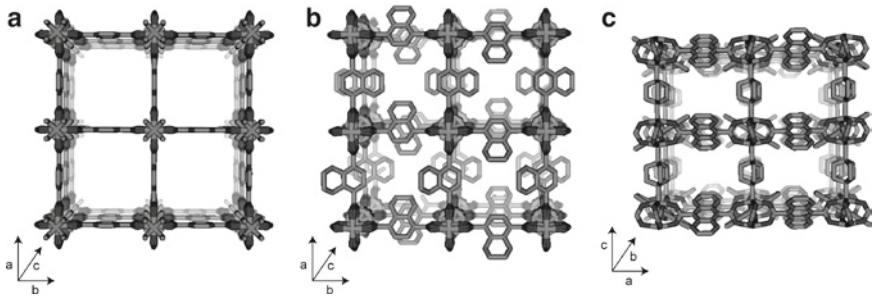

Fig. 2 Nanochannel structures of (**a**) $[Zn_2(bdc)_2ted]_n$, (**b**) $[Zn_2(ndc)_2ted]_n$, and (**c**) $[Zn_2(adc)_2ted]_n$ displayed by stick model. Hydrogen atoms and disordering atoms in the phenylene planes are omitted for clarity

positions were observed after the introduction of *p*-DVB in $[Zn_2(bdc)_2ted]_n$. However, the framework of $[Cu_2(bdc)_2ted]_n$ did not show such structural changes. The detailed framework changes in $[Zn_2(bdc)_2ted]_n$ was examined using synchrotron XRPD, which confirmed that introduction of *p*-DVB in the channel induces certain lattice expansion compared with the original host. From these data, averaged distances between *p*-DVB in the channels of $[Zn_2(bdc)_2ted]_n$ and $[Cu_2(bdc)_2ted]_n$ could be estimated to be 4.5 and 10.6 Å, respectively, suggesting a polymerizable closed packing structure of *p*-DVB in the channel of $[Zn_2(bdc)_2ted]_n$.

Table 1 Polymerization of St in Nanochannels of $[M_2(L)_2(ted)]_n$ at 70°C for 48 h

Host (Pore size [Å^2])	Adsorbed monomer amount (number/unit cell)[a]	Conversion (%)[a]	M_n (M_w/M_n)[b]	Tacticity[c] mm:mr;rr (m)
$[Cu_2(bpd)_2(ted)]_n$ (10.8×10.8)	3.1	81	14,000 (3.3)	19:40:41 (39)
$[Cu_2(bdc)_2(ted)]_n$ (7.5×7.5)	2.5	71	54,600 (1.6)	19:42:39 (40)
$[Cu_2(ndc)_2(ted)]_n$ (5.7×5.7)	2.2	58	10,100 (1.6)	19:40:41 (39)
$[Cu_2(adc)_2(ted)]_n$ (4.8×4.3)	1.6	0	–	–
$[Zn_2(bdc)_2(ted)]_n$ (7.5×7.5)	2.5	71	56,200 (1.7)	16:43:41 (38)
$[Zn_2(ndc)_2(ted)]_n$ (5.7×5.7)	2.1	56	11,100 (1.5)	17:42:41 (38)
$[Zn_2(adc)_2(ted)]_n$ (4.8×4.3)	1.6	0	–	–
Bulk polymerization[d]	–	–	37,600 (4.7)	16:42:42 (37)

[a] Determined by TGA
[b] Obtained by GPC calibrated by PSt standards
[c] Determined by ^{13}C NMR measurement in 1,1,2,2,-tetrachloroethane-d_2 at 100°C
[d] Bulk polymerization was carried out under a comparable condition to those employed in PCPs

Table 2 Polymerization of MMA in Nanochannels of $[M_2(L)_2(ted)]_n$ at 70°C for 7 h

Host (Pore size [Å^2])	Adsorbed monomer amount (number/unit cell)[a]	Conversion (%)[a]	M_n (M_w/M_n)[b]	Tacticity[c] mm:mr:rr (m)
$[Cu_2(bpd)_2(ted)]_n$ (10.8×10.8)	3.2	76	93,000 (4.8)	6:38:56 (25)
$[Cu_2(bdc)_2(ted)]_n$ (7.5×7.5)	2.6	74	73,100 (2.0)	8:40:52 (28)
$[Cu_2(ndc)_2(ted)]_n$ (5.7×5.7)	2.3	58	30,600 (2.4)	10:43:47 (31)
$[Cu_2(adc)_2(ted)]_n$ (4.8×4.3)	1.8	0	–	–
$[Zn_2(bdc)_2(ted)]_n$ (7.5×7.5)	2.7	76	69,100 (2.4)	8:40:52 (28)
$[Zn_2(ndc)_2(ted)]_n$ (5.7×5.7)	2.3	60	29,500 (2.4)	9:41:50 (30)
$[Zn_2(adc)_2(ted)]_n$ (4.8×4.3)	1.8	0	–	–
Bulk polymerization[d]	–	–	56,100 (6.4)	5:35:60 (22)

[a] Determined by TGA
[b] Obtained by GPC calibrated by PMMA standards
[c] Determined by ^{1}H NMR measurement in nitrobenzene-d_5 at 110°C
[d] Bulk polymerization was carried out under comparable condition to those employed in PCPs

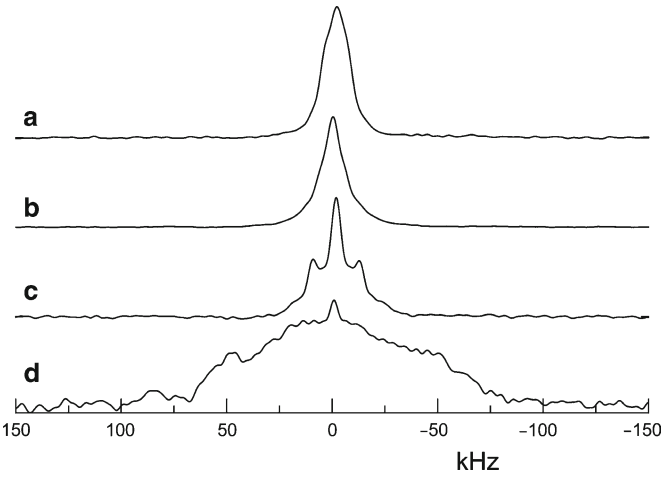

Fig. 3 Solid-state ^{2}H NMR spectra of St-d_8 adsorbed in the nanochannels of (**a**) $[Cu_2(bpd)_2ted]_n$, (**b**) $[Cu_2(bdc)_2ted]_n$, (**c**) $[Cu_2(ndc)_2ted]_n$, and (**d**) $[Cu_2(adc)_2ted]_n$ at 70°C

Table 3 Polymerization of VAc in Nanochannels of $[M_2(L)_2(ted)]_n$ at 60°C for 48 h

Host (Pore size [Å^2])	Adsorbed monomer amount (number/unit cell)[a]	Conversion (%)[a]	M_n (M_w/M_n)[b]	Tacticity[c] mm:mr:rr (m)
$[Cu_2(bpd)_2(ted)]_n$ (10.8×10.8)	5.3	49	48,000 (2.4)	22:49:29 (47)
$[Cu_2(bdc)_2(ted)]_n$ (7.5×7.5)	3.3	47	41,500 (1.7)	29:50:21 (54)
$[Cu_2(ndc)_2(ted)]_n$ (5.7×5.7)	2.7	0	–	–
$[Cu_2(adc)_2(ted)]_n$ (4.8×4.3)	1.9	0	–	–
$[Zn_2(bdc)_2(ted)]_n$ (7.5×7.5)	3.4	66	36,000 (2.0)	30:49:21 (55)
$[Zn_2(ndc)_2(ted)]_n$ (5.7×5.7)	2.6	0	–	–
$[Zn_2(adc)_2(ted)]_n$ (4.8×4.3)	1.8	0	–	–
Bulk polymerization[d]	–	–	n.d.[e]	22:50:28 (47)

[a] Determined by TGA

[b] Obtained by GPC calibrated by PMMA standards

[c] Determined by ^{13}C NMR measurement in DMSO-d_6 at 100°C after conversion to poly(vinyl alcohol) by saponification

[d] Bulk polymerization was carried out under comparable condition to those employed in PCPs

[e] The obtained polymer had high molecular weight portions over exclusion limit (M_w>5,000,000) of GPC column with extremely wide polydispersity (M_w/M_n>20)

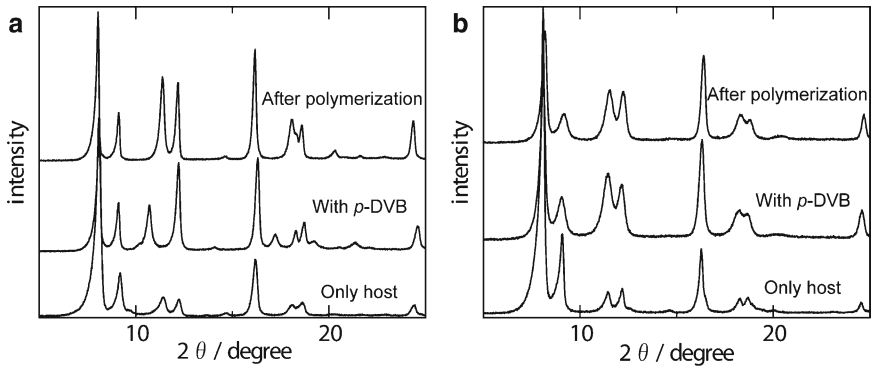

Fig. 4 XRPD patterns of (**a**) $[Zn_2(bdc)_2ted]_n$ and (**b**) $[Cu_2(bdc)_2ted]_n$ during the polymerization of *p*-DVB monomer in the nanochannels

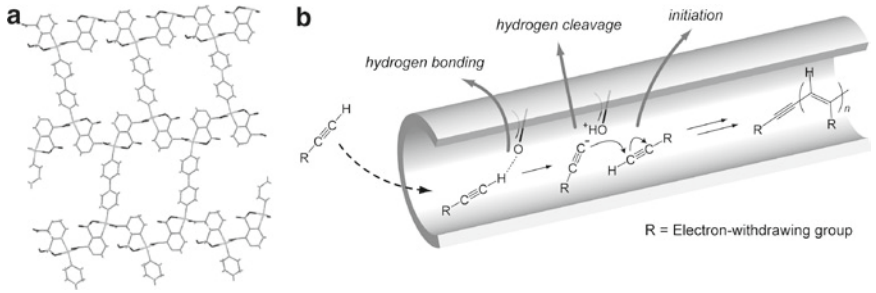

Fig. 5 (**a**) Nanochannel structure of $[Cu_2(pzdc)_2bpy]_n$. (**b**) Schematic illustration for nanochannel-promoted polymerization of acidic acetylenes in $[Cu_2(pzdc)_2bpy]_n$

Thus, the pore size, shape, and flexibility of PCPs strongly affect the dynamics and arrangement of the included monomers, and the behavior of the monomers is a key factor in promoting polymerization in the porous frameworks.

3.2 Catalytic Polymerization

It has been demonstrated that surface basic sites of PCPs successfully catalyze polymerization in the nanochannels. Thus, the pillared-layer complex $[Cu_2(pzdc)_2bpy]_n$ acted as a host for spontaneous polymerization of substituted acetylenes in a specific manner (Fig. 5) [67]. In the case of acidic monosubstituted acetylenes, the basic oxygen atoms from carboxylate ligands in $[Cu_2(pzdc)_2bpy]_n$ produced reactive acetylide species that subsequently initiated anionic polymerization in the nanochannel. Compared with a control experiment using a discrete model catalyst

(sodium benzoate), this polymerization system exhibited drastic acceleration of polymerization. For example, the reaction of methyl propiolate with the model catalyst at room temperature for 1 month gave only a trace amount of product. Increase in the reaction temperature to 70°C was also ineffective for polymerization. However, reaction of the acetylene monomer with $[Cu_2(pzdc)_2bpy]_n$ for 12 h at room temperature successfully provided the polymeric product. This unique catalytic polymerization mechanism in $[Cu_2(pzdc)_2bpy]_n$ was supported by IR measurement and computer simulation using a universal force field. The experiments with various combinations of acetylene monomers and host PCPs showed that an appropriate channel size, as well as the basic carboxylate moiety, is important for this spontaneous polymerization.

4 Control of Polymer Structures

4.1 Stereoregularity

One of the most important subjects in the field of polymer synthesis is stereocontrolled polymerizations. In particular, structural control of vinyl polymers to fabricate the desired stereoregularity (tacticity) is highly important, since tacticity strongly affects the properties of the polymer. Therefore, several research groups have intensively studied the control of the tacticity of vinyl polymers during solution radical polymerizations [68–73]. In these systems, the addition of fluoroalcohols or Lewis acids to the reaction media can lead to hydrogen bonding or coordinative interaction of the solvents or the additives with the polar groups in the monomers and/or the growing species, which causes stereospecific chain growth. However, this method can only be applied to monomers containing carbonyl group(s), and it is still uncertain whether steric or electronic interactions work on the stereostructures. Recently, stereocontrolled radical polymerization of vinyl monomers (St, MMA, and VAc) has been attained in nanochannels of $[M_2(L)_2ted]_n$ ($M = Cu^{2+}$ or Zn^{2+}), which led to an increase in isotacticity in the resulting polymers [65]. For example, the tacticity of Poly(methyl methacrylate) (PMMA) strongly depends on the pore size of the PCPs with an increase of 9% in isotacticity achieved by using $[Cu_2(ndc)_2ted]_n$ compared with that obtained from the bulk polymerization system (Table 2 and Fig. 6). When the VAc monomer was polymerized in the nanochannels of $[Zn_2(bdc)_2ted]_n$, the ratio of isotactic units in the Poly(vinyl acetate) (PVAc) structure clearly increased (8%) (Table 3). Because there is no specific interaction between the adsorbed monomers and the pore walls, effective through-space interactions by the nanochannels of the PCPs successfully induced the polymerizations with less stereo-bulky isotactic units. Thus, in this polymerization system, the nanochannel size effect on the tacticity of the vinyl polymers could be systematically studied, showing that controlled increase of isotacticity became possible in the polymerizations utilizing the size-tunable pores of PCPs.

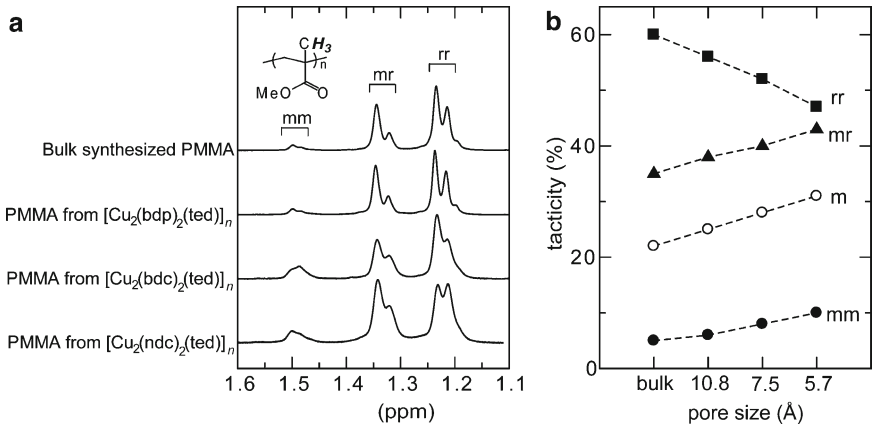

Fig. 6 (**a**) ^{1}H NMR spectra of Poly(methyl methacrylate) (PMMA) obtained from the nanochannels of $[Cu_2(L)_2(ted)]_n$ and the bulk condition in nitrobenzene-d_5 at 110°C. (**b**) Plot of nanochannel size effect on tacticity of PMMA

Much effort has also been devoted to stereocontrolled polymerization of the substituted acetylene monomers, because stereoregularity (*cis* and *trans* chain sequence) of resultant polyacetylenes affects their characteristic properties, such as conjugation length, conductivity, suprastructures, and processability [74–77]. A remarkably high stereoselectivity was achieved by the polymerization of substituted acetylenes in the nanochannels of $[Cu_2(pzdc)_2bpy]_n$ (Fig. 7) as determined by IR and UV-vis spectroscopies [67]. The narrow nanochannel structure can successfully direct the polymerization with *trans*-geometric addition, which strikingly contrasts with the result obtained by using a model catalyst (sodium benzoate) where only unfavorable cyclic byproducts (trisubstituted benzenes) and a *cis*-geometric polymer were obtained in very low yields.

4.2 Suppression of Cross-linking

The advent of efficient methods for controlling or suppressing cross-linking structures in polymerization reaction is required for the further development of functional polymer materials. For example, linear polymers bearing pendant vinyl groups in the backbones are attractive from the viewpoints of potential reactivity of the olefinic double bonds and application as polymer precursors [78, 79]. Usually, radical polymerization of DVBs in bulk or solutions results in the formation of hyper-branched network polymers, because the reactivity of the two vinyl moieties in DVBs is equivalent. However, a radical polymerization of DVBs in one-dimensional channels of $[M_2(bdc)_2ted]_n$ gave a linear polymer remaining pendant vinyl groups in all benzene rings, which was confirmed by solubility check and by IR,

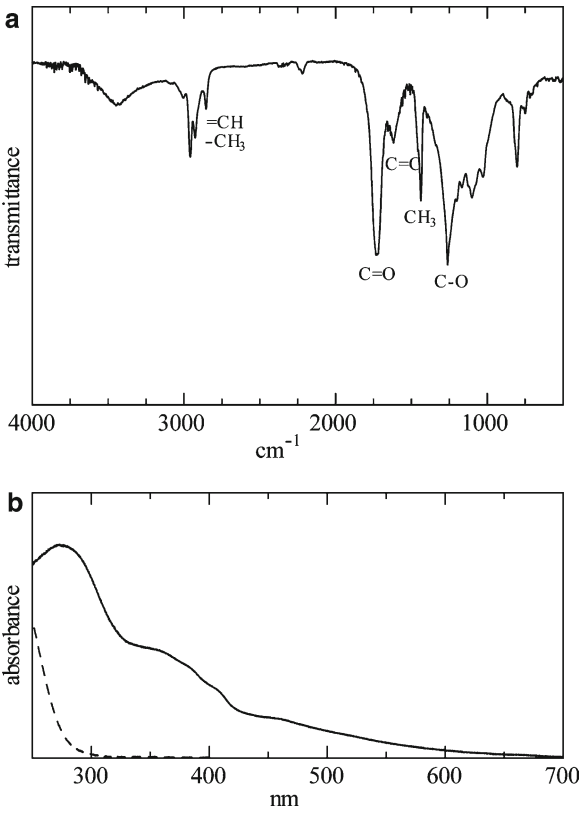

Fig. 7 (**a**) IR spectrum of poly(methyl propiolate) prepared in $[Cu_2(pzdc)_2bpy]_n$. The presence of a band at 970 cm^{-1} suggests that the *trans*-geometry is dominant in this polymer structure. (**b**) UV-vis absorption spectra of poly(methyl propiolate) prepared in $[Cu_2(pzdc)_2bpy]_n$ (solid line) and monomeric methyl propiolate (dot line) in chloroform. The appearance of a band at a longer wavelength (>480 nm) in the absorption spectrum of the polymer supports the highly conjugated *trans* form of poly(methyl propiolate)

UV-vis, and ^{1}H NMR spectroscopy [66]. For example, poly(*p*-DVB) obtained from $[Zn_2(bdc)_2ted]_n$ was soluble in various organic solvents such as THF, $CHCl_3$, DMF, DMSO, etc., which contrasts with the insoluble product formed from the usual radical polymerization of DVBs in solution and bulk. In the ^{1}H NMR spectrum of the polymer, peaks assignable to the β-carbon of vinyl groups were observed at 5.1 and 5.7 ppm. Comparison of the peak integrations between the aromatic and vinyl regions clearly shows that only one vinyl group of *p*-DVB was selectively polymerized to form the linear polymer, and unfavorable kink structures (branching and/or bonding through both 1,4-vinyl group) hardly formed during the reaction (Fig. 8). Thus, it is of considerable interest that the functional PCPs successfully directed the linearly extended polymerization of multivinyl monomers because of effective entrapment of the reactive propagating radical mediators in the one-dimensional nanochannels.

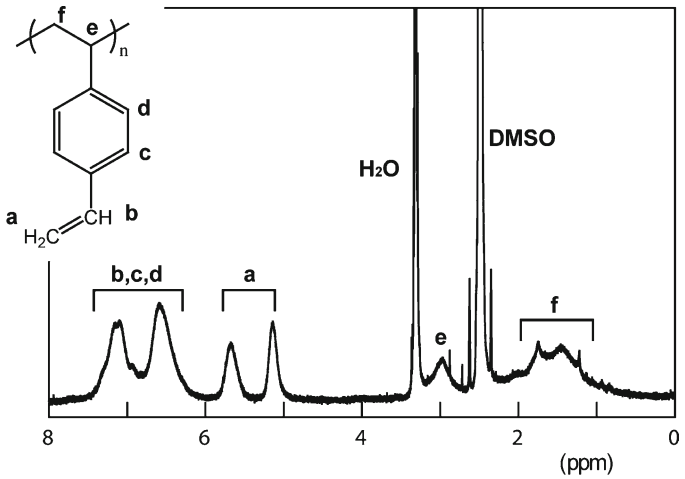

Fig. 8 ^{1}H NMR spectrum of poly(*p*-DVB) obtained from the nanochannel of $[Zn_2(bdc)_2ted]_n$ in DMSO-d_6. The ratio of the peak intensities of **a** to those of **b**, **c**, and **d** is found to be 2:5

To elucidate the importance and effect of channel size on this linear polymerization, polymerization of *p*-DVB in the framework of $[Cu_2(bpd)_2(ted)]_n$ with large open channels (pore size = 10.8×10.8 Å^2) was studied. In this case, the polymerization of *p*-DVB proceeded in high conversion (63%); however, the polymeric product isolated from the channels was insoluble in any solvents showing that semibranching cross-linked structures were formed in this large channel. This suggests that the design and control of channel size suitable for single molecular accommodation of *p*-DVB is also a key factor for successful selective linear polymerization.

Owing to the nonconjugated nature of its propagating radical, unfavorable chain transfer and termination reactions are observed particularly in the radical polymerization process of VAc. Thus, the resultant PVAc usually incorporates many branched structures. It is noteworthy that branch formations of PVAc were effectively suppressed during the polymerization in the nanochannels of PCPs [65]. The absolute value of the (M_w) weight-average molecular weight of PVAc prepared in $[Cu_2(bdc)_2ted]_n$, determined by multi-angle laser light scattering coupled with Gel permeation chromatography (GPC), was consistent with that obtained from a conventional GPC measurement using the same column. This fact clearly supports the less-branching linear structure of the obtained PVAc due to the constrained chain growth in the narrow one-dimensional nanochannel of $[Cu_2(bdc)_2ted]_n$.

4.3 Molecular Weight

To enhance and improve the properties of the polymeric materials, precision polymerization to control molecular weight and its polydispersity is particularly important. However, in the radical polymerization process, the control of molecular

weight is challenging because of the fact that the high reactivity of growing radical species usually causes unfavorable termination and chain transfer reactions. Recently, living radical polymerization of vinyl monomers in solution has emerged as an effective method for precision vinyl polymer synthesis, since this polymerization is free from the side reactions resulting from the introduction of dormant species and can thus give control of molecular weights [80–82].

It has been recently reported in the system of radical polymerizations of St and MMA utilizing the nanochannels of PCPs, that the molecular weight distributions of the resultant polymers became narrower with decrease in the host channel size, and eventually a value of 1.5 for M_w/M_n was attained in the polymerization of St using $[Zn_2(ndc)_2ted]_n$ (Table 1 and 2) [64, 65]. ESR spectroscopic measurements on propagating radicals in the nonmagnetic host $[Zn_2(bdc)_2ted]_n$, examined during the course of these polymerizations showed intense signals assigned to the propagating radical of both Polystyrene (PSt) and PMMA (Fig. 9), with the maximum radical concentrations of PSt and PMMA in $[Zn_2(bdc)_2ted]_n$ reaching 2.6 and 0.48 mmol kg^{-1}, respectively. These values are much higher than those detected in conventional solution radical polymerizations (10^{-4}–10^{-5} mmol kg^{-1}). It was also observed that after the polymerization of St in $[Zn_2(bdc)_2ted]_n$, the ESR signal for the propagating radical remains for 3 weeks even at 70°C. Thus, in this polymerization system, PCPs with small pore sizes could significantly stabilize the propagating radicals by efficient suppression of termination reactions in the nanochannels, realizing living radical polymerizations with narrow polydispersity of molecular weight.

Unlike St and MMA, the propagating radical of PVAc shows intractably high reactivity and less stability because of the lack of a conjugated substituent in the VAc monomer. Thus, achievement of a narrow molecular weight distribution of PVAc has still been limited, except for a few controlled living radical polymerization systems [83–88]. However, PVAc obtained from the nanochannels of PCPs showed small M_w/M_n values (e.g., M_w/M_n of PVAc prepared in $[Cu_2(bdc)_2ted]_n$ was 1.7) by GPC measurements, while PVAc prepared under similar bulk conditions

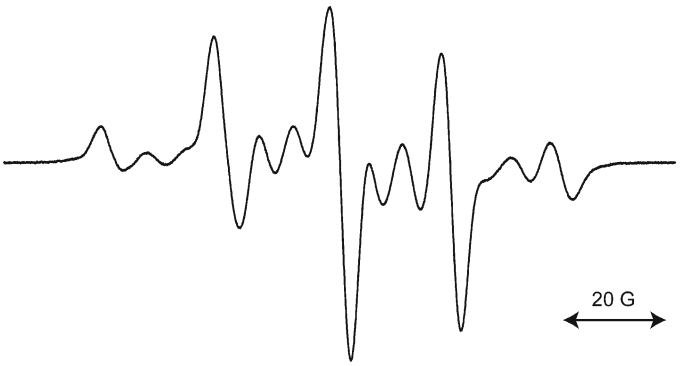

Fig. 9 ESR spectrum for propagating radical of Poly(methyl methacrylate) (PMMA) in the nanochannel of $[Zn_2(bdc)_2(ted)]_n$

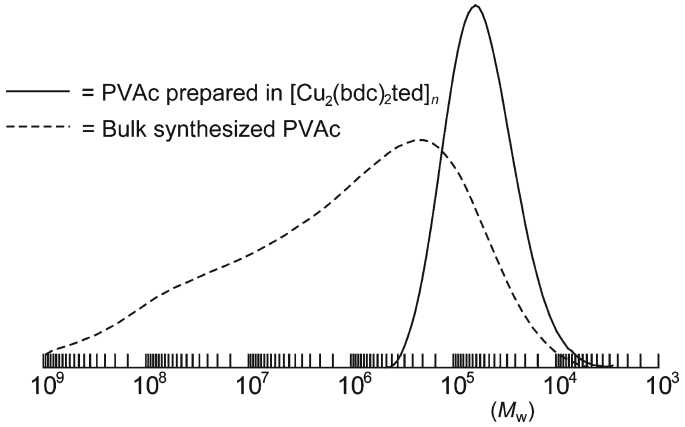

Fig. 10 Gel permeation chromatography (GPC) profiles of Poly(vinyl acetate) (PVAc) prepared in $[Cu_2(bdc)_2(ted)]_n$ and in the bulk condition

showed an extremely large polydispersity (M_w/M_n>20) of molecular weight caused by its hyper-branched structure derived from various side reactions (chain transfer and termination reactions) (Table 3 and Fig. 10) [65]. This illustrates the effect of narrow nanochannels in PCPs on the stabilization of growing PVAc radicals.

5 Concluding Remarks

The study on the polymerization of monomers encapsulated in channels of functional PCPs has provided significant opportunities for controlled polymerizations in terms of control of stereoregularity, topology, and molecular weight. The capability for designable nanochannels (regular channel structures, controllable channel size and surface functionality, and flexible frameworks) is one of the most powerful advantages of PCPs, which has led to systematic studies of inclusion polymerizations in microporous channels in these hosts. We believe that this polymerization system can provide a new aspect of controlled polymerizations, and is fundamentally important for the understanding of the role of pore size, geometry, and flexibility in attaining tailor-made polymerizations to obtain preferred polymer structures. From the viewpoint of applications, further research will be directed to the quest of polymer physics and properties in the nanochannels of PCPs, as well as construction of polymer-PCPs nanohybrids, in order to enhance the knowledge of applications to nanosize molecular-based devices.

Acknowledgments We thank all our collaborators and colleagues, whose names appear with us in a number of references, for their contributions. We are also grateful for financial supports from JST-PRESTO program, a Grant-in-Aid for Scientific Research in a Priority Area “Chemistry of

Coordination Space," and a Grant-in-Aid for Young Scientists (A) and (B) from the Ministry of Education, Culture, Sports, Science and Technology, Government of Japan.

References

1. Paleos CM (ed) (1992) Polymerization in organized media. Gordon & Breach, New York
2. Miyata M (1996) In: Reinhoudt D (ed) Comprehensive supramolecular chemistry, vol 10. Pergamon, Oxford, p 557
3. Farina M, Di Silvestro G, Sozzani P (1996) In: Reinhoudt D (ed) Comprehensive supramolecular chemistry, vol 10. Pergamon, Oxford, p 371
4. Moller K, Bein T (1998) Chem Mater 10:2950
5. Tajima K, Aida T (2000) Chem Commun 2399
6. Cardin DJ (2002) Adv Mater 14:553
7. Kobayashi S, Uyama H, Kimura S (2001) Chem Rev 101:3793
8. Serizawa T, Hamada KI, Akashi M (2004) Nature 429:52
9. White DM (1960) J Am Chem Soc 82:5678
10. Brown JF Jr, White DM (1960) J Am Chem Soc 82:5671
11. Chatani Y, Nakatani S, Tadokoro H (1970) Macromolecules 3:481
12. Allcock HR, Silverberg EN, Dundley GK (1994) Macromolecules 27:1033
13. Allcock HR, Dudley GK, Silverberg EN (1994) Macromolecules 27:1039
14. Farina M, Audisio G, Natta G (1967) J Am Chem Soc 89:5071
15. Farina M, Audisio G, Gramegna MT (1972) Macromolecules 5:617
16. Sozzani P, Di Silvestro G (1986) J Polym Sci Part A: Polym Chem 24:815
17. Miyata M, Morioka K, Takemoto K (1977) J Polym Sci Polym Chem Ed 15:2987
18. Miyata M, Kitahara Y, Osaki Y, Takemoto K (1984) J Incl Phenom 2:391
19. Bein T, Enzel P (1989) Angew Chem Int Ed 28:1629
20. Enzel P, Bein T (1989) J Phys Chem 93:6270
21. Enzel P, Bein T (1989) J Chem Soc Chem Commun 18:1326
22. Uehara H, Miyake M, Matsuda M, Sato M (1998) J Mater Chem 8:2133
23. Wu CG, Bein T (1994) Science 266:1013
24. Kageyama K, Tamazawa J, Aida T (1999) Science 285:2113
25. Lin VSY, Radu DR, Han MK, Deng W, Kuroki S, Shanks BH, Pruski M (2002) J Am Chem Soc 124:9040
26. Cardin DJ, Constantine SP, Gilbert A, Lay AK, Alvaro M, Galletero MS, Garcia H, Marquez F (2001) J Am Chem Soc 123:3141
27. Molenkamp WC, Watanabe M, Miyata H, Tolbert S (2004) J Am Chem Soc 126:4476
28. Sozzani P, Bracco S, Comotti A, Simonutti R, Valsesia P, Sakamoto Y, Terasaki O (2006) Nature Mater 5:545
29. Moulton B, Zaworotko MJ (2001) Chem Rev 101:1629
30. Janiak C (2003) Dalton Trans 2781
31. Kitagawa S, Kitaura R, Noro SI (2004) Angew Chem Int Ed 43:2334
32. Ockwig NW, Delgado-Friedrichs O, O'Keefe M, Yaghi OM (2005) Acc Chem Res 38:176
33. Férey G, Mellot-Draznieks C, Serre C, Millange F (2005) Acc Chem Res 38:217
34. Bradshaw D, Claridge JB, Cussen EJ, Prior TJ, Rosseinsky MJ (2005) Acc Chem Res 38:273
35. Kepert CJ (2006) Chem Commun 695
36. Kitagawa S, Noro SI, Nakamura T (2006) Chem Commun 701
37. Forster PM, Cheetham AK (2003) Top Catal 24:79
38. Kesanli B, Lin W (2003) Coord Chem Rev 246:305
39. Wu CD, Hu A, Zhang L, Lin W (2005) J Am Chem Soc 127:8940
40. Wu CD, Lin W (2007) Angew Chem Int Ed 46:1075

41. Fujita M, Kwon YJ, Washizu S, Ogura K (1994) J Am Chem Soc 116:1151
42. Seo JS, Whang D, Lee H, Jun SI, Oh J, Jeon YJ, Kim K (2000) Nature 404:982
43. Pan L, Liu H, Lei X, Huang X, Olson DV, Turro NJ, Li J (2003) Angew Chem Int Ed 42:542
44. Cho SH, Ma B, Nguyen SBT, Hupp JT, Albrecht-Schmitt TE (2006) Chem Commun 2563
45. Dybtsev DN, Nuzhdin AL, Chun H, Bryliakov KP, Talsi EP, Fedin VP, Kim K (2006) Angew Chem Int Ed 45:916
46. Hasegawa S, Horike S, Matsuda R, Furukawa S, Kinoshita Y, Kitagawa S (2007) J Am Chem Soc 129:2607
47. Uemura T, Horike S, Kitagawa S (2006) Chem Asian J 1:36
48. Eddaoudi M, Kim J, Rosi N, Vodak D, Wachter J, O'Keefe M, Yaghi OM (2002) Science 295:469
49. Chui SSY, Lo SMF, Charmant JPH, Orpen AG, Williams ID (1999) Science 283:1148
50. Kitaura R, Kitagawa S, Kubota Y, Kobayashi TC, Kindo K, Mita Y, Matsuo A, Kobayashi M, Chang HC, Ozawa T, Suzuki M, Sakata M, Takata M (2002) Science 298:2358
51. Higuchi M, Horike S, Kitagawa S (2007) Supramol Chem 19:75
52. Chen BL, Ockwig NW, Millward AR, Contreras DS, Yaghi OM (2005) Angew Chem Int Ed 44:4745
53. Schlichte K, Kratzke T, Kaskel S (2004) Micropor Mesopor Mater 73:81
54. Kosal ME, Chou JH, Wilson SR, Suslick KS (2002) Nature Mater 1:118
55. Matsuda R, Kitaura R, Kitagawa S, Kubota Y, Belosludov RV, Kobayashi TC, Sakamoto H, Chiba T, Takata M, Kawazoe Y, Mita Y (2005) Nature 436:238
56. Shin DM, Lee IS, Chung YK (2003) Inorg Chem 42:8838
57. Uemura K, Matsuda R, Kitagawa S (2005) J Solid State Chem 178:2420
58. Bradshaw D, Warren JE, Rosseinsky MJ (2007) Science 315:977
59. Serre C, Mellot-Draznieks C, Surblé S, Audebrand N, Filinchuk Y, Férey G (2007) Science 315:1828
60. Kitaura R, Seki K, Akiyama G, Kitagawa S (2003) Angew Chem Int Ed 42:428
61. Halder GJ, Kepert CJ, Moubaraki B, Murray KS, Cashion JD (2002) Science 298:1762
62. Moad G, Solomon DH (eds) (2006) The chemistry of radical polymerization, 2nd edn. Elsevier, Oxford
63. Matyjaszewski K, Davis TP (eds) (2002) Handbook of radical polymerization. Wiley-Interscience, Hoboken
64. Uemura T, Kitagawa K, Horike S, Kawamura T, Kitagawa S, Mizuno M, Endo K (2005) Chem Commun 5968
65. Uemura T, Ono Y, Kitagawa K, Kitagawa S (2008) Macromolecules 41:87
66. Uemura T, Hiramatsu D, Kubota Y, Takata M, Kitagawa S (2007) Angew Chem Int Ed 46:4987
67. Uemura T, Kitaura R, Ohta Y, Nagaoka M, Kitagawa S (2006) Angew Chem Int Ed 45:4112
68. Habaue S, Okamoto Y (2001) Chem Rec 1:46
69. Kamigaito M, Sato K (2008) Macromolecules 41:269
70. Lutz JF, Neugebauer D, Matyjaszewski K (2003) J Am Chem Soc 125:6986
71. Lutz JF, Jakubowski WD, Matyjaszewski K (2004) Macromol Rapid Commun 25:486
72. Wan D, Satoh K, Kamigaito M, Okamoto Y (2005) Macromolecules 38:10397
73. Hirano T, Ishii S, Kitajima H, Seno M, Sato T (2005) J Polym Sci Part A: Polym Chem 43:50
74. Maeda K, Goto H, Yashima E (2001) Macromolecules 34:1160
75. Nakako H, Nomura R, Tabata M, Masuda T (1999) Macromolcules 32:2861
76. Tabata M, Inaba Y, Yokota K, Nozaki Y (1994) J Macromol Sci Pure Appl Chem A31:465
77. Furlani A, Napoletano C, Russo MV, Feast WJ (1986) Polym Bull 16:311
78. Li Z, Day M, Ding JF, Faid K (2005) Macromolecules 38:2620
79. Koo JS, Smith PGR, Williams RB, Grossel MC, Whitcombe MJ (2002) Chem Mater 14:5030
80. Kamigaito K, Ando T, Sawamoto M (2001) Chem Rev 101:3689

81. Matyjaszewski K, Xia J (2001) Chem Rev 101:2921
82. Hawker CJ (1997) Acc Chem Res 30:373
83. Wakioka M, Baek KY, Ando T, Kamigaito M, Sawamoto M (2002) Macromolecules 35:330
84. Iovu MC, Matyjaszewski K (2003) Macromolecules 36:9346
85. Simms RW, Davis TP, Cunningham MF (2005) Macromol Rapid Commun 26:592
86. Koumura K, Satoh K, Kamigaito M, Okamoto Y (2006) Macromolecules 39:4054
87. Debuigne A, Caille JR, Jérôme R (2005) Macromolecules 38:5452
88. Debuigne A, Caille JR, Detrembleur C, Jérôme R (2005) Angew Chem Int Ed 44:3439

Top Curr Chem (2010) 293: 175–205
DOI 10.1007/128_2009_20

Published online: 4 December 2009

Designing Metal-Organic Frameworks for Catalytic Applications

Liqing Ma and Wenbin Lin

Abstract Metal-organic frameworks (MOFs) are constructed by linking organic bridging ligands with metal-connecting points to form infinite network structures. Fine tuning the porosities of and functionalities within MOFs through judicious choices of bridging ligands and metal centers has allowed their use as efficient heterogeneous catalysts. This chapter reviews recent developments in designing porous MOFs for a variety of catalytic reactions. Following a brief introduction to MOFs and a comparison between porous MOFs and zeolites, we categorize catalytically active achiral MOFs based on the types of catalytic sites and organic transformations. The unsaturated metal-connecting points in MOFs can act as catalytic sites, so can the functional groups that are built into the framework of a porous MOF. Noble metal nanoparticles can also be entrapped inside porous MOFs for catalytic reactions. Furthermore, the channels of porous MOFs have been used as reaction hosts for photochemical and polymerization reactions. We also summarize the latest results of heterogeneous asymmetric catalysis using homochiral MOFs. Three distinct strategies have been utilized to develop homochiral MOFs for catalyzing enantioselective reactions, namely the synthesis of homochiral MOFs from achiral building blocks by seeding or by statistically manipulating the crystal growth, directing achiral ligands to form homochiral MOFs in chiral environments, and incorporating chiral linker ligands with functionalized groups. The applications of homochiral MOFs in several heterogeneous asymmetric catalytic reactions are also discussed. The ability to synthesize value-added chiral molecules using homochiral MOF catalysts differentiates them from traditional zeolite catalysis, and we believe that in the future many more homochiral MOFs will be designed for catalyzing numerous asymmetric organic transformations.

L. Ma and W. Lin (✉)
Department of Chemistry, University of North Carolina, CB#3290, Chapel Hill, NC 27599, USA
e-mail: wlin@unc.edu

Keywords Chiral, Enantioselectivity, Heterogeneous·catalysis, Metal-organic frameworks, Porous, Size selectivity

Contents

Abbreviations

BDC	1,4-Benzenedicarboxylate acid
BET	Brunauer-Emmett-Teller
BINOL	1,1′-binaphthalene-2,2′-diol
BPDC	Biphenyl-4,4′-dicarboxylic acid
BTC	Benzene-1,3,5-tricarboxylate
MOFs	Metal-organic frameworks
SBU	Secondary building unit
TOF	Turn over frequency

1 Introduction

Metal-organic frameworks (MOFs), a new generation of hybrid materials built from organic bridging ligands and metal-connecting points, have received increasing attention over the past decade [1]. Much of the interest in MOFs arises from the tunability of such materials which allows their use in a number of applications [2–7]. One of the most extraordinary features of MOFs is their extremely high porosity. The resulting channels and cavities have sizes ranging from a few

Angstroms to several nanometers depending on the size of the ligands and the connectivity of the networks. The high porosity of MOFs has allowed their use in gas storage [8–11], most notably having shown promise in hydrogen storage which is one of the key hurdles for the future hydrogen economy.

The ability to incorporate catalytically active metal-connecting points or other functional groups into highly porous MOFs has allowed their applications in heterogeneous catalysis. Porous MOFs can be understood in analogy to the well-established microporous zeolites which have played a key role in catalytic processing of many important commodity chemicals. Zeolites are crystalline aluminosilicates constructed from interconnected SiO_4 and AlO_4 tetrahedra with charge-balancing organic and inorganic cations or protons. The resulting 3D frameworks are microporous with channels/cavities of up to 1.0 nm. These well-defined pore environments provide size- and shape-selectivity during the catalytic processes, and as such, zeolites have been widely used as selective catalysts in the petrochemical industry (such as fluid catalytic cracking and hydro-cracking). Such heterogeneous catalytic reactions improve gasoline quality, and significantly reduce the pollution from combustion engines.

Templating with different structure-directing agents (SDAs) has led to the synthesis of numerous zeolites with varied Si/Al molar ratios (and therefore varied acidity) and pore sizes and structures (Fig. 1). Such structural diversity is key to the processing of many organic molecules. However, the number of zeotypes is limited by the fixed tetrahedral coordination of the Si/Al connecting points and the oxide linker. It is also difficult to obtain zeolites with pore sizes larger than 1 nm, which limits the catalytic applications of zeolites to relatively small organic molecules (typically no larger than xylenes). Lastly, in spite of decades of research efforts, chiral

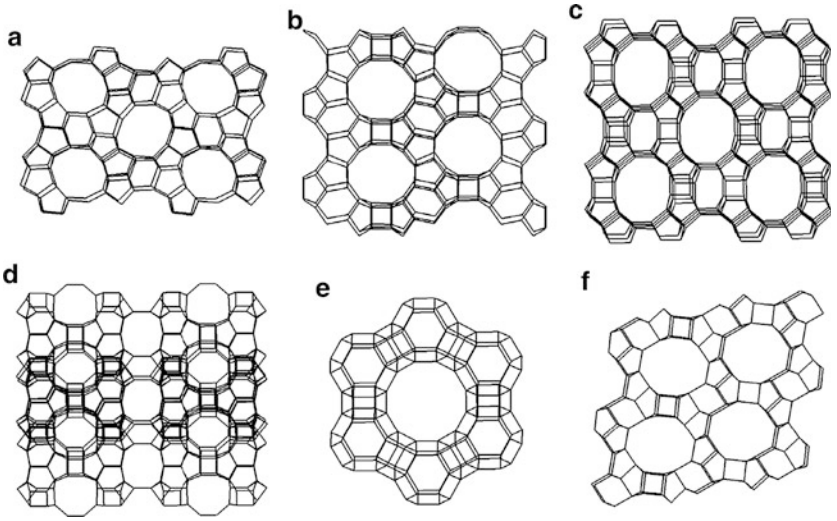

Fig. 1 Structures of zeolites ZSM-5 (**a**), mordenite (**b**), Beta (**c**), MCM-22 (**d**), zeolite Y (**e**), and zeolite L (**f**) (modified from [51])

zeolites still cannot be obtained in enantiopure form, which prevents applications of zeolites in catalytic asymmetric synthesis of value-added chiral molecules for the pharmaceutical, agrochemical, and fragrance industries.

Unlike zeolites that are built from interconnected tetrahedral aluminosilicates, MOFs can be constructed by linking a large variety of organic bridging ligands with many metal centers of diverse oxidation states and coordination geometries. Effectively, MOFs can be synthesized from an infinite number of metal/ligand combinations and thus have far greater diversity in structures, functional groups, and pore sizes and shapes. Greater tunability of porous MOFs should then allow for their use in catalytic reactions that cannot be realized with zeolites. Figure 2 exemplifies the structural tunability of MOFs. Para-aryl dicarboxylic acids of different lengths – 1,4-benzenedicarboxylate acid (BDC1,4-Benzenedicarboxylic acid), biphenyl-4,4′-dicarboxylic acid (BPDC) and *p*-terphenyl-4,4′-dicarboxylic acid – reacted with zinc(II) ions to lead to a series of isoreticular 3D porous MOFs. They are built from the same $Zn_4(\mu_4\text{-}O)(carboxylate)_6$ secondary building units (SBUs) which are further linked by dicarboxylate linkers to form cubic 3D networks. The pore and channel sizes of this family of isoreticular 3D MOFs can thus be readily tuned by simply adjusting the ligand length. The combination of a large inventory of organic bridging ligands and metal connectors has already led to numerous stable porous MOFs with a broad range of pore sizes and shapes.

Active catalytic sites in MOFs can be generated in several ways. First, the metal or metal cluster connecting points can be used to catalyze organic transformations. As shown in Scheme 1, a metal connecting point with a free coordinating site can be used as a Lewis acid catalyst after removal of coordinating solvent molecules from the axial positions of the metal center [12]. Metal cluster connecting points have also been used as active catalytic sites [13]. Second, active catalytic sites can be generated from the functional groups within a MOF scaffold (Scheme 2) [14, 15]. However, unlike traditional immobilized catalysts, the active catalytic sites generated in this fashion are arranged in a predictable and tunable manner due to the periodically ordered nature of the porous MOFs. Third, the catalytic activity of

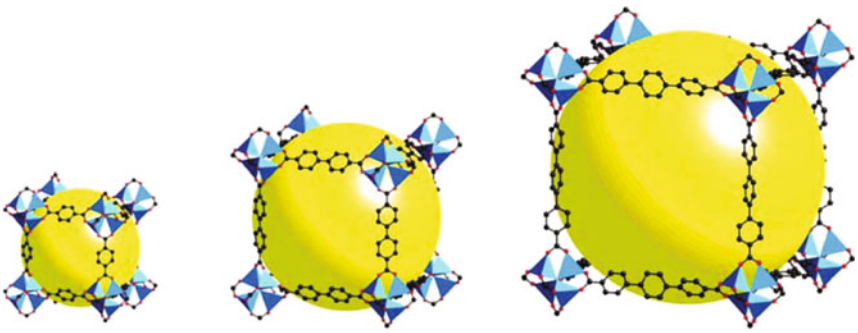

Fig. 2 MOFs constructed from linear dicarboxylate linkers showing different pore sizes as a result of different lengths of bridging ligands

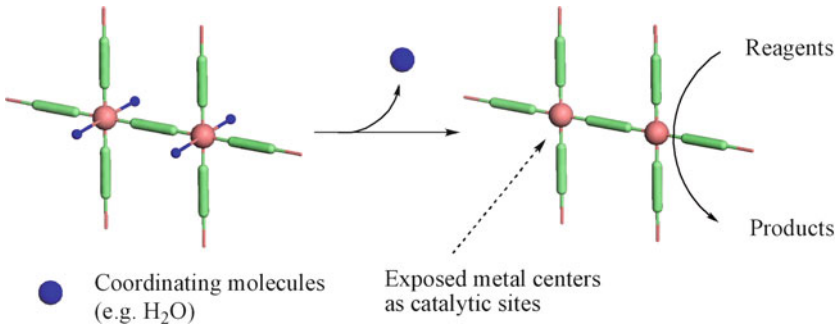

Scheme 1 Schematic illustrating the generation of unsaturated metal connecting points as active catalytic sites

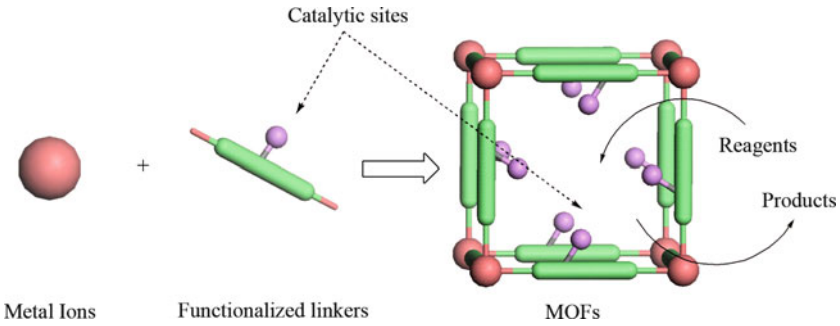

Scheme 2 Schematic showing the use of functional groups in the bridging ligands as active catalysts

MOFs can result from entrapped active catalysts, such as palladium or ruthenium nanoparticles (Scheme 3) [16, 17]. Finally, the pores and channels of MOFs can act as hosts with exquisite size selectivity for photochemical and polymerization reactions.

Among the many types of catalytic reactions, asymmetric catalysis is of great importance in industrial production of enantiomerically pure products. During the past few decades, much research effort has been devoted to the development of chiral zeolites and some other chiral porous materials having asymmetric catalytic sites. However, the traditional preparation procedures of zeolites require the removal of surfactant templates at the high temperatures of 400–550°C. Under such harsh conditions, the chirality of the preintroduced chiral surfactants, which are used to integrate silicate-surfactant assemblies into chiral conformations, is irreversibly destroyed. Therefore, an enantiomerically pure form of zeolite is not available to date. Compared to the syntheses of zeolites, homochiral MOFs can be

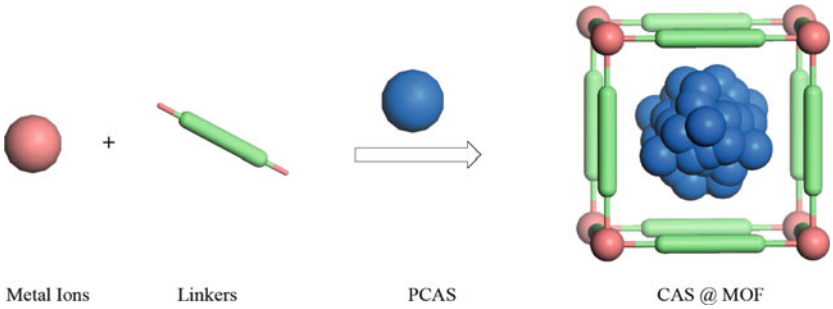

Scheme 3 Schematic representation of trapping catalytic active species (CAS) inside MOFs. (PCAS: precursor to CAS)

readily obtained under mild conditions and are expected to play an important role in heterogeneous asymmetric catalysis.

Although a very large number of MOFs have been reported in the past two decades, only a small number of them have been explored for catalytic applications. In this chapter we highlight recent developments in catalytically active MOFs. We first categorize achiral MOF catalysts based on the types of catalytic sites and organic transformations, followed by discussions on heterogeneous asymmetric catalysts based on homochiral MOFs.

2 Metal-Organic Frameworks as Achiral Catalysts

2.1 Metal Connecting Points in MOFs as Catalytic Sites

2.1.1 Cyanosilylation and Other Lewis Acid-Catalyzed Reactions

The metal-connecting points in MOFs often coordinate to labile solvent molecules or counter ions which can be replaced by organic substrates. The Lewis acidic nature of such metal centers can activate the coordinated organic substrates for subsequent organic transformations. Fujita and coworkers reported the first example of catalytically active MOFs based on this strategy in 1994 [18, 19]. When the linear bridging ligand 4,4′-bipyridine was treated with $Cd(NO_3)_2$, a colorless crystal with the composition of $[Cd(4,4'\text{-byp})_2(H_2O)_2](NO_3)_2\ 4H_2O$ (**1**) was obtained. The Cd(II) centers in **1** adopt a distorted octahedral geometry by coordinating to four pyridines at the equatorial positions, and two water molecules in the axial positions to form a 2D infinite network (Fig. 3). The stacking pattern of such 2D layers is illustrated in Fig. 3b. The substrates can be hosted by the cavity of the first layer (space-filled), and further interact with the Lewis acid Cd(II) catalytic center in the

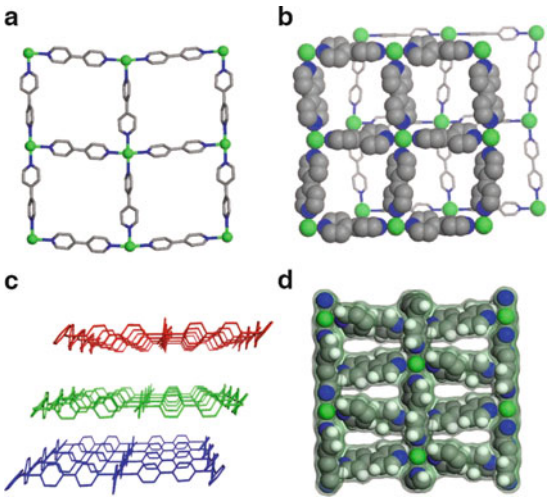

Fig. 3 Two dimensional networks of **1** (**a**), and the stacking pattern of two adjacent layers of **1** (**b**) and those layers were separated by each other by a distance of 4.8 Å (**c**). Packing diagram of **1** along *c* axis shows only very small open channels (**d**)

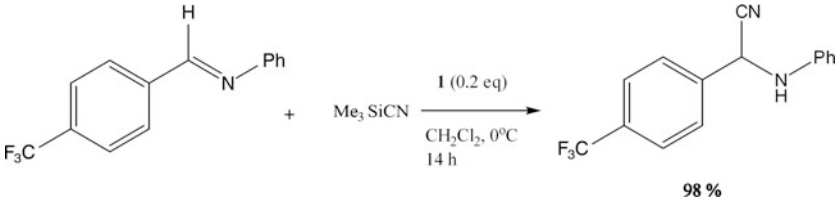

Scheme 4 Cyanosilylation of imines catalyzed by **1**

second layer (green ball). These layers are separated by an interlayer distance of 4.8 Å (Fig. 3c).

The activity of the Cd(II) centers in **1** as Lewis acid catalysts was illustrated by cyanosilylation of aldehydes and imines. For the cyanosilylation of imines, most of the reactions were complete within 1 h to afford aminonitriles in quantitative yield. When the crystals were immersed in a CH_2Cl_2 solution with imines, there was no detectable amount of entrapped imines in the solid, indicating that the open channels of the frameworks were too small to accommodate imines used in the reactions. It was thus suggested that the catalytic reactions might have exclusively taken place on the surfaces of the crystals.

The authors took advantage of the much slower cyanosilylation rate of CF_3-substituted imine to monitor the reaction process (Scheme 4). In order to prove that the cyanosilylation was catalyzed by solid **1** heterogeneously, the solid catalyst was filtered after 0.25 and 1 h of reaction, respectively. After the removal of the solid catalyst, the reaction was not promoted any further, and the conversion remained at 21 and 59%, respectively (Fig. 4). The catalytic reactivity of **1** was further

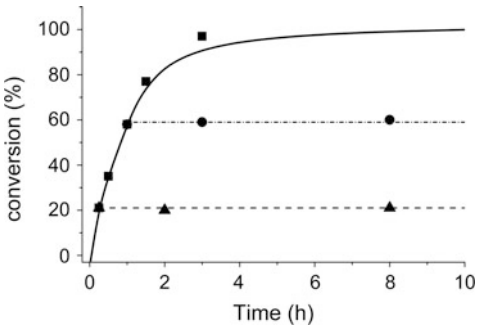

Fig. 4 Conversion of CF_3-substituted imine catalyzed by **1**. Dash and dot lines indicate the conversion after filtration of solid **1** at 0.25 and 1 h

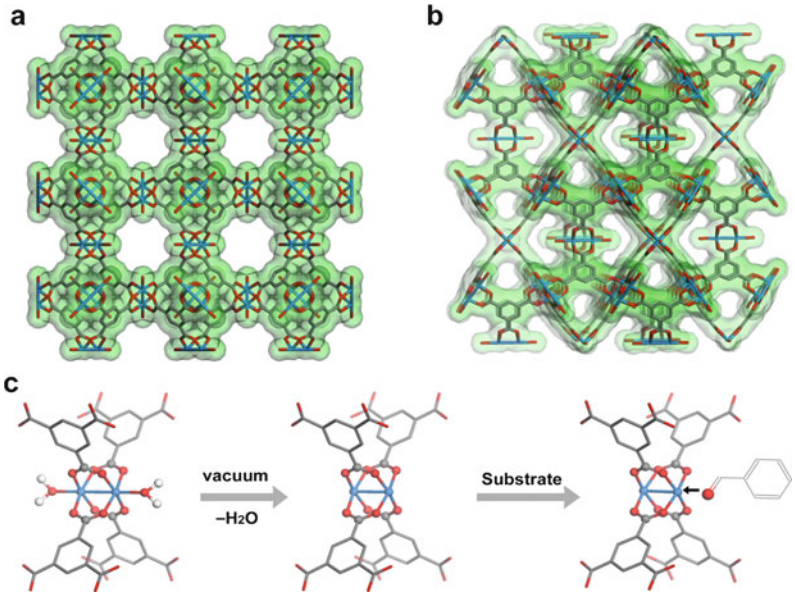

Fig. 5 Polymeric frameworks of **2** as viewed down the *c* axis (**a**) showing nanometer scale channels, and the projection on [101] plane (**b**); generation of the reagent accessible sites after dehydration of **2** (**c**)

compared with $Cd(Py_4)(NO_3)_2$ that bears the partial structure of **1**. $Cd(Py_4)(NO_3)_2$ promoted the reaction much less effectively, suggesting reaction rate enhancement in **1** as a result of stronger binding of the imine substrate to the hydrophobic grid cavities of **1**.

Kaskel and coworkers carried out similar cyanosilylation reactions with coordinatively unsaturated metal connecting points in 3D MOFs as heterogeneous catalysts [20]. The 3D framework $[Cu_3(BTC)_2(H_2O)_3]$ (**2**) (BTC: benzene-1,3,5-tricarboxylate) used in this study was first reported by Williams et al. [21]. The open framework of **2** is built from dimeric cupric tetra-carboxylate units (paddle-wheels) with aqua molecules coordinating to the axial positions and BTC bridging

ligands. The resulting frameworks possess channels of ~1 nm in size running through the [110] direction (Fig. 5a), and its porosity was confirmed by N_2 adsorption experiments which gave a Langmuir surface area of 918 $m^2\ g^{-1}$, and a pore volume of 0.33 $cm^3\ g^{-1}$.

As-synthesized **2** was first activated by heating at 373 K under vacuum to remove the H_2O molecules on the axial positions of the copper paddle wheels. The resulting coordinatively unsaturated Lewis acidic Cu(II) centers can coordinate to the aldehyde substrates to promote the cyanosilylation reaction (Fig. 5c). Activated **2** catalyzes the trimethylcyanosilylation of benzaldehydes with a very low conversion (<5% in 24 h) at 293 K. As the reaction temperature was raised to 313 K, a good conversion of 57% with a selectivity of 89% was obtained after 72 h. In comparison, less than 10% conversion was observed for the background reaction (without **2**) under the same conditions. The heterogeneous nature of this catalyst system was demonstrated by removing the solid from the reaction mixture after 8 h of initial reaction (8% conversion at this point). The conversion of the colorless filtrate did not increase any further after the removal of the solid catalyst.

The limitation of MOFs as heterogeneous catalysts was revealed in this study. First, the decomposition of the framework of **2** became apparent as the reaction temperature was raised above 333 K due to the reduction of Cu(II) to Cu(I) by aldehydes. Second, strong solvent inhibition effect was also observed. Electron-donating solvents such as THF competed with aldehydes for coordination to the Cu (II) sites, and no cyanosilylation product was observed in these solvents. Finally, the framework of **2** was not stable in some organic solvents, as demonstrated by the decomposition of **2** in CH_2Cl_2 even at room temperature. As a result, **2** gave the best activity for cyanosilylation of aldehydes in nonpolar solvents such as pentane in a limited temperature range.

Several other groups have also reported the use of metal-connecting points in MOFs as catalysts. For example, Lin and coworkers reported a series of lanthanide phosphonates possessing both Lewis and Brönsted acid sites that were capable of catalyzing cyanosilylation of aldehydes and ring opening of *meso*-carboxylic anhydrides [12]. These materials exhibit lamellar structures that can swell to facilitate the access of substrates with a wide range of dimensions. Long and coworkers reported a rigid 3D MOF with exposed Mn(II) centers residing in the open channels [22]. These Lewis acidic sites effectively catalyzed the cyanosilylation with a high level of size-selectivity due to the rigid 3D framework structure. The previously mentioned $[Cu_2(BTC)_2]$ was also reported as a Lewis acid catalyst for the isomerization of terpene derivatives [23].

2.1.2 Oxidation of Alcohols, Thiols, and Thio Ethers

The electron-deficient nature of some metal-connecting points and clusters makes the resulting MOFs efficient oxidation catalysts. It is well established that binuclear copper complexes can be used as oxidation catalysts with oxygen or H_2O_2 as the oxidant [24]. Mori and coworkers reported MOFs with $[Cu_2(OOCR)_4]$

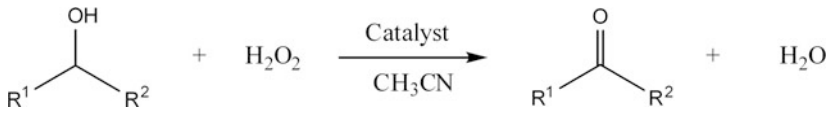

Scheme 5 Catalytic oxidation of alcohols by hydrogen peroxide

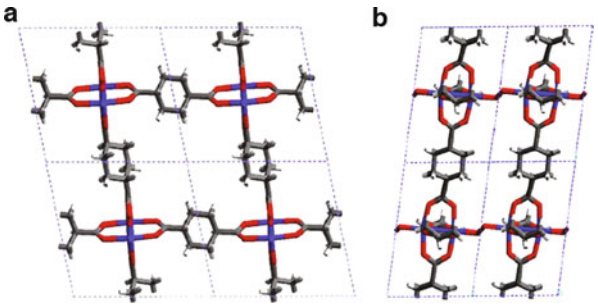

Fig. 6 (**a**) 2D structure of **3**, viewed along *c* axis. (**b**) Structure of frameworks **4**, viewed along the *b* axis, showing linking of 2D networks by the peroxo groups. (modified from [25])

paddle wheel units as heterogeneous catalysts for the oxidation of alcohols (Scheme 5) [25].

The 2D framework $[Cu_2(O_2CC_6H_{10}CO_2)_2]$, **3**, was synthesized by reacting 1, 4-cyclohexanedicarboxylic acid with a copper(II) salt. The 2D framework structure in **3** is built form linking the $[Cu_2(OOCR)_4]$ paddle wheel units with *trans*-1, 4-cyclohexanedicarboxylate bridging ligands. Addition of H_2O_2 to the suspension of frameworks **3** led to green copper peroxo framework **4**. Upon forming the peroxo complex **4**, 2D layers of $[Cu_2(O_2CC_6H_{10}CO_2)_2]$ grids were linked by the 1,2-*trans*-Cu-O-O-Cu species to form a 3D framework structure (Fig. 6).

The porosity of the complexes **3** and **4** was characterized by N_2 adsorption experiments. The adsorption isotherms showed typical Langmuir type isotherms, indicating the presence of micropores in both **3** and **4**. Analyses of the adsorption isotherms revealed the same effective pore diameter of 4.9 Å in both frameworks, and a BET surface area of 393.9 $m^2\ g^{-1}$ and 328.4 $m^2\ g^{-1}$ for **3** and **4**, respectively.

The catalytic activity of complex **3** was investigated by carrying out alcohol oxidation with H_2O_2 as the oxidant (Table 1). Complex **3** catalyzed the oxidation of primary alcohol, secondary alcohol and benzyl alcohols with high selectivity. The oxidation of 2-propanol showed faster reaction rate and higher conversion than that of cyclohexanol. Such a difference might be attributed to the smaller size of 2-propanol which made it easier to enter the cavities of the microporous framework. In terms of reaction mechanism, complex **4** could be considered as an active intermediate during the reaction process catalyzed by **3**. This assumption was confirmed by the detection of ketone when treating alcohols with **4** in the absence of H_2O_2.

Table 1 Oxidation of alcohol with H_2O_2 catalyzed by **3***

Entry	Substrate	Selectivity (%)	TOF (s^{-1})	Conversion (%) (h)
1[a]	2-Propanol	Acetone (>99%)	1.6×10^{-3}	17.1 (1)
2[b]	2-Propanol	Acetone (>99%)	5.8×10^{-3}	55.6 (3)
3[c]	Cyclohexanol	Cyclohexanone (>99%)	1.1×10^{-4}	14.3 (168)
4[b]	Cyclohexanol	Cyclohexanone (>99%)	1.6×10^{-4}	19.8 (168)
5[a]	Benzylalcohol	Benzaldehyde (>99%)	7.0×10^{-4}	16.7 (144)
6[b]	Benzylalcohol	Benzaldehyde (>99%)	1.5×10^{-3}	25.8 (144)
7[a]	1-Octanol	Octylaldehyde (>99%)	1.1×10^{-4}	10.8 (168)
8[b]	1-Octanol	Octylaldehyde (>99%)	1.6×10^{-4}	13.2 (168)

*Excess of H_2O_2 was used
[a]23-fold
[b]113-fold
[c]46-fold

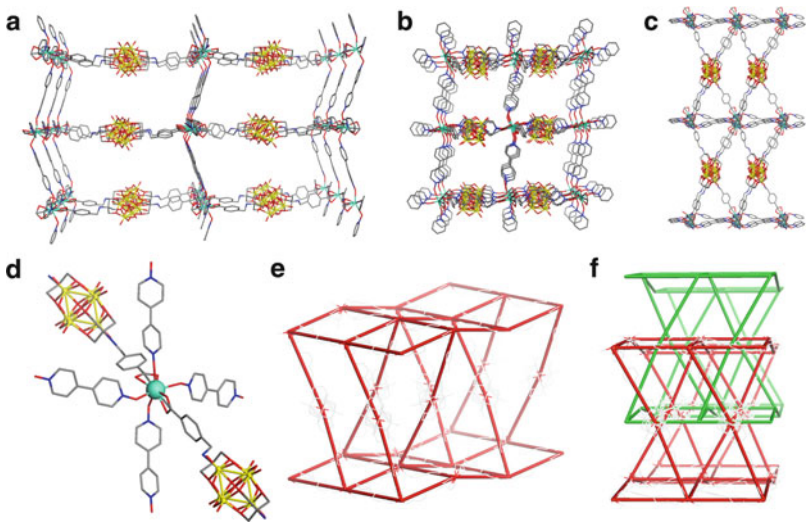

Fig. 7 2D sheets of Tb(III) centers interconnected by bpdo linkers leading to 3D networks **5** as viewed down the *a* axis (**a**); *b* axis (**b**) and *c* axis (**c**). (**d**) Tb coordination environment in **5**. (**e**) Simplified schemes of the networks (onefold shown) of **5**. (**f**) Schematic representation of the twofold interpenetrating networks of **5**

Hill et al. have demonstrated the sulfoxidation of thioethers using an MOF based on vanadium-oxo cluster V_6O_{13} building units [13]. The 3D MOF Tb $[V_6O_{13}\{(OCH_2)_3C\text{-}(NHCH_2C_6H_4\text{-}4\text{-}CO_2\}_2\{bpdo\}_2]$, (**5**, bpdo = 4,4′-bis(pyridine-N-oxide)) was prepared by slow diffusion between $Tb(NO_3)_3$ and bpdo/$[V_6O_{13}\{(OCH_2)_3C\text{-}(NHCH_2C_6H_4\text{-}4\text{-}CO_2)\}_2]^{4-}$ (**V-1**). Compound **5** is built from linking 2D grids comprising Tb(III) centers and bpdo units by **V-1** into the 3D framework. Two independent 3D networks in **5** interpenetrate to lead to

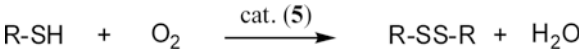

Scheme 6 Oxidation of thiols catalyzed by **5**

microporous channels with the dimensions of 8.0 × 5.2 Å along the crystallographic *a*-axis (Fig. 7).

The vanadium oxide clusters in **5** showed catalytic activity in the sulfoxidation of thioethers or thiols (Scheme 6). When *tert*-butylhydroperoxide (TBHP) was used as an oxidant, tetrahydrothiophene (THT) was oxidized much faster with **5** than in the control experiment without **5**. More importantly, such sulfoxidation could be performed with **5** as catalyst using ambient air as oxidant. However, formation of the desired product dipropylsulfane (PrSSPr) was very slow, and a 41% yield was obtained after 30 days at 45°C.

Several other MOFs have also been used as oxidation catalysts. Kim and coworkers used $[Zn_2(BDC)(L\text{-Lac})(DMF)]\cdot(DMF)$ as a heterogeneous catalyst for the oxidation of thioethers to sulfoxides by urea hydroperoxide (UHP) or hydrogen peroxide (H_2O_2) [26]. Its size selectivity was illustrated by the higher conversion of smaller sulfides over larger ones. Snejko and coworkers reported the use of $In_2(OH)_3(BDC)_{1.5}$ [27] and $[Sc_2(BDC)_3]$ [28] as active catalysts for the oxidation of alkylphenylsulfides.

2.2 MOFs Containing Functional Linkers as Catalytic Sites

2.2.1 Amide-Catalyzed Knoevenagel Condensation Reactions

In many MOFs, all of the coordination sites around the metal centers are occupied by linker ligands, and it is difficult to use the metal connecting points as catalytic sites in these materials. An alternative strategy in this case is to exploit the functional groups on the linker ligands for potential catalytic activities. In order to construct such catalytically active MOFs, the functional groups in the linker ligands must be able to sustain the conditions used for synthesizing the frameworks or can be regenerated in the postmodification of the frameworks. The functional groups within the resulting frameworks must be accessible to the reagents through the open channels. Kitagawa and coworkers reported a 3D MOF $\{[Cd(4\text{-btapa})_2(NO_3)_2]\cdot 6H_2O\cdot 2DMF\}$ (**6**, 4-btapa = 1,3,5-benzene tricarboxylic acid tris [*N*-(4-pyridyl)amid]) constructed by tridentate amide linkers and cadmium salt [14]. The pyridine groups on the ligand 4-btapa act as ligands binding to the octahedral cadmium centers, while the amide groups can provide the functionality for interaction with the incoming substrates (Scheme 7). Specifically, the – NH moiety of the amide group can act as electron acceptor whereas the –C=O group can act as electron donor to activate organic substrates for subsequent reactions.

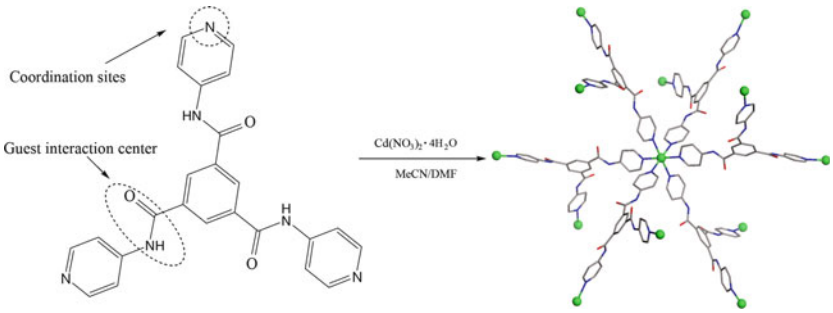

Scheme 7 Synthetic scheme for MOFs that contain amide groups in the bridging ligands

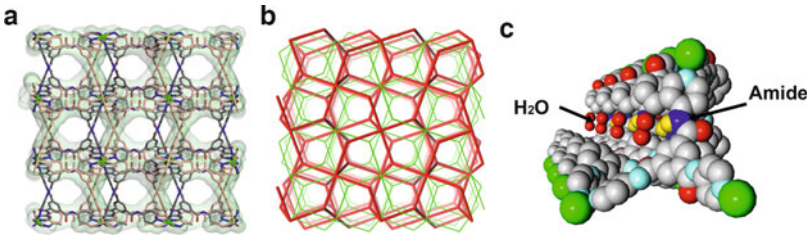

Fig. 8 Twofold interpenetrating structure of **6** showing 3D channels of dimensions of 4.7 × 7.3 Å (**a**), and its simplified scheme (**b**). (**c**) View of ordered amide groups facing the open channels of **6**, with H_2O molecules binding to –NH group through hydrogen bonding

Compound **6** adopts a twofold interpenetrating framework structure with free amide groups pointing towards to the open channels (Fig. 8). The resulting zigzag channels with dimensions of 4.7 × 7.3 Å are occupied by nitrate anions, water and DMF molecules.

The amide groups in **6** were used as weak bases to catalyze Knoevenagel condensation reactions of benzaldehyde with cyano compounds. Three cyano compounds with different sizes, malononitrile, ethyl cyanoacetate, and cyano-acetic acid *tert*-butyl ester, showed very different results. The smallest substrate, malononitrile, gave 98% conversion of the addition product, while the largest one, cyano-acetic acid tert-butyl ester, gave no conversion at all (Table 2). Such a guest-selective reaction indicated that the reaction was catalyzed inside the crystal channel instead of the surface. Much slower reaction and lower conversion were observed both for the desolvated sample of **6** and for the free ligand 4-btapa. In the desolvated sample of **6**, there is no porosity for the substrates to interact with the amide groups residing inside the solid, whereas the amide groups in the free ligand 4-btapa form intermolecular hydrogen bonds with each other and are thus not available to activate the cyano compounds for Knoevenagel condensation reactions.

Table 2 Knoevenagel condensation reaction catalyzed by **6**

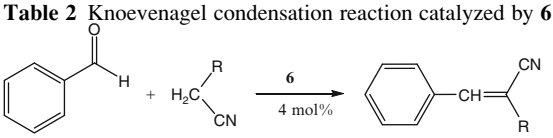

Run	Substrate	Molecule size	Conversion (%)
1	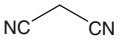	4.5 × 6.9 Å	98
2	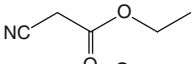	4.5 × 10.3 Å	7
3	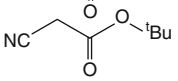	5.8 × 10.3 Å	0

All of these experimental observations are consistent with the heterogeneous nature of **6** as a weak base catalyst for Knoevenagel condensation reactions.

2.2.2 Grafting of Catalytically Active Functional Groups to the Unsaturated Metal Sites

Catalytically relevant functional groups can also be introduced by grafting onto unsaturated metal sites within MOFs. Ferey et al. reported a robust and highly porous MOF $[Cr_3(\mu_3\text{-}O)F(H_2O)_2(BDC)_3]$ (**7**) constructed from BDC and chromium (III) nitrate (also called MIL-101) [16, 29]. In situ IR spectroscopic studies via CO adsorption indicated that **7** has a number density of unsaturated Cr(III) sites of 1.0 mmol g^{-1}. Instead of directly using the unsaturated Cr(III) centers as catalytic sites, the authors grafted ethylenediamine (ED) onto the Cr(III) sites (Fig. 9c). **7** has

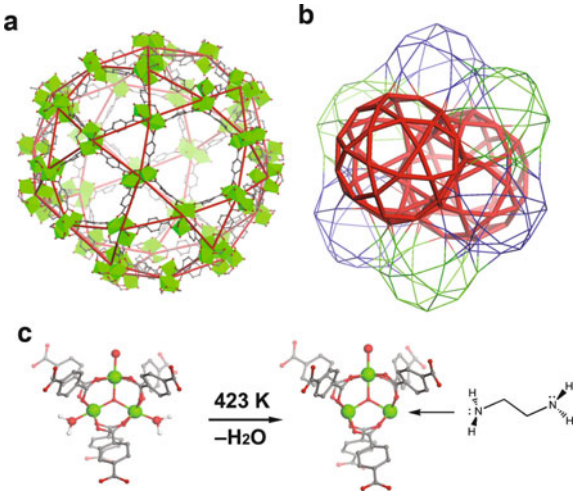

Fig. 9 (**a**) Perspective view of mesoporous cage of **7** showing hexagonal windows. (**b**) Two types of super cages, *red* and *green/blue*, representing the highly porous zeolite-type MOF 7. (**c**) Evolution of unsaturated chromium centers by removal of the bounding water molecules, and its accessibility to ethylenediamine (ED) molecules

an extremely high Langmuir surface area of 5900 $m^2\ g^{-1}$ owing to its zeolite-type structure having extraordinary large cages with diameters of 2.9 and 3.4 nm (Fig. 9a, b). Although ED takes up some of the space within the frameworks, the nitrogen uptake experiments still showed a large Langmuir surface area of 3555 $m^2\ g^{-1}$ for the ED-grafted **7**. As the uncoordinated ends of ED can act as base catalytic sites, ED-grafted **7** was tested for Knoevenagel condensation reactions. A significant increase in conversion was observed for ED-grafted **7** as compared to untreated framework **7** (98% vs 36%).

2.3 Entrapment of Catalytically Active Noble Metal Nanoparticles

Since the porosity and crystallinity of **7** were well maintained after ED grafting, the uncoordinated end of ED provides a site for further modification via encapsulation of noble metals. After being treated with aqueous HCl solution, the positively charged ammonium groups (from protonated ED) interacted with noble metal salts, such as $[PdCl_4]^{2-}$, which was later reduced into noble metal by $NaBH_4$. The resulting Pd nanoparticles entrapped into the framework for example showed similar catalytic activity as Pd/C in Heck coupling reactions.

With a similar approach, Fischer and coworkers entrapped Ru nanoparticles inside porous $[Zn_4O(BDC)_3]$ (MOF-5) by hydrogenolysis of the adsorbed volatile ruthenium species [Ru(COD)(COT)] (COD = 1,5-cyclooctadiene, COT = 1,3,5-cyclooctatriene) [17]. The included Ru nanoparticles had a size range of 1.5–1.7 nm, and the intact framework of MOF-5 was confirmed by different spectroscopic methods. The resulting solid Ru@MOF-5 was tested for oxidation of benzyl alcohol; however, only a modest conversion of 25% to benzyl aldehyde was obtained, and the XRD revealed the breakdown of the structure of MOF-5 as well as the loss of framework porosity. In contrast, the crystallinity of Ru@MOF-5 remained when it was used to catalyze the hydrogenation of benzene to cyclohexane with 25% conversion under 3 bar H_2 at 75°C (Scheme 8).

2.4 MOFs as Reaction Hosts with Size Selectivity

2.4.1 Reaction Host for Photochemical Synthesis

Due to the highly ordered structures of MOFs, pores of specific sizes and shapes can be purposely constructed and used as nano-reactors for size-selective reactions. Li and coworkers synthesized a 3D MOF $[Co_3(bpdc)_3(bpy)]\cdot 4DMF\cdot H_2O$ (**8**, bpdc: biphenyldicarboxylate, bpy: 4,4′-bipyridine) by a solvothermal reaction of 1-D polymer $[Co(bpdc)(H_2O)_2]\cdot H_2O$ and 4,4′-bipyridine [30]. The resulting twofold interpenetrating 3D porous framework (Fig. 10) showed great thermal stability. The

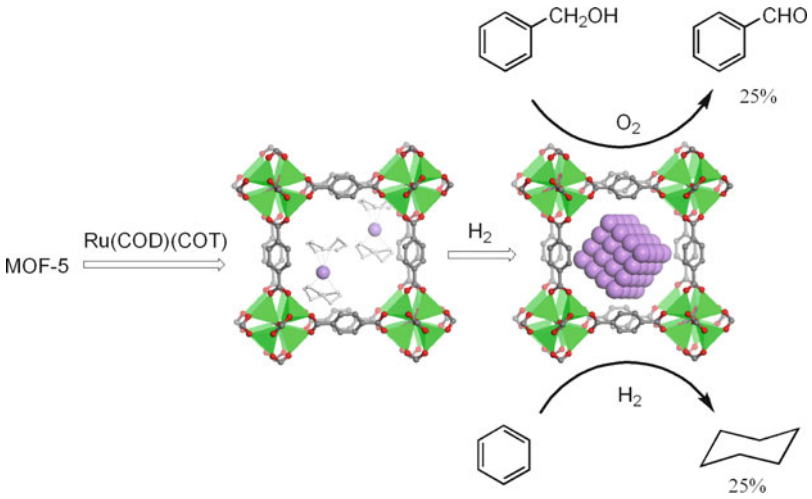

Scheme 8 Schematic for the formation of Ru@MOF-5 and its applications on alcohol oxidation and benzene hydrogenation

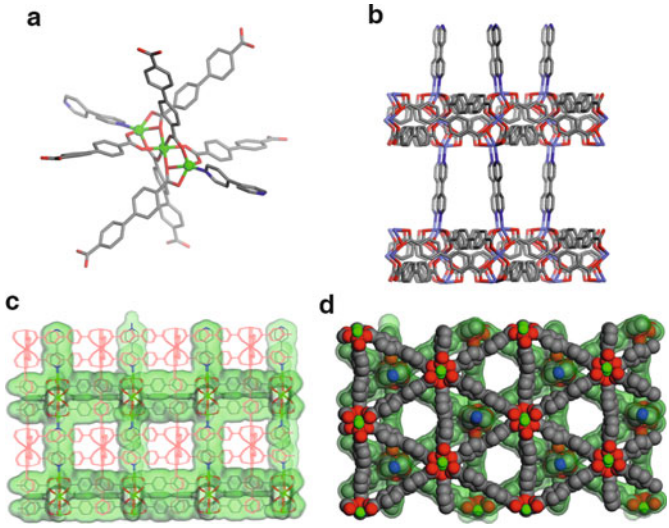

Fig. 10 (**a**) Coordination environment of Co, showing the building unit of $[Co_3(bpdc)_3(bpy)]$ (**8**). (**b**) Packing diagram of one of the two nets of **8** viewed down the *b* axis. (**c**) Twofold interpenetrating 3D networks viewed down the *a* axis. (**d**) Space-filled model of **8** viewed perpendicular to the (001) plane

framework structure remained essentially unchanged even after evacuating the pristine sample at 300°C.

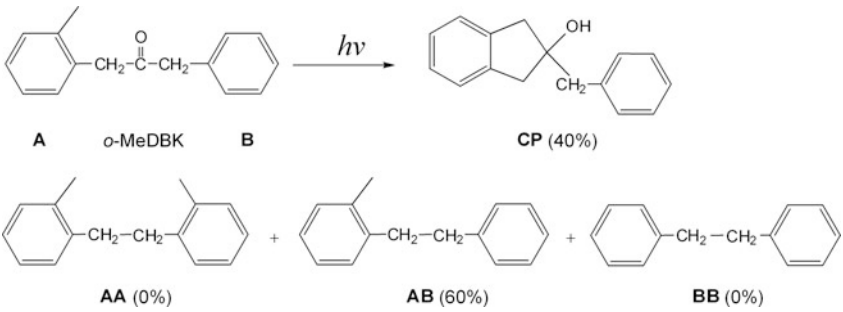

Scheme 9 Schematic illustration photoreaction of *o*-MeDBK

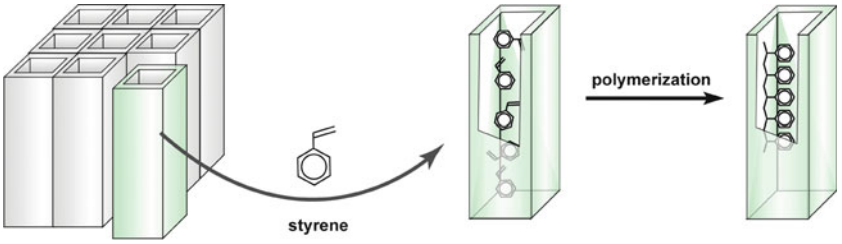

Fig. 11 Schematic illustration of styrene polymerization in the 1-D channels within the MOFs (courtesy of Professor Kitagawa)

Further analysis of the channels of **8** shown in Fig. 10d revealed the existence of supercages with the size of 11 × 11 × 5 Å, which are interconnected through narrower windows with a maximum dimension of 8 Å. The supercages and channels in **8** were tested as hosts for size-selective reactions. The photochemistry of *o*-methyl dibenzyl ketone (*o*-MeDBK) was examined utilizing **8** as the reaction host (Scheme 9). This type of photochemical reactions was extensively studied using FAU and MFI zeolites as hosts [31]. During the photoreaction, the *o*-MeDBK in the singlet state can undergo intramolecular hydrogen abstraction followed by cyclization to produce cyclopentanol, **CP**. On the other hand, α cleavage followed by decarbonylation forms a geminate pair of hydrocarbon radicals, which randomly recombine to afford products **AA**, **AB**, and **BB**. The photolysis of *o*-MeDBK in the presence of **8** produced CP in 40% yield along with the single radical recombination product **AB** in 60% yield. The exclusive production of **AB** was rationalized by a "cage effect" of 100% efficiency (for comparison, the same photolysis in NaX has a cage effect of 70%). Only 50% of the overall product could be extracted from the solid. The remaining product had to be recovered by breaking down the framework **8** via soaking in water. 1-D compound $[Co(bpdc)(H_2O)_2]\cdot H_2O$ could be recycled after breaking down **8**.

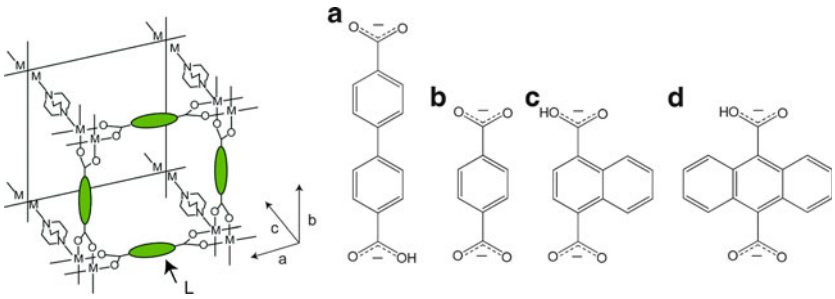

Fig. 12 Combination of different metal (Cu^{2+} or Zn^{2+}) with different size of linker ligands **L** (**a–d**) to result in 3D MOF with open channels along the *c* axis

Table 3 Polymerization of styrene in nanochannels of **9** and **10** at 70°C for 48 h

Host (pore size [Å]^2	Adsorbed monomer (number/unit cell)	Conversion (%)	$M_n(M_w/M_n)$
9a (10.8 × 10.8)	3.1	81	14,000 (3.3)
9b (7.5 × 7.5)	2.5	71	54,600 (1.6)
9c (5.7 × 5.7)	2.2	58	10,100 (1.6)
9d (4.8 × 4.3)	1.6	0	
10b (7.5 × 7.5)	2.5	71	56,200 (1.7)
10c (5.7 × 5.7)	2.1	56	11,100 (1.5)
10d (4.8 × 4.3)	1.6	0	
Bulk polymerization			37,600 (4.7)

2.4.2 Reaction Host for Polymerization

Certain types of reactions, such as polymerization, in the confined nanoscale channels/space may have different pathways compared with those in open space. Kitagawa and coworkers have utilized size-tunable MOFs as reactions hosts for radical polymerization of activated monomers, such as styrene, divinylbenzene, substituted acetylenes, methyl methacrylate, and vinyl acetate (Fig. 11) [32–35]. *Para*-dicarboxylate linkers of different sizes, **a–d**, were used to link Cu^{2+} and Zn^{2+} centers to form 2D sheets which were further linked by triethylenediamine to form 3D frameworks **9a–d** (for Cu^{2+}) and **10b–d** (for Zn^{2+}) that possess 1-D channels (Fig. 12).

Owing to the different size of linker ligands **a–d**, the resulting frameworks possessed open channels of varied sizes from 4.3 × 4.8 Å^2 to 10.8 × 10.8 Å^2. Polymerization of styrene was performed using **9a–d** and **10b–d** as hosts at 70°C. Since styrene has a slightly larger dimension than the channels in **9d** and **10d**, as expected, no conversion was observed when these two frameworks were used (Table 3). Most importantly, the molecular weight distribution (i.e., polydispersity index M_w/M_n) of polystyrenes produced within the nanochannels was narrower than

those prepared by bulk synthesis. This unique capability of molecular weight control was further examined by ESR measurement. Intense signals assigned to the propagating radicals of polystyrene were observed, reaching 2.6 mmol kg^{-1} in **10b**, which is significantly higher than those detected in conventional solution radical polymerizations (10^{-4}–10^{-5} mmol kg^{-1}). The nanochannels could thus better stabilize the propagating radicals and suppress the termination reactions, leading to smaller and more desirable M_w/M_n values.

3 Homochiral MOFs as Asymmetric Catalysts

3.1 General Strategies for Homochiral MOF Synthesis

As illustrated in cyanosilylation and other lewis acid-catalyzed reactions, applications of MOFs in achiral catalysis suffer from several limitations when compared with traditional inorganic oxide catalysts, including limited thermal and hydrolytic stabilities. It will thus be difficult for MOFs to compete against zeolites for the reactions that require high temperatures and aggressive solvents. On the other hand, no known zeolites can be used to catalyze enantioselective reactions. Given that most asymmetric catalytic reactions are carried out in nonaggressive solvents under mild conditions, MOFs appear to be ideally suited for such applications owing to the ability to prepare chiral MOFs with large open channels in a modular fashion.

Compared to relatively few examples of MOF-based achiral catalysts, there are even fewer examples of homochiral MOFs used in asymmetric catalytic reactions. Several distinct strategies can be used to construct homochiral MOFs. Ideally, crystallization of homochiral MOFs via self-resolution from achiral linker ligands is the most economical way to accomplish such a goal. However, the resulting bulk samples, in almost all of the cases, contain both enantiomorphs and are thus racemic. Aoyama and coworkers successfully obtained homochiral MOFs in the bulk from achiral ligands by carefully controlling nucleation in the crystal growth process [36]. Zheng and coworkers recently reported the synthesis of homochiral MOFs from achiral ligands by chemically manipulating the statistical fluctuation of the formation of enantiomeric pairs of crystals [37]. Growing MOF crystals under chiral influences is another approach to obtain homochiral MOFs using achiral linker ligands. Rosseinsky and coworkers have introduced a chiral coligand to direct the formation of homochiral MOFs by controlling the handedness of the helices during the crystal growth [38, 39]. Morris and coworkers utilized ionic liquid with chiral cations as reaction media for synthesizing MOFs, and successfully obtained homochiral MOFs even though they do not contain cationic part of the ionic liquid [40]. The most reliable strategy for synthesizing homochiral MOFs is, however, to use the readily available chiral linker ligands for their construction. A number of homochiral MOFs with open framework structures were synthesized

by this method in recent years [41–46]. All of the homochiral MOFs examined for asymmetric catalytic reactions so far have been made using this strategy.

3.2 *Homochiral MOFs with Interesting Functionalities and Reagent-Accessible Channels*

Although a number of chiral building blocks can be used to construct homochiral MOFs, Lin and coworkers focused on enantiopure 1,1′-binaphthyl-derived linker ligands because the related 1,1′-bi-2,2′-naphthol (BINOL) and 2,2′-bis(diphenylphosphino)-1,1′-binaphthyl (BINAP) are among the most widely used chiral ligands for homogeneous asymmetric catalysis [47, 48]. They have successfully constructed homochiral MOFs using 1,1′-binaphthyl-derived chiral bridging ligands containing orthogonal functional groups that can be used to coordinate to catalytically active metal centers to enhance enantioselectivity. One of the advantages of using the 1,1′-binaphthyl moiety as the chiral backbone is the ability to

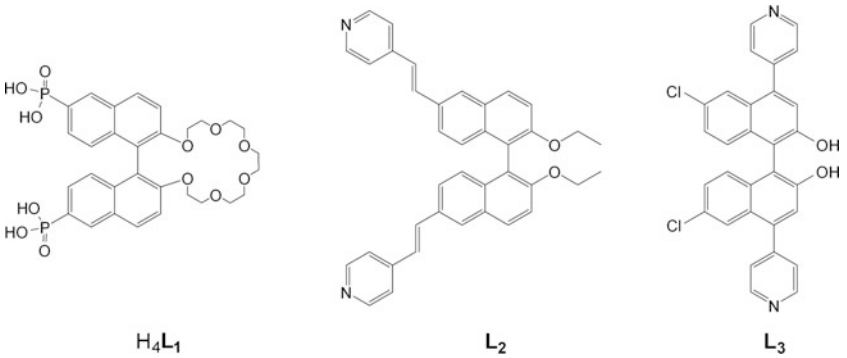

Scheme 10 Homochiral bridging ligands derived from BINOL

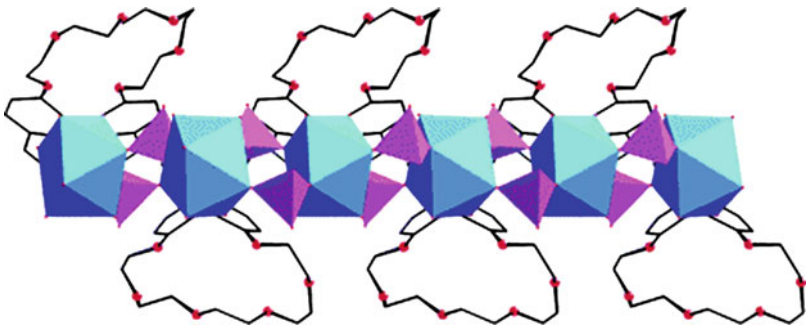

Fig. 13 Chiral crown ether pillars on lamellar lanthanide bisphosphonate **11**

selectively functionalize at specific positions. As shown in Scheme 10, a variety of linking groups such as pyridine, phosphonic acid, and carboxylic acid can be selectively introduced to the 3,3′, 4,4′, and the 6,6′ positions of the 1,1′-binaphthyl moiety. Moreover, the length of the linker groups can be readily adjusted in order to tune the framework structure and porosity of the resulting materials.

The Lin group has prepared a number of homochiral MOFs based on 1,1′-binaphthyl-derived bridging ligands that contain additional functional groups for potential enantionselective recognition and separation processes. For example, homochiral lanthanide bisphosphonate MOF $[Ln_2(H_2\mathbf{L_1})_2(CH_3OH)]\cdot H_4L\cdot 3HCl\cdot 6H_2O$ (**11**) was built from chiral bridging ligand $\mathbf{L_1}$ containing crown ether groups (Fig. 13) [42], which are potentially useful in bulk chiral separation of racemic ammonium salts (such as protonated amino acid derivatives). Although these lamellar solids maintained their framework structures after the removal of guest molecules, the limited porosity has precluded their application in enantioselective separations.

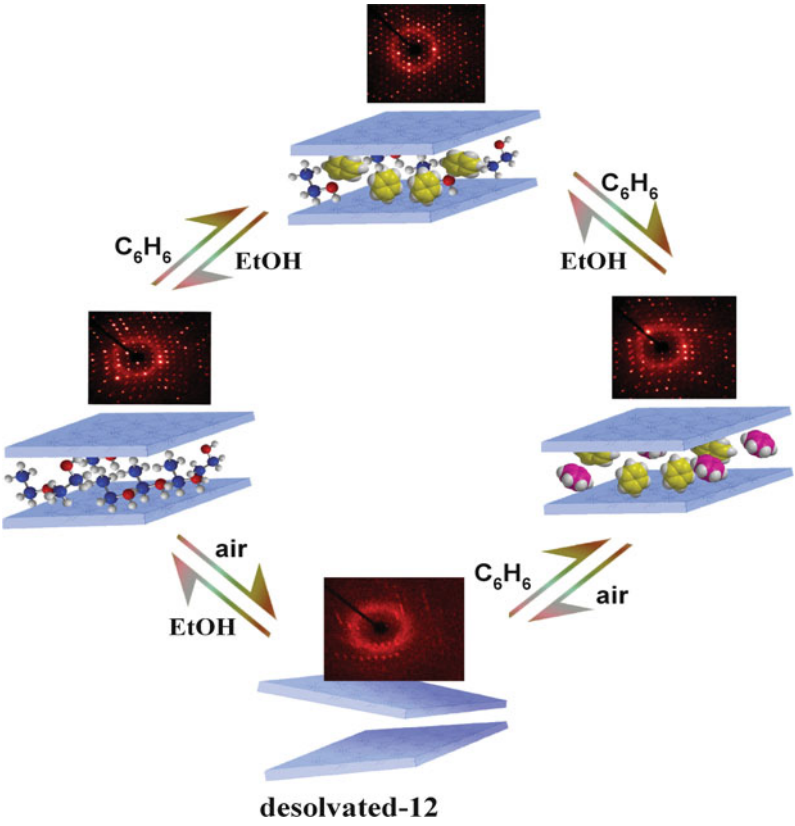

Fig. 14 Schematic representation of the reversible single-crystal to single-crystal and single-crystal to amorphous to single-crystal transformation processes of **12**

An effective MOF-based heterogeneous asymmetric catalyst needs to satisfy two requirements: the ability to maintain the framework structure under catalytic conditions and the facile transport of the reagents and products through the open channels in order for the substrates to access the active catalytic sites. Increasing the length of the bridging ligands may be a feasible way to create more solvent/reagent accessible channels built with the frameworks. However, longer bridging ligands may lead to framework catenation which will reduce the pore size [9]. Another undesired effect caused by the longer bridging ligands is the framework distortion after the removal of guest molecules. In order to probe the feasibility of designing homochiral MOFs that satisfy both of these requirements, Lin et al. synthesized a highly porous homochiral MOF $[Cd(\mathbf{L_2})_2(ClO_4)_2]\cdot 11EtOH\cdot 6H_2O$ (**12**) based on 1-D coordination polymers that were built from linking $Cd(ClO_4)_2$ with the elongated di-pyridyl ligand $\mathbf{L_2}$ [43]. Compound **12** can readily exchange solvent molecules upon exposing the pristine crystals to a vapor of other solvents, and interestingly, the solid underwent single-crystal-to-single-crystal transformation during the solvent exchange processes. The pristine solid lost crystallinity upon removal of the solvent molecules in air, but the crystallinity was regained upon exposure the amorphous solid to solvent molecules (Fig. 14). These results suggest that the framework structures of homochiral MOFs can be maintained during potential heterogeneous asymmetric catalytic reactions and true heterogeneous asymmetric catalysts can be built from homochiral MOFs.

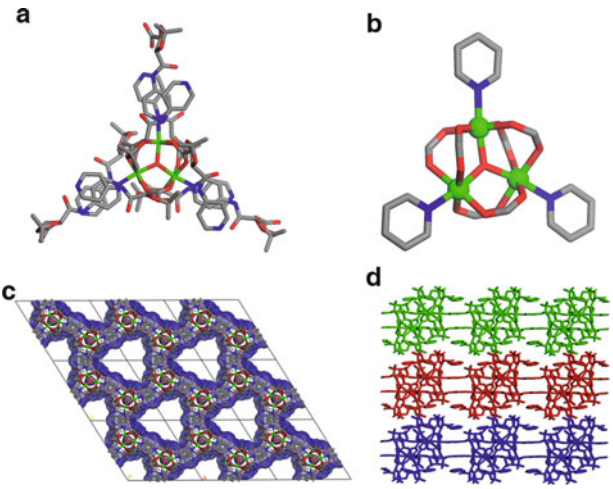

Fig. 15 (**a**) $[Zn_3(\mu\text{-}O)(\mathbf{L_4})_6]$ SBUs in (**13**). (**b**) Coordination environment or metal centers of **13**. (**c**) Large 1-D equilateral triangular shape channel along the *c* axis, with a size of 13.4 Å. (**d**) Stacking patterns of 2D layers (depicted in *different colors*) as viewed along the *a* axis

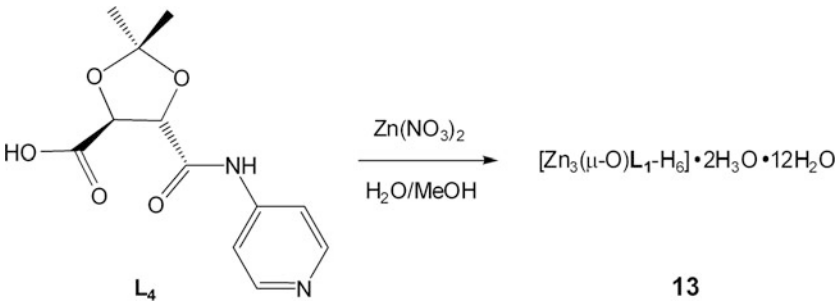

Scheme 11 Synthesis of homochiral **13**

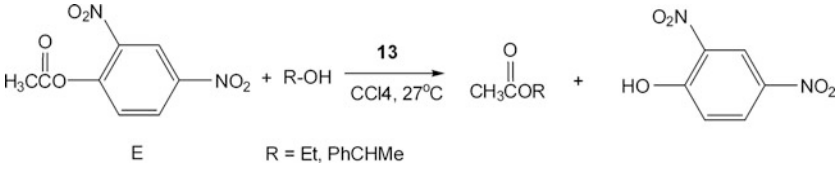

Scheme 12 Transesterfication of esters catalyzed by **13**

3.3 Nonchiral Active Sites Within the Homochiral Framework Structures

Kim and coworkers reported the first example of asymmetric catalysis using a homochiral MOF, albeit with a very modest enantioselectivity (ee) [41]. Chiral porous $[Zn_3(\mu_3\text{-}O)(L_4\text{-}H)_6]\cdot 2H_3O\cdot 12H_2O$ (**D-POST-1**, or **13**) was synthesized from a solvothermal reaction of $Zn(NO_3)_2$ and enantiopure chiral ligand $\mathbf{L_4}$ which is from readily derived from D-tartaric acid (Scheme 11). The oxo-bridged zinc trinuclear unit in **13** is coordinated by six carboxylate groups to form a SBU, which is further interconnected through zinc ions and pyridyl groups to result in large chiral 1D channels of ~13.4 Å along the *c* axis (Fig. 15).

Each trinuclear zinc unit contains six pyridyl groups, three of which are coordinated to the zinc ions, and two of the remaining three protonated. These exposed pyridine groups showed catalytic activity in the transesterification of ester **E** (Scheme 12). When racemic 1-phenyl-2-propanol was used, the ester product exhibited a modest ~8% ee in favor of the *S*-enantiomer.

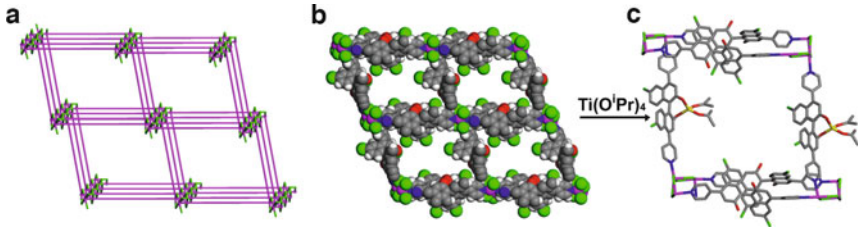

Fig. 16 (**a**) Schematic representation of the 3D framework of **14** showing the zigzag chains of $[Cd(\mu\text{-}Cl)_2]_n$ along *a* axis. (**b**) Space-filling model of **14** as viewed down the *a* axis, showing large 1D chiral channel (1.6 × 1.8 nm). (**c**) Schematic representation of the active (BINOLate)$Ti(O^iPr)_2$ catalytic sites in the open channels of **14**

Table 4 Ti(IV)-catalyzed $ZnEt_2$ additions to aromatic aldehydes[a]

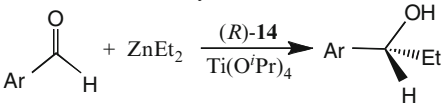

Ar	BINOL/$Ti(O^iPr)_4$		**14**•Ti	
	conv.%	ee%	conv.%	ee%
1-Naph	>99	94	>99	93
Ph	>99	88	>99	83
4-Cl-Ph	>99	86	>99	80
3-Br-Ph	>99	84	>99	80
4′-G_0OPh	>99	80	>99	88
4′-G_1′OPh	>99	75	73	77
4′-G_1OPh	>99	78	63	81
4′-G_2′OPh	95[b]	67[b]	0	–

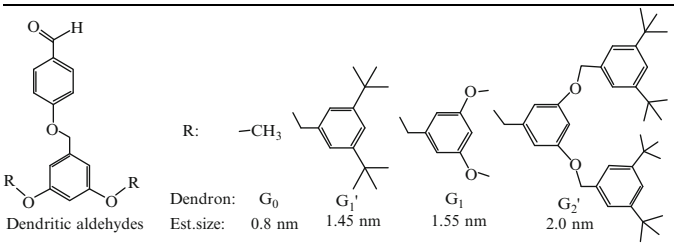

[a]All the reactions were conducted with 13 mol% of **14** or 20 mol% BINOL and excess amounts of $Ti(O^iPr)_4$ at room temperature for 12 h. Conversions were determined by GC or NMR, while ee% values were determined on chiral GC or HPLC for all the secondary alcohols except for 4′-G_2′OPh whose ee% was determined by NMR spectrum of its Mosher's ester

[b]With 40 mol% BINOL

3.4 *Postmodification of Homochiral MOFs Bearing Bridging Ligands with Orthogonal Functionalities*

3.4.1 High Enantioselective Diethylzinc Addition Reactions

The Lin group used a postsynthetic modification strategy to generate a highly active and enantioselective heterogeneous catalyst from homochiral MOFs bearing bridging ligands with orthogonal functionalities. Slow vapor diffusion of diethyl ether into the mixture of (*R*)-6,6′-dichloro-2,2′-dihydroxyl-1,1′-binaphthyl-bipyridine (**L_3**) and $CdCl_2$ in DMF/MeOH led to 3D homochiral MOF $[Cd_3(\mathbf{L_3})_3Cl_6]\cdot 4DMF\cdot 6MeOH\cdot 3H_2O$ (**14**) [15]. The 3D framework structure of **14** resulted from linking 1D zigzag $[Cd(\mu\text{-}Cl)_2]_n$ SBUs by the **L_3** ligands via pyridine coordination and had the largest channel opening of 1.6 × 1.8 nm running along the *a* axis (Fig. 16). More importantly, one third of the chiral dihydroxy groups in **14** are facing the open channels, which makes them accessible to secondary metal centers.

The porous solid **14** was pretreated by $Ti(O^iPr)_4$ to generate the grafted Ti-BINOLate species. The resulting active "**14**·Ti" species efficiently catalyzed the diethylzinc addiction reactions in a level of ee (up to 93%) that is comparable to the homogeneous analogue (94% ee) (Table 4). The heterogeneous nature of this solid catalyst was confirmed by the nonreactive supernatant from a mixture of **14** and Ti $(O^iPr)_4$. Moreover, a set of control experiments were performed using aldehydes

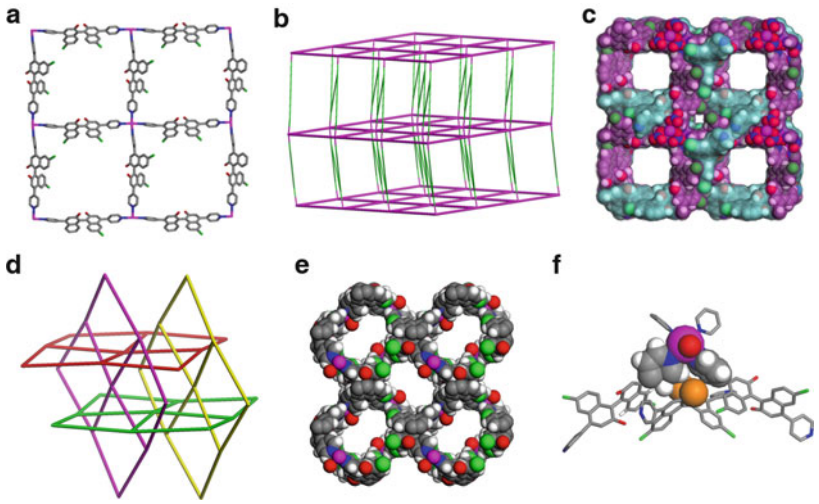

Fig. 17 (**a**) The 2D square grid in **15**. (**b**) Schematic representation of the 3D framework of **15**. (**c**) Space-filling model of **15** as viewed down the *c* axis, the twofold interpenetrating networks are shown with *blue and violet colors*. (**d**) Schematic representation of the interpenetration of mutually perpendicular 2D grids in **16**. (**e**) Space-filling model of **16** as viewed down the *c* axis. (**f**) Schematic representation of steric congestion around the chiral dihydroxyl group of **L_3** (*orange sphere*) arising from the interpenetration of mutually perpendicular 2D grids in **16**

with different size from 0.8 to 2.0 nm to show that the aldehydes are accessing the Ti active sites in the interior of crystals of **14**. Decreased conversion was found when larger aldehyde was used, and no conversion of aldehyde $G_2'$with size of 2.0 nm was used, which is larger than the size of the open channels of the framework. Such a size-dependant conversion further illustrated the heterogeneous nature of the **14**·Ti catalysts and that the catalytic reactions occur inside the open channels of the solid (instead of external surfaces of the solid).

3.4.2 Catalytic Activities Determined by Framework Structures

The chloride anions coordinate to the Cd centers to give $[Cd(\mu\text{-}Cl)_2]_n$ SBUs in **14**. It is well-established that the MOF structures critically depend on the anions used during the crystal growth. While using the same ligand $\mathbf{L_3}$, Lin et al. obtained two different homochiral MOFs $[Cd_3(\mathbf{L_3})_4(NO_3)_6]\cdot 7MeOH\cdot 5H_2O$ (**15**) and $[Cd(\mathbf{L_3})_5(ClO_4)_2]\cdot DMF\cdot 4MeOH\cdot 3H_2O$ (**16**) when $Cd(NO_3)_2$ and $Cd(ClO_4)_2$ were used as the metal sources [44]. Compound **15** shows twofold interpenetrated structure of two sets of 3D frameworks, which are constructed by 2D grids and 1D zigzag polymeric chains. Large channels with dimension of 13.5 × 13.5 Å exist along the *c* axis (Fig. 17c). Compound **16** adopts 3D network from highly interpenetrated 2D grids, resulting 1D channels with size of 1.2 × 1.5 nm (Fig. 17e).

Compound **15** was activated by $Ti(O^iPr)_4$ to lead to an active heterogeneous asymmetric catalyst for the diethylzinc addition to aromatic aldehydes with up to 90% ee. However, under the same conditions, a mixture of **16** and $Ti(O^iPr)_4$ was inactive in catalyzing the diethylzinc addition to aromatic aldehydes. Careful investigation of the structure of **16** revealed the close proximity of the Cd $(py)_2(H_2O)_2$ moiety in one 2D grid with the dihydroxyl groups of the other 2D grid, which made the dihydroxyl groups inaccessible to $Ti(O^iPr)_4$. When treated with $Ti(O^iPr)_4$, compounds **15** and **16** had entirely different activities due to the

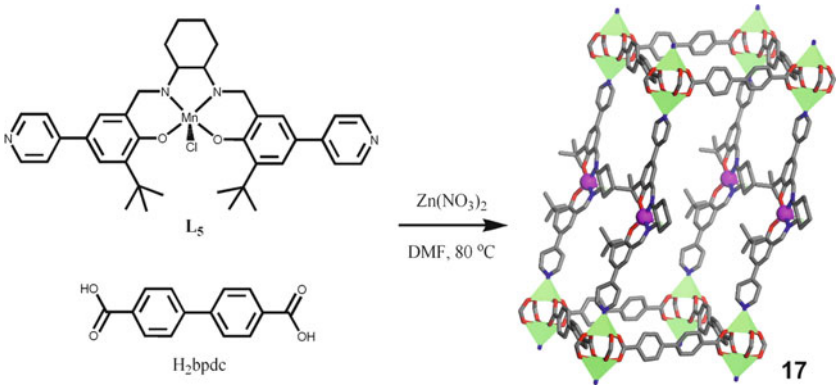

Scheme 13 Synthesis and framework structure of **17**

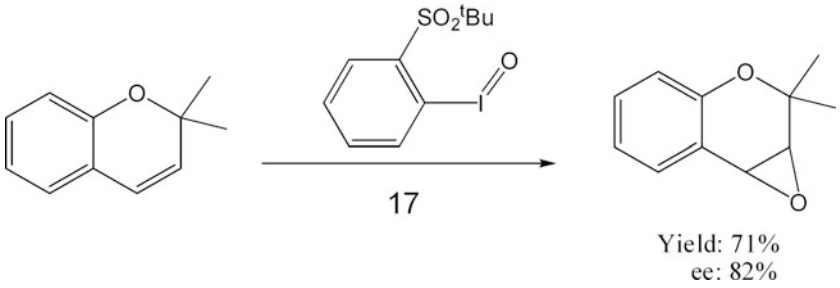

Scheme 14 Asymmetric epoxidation catalyzed by **17**

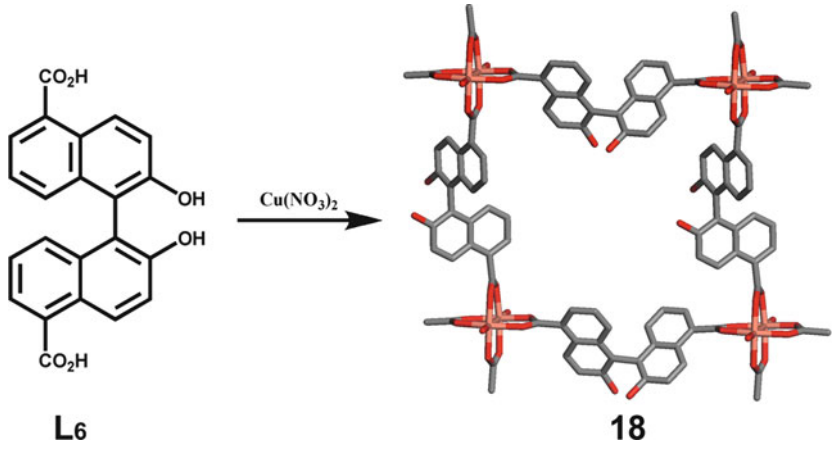

Scheme 15 Schematic representation of the synthesis of **18** and the connectivity of $\mathbf{L_6}$ and copper paddle wheels

subtle structure differences. The finding of such a drastic difference in catalytic activity is remarkable since **15** and **16** were built from exactly the same building blocks, and this finding highlights the important role of the framework structure in determining the catalytic performance.

3.5 Homochiral MOFs with Precatalysts as Building Blocks

An alternative approach to catalytically active homochiral MOFs is to incorporate directly chiral metal complexes which are either active catalysts or precatalysts into the framework structures. For example, Hupp and coworkers have combined $\mathbf{L_5}$ and H_2bpdc with $Zn(NO_3)_2$ and obtained twofold interpenetrating 3D networks $[Zn_2(bpdc)_2\mathbf{L_5}]\cdot 10DMF\cdot 8H_2O$ (**17**) (Scheme 12) [46]. While the channels along

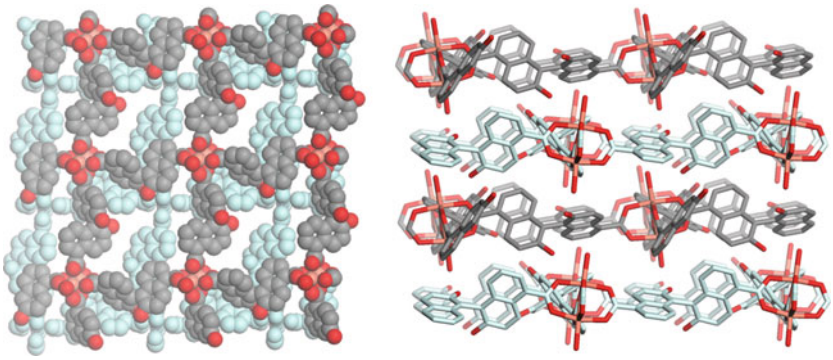

Fig. 18 Space-filled model of **18** as viewed down the *b* axis (left) and the stacking patterns of 2D grids as viewed along the *c* axis

Table 5 Asymmetric ring-opening reaction of epoxide with amine

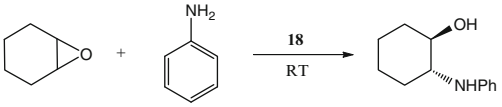

Catalyst	Solvent	Time/h	Yield (%)	ee (%)
18	Toluene	48	54	45
18	None	24	51	51
(*S*)-BINOL	None	24	3	2

the *b* axis are blocked as the result of interpenetration, channels in the *a* and *c* directions still remain with size of 6.2 × 6.2 Å and 6.2 × 15.7 Å, respectively (Scheme 13).

The orientation of $\mathbf{L_5}$ in the frameworks makes all Mn(III) sites accessible through the channels. The resulting open frameworks with built-in (salen)Mn complexes showed catalytic activity towards asymmetric olefin epoxidation reactions. In the asymmetric epoxidation of 2,2-dimethyl-2*H*-chromene catalyzed by **17** (Scheme 14), 71% yield and 82% ee were obtained. No significant decrease of catalyst activity was observed during the reaction and the catalyst could be recycled and reused several times. Notably, the heterogeneous catalyst **17** has shown higher activity than the homogeneous counterpart, albeit with slightly lower ee.

Using a similar approach to the Lin group, Tanaka and coworkers synthesized homochiral MOFs $[Cu_2(\mathbf{L_6})_2(H_2O)_2]MeOH.H_2O$ (**18**) from 2,2′-dihydroxyl-1,′1-binaphthyl-5,5′-dicaroxylatic acid ($\mathbf{L_6}$) and $Cu(NO_3)_2$ [45]. The copper paddle-wheel SBUs in **18** were linked by BINOL scaffolds through 5,5′ positions (Scheme 15). The resulting 2D square grid networks are stacked along the *b* axis with a interlayer Cu–Cu distance of 15.6 Å (Fig. 18).

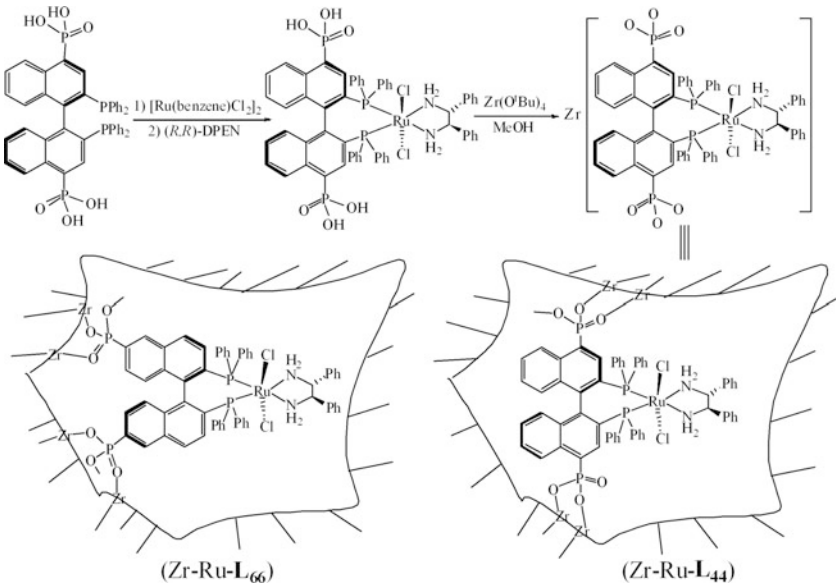

Scheme 16 Schematic representation of formation of zirconium phosphonate-based chiral porous hybrid materials

The homochiral framework **18** is capable of catalyzing the asymmetric ring-opening of epoxides with amines. Compound **18** shows moderate catalytic activity with up to 54% yield and 51% ee (Table 5). The control experiments were carried by using *S*-BINOL as catalyst, and only negligible yield and ee were obtained. The mechanism for this reaction however remained unclear.

Lin and coworkers have reported zirconium phosphonate-derived Ru-BINAP systems (Scheme 16) [49]. Zirconium phosphonate-based chiral porous hybrid materials containing the Ru(BINAP)(diamine)Cl_2 precatalysts showed excellent enantioselectivity (up to 99.2% ee) in the asymmetric hydrogenation of aromatic ketones. These catalysts were also readily recovered by centrifugation and reused for up to 10 times without significant loss of catalyst activity and enantioselectivity. Related zirconium phosphonates containing Ru(BINAP)$(DMF)_2Cl_2$ precatalysts were successfully used for asymmetric hydrogenation of β-keto esters with up to 95% ee [50].

4 Conclusions and Perspectives

This chapter has summarized recent developments in the rational design of catalytically active MOFs. Their applications in both achiral and asymmetric catalysis were surveyed. Three distinct approaches have been developed to construct catalytically MOFs, including the use of unsaturated metal-connecting points as catalytic centers, the use of functional groups in the bridging ligands as active sites, and the entrapment of catalytically active species inside the channels and pores of MOFs. The use of channels and pores in MOFs as hosts for size- and shape-selective reactions was also discussed. Limited thermal and hydrolytic stabilities of MOFs however present major hurdles for their practical applications in achiral catalysis, particularly for the reactions that can be effectively catalyzed by microporous inorganic oxides such as zeolites. Homochiral MOFs on the other hand can be used as heterogeneous catalysts for stereoselective reactions which cannot be catalyzed by zeolites. Compared to the MOFs available for achiral catalysis, only a very small number of homochiral MOFs have so far been developed for heterogeneous asymmetric catalysis due to the challenge in designing homochiral MOFs with large enough open channels to allow the access of typically large prochiral reagents. Research on asymmetric catalysis using homochiral MOFs has barely scratched the surface. Many more catalytically active systems will be developed and used for stereoselective organic transformations in the coming years.

Acknowledgments We would like to acknowledge National Science Foundation for financial support. We also thank former coworkers Drs. Aiguo Hu, Chuan-De Wu, and Helen L. Ngo for their invaluable contributions to the research program in the Lin group.

References

1. Batten SR, Robson R (1998) Angew Chem Int Ed 37:1460
2. Moulton B, Zaworotko MJ (2001) Chem Rev 101:1629
3. Evans OR, Lin W (2002) Acc Chem Res 35:511
4. Ferey G, Mellot-Draznieks C, Serre C, Millange F (2005) Acc Chem Res 38:217
5. Yaghi OM, O'Keeffe M, Ockwig NW, Chae HK, Eddaoudi M, Kim J (2003) Nature 423:705
6. Hill RJ, Long DL, Champness NR, Hubberstey P, Schroder M (2005) Acc Chem Res 38:335
7. Bradshaw D, Warren JE, Rosseinsky MJ (2007) Science 315:977
8. Rosi NL, Eckert J, Eddaoudi M, Vodak DT, Kim J, O'Keeffe M, Yaghi OM (2003) Science 300:1127
9. Kesanli B, Cui Y, Smith MR, Bittner EW, Bockrath BC, Lin W (2005) Angew Chem Int Ed 44:72
10. Chen B, Zhao X, Putkham A, Hong K, Lobkovsky EB, Hurtado EJ, Fletcher AJ, Thomas KM (2008) J Am Chem Soc 130:6411
11. Pan L, Parker B, Huang X, Olson DH, Lee JY, Li J (2006) J Am Chem Soc 128:4180
12. Evans OR, Ngo HL, Lin WB (2001) J Am Chem Soc 123:10395
13. Han JW, Hill CL (2007) J Am Chem Soc 129:15094

14. Hasegawa S, Horike S, Matsuda R, Furukawa S, Mochizuki K, Kinoshita Y, Kitagawa S (2007) J Am Chem Soc 129:2607
15. Wu CD, Hu A, Zhang L, Lin WB (2005) J Am Chem Soc 127:8940
16. Hwang YK, Hong DY, Chang JS, Jhung SH, Seo YK, Kim J, Vimont A, Daturi M, Serre C, Ferey G (2008) Angew Chem Int Ed 47:4144
17. Schroeder F, Esken D, Cokoja M, van den Berg MWE, Lebedev OI, van Tendeloo G, Walaszek B, Buntkowsky G, Limbach HH, Chaudret B, Fischer RA (2008) J Am Chem Soc 130:6119
18. Fujita M, Kwon YJ, Washizu S, Ogura K (1994) J Am Chem Soc 116:1151
19. Ohmori O, Fujita M (2004) Chem Commun 14:1586
20. Schlichte K, Kratzke T, Kaskel S (2004) Microporous Mesoporous Mat 73:81
21. Chui SSY, Lo SMF, Charmant JPH, Orpen AG, Williams ID (1999) Science 283:1148
22. Horike S, Dinca M, Tamaki K, Long JR (2008) J Am Chem Soc 130:5854
23. Alaerts L, Seguin E, Poelman H, Thibault-Starzyk F, Jacobs PA, De Vos DE (2006) Chem Eur J 12:7353
24. Striegler S (2006) Tetrahedron 62:9109
25. Kato CN, Hasegawa M, Sato T, Yoshizawa A, Inoue T, Mori W (2005) J Catal 230:226
26. Dybtsev DN, Nuzhdin AL, Chun H, Bryliakov KP, Talsi EP, Fedin VP, Kim K (2006) Angew Chem Int Ed 45:916
27. Gomez-Lor B, Gutierrez-Puebla E, Iglesias M, Monge MA, Ruiz-Valero C, Snejko N (2002) Inorg Chem 41:2429
28. Perles J, Iglesias M, Martin-Luengo MA, Monge MA, Ruiz-Valero C, Snejko N (2005) Chem Mat 17:5837
29. Ferey G, Mellot-Draznieks C, Serre C, Millange F, Dutour J, Surble S, Margiolaki I (2005) Science 309:2040
30. Pan L, Liu HM, Lei XG, Huang XY, Olson DH, Turro NJ, Li J (2003) Angew Chem Int Ed 42:542
31. Turro NJ (2000) Acc Chem Res 33:637
32. Uemura T, Kitaura R, Ohta Y, Nagaoka M, Kitagawa S (2006) Angew Chem Int Ed 45:4112
33. Uemura T, Ono Y, Kitagawa K, Kitagawa S (2008) Macromolecules 41:87
34. Uemura T, Kitagawa K, Horike S, Kawamura T, Kitagawa S, Mizuno M, Endo K (2005) Chem Commun 48:5968
35. Uemura T, Hiramatsu D, Kubota Y, Takata M, Kitagawa S (2007) Angew Chem Int Ed 46:4987
36. Ezuhara T, Endo K, Aoyama Y (1999) J Am Chem Soc 121:3279
37. Wu ST, Wu YR, Kang QQ, Zhang H, Long LS, Zheng ZP, Huang RB, Zheng LS (2007) Angew Chem Int Ed 46:8475
38. Kepert CJ, Prior TJ, Rosseinsky MJ (2000) J Am Chem Soc 122:5158
39. Bradshaw D, Prior TJ, Cussen EJ, Claridge JB, Rosseinsky MJ (2004) J Am Chem Soc 126:6106
40. Lin Z, Slawin AMZ, Morris RE (2007) J Am Chem Soc 129:4880
41. Seo JS, Whang D, Lee H, Jun SI, Oh J, Jeon YJ, Kim K (2000) Nature 404:982
42. Ngo HL, Lin WB (2002) J Am Chem Soc 124:14298
43. Wu CD, Lin WB (2005) Angew Chem Int Ed 44:1958
44. Wu C, Lin W (2007) Angew Chem Int Ed 46:1075
45. Tanaka K, Oda S, Shiro M (2008) Chem Commun 820
46. Cho SH, Ma BQ, Nguyen ST, Hupp JT, Albrecht-Schmitt TE (2006) Chem Commun 2563
47. Berthod M, Mignani G, Woodward G, Lemaire M (2005) Chem Rev 105:1801
48. Miyashita A, Yasuda A, Takaya H, Toriumi K, Ito T, Souchi T, Noyori R (1980) J Am Chem Soc 102:7932
49. Hu AG, Ngo HL, Lin WB (2003) J Am Chem Soc 125:11490
50. Hu AG, Ngo HL, Lin WB (2004) Angew Chem Int Ed 43:2501
51. Cejka J, Wichterlova B (2002) Catal Rev Sci Eng 44:375

Top Curr Chem (2010) 293: 207–258
DOI 10.1007/128_2009_8

Published online: 19 September 2009

Magnetic and Porous Molecule-Based Materials

Nans Roques, Veronica Mugnaini, and Jaume Veciana

Abstract In this chapter, we give an overview of the recent state-of-the-art research of porous and magnetic molecule-based materials. The subject is introduced by a section devoted to the fundamentals of magnetism in molecular magnets, with special attention to the design strategies to prepare molecular magnetic materials. We will then focus on the two main families of materials combining porosity and magnetism: the purely organic and the metal-organic porous magnetic materials. For both families, a selection of the most representative examples has been made. A complete section is devoted to magnetic and porous materials with flexible frameworks, an area of emerging importance in this field, because of their wide range of applications. Finally, we conclude with a brief overview on the most recent approaches for the future development of these materials.

Keywords Magnetism • Metal-organic frameworks • Open-shell organic molecules • Porosity • Purely-organic frameworks

Contents

N. Roques, V. Mugnaini, and J. Veciana (✉)
Institut de Ciencia de Materials de Barcelona (ICMAB-CSIC), Networking Research Center on Bioengineering, Biomaterials and Nanomedicine (CIBER-BBN), Campus Universitari de Bellaterra, E-08193, Cerdanyola, Spain
e-mail: vecianaj@icmab.es

N. Roques
CNRS ; LCC (Laboratoire de Chimie de Coordination) ; 205, route de Narbonne, F-31077 Toulouse, France
Université de Toulouse ; UPS, INPT ; LCC ; F-31077 Toulouse, France

1 Introduction

Since Flanigen and co-workers reported the synthesis of the first zeolite analogues – the microporous aluminophosphonate solids [1] – the number of synthetic porous solids has increased significantly. Over the past 30 years, in addition to the large number of porous phosphates described in the literature, new oxygen-containing porous materials have been obtained, combining phosphites, oxofluorides and oxochlorides, fluorides, nitrides, sulphates, sulphides, selenites, halides, germinates, arsenates, and cyanides with a large list of metal ions [2–4]. Together with the rapid development of these inorganic porous materials, a new class of porous solids emerged around 15 years ago, when organic molecules were introduced as direct constituents of porous structures. These porous solids result from the reaction between inorganic and organic species (the latter mainly containing O and/or N donor atoms) to build open-frameworks whose skeletons contain both organic and inorganic moieties mainly linked by strong bonds [5], at variance to supramolecular chemistry. According to the dimensionality of the inorganic framework, Férey classified these new porous materials into four different categories [6] (an alternative classification has been proposed by Cheetham and co-workers [7]) (Fig. 1). Thus, the introduction of organic connectors can induce pillaring between infinite inorganic 2-D layers or allow connecting infinite inorganic 1-D chains. These 2-D and 1-D systems are usually referred to as organic-inorganic hybrid materials, in contrast to the pure inorganic 3-D zeolites. Eventually, organic linkers could also be arranged around single ions or discrete polymetallic species, as in coordination chemistry, to afford 0-D structures, as far as the inorganic part is concerned. These 0-D inorganic structures will be referred from now on as coordination polymers or with the more general acronym MOFs (metal-organic frameworks).

Since the beginning of the 2000s, thousands of publications describing open-framework coordination polymers have been reported [8–15]. The reason why

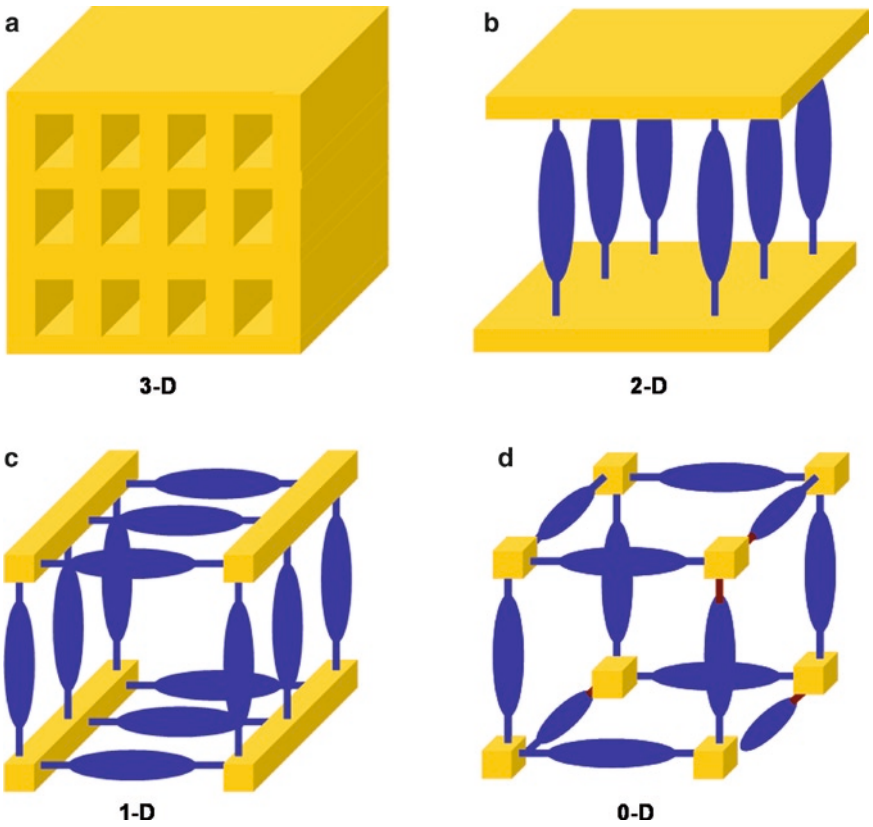

Fig. 1 Classification of porous structures depending on the dimensionality of the inorganic subnetwork. (**a**) 3-D pure "inorganic"-based framework; (**b**) Pillared 2-D "inorganic" layers through multitopic organic linkers; (**c**) 1-D "inorganic" chains linked through multitopic organic linkers; (**d**) Coordination polymers resulting from the connection of 0-D "inorganic" species (metal-organic assemblies or isolated metal ions) thanks to multitopic organic linkers. The design of this figure has been inspired from ref 6

these materials have attracted so much attention is twofold. First, and compared to "classical" porous solids, it consists in the potentiality offered by organic chemistry to design organic multitopic ligands combined with the huge number of metal ions and polynuclear species, previously isolated in coordination chemistry, providing an almost endless number of possibilities for creating new MOFs. Therefore, numerous examples of nanoporous coordination polymers have been reported in the last few years, showing diverse topologies, rigid or dynamic frameworks, increasingly higher pore sizes and specific surfaces, and various pore shapes and chemical nature [16]. The second reason is related to the important applications expected for these coordination polymers. As organic-inorganic zeolite analogues, these systems have shown relevant properties in the areas of ion exchange [17–22], separation processes, [23] and catalysis [24–26]. Particularly, their potential use in gas storage

applications [27–29] has greatly contributed to the expansion of this research line. For instance, Férey, Kitagawa, Yaghi, and co-workers have shown the ability of some MOFs in the sorption of carbon dioxide [30], methane [31–35], and hydrogen [27], domains of paramount importance concerning pollution and energy problems. Such results, together with the efficiency recently shown by some of these porous solids for industrial applications [36–39], make us think that MOFs-based gas storage devices will be developed in the near future. However, as far as properties are concerned, the major revolution comes from the large diversity of elements – metal ions or polynuclear species and organic molecules – involved in the direct composition of the open-framework. This situation opens new perspectives in the design of a second generation of multifunctional porous materials [40–42], which combine classical applications of zeolites associated to their inherent porosity character with the development of novel chemical and physical properties, such as, among others, magnetic, conductive, and/or optical properties (for a complete review on multifunctional open-framework materials see [43]).

Since magnetic open-framework materials are probably the most abundant among multifunctional porous materials reported to date, we aim to give, in this chapter, a short overview on the different types of magnetic and porous coordination polymers, although, due to the large number of examples so far described in the literature, we have decided to focus on representative cases. Therefore, in order to proceed in a pedagogic fashion, the second section will describe the main approaches used so far to construct molecule-based magnetic materials. Using the given information as a starting point, we will hence demonstrate, in the third and fourth sections, that the same tools and rules can be used to design magnetic and porous frameworks. Particularly, the third section will focus on purely organic open-frameworks, an emerging new class of porous solids composed of only organic molecules bonded by weak interactions, whose design takes advantage of supramolecular chemistry. The fourth section will be devoted to metal-organic coordination polymers and to some representative cases of MOFs. In the fifth section, we will show some cases reporting the most remarkable properties of coordination polymers: their dynamic structural transformations due to their flexible structures, which could be used to modulate the magnetic properties. Finally, the last section will be dedicated to the state-of-the-art research in this field, giving some representative examples on recent investigations focused on magnetic nanoporous materials.

2 Molecular Magnetic Materials: General Concepts

Magnetism has long attracted the imagination and attention of the scientific community, and magnets have been essential for the transformation of our society into the high-technology one of today [44]. Particularly, the remnance and hysteresis phenomena associated with magnetic materials are fascinating: hysteretic materials retain part of their magnetization and hence, can store information below their critical

temperature [45]. This characteristic explains the wide spreading study of molecule-based magnets for their application in modern technology as well as in the field of nanotechnology [46].

A magnetic material always consists of a spin-bearing moiety responsible for the magnetic behaviour. According to the nature of the spin site – also named magnetic unit – magnetic materials can be classified into traditional magnets, composed only of inorganic magnetic units, and molecule-based magnets, incorporating molecules in their structures. These latter ones will be the subject of this section [47].

A single spin-bearing moiety cannot be responsible for the magnetic character of a magnet, since magnetism is a bulk phenomenon, i.e., it is never associated with the presence of a single spin or many isolated spins, but rather with the presence of many interacting spins in bulk materials. Therefore, a magnet does not only consist in a magnetic unit, but also in a connector or spacer (either an organic or an inorganic species) able to propagate the magnetic interactions among the magnetic units. These connecting species can be either magnetically non-active or magnetically active. While magnetically non-active ligands are only responsible for the transmission of the exchange interactions by properly placing the spin-bearing sites in space, magnetically active spacers might play, in addition, an active role in the determination of the final magnetic properties of the material. A particular case is represented by pure organic magnets, where the magnetic unit is an organic open-shell molecule and the interaction between the spins is mediated by non-covalent bonds, such as hydrogen bonds, and therefore, no spacers, neither organic nor inorganic, are needed [48, 49], as will be described in Section 3. The main factors that contribute to the overall magnetic behaviour in molecule-based magnets are: (1) the topology of the molecules and (2) the molecular packing. The shape of the molecules and their electronic structure play a crucial role in determining the crystallographic structure, while the magnetic interaction or coupling between the spins through covalent and/or non-covalent bonds depends on the molecule packing that ultimately governs the cooperative behaviour. Hence, the molecular topology and the packing are of utmost importance for the interaction of the spins and the magnetic ordering at a characteristic temperature, named the critical temperature. Such a temperature will be determined by the strength of the magnetic interactions between the spins as well as by the dimensionality of such interactions. One of the goals of the research on molecular magnetism is to achieve a molecular material with a residual permanent magnetization at zero-field for an as-high-as-possible critical temperature, below which all spins of the magnetic units are ordered. The ordering of the spins may lead to three different types of cooperative magnetic behaviours: ferromagnetism, ferrimagnetism, and antiferromagnetism. In the case of ferromagnetism, the structure allows for a parallel alignment – ferromagnetic coupling – of all the spins in the ordered phase [50]. In both ferrimagnets and antiferromagnets there is an antiparallel alignment or antiferromagnetic coupling of the spins of neighbouring spin carriers. When the individual magnetic moments are different, the result is a non-zero total magnetic moment of the bulk material and the material is ferrimagnetic. Instead, when there is an antiparallel coupling of spins of identical magnetic moments, the magnetizations of the two sublattices cancel and

the material shows antiferromagnetism, with a total null magnetic moment. Since states of low-spin (LS) multiplicity are often more stable than states of high-spin (HS) multiplicity, and the structural and electronic requirements for achieving ferromagnetic couplings are much stricter than for antiferromagnetic ones, antiferro- and ferrimagnetism are much more common than ferromagnetism in nature.

2.1 Molecule-Based Magnetic Materials: Why?

Nowadays, research on molecule-based magnetic materials is focused on the study of molecular compounds, combining magnetic properties normally associated with inorganic materials with the chemical flexibility of their molecular tectons. While traditional inorganic materials, during their synthesis, are subjected to high temperatures, which ensure thermodynamic stability but limit chemical flexibility, one of the advantages provided by molecules is the possibility to alter and modulate the interactions between the building blocks, changing the structure of the molecule by means of organic chemical methods [51]. Moreover, if a multifunctional organic molecule is used as a synthon of the magnetic material, the result could be a multifunctional molecule-based magnetic material.

The increasing interest in molecular magnetism is explained not only by the larger malleability of molecular tectons but also by the large variety of possible applications of molecular magnetic materials into the emerging field of nanotechnology. Thus, molecular materials have emerged in many application areas such as data storage and quantum computation and the design of new conductors and superconductors, or novel non-lineal optical materials [44]. The presence of magnetism in such materials makes molecular magnetism even more interesting. Nevertheless, it remains a challenge to prepare a magnetic molecular material showing bistability at room temperature or above because of the difficulties in predicting not only the spatial arrangement of the molecules but also the strength of their magnetic interaction and hence, their bulk magnetic properties, which depend on both the architecture of the material and the cooperative intermolecular magnetic interactions.

2.2 Magnetic Interactions in Molecular Materials

The most interesting magnetic properties of a material are represented by ferromagnetism and ferrimagnetism, since they give rise to spontaneous magnetization below the critical temperature. Generally, the different behaviour of magnetic materials is explained on the basis of the magnetic exchange coupling, J, which describes the interaction between two spins and is defined by the effective spin Hamiltonian, $\hat{H} = -2JS_1S_2$, where $2J$ is the energy separation between the singlet and the triplet states. A positive J indicates ferromagnetic coupling, while a negative J indicates antiferromagnetic coupling. Generally, a parallel coupling between the spins occurs when the interacting magnetic orbitals are strictly orthogonal to each other, while if they have non-zero overlap, an antiparallel alignment will be favoured.

To have a bulk ferromagnet it is necessary that parallel couplings dominate along the three directions of the lattice, but the orthogonality conditions are difficult to impose on all the neighbours of a given spin at the same time, hence, making ferromagnetic behaviour a rarity. By contrast, antiferromagnetism is more common, since magnetic orbitals tend to overlap each other along the three directions of the lattice, favouring the antiparallel alignment of spins.

In the case of molecular materials, the first evidence of a purely organic compound with ferromagnetic interactions was given in the late 1960s when such interactions were identified in the case of galvinoxyl radicals [52] (Fig. 2).

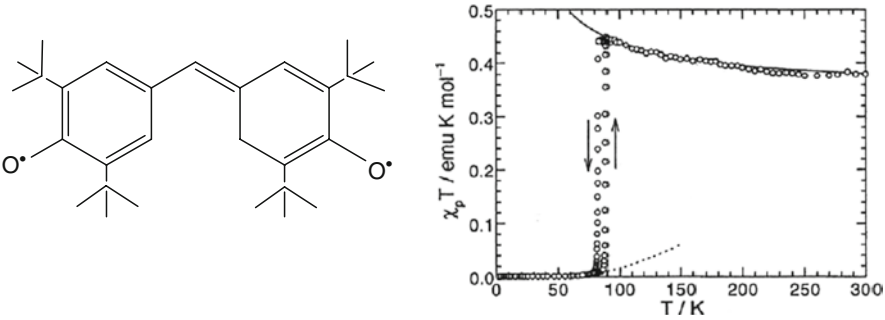

Fig. 2 Molecular formula (left) and magnetic susceptibility (right) of galvinoxyl radical. Reprinted from ref 52 [Blundell SJ, Pratt FL, "Organic and Molecular Magnets", (2004) J Phys Condens Matter 16:R771] with permission of IOP publishing Ltd

In the specific case of galvinoxyls, the small intermolecular SOMO–SOMO overlap, together with the excited charge transfer configurations, involving intermolecular interactions between the singly occupied molecular orbital (SOMO) on one molecule and the fully occupied molecular orbital on the other is responsible for the parallel alignment of the spins of neighbouring molecules. Thus, the small intermolecular SOMO–SOMO overlap can be considered as a requirement for ferromagnetic interactions in an organic compound, but only if the SOMOs are close enough for the electrostatic repulsion of neighbouring electrons to become effective [52]. Therefore, unpaired electrons interact ferromagnetically when the overlap integral is null or close to zero, a situation occurring for orthogonal orbitals, and when, at the same time, the exchange integral is significant [53]. Moreover, the propagation of the magnetic interactions along the three directions of the space depends strongly on the geometry of the molecule and its nature as well as on the type of packing forming the network of the solid.

2.3 Design Strategies for Molecular Magnetic Materials

Two different synthetic approaches to obtain molecule-based magnetic materials can be envisioned: (1) the organic approach and (2) the metal-organic approach. The first approach uses only organic molecules as magnetic units, i.e., organic free

radicals or radical-ions and no metallic ions, while in the second approach metal ions are always used as magnetic units.

2.3.1 Organic Approach

Organic radicals interacting through appropriate non-covalent bonds that allow the propagation of the magnetic interactions have been largely used as magnetic synthons following a methodology, herein called organic approach, which results in completely organic magnets. Functional groups attached to the skeleton of magnetic synthons may form supramolecular interactions that influence the solid-state structure and provide new pathways for intermolecular magnetic exchange interactions. According to the description given by Kahn in the late 1990s, magnetism is a "supramolecular function," related to the supramolecular interactions between spin-bearing molecules [54]. However, the interactions mediated by non-covalent bonds are generally very weak and extremely difficult to control. This limitation generally found for purely organic magnets is the reason why they are very rare. Moreover, their bulk magnetic order generally occurs only at very low temperatures. In purely organic magnets, the organic spin-bearing sites are open-shell molecules such as free radicals or radical ions. Most representative examples of radicals that show bulk magnetism are α-nitronyl nitroxide, verdazyl, and triphenylmethyl radicals (Fig. 3).

All these molecules share stability and persistency and take part neither in dimerization reactions nor in any other kind of addition reactions that could disrupt the presence of the unpaired electron. Moreover, the radical building blocks show enough persistency to assemble into crystalline structures where they remain isolated from one another and maintain their open-shell character.

According to the model described by McConnell, ferromagnetic interactions occur when the molecules closer in space have spin densities contacts of opposite sign [52, 55]. In contrast, antiferromagnetic interactions take place when a direct

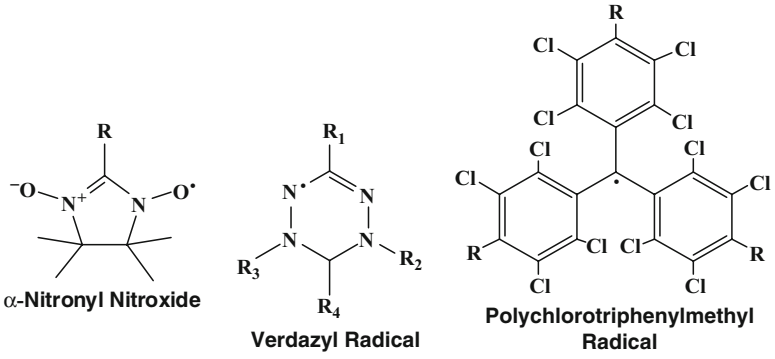

Fig. 3 Molecular formulas of the three families of stable radicals used as synthons to prepare molecular magnetic materials

overlap of the SOMOs of neighbouring molecules occurs. Because of that, the introduction of appropriate substituents into specific positions of the radical skeleton will change its packing motif, thus modifying the intermolecular magnetic exchange pathways and generating either ferromagnetic or antiferromagnetic interactions. One of the most efficient methods to modify intermolecular magnetic interactions is based on the use of hydrogen bonds, which provide a directional pathway for the transmission of magnetic interactions in several pre-established spatial directions [55, 56]. Consequently, they are the interaction of choice to design the final architecture of a material and hence, the nature and dimensionality of the magnetic interactions.

In the case of nitroxides and substituted nitroxides, the degree of delocalization of unpaired electron density is the key factor in controlling the resulting magnetic behaviour. Small changes can lead to significant modifications of the crystal structure, thereby altering the orbital overlaps and the magnetic interactions between unpaired spins on neighbouring molecules and hence, the bulk magnetic behaviour. To build organic magnets based on nitroxides, α-nitronyl nitroxides have been largely used as magnetic synthons. While in nitroxides such as TEMPO, the nitroxide group is isolated from the rest of the molecule, in α-nitronyl nitroxides there are two equivalent nitroxide groups whose unpaired electron is in a π* orbital. These are roughly equally localized onto the nitrogen and oxygen atoms, while the carbon atom located in-between the two nitroxide functions is a node in the SOMO (Fig. 4). Most of the spin density is located onto the ONCNO part of the five-membered ring, being positive in the NO groups and negative in the central C(sp^2) atom [53, 55, 57]. The α-nitronyl nitroxide radicals generally form 1-D or 2-D networks built by hydrogen bonds. The relative orientation of radicals depends on the position of the substituents on the nitroxide skeleton that rules the crystal packing and hence, the magnetic behaviour of the material.

Long-range ferromagnetism was reported for the first time by Kinoshita et al. [58, 59], the β-phase of *p*-nitrophenyl α-nitronyl nitroxide being the first example of a purely organic ferromagnet (Fig. 5) [60]. This compound was a seminal starting molecule to build organic ferromagnets that inspired the work of many researchers.

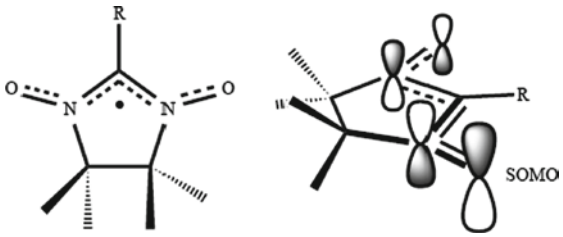

Fig. 4 General chemical structure of the family of α-nitronyl nitroxides and a representation of their singly occupied molecular orbitals (SOMO). Reprinted from ref. 55 [Amabilino DB, Cirujeda J, Veciana J, "Crystal architectures of organic molecular-based magnets", (1999) Phil Trans R Soc Lond A 357:2873] by permission of The Royal Society, Copyright 1999

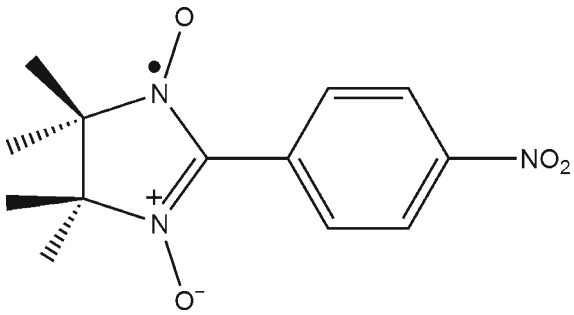

Fig. 5 Molecular formula of the *p*-nitrophenyl α-nitronyl nitroxide

Much effort has been spent on the investigation of the role of substituents and their position on the phenyl ring of α-nitronyl nitroxides [53]. The examples reported in the literature show that it has been possible to tune the magnetic interaction of α-nitronyl nitroxide-based materials by changing the type and position of the hydrogen bonding substituents that modify the crystal packing of the material. However, the extent of the magnetic interactions mediated through hydrogen bonds is quite low and hence, the critical temperature of these compounds is far from room temperature and below 4 K in most cases. Verdazyl radicals have also been investigated as tectons for molecule-based magnetic materials [61]. Their planar rings, together with the relative lack of bulky substituents and the presence of hydrogen bonding acceptor sites, make these radicals good candidates for the generation of magnetic materials [62]. Polychlorotriphenylmethyl (PTM) radicals were also successfully used for the preparation of purely organic magnetic materials, as will be reported in Section 3 [63].

2.3.2 The Metal-Organic Approach

Generally speaking, the so-called metal-organic approach consists of combining a magnetically active metal ion with an organic unit that acts as a polytopic ligand and in some cases may also be a spin-bearing unit. This strategy leads to magnetic materials with higher critical temperatures than purely organic magnets. Two main families can be distinguished. On one side are the magnets formed by magnetically active metal ions and organic moieties with a closed-shell electronic structure. In this case, the magnetic behaviour originates from the metal ion and the organic ligand has only a structural function promoting the magnetic interaction [52]. On the other side, magnets can also be formed by an organic ligand with an open-shell character combined with magnetically active metal ions. In the following subsections, we will summarize the most important aspects of both families of compounds that use the metal-organic approach.

Use of Closed-Shell Ligands

When using closed-shell ligands in the metal-organic approach, the organic moiety acts as polytopic ligand coordinating the metal ion, providing a good pathway for exchange coupling. By varying the nature, size, and the topicity of the ligand it is possible to prepare an infinite number of materials as well as tune their magnetic properties.

Many different compounds can be used as diamagnetic ligands with the role to space and transmit magnetic interactions. As it will be described in detail in Section 4.3.1, pyridine and pyrimidine derivatives can readily coordinate with metal ions and hence, give a MOF with generally weak magnetic character. However, pyridine derivatives (such as bipyridine) have been effective in the preparation of solids, showing both porosity and spin-crossover (SCO) phenomena. To increase the magnetic coupling between metal centres bearing unpaired electrons, shorter bridges – such as oxo, cyano, or azido – are usually needed. For example, the oxalate dianion (as will be shown in Section 4.1.2) is widely used as a bridging ligand to enable strong magnetic interactions between metallic centres when adopting the bidentate coordination mode. Acting as a rigid bidentate ligand, the oxalate dianion facilitates the formation of open-frameworks and modulates magnetic interactions. The role of the most representative linkers for the preparation of magnetic and porous coordination polymers will be discussed with examples in Section 4.

The most frequently used magnetic metal ions are of the transition series, but recently the world of lanthanides has also been investigated. These ions are attractive because, in some cases, they show magnetic anisotropy that renders them suitable to give bulk magnetism. Nevertheless, their lone electrons reside in the more internal *f* orbitals, resulting in magnetic interactions of one magnitude smaller than those involving transition metal ions. Another disadvantage of these ions is represented by the high coordination numbers, as compared to *d*-block transition metal ions, which may cause difficulty in controlling the synthetic reactions and thereby, the structures of the products [64].

Use of Organic Open-Shell Ligands

The methodology based on the use of a magnetic metal ion and an organic open-shell molecule, named the “metal-radical approach”, was originally introduced in the 1980s by the groups of Rey, Gatteschi and co-workers [50]. The leading idea is to combine the magnetic character of an organic radical ligand with a metal centre through coordination chemistry. Such units form a network of alternating stable radicals and metal ions, in which both constituents are generally antiferromagnetically coupled and have distinct magnetic moments, leading to a ferrimagnetic material [65]. The presence of the spin on both the metal ions and the radical represents an improvement in the magnetic properties with respect to those of closed-shell ligands with comparable sizes and, for this reason, is one of the most attractive strategies

for the design of molecule-based magnetic materials, especially if one wants to use large ligands generating open-framework structures. When metals and open-shell molecules are engaged in sufficiently strong exchange interactions, this approach leads to the preparation of networks with long-range magnetic order and high critical temperatures. The strength of magnetic interactions as well as the magnetic dimensionality of the molecular material are generally enhanced in comparison with that of systems made up from magnetic metal ions and closed-shell coordinating ligands [66]. The first requirement to build magnetic materials via the metal-radical approach is the availability of stable radicals able to coordinate or chelate the metal ions, and that can be easily modified allowing the design of multidimensional structures [67].

Nitrogen-based radicals like nitroxides and verdazyl derivatives fulfill the basic requirements, since they share high stability and persistency and can be functionalized to coordinate metal ions. Charged radicals such as tetracyanoethylene [68, 69] and tetracyanoquinone radical anions have also been reported [70], and a special case is represented by the *o*-quinone ligands that can be found in different oxidation states in valence tautomeric compounds [71]. Recently, PTM radicals substituted with carboxylate groups have been used to obtain metal-radical coordination polymers, which, in some cases, exhibit porous structures and relevant magnetic properties. Example of such porous magnets will be reported in detail in Section 4.3.3 [72].

3 Purely Organic Porous Magnetic Materials

As introduced in the previous section, different families of open-shell tectons have been used to prepare purely organic magnetic molecular materials following the organic approach. α-Nitronyl nitroxide derivatives, substituted with hydrogen bond donors to favour the packing and hence, the propagation of proper magnetic interactions, have been reported [53]. In these magnets, non-covalent hydrogen bonds play a key role in the magnetic behaviour, since they are responsible for the directional propagation of the magnetic interactions. However, the resulting coupling between the magnetic units is rather weak. For the second family of open-shell ligands, the verdazyl radicals, it has been reported how its small size, together with the planarity and π-stacking, results in strong magnetic exchange interactions, even when the two radical sites are quite far apart [61]. In all such examples, the organic tecton was a small molecule to transmit more effectively the magnetic interactions and consequently, the resulting material showed structure with close frameworks. However, as highlighted in the introductory part, the field of porous materials is of increasing interest due to its huge range of applications. So the question is: Is it possible to combine magnetic ordering and porosity in the same material? A positive answer was given by the preparation of purely organic open-frameworks showing magnetic properties using open-shell tectons with a trigonal symmetry [63]. The key point in this approach is the use of propeller-like trigonal free radicals, based

upon PTM structure, that are stable and persistent and that can be functionalized with a great variety of functional groups. The chemical stability of PTM radicals, due to the presence of six bulky chlorine atoms in the *ortho*-positions with respect to the central C-atom, makes them suitable organic magnetic units. The presence of the chlorine atoms is also responsible for the high localization onto the central sp^2 hybridized carbon atom of the electron spin density as well as for the twisting of the three phenyl rings, resulting in a propeller like structure of the radical. Even though PTM derivatives do not have a planar structure, and consequently, often show unpredictable packing, the rigidity and bulkiness of these open-shell molecules prevent in many cases their interpenetration, giving rise to solids with open-frameworks being one of the few examples of porous magnets. Thus, the introduction on the triphenyl methyl skeleton of groups capable of forming hydrogen bonds enables the formation of multidimensional interactions. Indeed, PTM radicals functionalized with several carboxylic groups are able to form robust and well-defined 2-D or 3-D frameworks that allow the propagation of weak ferromagnetic interactions [73, 74]. So far, four carboxylic -substituted PTM derivatives are available, named PTMMC, PTMDC, PTMTC, and PTMHC, according to the number of carboxylic functions (1, 2, 3, and 6, respectively), introduced onto the triphenylmethyl skeleton (Fig. 6).

The monocarboxylic PTMMC derivative does not form a rigid framework but gives an insight into the mechanism of the formation of intermolecular hydrogen bonds and transmission of magnetic interactions betwen bonded molecules in these fully chlorinated radicals [75]. PTMMC was synthesized and then crystallized following two different procedures that resulted in two phases, the α-phase and the β-phase. In the α-phase, obtained by diffusion of *n*-hexane into a dichloromethane solution of the radical, the PTMMC molecules associate into hydrogen-bonded centrosymmetric $[R_2^2(8)]$ dimeric synthons and show weak dominant ferromagnetic interactions. In the β-phase, obtained by slow evaporation of a radical solution in ethanol, the $[R_2^2(8)]$ dimeric synthons observed in the α-phase are disrupted by ethanol molecules. The ability of ethanol to form hydrogen bonds with the carboxylic groups of the radical leads to the disruption of any direct hydrogen bond between PTMMC radicals. In this phase, dominant antiferromagnetic interactions were found. The two different magnetic behaviours found in the α- and β-phase reveal that the propagation of ferromagnetic interaction mostly occurs through the

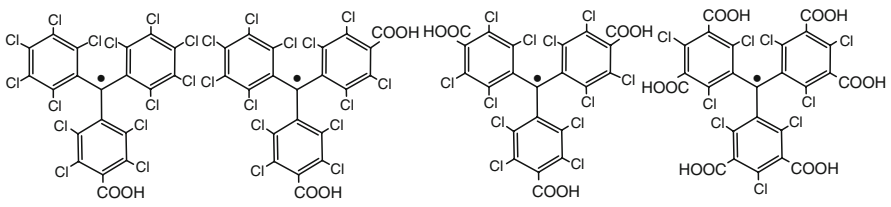

Fig. 6 Molecular formulas of the carboxy-substituted PTM derivatives (PTMMC, PTMDC, PTMTC, and PTMHC)

pathways defined by direct intermolecular hydrogen bonds between the carboxylic functions of PTM radicals.

Crystallization of PTMDC, following the same methodology used to obtain the α-phase of PTMMC, yields a robust extended hydrogen-bonded network named POROF-1, where POROF refers to pure organic radical open-framework. The presence of two carboxylic functions increases the dimensionality of the resulting structure and the intermolecular hydrogen-bonded connections between PTMDC radicals create a primary structure consisting of 2-D hydrogen-bonded sheets. Each molecule adopts two hydrogen-bonded motifs, the expected dimeric [$R_2^2(8)$] and the unusual hexameric [$R_6^6(24)$] unit, and these represent the repetitive units in POROF-1. The packing of the resultant 2-D layers creates an open-framework with 1-D channels, which are stable up to 275°C, even after the removal of included solvent molecules [76]. Magnetic measurements revealed weak antiferromagnetic interactions between the radical units at low temperature. In the case of the tricarboxylic PTM derivative, the presence of three carboxylic substituents allowed the preparation of a robust porous extended hydrogen-bonded 2-D network, POROF-2 [48, 49]. In POROF-2 , the repetitive unit is the hexameric [$R_6^6(24)$] motif, formed by six mutually hydrogen-bonded PTMTC molecules (Fig. 7a).

Each PTMTC molecule participates in the construction of three identical hexameric units that propagate along a plane (Fig. 7b). These 2-D layers stack through

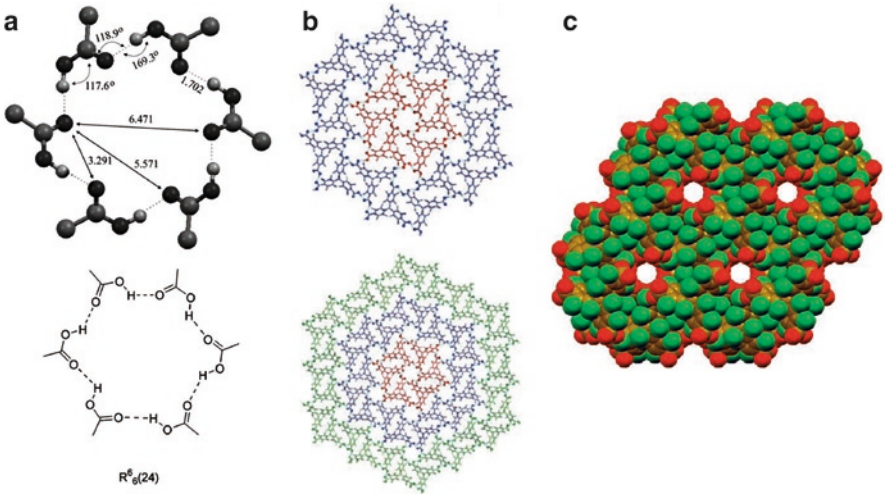

Fig. 7 (**a**) Geometrical characteristics of the hexameric [$R_6^6(24)$] ring formed by intermolecular hydrogen bonds of six PTMTC radicals. (**b**) Stepwise growth of the 2-D hydrogen-bonded sheets in POROF-2. (**c**) Space-filling representation showing the tubular channels. Reproduced with permission of ref 48 [Maspoch D, Domingo N, Roques N, Wurst K, Tejada J, Rovira C, Ruiz-Molina D, Veciana J, "Structural and Magnetic Modulation of a Purely Organic Open Framework by Selective Guest Inclusion" (2007) Chem Eur J 13:8153]. Copyright Wiley-VCH Verlag GmbH & Co. KGaA

Cl···Cl interactions and the resulting 3-D structure presents channels that can accommodate a sphere of 5.2 Å diameter (Fig. 7c). As for the magnetic properties, POROF-2 presents paramagnetic behaviour from 300 to 5 K, and a bulk ferromagnetic ordering below 2 K. It should be noted that POROF-2 is a unique example of a porous, purely organic structure, which shows long-range ferromagnetic ordering.

A PTM derivative with six carboxylic groups in the *meta* positions (PTMHC) forms 3-D hydrogen bonded open-framework. In this compound a solvent-free crystallization was not possible and mixtures of THF or diethyl ether and *n*-hexane were used. When using THF, the PTM hydrogen bonded network and thus, the transmission of the magnetic interactions are disrupted to yield a paramagnetic solid. However, when diethyl ether is used, the resulting crystal structure contains solvent molecules that only partially disrupt the expected 3-D hydrogen bonded structure. The resulting primary structure is formed by 2-D corrugated layers, with a $[R_6^6(48)]$ repetitive unit formed by six PTMHC molecules. For each molecule, three carboxylic groups are hydrogen bonded to solvent molecules, while the three remaining carboxylic groups interact with three other PTMHC molecules to give three identical hexameric units. The magnetic behaviour of this compound is very similar to that of POROF-2. Thus, in the range 20–300 K, this compound behaves as a paramagnet, and below 20 K, very weak intermolecular ferromagnetic interactions are present, and long-range magnetic ordering is expected at very low temperatures.

The availability of a family of carboxylic substituted organic open-shell compounds and the investigation of their magnetic properties allow some general observations on the behaviour of these radicals as synthons for magnetic materials: (1) increase in the number of carboxylic groups is accompanied by reduction of chlorine–chlorine contacts in the solid state; these latter contacts are usually responsible for antiferromagnetic interactions in this type of material; (2) the change in the position (*meta* versus *para*) of carboxylic groups does not appear to modify the ferromagnetic nature of the intermolecular magnetic interactions in the bulk material.

4 Metal-Organic Porous Magnetic Materials

Together with purely inorganic and molecular hybrid porous materials, coordination polymers, or 0-D zeotype systems, according to Férey's classification [6], have experienced a gigantic evolution along the last few years. Interest in this latter family of material is threefold when porosity and magnetism are combined in the same material. First, the huge versatility of molecular chemistry provides a large number of ligands whose shape and topology can be controlled. Second, and of paramount importance in the building of magnetic materials, these ligands have proven to provide good superexchange pathways. Finally, such materials may benefit from crystal engineering techniques to arrange, in a predictable fashion, transition metal ions or already identified polymetallic assemblies with organic or preformed metal-organic tectons.

In this section, we aim to give representative examples of magnetic and porous coordination polymers. We have selected examples that combine porosity and relevant magnetic properties, ranging from strong magnetic exchange interactions to magnetic ordering, to single-molecule magnet (SMM) behaviours. Since the efficiency of superexchange interactions between metal ions through bridging ligands is strongly related to the distance between the magnetic units and their relative orientation, the different examples have been divided into three subsections.

Section 4.1 will be devoted to porous and magnetic solids constructed around carboxylate-based ligands (O–C–O), which allow the formation of 1-D, 2-D or 3-D M–O–C–O–M and/or M–O–M subnetworks with magnetically active metal ions. In these systems, organic molecules are either small or extended polytopic ligands, but the magnetic properties are governed by the M–O–C–O–M or M–O–M structural motifs, which lead to strong interactions compared to the magnetic pathways defined by bridged metal ions through multitopic ligands. Section 4.2 will review examples of coordination polymers obtained by connecting metal-organic polymetallic species through polytopic organic ligands. In this class of polymers, magnetic properties are closely related to the magnetic properties of the "father" cluster and long-range magnetic ordering will only be observed if the organic ligands allow magnetic interactions between the polymetallic centres. Section 4.3 will deal with porous and magnetic coordination polymers where single ions are also connected through polytopic organic ligands. In this case, observation of magnetic properties for the bulk material will mainly depend on the distance separating the magnetic units and on the ability of the ligands to furnish efficient magnetic superexchange pathways between magnetically active metal ions.

4.1 Carboxylate-Based Porous Networks

A detailed review on carboxylate-based open-frameworks has been recently published [15]. As already mentioned, in order to obtain magnetic open-frameworks, the challenge is to control both pores size and chemical nature, together with the strength of magnetic interactions between spin-bearing moieties. In such a context, the use of short organic ligands, which favour the formation of 1-D, 2-D, and 3-D M–O–C–O–M and M–O–M carboxylate-based networks, will mediate strong magnetic interactions between magnetic units in 1-D, 2-D, and 3-D and yield, in some cases, open-framework architectures.

For this purpose, some of the most used ligands are formate (**1**), oxalate (**2**), malonate (**4**), succinate (**5**), fumarate (**6**), and glutarate (**7**) (Fig. 8). Oxamate-based ligands (**3**), inspired by the seminal work of Kahn and co-workers, have also attracted attention as nitrogen-containing oxalate analogues, since they tend to bridge metal ions not only through M–O–C–O–M but also through M–N–C–N–M motifs, which facilitate magnetic interactions. In this subsection, we include examples of magnetic porous solids constructed around the above ligands.

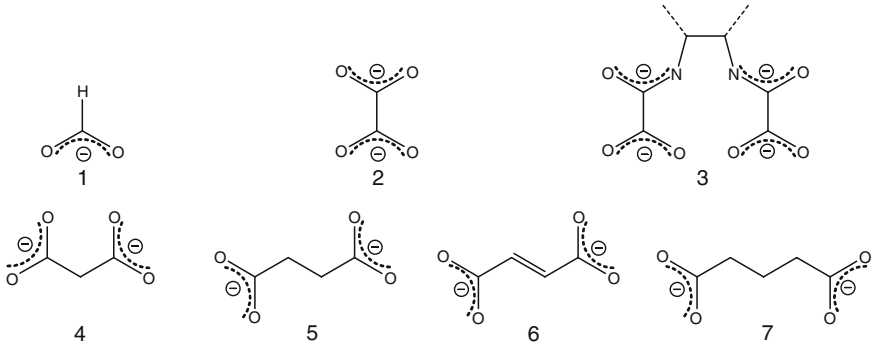

Fig. 8 Most used ligands to prepare coordination polymers with open-frameworks

4.1.1 Metal-Formate Networks

The formate ion (**1**) (Fig. 8) is the smallest and simplest carboxylate ligand, and has been widely used to prepare open-framework architectures showing high thermal stability even in the absence of guest solvent molecules [38]. The short $HCOO^-$ bridge is particularly efficient for the magnetic coupling between magnetically active metal ions. Moreover, the absence of any bulky substituent in **1** favours *anti–anti* coordination modes. Therefore, several magnetic open-framework metal formates showing 1-D, 2-D, and 3-D M–O–C–O–M/M–O–M subnetworks have been reported [77–81]. A representative example of this family of porous and magnetic solids is given by the compound $Mn_3(\mathbf{1})_6{\cdot}CH_3OH{\cdot}H_2O$, reported by Kobayashi, Kurmoo, and co-workers [82]. This solid possesses a diamondoid framework with high stability and flexibility for the inclusion of many types of guests. It exhibits 1-D channels with dimensions of 4 × 5 Å (32% of the total volume cell), where each node comprises $MnMn_4$ tetrahedral clusters built around a central Mn(II) ion, connected to four Mn(II) ions located at the apices via formate ligands to generate a 3-D M–O–C–O–M/M–O–M network. The network is robust up to 533 K and exhibits a particularly rich guest-modulated magnetic behaviour, as it will be explained in detail in Section 5.1. Both the as-synthesized and the evacuated solid show long-range magnetic ordering, with a critical temperature close to 8 K (Fig. 9).

Several additional examples of formate-based open-framework magnetic materials presenting long-range magnetic order have been reported. Depending on the metal ions used, the structural topology, the nature of guest molecules, and the use of ancillary ligands or ammonium templates, different kinds of magnetic ordering have been observed in the related materials, which order magnetically below temperatures ranging from 8 to 35.6 K [77–83]. Among them is the coordination polymer of formula $Mn(\mathbf{1})_3{\cdot}0.5CO_2{\cdot}0.25HCOOH{\cdot}0.75H_2O$, reported by Sessoli and co-workers, which shows particularly interesting porosity and traps CO_2 molecules in its cavities [83].

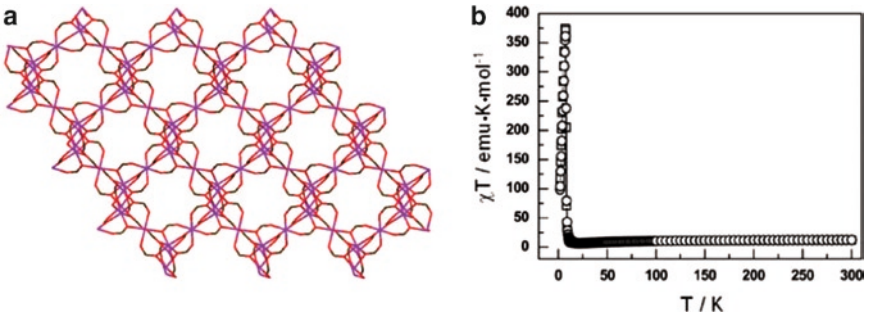

Fig. 9 (**a**) Structure of evacuated $[Mn_3(\mathbf{1})_6]$ showing the 1-D channels. (Mn, *purple*; O, *red*; C, *brown*). (**b**) Temperature dependence of the χ•T product for an applied magnetic field of 100 Oe. Reproduced from ref. 82 by permission of The Royal Society of Chemistry. http://dx.doi.org/10.1039/b314221c

4.1.2 Metal-Oxalate Networks

As in the case of formate, the dicarboxylate oxalate ion (**2**) (Fig. 8), which acts as a rigid ambidendate ligand, facilitates the formation of open-framework coordination polymers and mediates the magnetic interactions between magnetic metal ions through similar "inorganic" M–O–C–O–M or M–O–M subnetworks. So far, the use of such a ligand has led to several examples of mixed-valence polymers with 2-D and 3-D open-framework architectures, respectively. In the first case, the 2-D coordination polymers are described with the common formula $(A)\cdot[M^{II}M^{III}(\mathbf{2})_3]$, where A can be an ammonium, an alkali-metal, or a bis-cyclopentadienyl M(III) complex such as $[Cp_2M^{III}]^+$ [84–92]. Overall, the crystal structure shows a templated framework formed by alternating M(II) and M(III) metal ions through oxalate ligands in a 2-D honeycomb-like lattice, the positively-charged species being located in the channels resulting from the packing of the different layers (Fig. 10a). Various formulae are observed for 3-D MOFs resulting from the oxalate coordination chemistry: $[M_2^{II}(\mathbf{2})_3]$, $[M^{I}M^{III}(\mathbf{2})_3]$ and $[M^{II}M^{III}(\mathbf{2})_3]$ [93–95]. These compounds are based on an oxalate-bridged (10,3)-chiral network able to host in its 1-D channels cationic metal complexes such as $[M^{II}(2,2'\text{-bpy})_2]^{2+}$ (2,2'-bpy = 2,2'-bipyridine) (Fig. 10b).

The wide range of possible combinations of M(II) and M(III) magnetically active metal ions afford long-range anti-, ferro- and ferrimagnetic behaviours [96–99]. Depending on the material, magnetic ordering temperatures range from 8 K up to 70 K. However, the main drawback of oxalate-based frameworks is related to the presence of cationic species within their channels, since their removal or exchange leads to the collapse of the open-framework. To date, and to the best of our knowledge, the only exception is $Na_2(N(CH_3)_3Ph)_5[Cr(\mathbf{2})_3]_2Cl\cdot 5H_2O$, which maintains its structure on cation exchange or partial thermal removal of the template [100].

The possibility to combine several physical properties in the same molecular material has greatly contributed to the development of this family of coordination polymers. Added to the already mentioned chiral characteristics presented by some

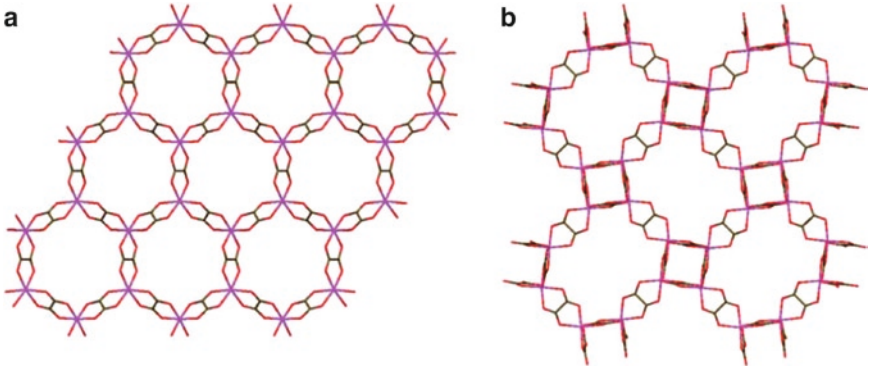

Fig. 10 Projection of the two representative templated lattices constructed from using oxalate ligands. (**a**) 2-D honeycomb framework of (A)•[M(II)M(III)(**2**)$_3$] (where A refers to ammonium cations, alkali-metal cations, or $Cp_2M(III)$). (**b**) Chiral (10,3)-network observed in [M(II)$_2$(**2**)$_3$], [M(I)M(III)(**2**)$_3$], and [M(II)M(III)(**2**)$_3$]. (M, *purple*; O, *red*; C, *brown*. Cationic templates are omitted for clarity). Adapted from ref 43 [Maspoch D, Ruiz-molina D, Veciana J (2007) Chem Soc Rev 36:770, "Old materials with new tricks: multifunctional open-framework materials"] by permission of The Royal Society of Chemistry, http://dx.doi.org/ 10.1039/b501600m

of these solids and interest in the quest for optically active molecular materials [101, 102], a strategy based on functional cationic templates has also been successfully developed. For instance, Coronado and co-workers have reported a series of magnetic conductors using tetrathiafulvalene (TTF) radical cations as cationic counterparts [103, 104]. A representative example of this is given by the material [BEDT-TTF]$_3$ [MnCr(**2**)$_3$], where BEDT-TTF stands for bis(ethylenedithio)TTF, which alternates magnetic oxalate-based anionic layers with conductive positively-charged BEDT-TTF. This molecular solid behaves as a magnet below 5.5 K and is metallic down to at least 0.2 K [105].

In the race to obtain molecular materials showing robust structures and higher magnetic ordering temperatures, two more examples have to be highlighted before closing this subsection. Related to the structure robustness, Li and co-workers reported a series of coordination polymers of general formula [M^{II}(**2**)(4,4'-bpy)]$_n$ (M = Fe, Co, Ni) [106, 107]. These solids result from the linkage of metal-oxalate chains through 4,4'-bipyridine ancillary ligands, and show rectangular-shape channels with dimensions of 5 × 8 Å and are stable up to 563–613 K. Furthermore, magnetic properties revealed a spontaneous antiferromagnetic ordering with transition temperatures of 12, 13, and 26 K for the Fe-, Co-, and Ni-based materials, respectively. These results are attributed to the combination of both the strong magnetic exchanges within the 1-D metal-oxamate chains and the weaker ones mediated through the bipyridine connectors.

Julve, Lloret, and co-workers have reported several isomorphous oxalate-based coordination polymers presenting magnet behaviour through spin canting below 40 and 70 K [108, 109]. Among them, the 3-D and chiral coordination polymer [Fe$_2$(**2**)$_2$(OH)Cl$_2$]·EtNH$_3$·2H$_2$O is the most interesting. This material possesses helical

channels (ca. 12 × 6 Å), in which the alkyl ammonium and water molecules are associated through hydrogen bonds. The structure is constructed around Fe(II)-oxalate chains interconnected through hydroxo-bridges. Remarkably, this coordination polymer undergoes a non-reversible solid–solid transformation together with a colour change when the crystals are exposed to air. In this transformation, a proton transfer occurs between the hydroxo bridge and one of the host water molecules, thus forming a new compound $o[Fe_2(\mathbf{2})_2(O)Cl_2]\cdot EtNH_3\cdot H_3O\cdot H_2O$. Even though this transformation leads to a decrease in channel symmetry, the new solid still behaves like a magnet below 70 K [109].

4.1.3 Metal-Oxamate Networks

Like their fully oxygenated analogues, oxamate-based ligands (**3**) (Fig. 8) have also gained much attention in the field of molecular magnetism, and some of the first examples of molecule-based magnets were obtained following the rational-design strategy developed by Kahn and co-workers. In this pioneering work, mononuclear oxamato copper(II) complexes $[Cu(\mathbf{3})]^{2-}$ were used as bis(bidentate) metallo-ligands toward fully solvated metal ions to form heterobimetallic 1-D coordination polymers through M–O–C–O–M and M–N–C–N–M repeat units. Depending on the interchain interactions, the ferrimagnetic chains $[M^{II}Cu(\mathbf{3})]$ (M = Mn, Fe, Co, Ni) show either ferromagnetic (T_C = 4.6–9 K) [110–113] or antiferromagnetic order (T_N = 2.4–3 K) [113, 114]. In subsequent work, Kahn, Stumpf, and co-workers prepared the corresponding oxamato-bridged $M_2^{II}Cu_3$ 2-D planar species (M = Mn, Fe, Co, Ni) presenting either an open-framework structure or a perpendicular interlocked disposition of honeycomb hexagonal planes depending on the nature of the counter-cation, which could be an alkaline [115] or an alkylammonium [116–118] cation as in the case of oxalate-based networks, or even a substituted pyridinium derivative of nitronyl nitroxide [119–122]. Unlike their 1-D analogues, these compounds have a higher ordering temperature, with T_C values up to 37 K. These examples perfectly illustrate the influence of the structural dimensionality upon the magnetic ordering temperature. Moreover, the change in anisotropy of the incorporated metal ion plays a fundamental role. Generally, Mn_2Cu_3 planes behave as soft magnets (H_c = 10 Oe) [116, 117, 119], whereas Co_2Cu_3 ones are hard magnets (H_c = 25 Oe) [121]. This is due to the large differences in magnetic anisotropy, with Co(II) ions being highly anisotropic and Mn(II), isotropic. Inspired by this work, Julve, Lloret, and Journaux extended this well-known "complex as ligand" approach by using oligonuclear complexes of late first row transition metal ion, from mono- to trinuclear, working with related aromatic-substituted mono-, di-, and tri-oxamate-based molecules (**8–10**) as ligands (Fig. 11) (for a detailed review on this strategy, see [123]).

This strategy was particularly elegant, since the reaction between the oxamate ligands with metal ions afforded pre-defined metallotectons. For example, coordination of Cu(II) through the bidentate N,O-oxamate donor set of **8** was aimed to afford the linear, ditopic metallotecton $[Cu^{II}(\mathbf{8})]^{2-}$, while reaction of the same

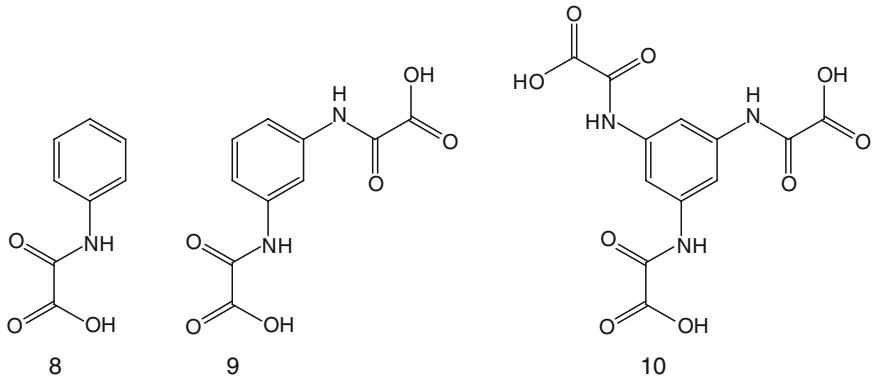

Fig. 11 Aromatic-substituted mono-, di-, and tri-oxamate-based molecules used as polytopic ligands

molecule with Ni(II) or Co(II) targeted the trigonal and tritopic building blocks $[Ni^{II}(\mathbf{8})]^{4-}$ and $[Co^{II}(\mathbf{8})]^{4-}$, respectively. Mono-, di-, tri-, hexa-, octa-, and nonanuclear complexes were prepared via blocking the outer *cis* carbonyl-oxygen atoms of the oxamate groups with well-known nitrogen-based metallamacrocycles stoppers. Careful magneto-structural correlations on metallotectons involving ligands **9** or **10** confirmed that the weak intramolecular interactions mediated through the *meta*-substituted phenyl rings are ferromagnetic and could be masked by the intermolecular antiferromagnetic interactions and/or magnetic anisotropy effects. On this basis, the already identified H-shaped metallo-ligand $[Cu^{II}(\mathbf{9})]^{4-}$ an its methylated analogue $[Cu^{II}(\mathbf{Me_3}\text{-}\mathbf{9})]^{4-}$ were reacted with Co(II) to afford the neutral heterobimetallic 2-D coordination polymers $[Co_2^{II}Cu_2^{II}(\mathbf{9})_2(H_2O)_6]\cdot 6H_2O$ and $[Co_2^{II}Cu_2^{II}(\mathbf{Me_3}\text{-}\mathbf{9})_2(H_2O)_6]\cdot 6H_2O$ (Fig. 12). The crystal structure of $[Co_2^{II}Cu_2^{II}(\mathbf{9})_2(H_2O)_6]\cdot 6H_2O$ shows a brick-wall 2-D architecture of (6,3) net topology [124]. In these isostructural solids, each $Co_2^{II}Cu_2^{II}$ rectangular corrugated layer is made up of oxamato-bridged $Co^{II}Cu^{II}$ linear chains running parallel to the *a*-axis, which is further connected through two *m*-phenylenediamidate bridges between the Cu(II) ions to give binuclear metallacyclic cores of the cyclophane-type, which define the short edge of the rectangle. The adjacent planes stack above each other to give an infinite array of interdigitated layers along the *b*-axis. This packing is mediated through weak hydrogen bonds and the neighbouring layers are displaced in a parallel manner along the *a*-axis: As a consequence, small square pores that are occupied by hydrogen bonded crystallization water molecules are formed.

In this series of metallacyclophane-based $Co_2^{II}Cu_2^{II}$ layered compounds, the double *meta*-substituted phenylene linkers ensure a ferromagnetic interaction between the oxamato-bridged ferrimagnetic chains. Hence, the complex $[Co_2^{II}Cu_2^{II}(\mathbf{9})_2(H_2O)_6]\cdot 6H_2O$ behaves as a metamagnet, with a long-range 3-D antiferromagnetic ordering ($T_N = 8.5$ K) and a ferromagnetic-like transition at a critical field of 1.2 kOe, which is sufficient to overcome the weak interlayer antiferromagnetic interactions. In contrast, the complex

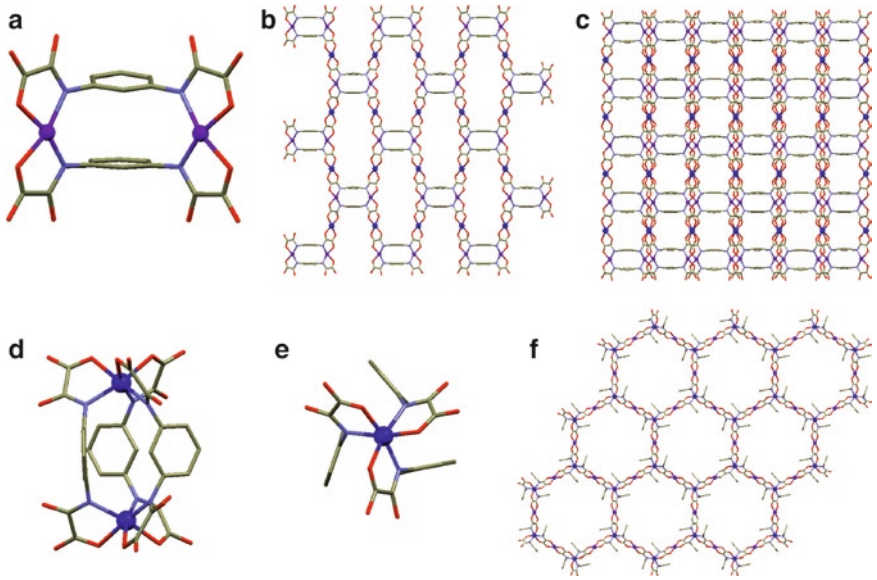

Fig. 12 "Metal-oxamate" approach for coordination polymers $Co(II)_2Cu(II)_2(\mathbf{9})_2(H_2O)_6 \bullet 6H_2O$ (A-C) and $Li_5[Li_3M(II)_2\mathbf{9}_3\ (H_2O)_6] \bullet 31H_2O$ (M = Ni and Co) (**d-f**). (**a**) H-shape metallo-ligand $Cu(II)(\mathbf{9})^{4-}$. (**b**) Corrugated layer resulting from the reaction of the H-shape metallo-ligand with Co(II) ions. (**c**) Packing of the corrugated layers showing square-like channels running along the *b*-direction. *Side* (**d**) and *top* (**e**) view of the hexatopic metallo-ligand $[M(II)_2\mathbf{9}_3]^{8-}$ (M = Ni or Co). (**e**) Reaction of hexatopic metallo-ligands with Li^+ or Mn^{2+} metal ions afford a 3-D honeycomb architecture of (6,4) net topology with large channels running along the *c* direction. (From (**a**) to (**c**): Cu, *purple*; Co, *blue*. From (**d**) to (**e**): Co or Ni, *blue*; Li or Mn, *purple*. In all cases: O, *red*; C, *brown*, N, *light blue*. Cationic templates and water molecules are omitted for clarity) (the figure design has been inspired from refs 124 and 125)

$[Co_2^{II}Cu_2^{II}(\mathbf{Me_3\text{-}9})_2(H_2O)_6]\cdot 6H_2O$ shows a long-range (most likely 2-D) ferromagnetic order at $T_C = 24.0$ K because of the minimization of the interlayer magnetic interactions that would lead to well-isolated planes of Ising-type magnetic anisotropy. The differences observed between the two coordination polymers in the magnetic ordering are attributed to the presence of the methyl substituents on the ligands, which, in the second case, tend to separate the planes from each other, thus weakening the interlayer interactions.

Very recently, a series of isostructural 3-D open-framework architectures have been obtained following a comparable approach. In this case, the dinickel(II) and dicobalt(II) complexes $[M_2^{II}(\mathbf{9})_3]^{8-}$ act as hexatopic ligands toward fully solvated Li^+ or Mn^{2+} ions to give anionic heterobimetallic 3-D compounds of general formula $[Li_3M_2^{II}(\mathbf{9})_3(H_2O)_6]_n^{5n-}$ and $[Mn_3M_2^{II}(\mathbf{9})_3(H_2O)_6]_n^{2n-}$, respectively [125]. The crystal structures of the lithium salts $Li_5[Li_3M_2^{II}(\mathbf{9})_3(H_2O)_6]\cdot 31H_2O$ (M = Ni, Co) show a 3-D honeycomb architecture of (6,4) net topology. The crystal lattice of these two isostructural compounds consists of an infinite parallel array of anionic

oxamate-bridged $Li_3M_2^{II}$ hexagonal layers growing in the *ab* plane; the adjacent layers are interconnected through three *m*-phenylenediamidate bridges between the M(II) ions to give binuclear metallacryptand cores of the meso-helicate-type, which act as pillars of the hexagonal prismatic structure. Overall, this leads to an open-framework structure showing hexagonal pores of ca. 22.5 Å in diameter (along the *c*-direction), where hydrogen bonded water crystallization molecules and solvated Li^+ species $[Li(H_2O)_6]^+$ are located. The magnetic properties of this family of metallacryptand-based $M_3^IM_2^{II}$ open-framework compounds depend mainly on the diamagnetic or paramagnetic nature of M(I) and on the magnetic anisotropy of M(II). Hence, the compounds $Li_5[Li_3M_2^{II}(\mathbf{9})_3(H_2O)_6]\cdot 31H_2O$ (M = Ni, Co) behave as isolated M_2^{II} complexes with weak ferromagnetic interactions between the M(II) ions (M = Ni, Co) across the three *meta*-substituted phenylenediamidate bridges within the metallacryptand core [J = +3.2 (M = Ni) and +1.0 cm^{-1} (M = Co)]. Similarly, the three *meta*-substituted phenylene linkers ensure a ferromagnetic interaction between the oxamato-bridged ferrimagnetic planes in the compounds $Li_2[Mn_3M_2^{II}(\mathbf{9})_3(H_2O)_6]\cdot 22H_2O$ (M = Ni, Co), which lead to a long-range 3-D ferromagnetic order at T_C = 6.5 K for both of them.

4.1.4 Fumarate-, Glutarate-, Malonate-, and Succinate-Based Networks

Numerous examples of metal channel-like magnetic complexes synthesized using malonate (**4**), succinate (**5**), fumarate (**6**), and glutarate (**7**) ligands (Fig. 8) have been reported. For most of these porous solids, a 3-D framework is obtained by connecting 2-D carboxylate-based layers with bifunctional ligands, the same ligands also acting as pillars [126–132]. This topology usually defines 1-D channels running parallel to the layers. However, from a magnetic point of view, these solids rarely show long-range magnetic ordering. An exception to this topology was found in the malonate complex [Cu(**4**)(DMF)], which shows a 3-D chiral diamond-like open-framework resulting from the connection of Cu(II) ions through malonate linkers and behaves as a ferromagnet below 2.6 K [133].

Especially attractive from a magnetic point of view are the open-frameworks involving infinite M–O–M type linkages. For example, Forster and Cheetham have described a nickel succinate $[Ni_7(\mathbf{5})_6(OH)_2(H_2O)_2]\cdot 2H_2O$ with infinite Ni–O–Ni connectivity, and exhibiting 1-D hydrophobic channels composed of large cavities of dimensions of 8 Å and narrower apertures of 4 Å [134]. This material exhibits a high thermal stability up to 673 K and may be magnetically frustrated. Similarly, the nickel glutarate $[Ni_{20}(\mathbf{7})_{20}(H_2O)_8]\cdot 40H_2O$ reported by Guillou et al. presents an infinite Ni–O–Ni connectivity with very large intersecting 20-membered ring channels and a pure ferromagnetic ordering at 4 K [135]. The porosity characteristics of this material are particularly interesting, since it can be dehydrated at 423 K and slowly rehydrated under air at room temperature, and when the sample is activated at 473 K shows a surface area of 346 $m^2\cdot g^{-1}$. Also, an open-framework showing ferrimagnetic behaviour below 20 K has been prepared by the same authors using succinate (**5**) ligands. The porous solid $[Ni_7(\mathbf{5})_4(OH)_6(H_2O)_3]\cdot 40H_2O$ shows 1-D

connected Ni–O–Ni chains and presents a reversible dehydration/hydration process, with a specific surface of 135 $m^2 \cdot g^{-1}$ for its activated form [136].

4.2 *Networks Based on Metal-Organic Polynuclear Species and Polytopic Organic Ligands*

So far, most part of the porous and magnetic coordination polymers we have described are constructed around 1-D, 2-D, or 3-D "inorganic" subnetworks. However, discrete di-, tri-, tetranuclear, and higher nuclearity metal-organic assemblies, such as the carboxylate-based paddle-wheel copper acetate and trimeric zinc or iron acetates are suitable building blocks – commonly called secondary building block units (SBUs) - for polymerization reactions involving polytopic ligands [10]. Such clusters are spaced in defined geometries depending on their own geometry and the geometry of the polytopic ligands. As a result, extended coordination polymers with high porosity and predictable structures are typically obtained. Using a cluster with an inherent property, one can then imagine distributing these SBUs in a desired way along the 3-D of space to create porous solids with novel functionalities. For example, catalytic clusters may be included in the skeleton of a porous structure, increasing the accessibility for these units and, therefore, enhancing their catalytic properties. From the magnetic point of view, the assembly of clusters also provides an excellent route to magnetic porous solids. The advantages of this strategy are obvious, since on one hand larger pores can be obtained from large cluster units and, on the other, the functional framework inherits the interesting physical properties derived from the clusters. However, since magnetic properties in the bulk are resulting from cooperative effects, the ligands used have to allow the establishment of magnetic interactions between the magnetically active SBUs, while the magnetic interactions between the metal ions within the SBU will also greatly influence the overall magnetic behaviour. This subsection gives a few representative examples of porous and coordination polymers constructed around metal-organic SBUs, starting with high nuclearity species, and then, examples of magnetic MOFs constructed around more common low nuclearity metal-organic clusters.

4.2.1 High Nuclearity Metal-Organic SBUs

Despite the numerous examples of high nuclearity metal-organic clusters presenting SMM behaviour reported in the literature since the beginning of the nineties, only a few examples of multidimensional coordination polymers using such clusters as SBUs behaving as SMMs have been described [137–140]. These systems are based upon the assembly of SMM acting as SBUs, thanks to coordination bonds [137], diamagnetic metal ions [138], and/or hydrogen bonds [139]. Among them, the isostructural coordination polymers of formula $\{[Mn_{19}Na(\mu_4\text{-}O)_9(\mu_3\text{-}O)(\mu_3\text{-}OH)_3(O_2$

$CMe)_9(pd)_9(H_2O)_3][OH]\}_n$ and $\{[Mn_{19}Na(\mu_4\text{-}O)_9(\mu_3\text{-}O)(\mu_3\text{-}OH)_3(O_2CMe)_9(mpd)_9(H_2O)_3][OH]\}_n$ (pd = propanediolate, mpd = 2-methyl-propanediolate) reported by Christou and co-workers [140] are the only ones that show an open-framework architecture. In these coordination polymers, the structure is constructed around the Mn_{19} SBUs containing seven Mn(II) and 12 Mn(III) ions. The manganese–oxygen core of each SBU consists of three equilateral triangles stacked one above the other. The basal triangle contains ten manganese ions, nine at its edges and the tenth near its centre, whereas the middle and apex triangles contain six and three manganese ions, respectively, all of which lie on their edges. The manganese ions of the core are held together by nine $\mu_4\text{-}O^{2-}$, one $\mu_3\text{-}O^{2-}$, and three $\mu_3\text{-}OH^-$ ions, resulting in an overall triangular-pyramidal frustum topology. The peripheral ligation is completed by nine bridging propanediolate ligands, nine bridging O_2CMe^- ligands, and three terminal H_2O molecules. Each Mn_{19} aggregate is connected through three $\mu_3\text{-}O_2CMe^-$ ligands to a Na^+ ion, while these SBUs are also directly interconnected through $\mu_3\text{-}O_2CMe^-$ ligands. Examination of the two structures reveals highly ordered 3-D structures that contain large rectangular channels with dimensions of approximately 12 × 16 Å (Fig. 13a). These channels are nearly empty, containing only a very small proportion of H_2O molecules and OH^- counterions, and originate a void space of approximately 44%. The SMM behaviour of these extended systems was confirmed, thanks to magnetisation versus dc field measurements. Below 1.1 K, they show magnetic hysteresis loops and their coercivity increases with decreasing temperature (Fig. 13b).

Besides these two examples, a series of open-framework architectures showing rather weak antiferromagnetic interactions have also been constructed around Ln_7 [141] and Mn_6 [142, 143] SBUs. In the latter SBU, the 3-D coordination polymer

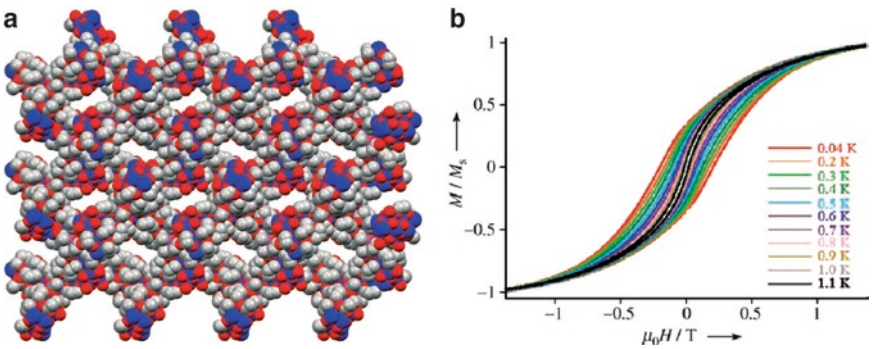

Fig. 13 (**a**) Space filling representation (along the *c* axis) for the polymeric structure of $\{[Mn_{19}Na(\mu_4\text{-}O)_9(\mu_3\text{-}O)(\mu_3\text{-}OH)_3(O_2CMe)_9(pd)_9(H_2O)_3][OH]\}_n$ showing the large channels (Na, *pink*; Mn, *blue*; O, *red*; C, *grey*; OH^- anions and water molecules are omitted for clarity). (**b**) Field dependence of the magnetization (hysteresis loop) for single crystals of the same solid at the indicated temperatures; the magnetization (*M*) is normalized to its saturation value. Reproduced with permission of ref 140 [Moushi EE, Stamatatos TC, Wernsdorfer W, Nastopoulos V, Christou G, Tasiopoulos AJ "A Family of 3D Coordination Polymers Composed of Mn19 Magnetic Units" (2006) Angew Chem Int Ed 45:7722]. Copyright Wiley-VCH Verlag GmbH & Co. KGaA

reported by Ovcharenko et al. in 2004 perfectly illustrates the difficulty in obtaining relevant magnetic properties in the final solid [143]. Substitution of preformed $[Mn_6(O_2)Piv_{10}]$ (piv = pivaloate) afforded magnetic clusters linked through magnetically active α-nitronyl nitroxide ditopic ligands. This coordination polymer has a 3-D open-framework diamond-like structure and shows the onset of weak antiferromagnetic interactions at low temperatures.

4.2.2 Tetra- and Trinuclear Metal-Organic SBUs

Tetra- and trinuclear SBUs have also been reported as constituents of porous and magnetic coordination polymers. Coordination polymers constructed around Co_4 [144] and cubane-like Ln_4 [145] assemblies have been reported, and these systems present contrasting porosity and robustness, but show only weak and predominant antiferromagnetic interactions at low temperature. Very recently, Yang and co-workers described a series of 3-D lanthanide-transition MOFs constructed around two distinct tetranuclear units of Ln_4 cubanes and chair-like Cu_4 clusters [146].

More interesting from a magnetic point of view is the porous coordination polymer reported by Wu and co-workers [147]. This solid is built from tetranuclear Co(II) citrate clusters as octahedral linkers and Co(II) ions as trigonal nodes. This connectivity shows an anatase topology with channels of 9.5 × 4.3 Å along two directions, leading to an apparent Langmuir surface area of 939 $m^2 \cdot g^{-1}$ and a pore volume of 0.31 $cm^3 \cdot g^{-1}$. This material behaves as a 3-D canted antiferromagnet with a magnetic hysteresis loop observed at 2 K.

Trinuclear metal-organic building blocks, such as Cr_3 or Fe_3 containing assemblies, have been used by Férey and co-workers to build highly porous and robust coordination polymers [30]. An example of an MOF-based trimeric structural unit was described by Barthelet et al. [148]: the coordination polymer $[V^{III}(H_2O)]_3O(C_8O_4H_4)_3(Cl \cdot 9H_2O)$ exhibits a 3-D framework built from octahedral vanadium trimers, joined via isophthalate anionic linkers to delimit cages where water molecules and chlorine ions are occluded. Although the trimeric clusters are connected along three directions, the 120° triangular topology of V(III) ions in each cluster induces a spin-frustration of their magnetic moments and therefore, a lowering of the temperature for magnetic ordering.

4.2.3 Binuclear Metal-Organic SBUs

One of the most frequently used SBUs is the binuclear paddle-wheel copper (II) dimer. In this motif, the two copper ions are strongly interacting in an antiferromagnetic fashion. This dimeric building-block supplies a square planar building block with four grafting sites, therefore, its connection provides coordination polymers combining relevant magnetic properties with contrasted porosity by an appropriate choice of ligands.

In 1999, Williams and co-workers were the first to report the magnetic properties of a porous structure based on the connectivity of paddle-wheel Cu(II) dimers through 1,3,5-benzenetricarboxylate ligands (BTC), with a 3-D structure with formula $[Cu_3(BTC)_2(H_2O)_3]$, referred to as HKUST-1[149, 150]. The connectivity between square planar copper-based SBUs and trigonal organic ligands afford a 3-D network showing channels with fourfold symmetry and a diameter of 9 Å. In addition, the structure remains crystalline up to 513 K. Water molecules that fill the channels can be readily removed at 373 K without a loss of structural integrity. Resulting voids give a surface area of 917.6 $m^2 \cdot g^{-1}$, a calculated density of 1.22 $g \cdot m^3$, and an accessible porosity of nearly 41% of the total volume cell. Interestingly, additional experiments of the activated HKUST-1 showed that pore functionalization is possible without losing the overall structural information. Added to these particularly interesting structural characteristics, HKUST-1 presents relevant magnetic properties [150]. As shown in Fig. 14, this porous coordination polymer shows a minimum in its χ versus T plot at around 70 K and an increase at lower temperatures. Fitting high-temperature data to the Curie–Weiss law gives a positive Weiss constant of 4.7 K. This magnetic behaviour can be explained by the presence of the expected strong antiferromagnetic interactions within Cu(II) dimer and weaker ferromagnetic interactions between Cu(II) dimers, which are mediated through the *meta*-substituted phenyl rings of the ligands.

Other magnetic porous solids have been prepared using the paddle-wheel Cu(II) dimer as SBUs [151–156]. For instance, Zaworotko and co-workers proposed to combine such molecular square building blocks with the 1,3-benzenedicarboxylate ligand (*m*-BDC), i.e., a V-shape spacer, to generate two porous frameworks, according to the self-assembly of two different SBUs: a triangular SBU, formed by three connected paddle-wheel Cu(II) dimers, or a square SBU, formed by four connected

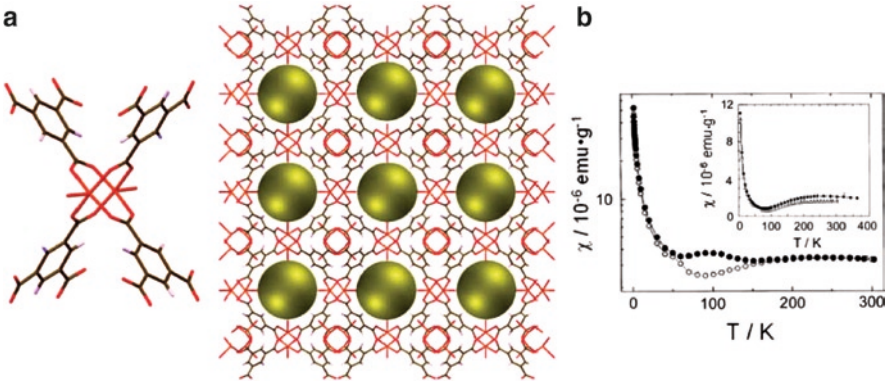

Fig. 14 (a) Paddle-wheel copper (II) tetracarboxylate building block for $[Cu_3(C_9O_6H_3)_2(H_2O)_3]$ and view of the open-framework showing nanochannels with fourfold symmetry. The empty space is represented as yellow spheres. (Cu, *orange*; O, *red*; C, *brown*; H, *white*). (**b**) Zero-field cooled (○) and field-cooled (•) temperature dependent magnetic susceptibility. Reprinted with permission from ref 150. Copyright 2000, American Institute of Physics.

paddle-wheel Cu(II) dimers. The first of such structures, $[(Cu_2(py)_2(m\text{-}BDC)_2)_3]_n$, was generated from the self-assembly of the triangular SBU to yield a Kagomé lattice with hexagonal channels presenting dimensions of 9.1 Å [151, 152]. The second structure, $[(Cu_2(py)_2(m\text{-}BDC)_2)_4]_n$, was generated from the self-assembly of Cu(II) dimers with a square topology to lead a 2-D network with channels formed by narrowed windows (1.5 × 1.5 Å) and large cavities with maximum dimensions close to 9.0 × 9.0 × 6.5 Å [153]. As for HKUST-1, the Kagomé lattice shows high rigidity in the absence of solvent guest molecules and pyridine ligands, which can be removed at a temperature of 473 K without losing crystallinity. Its most interesting feature is the report of remnant magnetization even at room temperature, due to the magnetic spin frustration associated with its triangular lattice [154], although this result seems to be controversial based upon the molecular character of this material. In contrast, the 2-D framework with a square-like arrangement of the dimeric units does not present any remnant magnetization due to lack of any geometrical frustration. In this context, its magnetic behaviour is comparable to that already observed for HKUST-1, with Cu···Cu intradimer antiferromagnetic interactions of −238 cm^{-1}, but with antiferromagnetic interdimer interactions of −85 cm^{-1}. Examples based on ligands such as 1,3,5,7-adamantane tetracarboxylate and 1,2,4,5-benzenetetracarboxylate have also been reported. In the first case, the porous coordination polymers formed present a typical inorganic platinum sulphide-based topology, a high porosity and a surface area of 560 $m^2 \cdot g^{-1}$ for their activated form [155]. For the second ligand, a 2-D coordination structure with rectangular pores of 6.0 × 7.0 Å is obtained [156]. In both solids, strong antiferromagnetic Cu···Cu intradimer antiferromagnetic interactions are observed.

Finally, channel-like magnetic frameworks built from the spacing of dimers other than the paddle-wheel dimer can also be found. To date, coordination polymers composed of nitrogen-bridge [157], oxo-bridge [156, 158], carboxylato-bridge [156, 159], and mixed oxo/carboxylato-bridge [160] dimers have been reported. For example, Liu et al. reported a family of coordination polymers formed around dicobalt(II) building blocks linked through nicotinate ligands that show robust open-framework structures up to 570 K, with antiferromagnetic coupling within the cobalt dimers [160].

4.3 Networks Based on Isolated Metal Ions and Polytopic Organic Ligands

A large variety of open-framework solids prepared using carboxylate ligands composed of a six-member ring (phenyl or a cyclohexane) backbone substituted with two or more carboxylate functional groups are known. However, even though the magnetic properties of many of them are not described, the magnetic exchange interactions between metal ions are expected to be weaker in comparison with the coordination polymers described so far in this section. For example, two complexes formed by Ni(II) macrocycles linked by BTC ligands show structures

with large channels (ca. 11 Å), but they only behave as paramagnets with very weak antiferromagnetic interactions at low temperatures [161]. Similarly, other coordination polymers prepared using benzene carboxylates with the general formula $CH_{6-n}(COO^{-})_n$ exhibit comparable weak interactions [162–164]. Besides these examples, different kinds of ligands such as N-containing or mixed N- and COOH-containing polytopic ligands have also been successfully used in the construction of porous and magnetic MOFs. This subsection provides some examples of coordination polymers obtained by this approach, or using both polytopic COOH and N-based ligands. In the last part, a strategy inspired from the "metal-radical" approach [50], which is based on the use of paramagnetic-organic polytopic open-shell ligands, is highlighted.

4.3.1 Nitrogen-Based Polytopic Ligands

Open-frameworks constructed around ditopic N-based ligands such as bipyridine have been recently reviewed. These systems show contrasting porosities, but ligands such as bipyridine usually afford solids only presenting antiferromagnetic interactions at low temperatures [5]. Examples based on tetratopic ligands such bispyrazolate, bistriazolate, or extended versions of bipyridine, among others, have also been described [165]. If these ligands do not allow an efficient transmission of magnetic interactions between isolated metal centres, porous solids showing SCO properties can be accessed [166, 167]. For example, Kepert and co-workers have reported a series of nanoporous SCO coordination polymers based on extended 4,4'-bipyridine derivatives as ditopic ligands (Fig. 15).

The complexes $[Fe_2(ligand)_4(NCS)_4]\cdot\times$ guest (guest = ethanol, acetone) consist of almost orthogonal doubly-interpenetrated 2-D (4,4) rhombic grid layers built from the linkage of Fe(II) by different ditopic ligands. In the coordination polymer

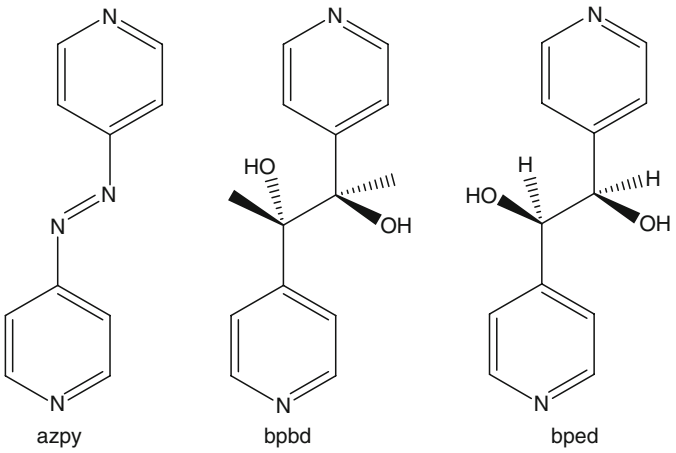

Fig. 15 Extended 4,4'-bipyridine used as ditopic ligands

of $[Fe_2(azpy)_4(NCS)_4]$·EtOH, this interpenetration leads to the formation of two kinds of 1-D channels with dimensions of 10.6 × 4.8 and 7.0 × 2.1 Å, respectively [166]. These channels run in the same direction and are filled with ethanol molecules. Loss of guest ethanol occurs at 373 K and is accompanied by several reversible structural changes. The as-synthesized sample exhibits a constant effective magnetic moment of 5.3 μB between 300 and 150 K. Below this temperature, the magnetic moment decreases, reaching a constant value of 3.65 μB due to the SCO interconversion from a fraction of the Fe(II) ions in the material. In contrast, the evacuated sample does not show SCO behaviour, but exhibits a constant magnetic moment around 5.1 μB corresponding to two crystallographic HS Fe(II) ions.

Smaller and simpler molecules such as imidazole or pyrimidinol derivatives have also been used with success to construct porous and magnetic solids. Compared to their extended analogues, they offer shorter magnetic exchange pathways that help generate stronger magnetic interactions between isolated magnetically active metal ions. For instance, Gao, You, and co-workers have reported a family of Co(II) imidazolates (im) complexes showing a variety of open-framework structures with different magnetic behaviours [168]. In this case, the rational use of solvents and counter-ligands plays a key role to obtain a collection of polymorphic 3-D porous Co(II) structures: $[Co(im)_2]$·0.5py, $[Co(im)_2]$·0.5Ch, $[Co(im)_2]_2$, $[Co(im)_2]_4$, and $[Co_5(im)_{10}$·0.4 $Mb]_5$ (py = pyridine, Ch = cyclohexanol, Mb = 3-methyl-1-butanol). Complexes $[Co(im)_2]$·0.5py and $[Co(im)_2]$·0.5Ch are isostructural, formed by Co(II) centres linked into boat- and chair-like six-membered rings connected in an infinite diamond-like net. This conformation affords 1-D channels of dimensions 5.3 × 10.4 Å and 6.6 × 8.4 Å (Fig. 16a). The crystal structure of $[Co(im)_2]_4$ shows four-membered ring Co(II) units, which are doubly-connected to wavelike or double crankshaft-like chains. These chains intersect with those running along the perpendicular axis by means of the common four-rings at the wave peaks. Three such frameworks are interwoven and linked by the imidazolates at the Co(II) ions, and the resultant 3-D framework presents 1-D helical channels of dimensions 3.5 × 3.5 Å (Fig. 16b). Similarly, the MOF $[Co(im)_2]_2$ shows identical units connected into chain units. These chains are linked by imidazolate ligands along the other two directions to give a 3-D framework with a pore openings of 4.0 × 4.0 Å (Fig. 16c). Of special structural interest is the complex $[Co_5(im)_{10}$·0.4 $Mb]_5$, which shows an open structure of zeolitic topology (Fig. 16d). In all polymorphous frameworks, the imidazolates ensure antiferromagnetic coupling between Co(II) ions. However, the uncompensated antiferromagnetic couplings arising from particular stoichiometries and topologies lead to spin-canting phenomena that are particularly sensitive to the structural characteristics. Thus, compound $[Co(im)_2]$·0.5py is an antiferromagnet with $T_N = 13.1$ K , while $[Co(im)_2]$·0.5Ch shows weak ferromagnetism below 15 K (Fig. 16e). Relatively strong ferromagnetism is observed below 11.5 K for $[Co(im)_2]_4$, with a coercive field of 1,800 Oe at 1.8 K, while the strongest ferromagnetism of the series is observed in $[Co(im)_2]_2$, which has a T_C of 15.5 K and a coercive field of 7,300 Oe at 1.8 K (Fig. 16f). The compound $[Co_5(im)_{10}$·0.4 $Mb]_5$ behaves as a hidden-canted antiferromagnet with a magnetic ordering temperature of 10.6 K.

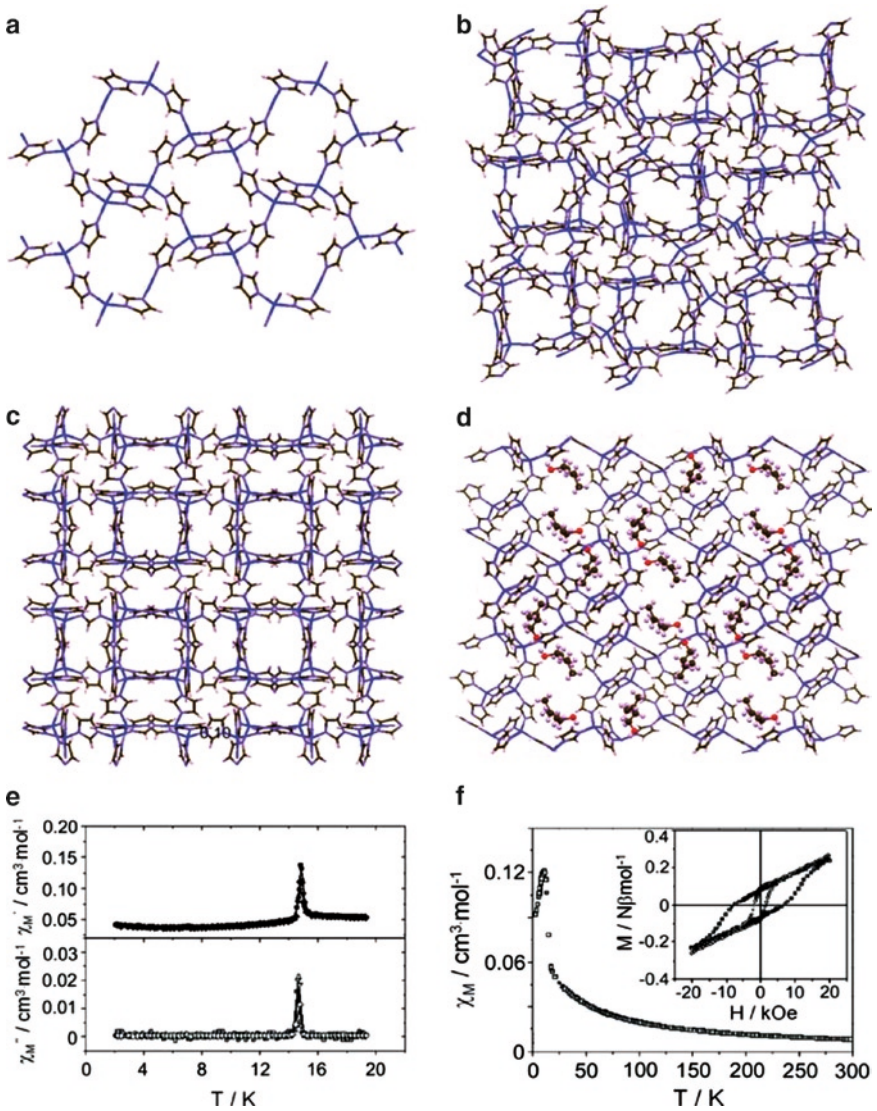

Fig. 16 Views and magnetic properties of the open-framework coordination polymers based on cobalt imidazolates. (**a**) Evacuated $[Co(im)_2]\cdot 0{\bullet}5Ch$. (**b**) $[Co(im)_2]_4$. (**c**) $[Co(im)_2]_2$. (**d**) $[Co_5(im)_{10}{\bullet}0.4Mb]_5$. (**e**) Plots of temperature dependence of ac susceptibility obtained at 0.1 Oe field for $[Co(im)_2]$ 0.5Ch. A peak appears at 15 K, which is indicative of the ferromagnetic character of this compound. (**f**) Plot of the thermal evolution of the χ_M for $[Co(im)_2]_2$ at 10 kOe field. The inset shows the hysteresis loop at 1.8 K (□) and 5.0 K (○). (Co, *blue*; O, *red*; C, *brown*; N, *violet*; H, *white*. Solvent guest molecules in (**d**) are represented as spheres) Reprinted from ref 168 [Tian YQ, Cai C-X, Ren X-M, Duan C-Y, Xu Y, Gao S, You X-Z, "The Silica-Like Extended Polymorphism of Cobalt(II) Imidazolate Three-Dimensional Frameworks: X-ray Single-Crystal Structures and Magnetic Properties" (2003) Chem Eur J 9:5673]. Copyright Wiley-VCH Verlag GmbH & Co. KGaA. Reproduced with permission

Ligands such as pyrimidin-2-ol [169] and pyrimidin-4-ol [170] have also been extensively used in this material chemistry. In 2006, Galli, Navarro, and co-workers reported a series of microporous and isomorphous coordination polymers based on 5-X-pyrimidin-2-olate ligands (referred to as 5-X-2-pymo; X = H, Cl, Br, I) [171]. All the complexes are isomorphous, with a formula $[Co(5\text{-X-2-pymo})]_n$, and show a diamondoid 3-D topology. Depending on the substituent X, important changes are observed for the magnetic properties at low temperatures. While the pyrimidinolate ligands transmit antiferromagnetic coupling between Co(II) ions, the uncompensated antiferromagnetic coupling arising from the diamondoid topology leads to magnetic ordering through spin-canting phenomena below T_N, ranging from 20 to 23 K. The spin-canting phenomena are sensitive to the ligand structure and a significant enhancement of the magnetic hardness takes place in the halo-substituted derivatives compared to the hydrogenated analogues. Thus, the coercive fields decrease in the following sequences: 2,500, 1,000, 775, and 500 Oe for X = Br, Cl, I and H, respectively, while the remnant magnetisation follows the trend 0.0501 μB for X = Br, 0.0457 μB for X = Cl, and 0.0358 μB for X = H. Interestingly, the authors also reported the preparation of molecular alloys (X = 0.5 Br + 0.5 Cl or 0.5 Br + 0.5 I), which are intermediate properties compared to the above examples.

4.3.2 Nitrogen and Carboxylic-Based Polytopic Ligands

Polymeric architectures generated by the linkage of magnetically active metal ions through mixed carboxylic and *N*-based ligands, or through ligands combining both functionalities, have also been reported [172–178].

A perfect illustration of this approach is given by the coordination polymer $\{[Co_3(IDC)_2(4,4'\text{-bpy})3]\cdot 6H_2O\cdot DMF\}_n$ reported by Cao and co-workers [175]. In this porous solid, reaction between imidazoledicarboxylic acid ($IDCH_3$) and Co(II) ions yields triangular SBUs. These SBUs exchange corners to afford a 2-D-honeycomb-like network with 24-membered metallacycles composed of six IDC^{3-} anions and six Co(II) cations. The different graphene-like layers are pillared, thanks to 4,4'-bipyridine, the nitrogen atoms completing the coordination sphere of Co(II) ions belonging to neighbouring layers.

As a result of this connectivity, hexagonal channels running parallel to the 4,4'-bipyridine are obtained (Fig. 17). These channels, which present a 12 Å diameter, are filled with water and DMF molecules. Guest solvent molecules departure is completed at a temperature of 450 K without losing the structural integrity, and both the as-synthesized and evacuated samples show weak Co···Co antiferromagnetic interactions at low temperature.

One of the most successful families is represented by a series of polymers built from the linkage of metallic carboxylate chains through 4,4'-bipyridine spacers [176]. As an example, the coordination polymer $[Cu(C_4H_4O_4)(4,4'\text{-bpy})(H_2O)_2]\cdot 2H_2O$ is formed by the connection of chains of Cu(II) metal ions bridged by succinate ligands through 4,4'-bipyridine molecules. This 3-D framework shows weak ferromagnetic interactions and channels, in which the water molecules are located.

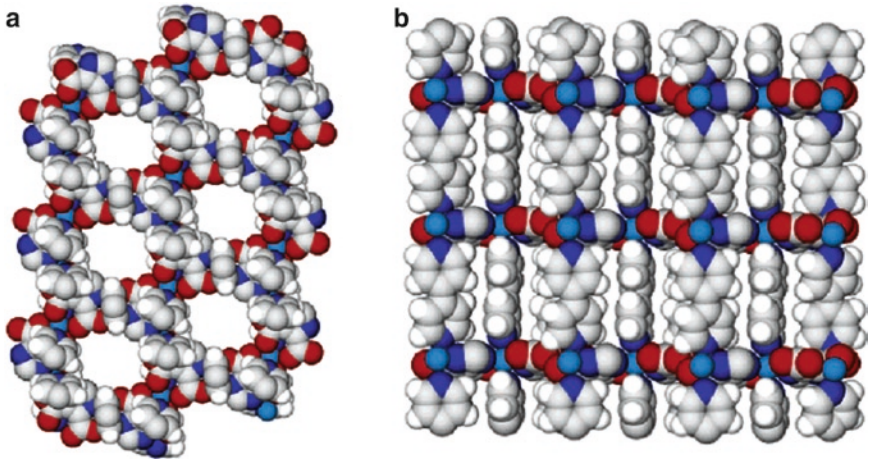

Fig. 17 Open-framework architecture of $\{[Co_3(IDC)_2(4,4'\text{-bpy})3]\cdot 6H_2O\cdot DMF\}_n$. (**a**) Top view showing the 12 Å in diameter hexagonal channels. (**b**) Side view showing the graphene-like layers pillared through bipyridine ligands (Co, *light blue*; O, *red*; N, *dark blue*; C, *grey*; H, *white*) Reprinted with permission from ref 175. Copyright 2005, American Chemical Society

Almost similar connectivity and magnetic properties are observed in the porous solid $[Fe(C_4O_4)(4,4'\text{-bpy})(H_2O)_2]\cdot 3H_2O$ [177]. Chains of Fe(II) metal ions bridged by squarate ligands are connected through 4,4'-bipyridines to form a framework with 1-D channels filled with water molecules. Interestingly, the dehydration/rehydration process in this coordination polymer, as well as in other isostructural polymers with other metal ions, is fully reversible and accompanied with a continuous change of the colour [178].

4.3.3 Organic Open-Shell Polytopic Ligands

In all the examples described so far, it can be noted that when the distance between metal ions increases, the magnetic coupling decreases. As already introduced in Section 2, magnetic coupling between metal ions generally takes place through a superexchange mechanism involving the ligands, a mechanism that is dependent on their relative orientations, and especially on the distance between magnetically active metals. Since the synthesis of larger pore sizes in coordination polymers is usually achieved by using longer organic spacers, the preparation of porous materials with increasing pore size dimensions and simultaneous long-range magnetic properties is a challenge.

The use of organic radicals as polytopic ligands is particularly attractive since these molecules are expected to act as magnetic relays between metal ions, thus allowing larger magnetic couplings and dimensionalities compared to those built from diamagnetic polytopic ligands [179]. However, the number of examples showing

high dimensionality architectures is limited due to synthetic considerations linked to ligand preparation and the coordination polymer formation [180]. In order to prepare porous and magnetic coordination polymers following this approach, the organic open-shell ligands must fulfill a series of conditions. They must have the correct geometry to induce the formation of open-framework structures, exhibit high chemical and thermal stability, and be able to interact magnetically with transition metal ions. To fulfill all three conditions, a strategy based on the use of polychlorinated triphenylmethyl tricarboxylic acid radical (PTMTC) as ligands has been developed. The conjugated base of the PTMTC radical can be considered an expanded version of the BTC ligand, where the benzene-1,3,5-trityl unit has been replaced by an sp^2 hybridized carbon atom decorated with three 4-substituted 2,3,5,6-tetrachlorophenyl rings. Therefore, PTMTC would be expected to yield open-frameworks structures similar to BTC. In addition, polychlorinated triphenylmethyl radicals have their central carbon atom, where most of the spin density is localized, sterically shielded by the encapsulation, with six bulky chlorine atoms that greatly increase their lifetime and thermal and chemical stability [181]. A family of monomeric complexes using a similar PTM radical with only one carboxylic group (PTMMC) has confirmed the feasibility of this type of carboxylic-based radicals to interact magnetically with metal ions [72, 182, 183].

Using these types of open-shell polytopic ligands, a series of metal-organic radical open-framework (MOROF-n), Fig. 18 have been prepared. Interestingly, the crystal structure of $[Cu_3(PTMTC)_2(py)_6(EtOH)_2(H_2O)]$ (MOROF-1) reveals a 2-D honeycomb (6,3) network with very large 1-D hexagonal nanopores measuring 3.1 and 2.8 nm between opposite vertices and composed of a ring of six metal units and six PTMTC radicals. The long through-space distances between the magnetic Cu(II) ions in MOROF-1 do not prevent long-range magnetic ordering. Each open-shell PTMTC ligand is able to magnetically bridge three Cu(II) ions and, therefore, extend the magnetic interactions across the infinite layers, giving a

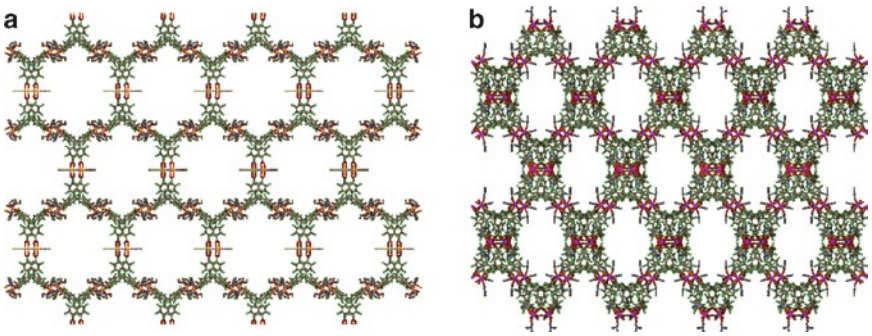

Fig. 18 Open-framework architectures for (**a**) MOROF-1 and (**b**) MOROF-4. (**a**) has been adapted from ref 63, by permission from Macmillan Publishers Ltd: Nature Materials. Copyright (2003). http://dx.doi.org/10.1038/nmat834. (**b**) has been adapted from ref 186 by permission of The Royal Society of Chemistry. http://dx.doi.org/10.1039/b802196a

ferrimagnetic layer. The solid thus shows an overall magnetic ordering at low temperatures, around 2 K [63], which is probably produced by the magnetic dipolar interactions between the large magnetic moments developed in each layer at this temperature.

Reaction of the PTMTC ligand with Co(II) ions yielded two other supramolecular Co(II)-based MOROF, namely $[Co(PTMTC)(4,4'\text{-bpy})(H_2O)_3]\cdot 6EtOH\cdot 2H_2O$ (MOROF-2) and $[Co_6(PTMTC)_4(py)_{17}(H_2O)_4(EtOH)]$ (MOROF-3). MOROF-2 presents an unprecedented $(6^3)\cdot(6^8\cdot 8^1)$ topology and exhibits helical nanochannels of dimensions 13.2 × 9.4 Å, along with antiferromagnetic interactions [184]. MOROF-3 exhibits a (6,3)-helical network with large 17.5 × 6.8 Å 1-D channels and a bulk magnetic ordering below 1.8 K [185]. More recently, the same ligand has also been reacted with magnetic Ln(III) ions to afford a series of highly porous and magnetic coordination polymers. As an example, the coordination polymer $[Tb(PTMTC)(DMF)_3]$ (MOROF-4) shows a diamond-like architecture resulting from the corner sharing of tetrahedron SBUs made by 4 PTMTC ligands and 8 Tb(III) ions. Similar to some zeolite structures such as sodalite, the connectivity of the large SBUs in MOROF-4 creates large pore sizes of dimension 22.2× 11.3 Å and generates 2-D channels running along the *a* and *b* axes. These cavities are large enough to endow this material with a total potential void volume of 61.7% of the cell volume. In this solid, PTMTC-Tb(III) ferromagnetic interactions are observed at a low temperature [186].

5 Magnetic and Porous Materials with Flexible Frameworks

One of the most remarkable characteristics of many molecule-based porous materials is their structural flexibility [187]. This feature not only concerns 0-D coordination polymers, but all the dimensionalities of the inorganic subnetworks, as well as pure organic porous materials. Thus, dynamic structural transformations such as the selective removal and resorption of solvent molecules followed by reversible crystal transformations have become one of the most intriguing properties observed for these porous materials ([188] and references cited therein). So far, two main types of dynamic structural transformations have been described. The first class deals with a reversible crystal-to-amorphous transformation that occurs when the framework collapses upon removal of guest solvent molecules and regenerates under initial or similar conditions. The second type corresponds to frameworks showing a phase transition; a crystal-to-crystal transformation. In the latter case, although removal or exchange of guest molecules results in reversible structural changes within the network, the crystalline character is maintained throughout. The structural flexibility of the coordination polymer originates from the changes in the degree of freedom (rotations, stretching, scissoring, breathing, etc.) of bonds (coordination bonds, hydrogen bonds, π–π stacking, van der Waals interactions) linking the units in the polymeric material. Thus, when a structural variation is induced by an external perturbation, for example on uptake/release of

guest molecules, a cooperative transformation of the macroscopic structure occurs, but causes no wide-range degradation of the crystal phase. An excellent account of main factors involved in such dynamic structural transformations has been published by Kitagawa et al. [40].

Recently, several authors have pointed out the possibility of using these reversible structural transformations to design a novel generation of multifunctional porous solids suitable as potential sensors. Since most of the functionalities known in porous solids are closely dependant on their crystal structure, reversible transformations upon sorption/removal of guest molecules can conveniently induce reversible modifications of the associated functionalities. This, together with the high selectivity usually shown for dynamic solids, provides the ideal scenario for researchers to create selective sensing open-frameworks for molecular recognition. Some recent examples of dynamic porous solids exhibiting tuneable magnetic properties will be presented, and a rare example of a MOF showing fascinating gas induced modulation of magnetic properties will be highlighted.

5.1 Solvent-Induced Modulation of Magnetic Properties

Kahn's group can be considered pioneer in the discovery of coordination polymers that combine both porosity and magnetism, coupled with the modulation of magnetic properties arising from guest-induced phenomena [189, 190]. In their seminal paper, published in 1999 [191], they first introduced the concept of a "molecular magnetic sponge" for a coordination polymer. As an example of these sponge-like polymers, the compound $[CoCu(obbz)(H_2O)_4]\cdot 2H_2O$, (obbz = N,N'-bis(2-carboxyphenyl)oxamido) shows a two-step reversible hydration/dehydration process followed by a dramatic change in the magnetic properties [192]. As a consequence of the first dehydration at 373 K, the discrete units link together to form a 1-D structure that behaves as a ferrimagnet with no ordering down to 2 K. A second dehydration process takes place on heating the sample up to 473 K. The resulting presumed 2-D structure still behaves as a ferrimagnet, but with a critical temperature of 30 K. All these processes are completely reversible, and the material can be rehydrated after cooling with the recovering of the initial magnetic properties.

Several examples of porous and magnetic coordination polymers showing solvatomagnetic effects have been reported. In 2003, the open-framework coordination polymer $[Cu_3(PTMTC)_2(py)_6(EtOH)_2(H_2O)]$ (MOROF-1; see also Section 4.3.3), which combines very large pores (3.1 × 2.8 nm, and a 65% void volume) with magnetic ordering around 2 K, was reported [63]. Added to these properties, another particularly interesting feature was observed for this material: the reversible "shrinking-breathing" process observed on solvent uptake and release, which, in turn, induces changes in magnetic properties (Fig. 19a).

On removal from solution and exposed to air, crystalline MOROF-1 loses guest solvent molecules very rapidly, becoming an amorphous magnet with a lower critical temperature (Fig. 19b). The critical temperature is determined not only by the

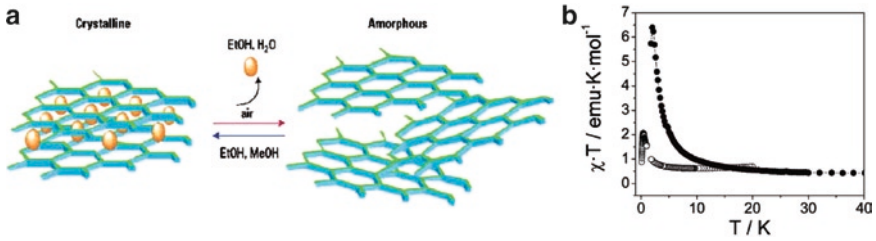

Fig. 19 (**a**) Schematic representation of the reversible crystal-to-amorphous transformations in MOROF-1. Reprinted from ref 193, by permission from Macmillan Publishers Ltd: Nature Materials. Copyright 2003. http://dx.doi.org/10.1038/nmat837. (**b**) Plot of χ_M·T versus temperature for as-synthesized (•) and evacuated (○) MOROF-1. The graph has been adapted from ref 63

strength of the magnetic interactions between the spins but also by the dimensionality of such interactions and hence, the crystal packing of the network. However, the evacuated sample of MOROF-1 experiences a transformation, recovering its original crystallinity and magnetic properties after exposure to ethanol solvent. Unexpectedly, this behaviour is only observed when MOROF-1 is exposed to small alcohols like methanol and ethanol, showing a large selectivity for these two molecules among 16 larger alcohols assayed [63]. Contrasted solvatomagnetic effects have been described in several molecular porous materials reported by Kurmoo and co-workers. For example, reversible dehydration/rehydration processes in the porous and magnetic solids $[Co_3(OH)_2(\mathbf{2})_2]\cdot 3H_2O$ and $[Ni_3(OH)_2(C_8O_2H_{10})_2(H_2O)_4]\cdot 2H_2O$ induces reversible transformations from ferromagnetic to antiferromagnetic ordering and from ferromagnetic to ferrimagnetic ordering, respectively (Fig. 20b) [194, 195].

In contrast to the large structural transformations experienced by MOROF-1, where volume variations close to 30% are observed between the as-synthesized and the amorphous guest-free solid, these latter interconversions are accompanied by subtle changes in crystal structure. For example, the dehydration process in $[Co_3(OH)_2(\mathbf{2})_2]\cdot 3H_2O$ only involves minimum changes in its structure, with almost no change in the coordination environment of the metal ions (Fig. 20a). This fact clearly suggests that the ferromagnetic ground state in the hydrated phase may be caused by the presence of significant magnetic exchange coupling through the hydrogen bonded water molecules located within the channels.

The influence of sorbed guest molecules on magnetic properties was also nicely evidenced in the diamondoid coordination polymer $[Mn_3(\mathbf{1})_6]\cdot CH_3OH\cdot H_2O$, in which the magnetic ordering temperature depends on the guest molecules in the framework (very recently, guest influence on magnetic properties in a series of isomorphous compounds of formula $[Fe_3(\mathbf{1})_6]\cdot$x guest (with x = iodine, THF, furan, benzene, acetonitrile, and acetone) has also been explored in detail [196]). Indeed, magnetic measurements of the as-synthesized or evacuated sample show a long-range magnetic ordering with a critical temperature close to 8 K. However, this critical temperature can be modulated from 5 to 10 K by the sorption of several

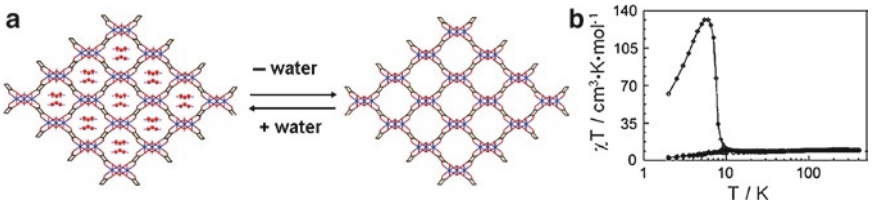

Fig. 20 Structure and magnetic properties in $[Co_3(OH)_2(\mathbf{2})_2]\cdot 3H_2O$ (**a**) Almost similar as synthesized and evacuated solids (water molecules are represented as spheres). (**b**) Strong modulation of the magnetic properties between as-synthesized (○) and evacuated (•) materials. Reproduced from ref 43 by permission of The Royal Society of Chemistry. http://dx.doi.org/10.1039/b501600m

types of guest molecules. This transformation can be explained by the small changes of the Mn–O–Mn bond angles – the larger the angle, the smaller the T_C – which are modulated on absorption of guest molecules. Very recently, the same authors have also shown this framework to become optically active when enantiomerically pure 2-chloropropan-1-ol molecules are inserted in its channels [197]. The apohost framework is achiral but incorporates channels of opposite handedness (+) *P* and (−) *M*. Upon insertion of either *R* or *S* chiral solvent molecules the two corresponding chiral solids – *R* and *S*, respectively, are obtained. These results are explained by the fact that in the obtained chiral *R* framework the *R* molecules better match the *M* channels and are disordered in the *P* channels, while in the *S* framework the *S* molecules are ordered in the *P* channels and disordered in the *M* channels. In contrast, with the addition of a racemic solvent mixture, the meso compound can be obtained. In this case, random disorder of the two guests in both kinds of channels is observed. All the solids resulting from these loading experiments show a ferrimagnetic ground state. Nevertheless, compared to the host framework, the Curie temperature decreases to 7.6 K for both *R* and *S* solids, while it slightly increases to 8.3 K in the *meso* form. In the chiral solids, additional interactions between the framework and ordered guest solvent molecules through hydrogen bonds or other electrostatic forces are responsible for the decrease in magnetic ordering temperature.

Porous solids such as Prussian Blue analogues [198, 199], in which CN^- spacers connect magnetic metal ions in the three directions, deserve to be commented upon since they could exhibit important changes in their magnetic properties and colors upon dehydratation/rehydration processes [200–202]. For example, Ohkoshi, Hashimoto, and co-workers have recently reported $Co[Cr(CN)_6]_{2/3}\cdot zH_2O$, a pink ferromagnetically-coupled magnet with a T_C of 28 K that reversibly transforms into a blue antiferromagnetically-coupled magnet with a T_C of 22 K on dehydration [203]. Such solvatomagnetism and solvatochromism are ascribed to the adsorption and desorption of ligand water molecules at the Co(II) centres. Such processes change the coordination geometry at Co(II) from six-coordinate pseudo-octahedral to four-coordinate pseudo-tetrahedral coordination, thus modulating the magnetic

interactions from ferromagnetic coupling in the hydrated solid to antiferromagnetic ones in the apohost.

Very recently, Sutter and co-workers reported a series of nanoporous and chiral magnets showing switchable ordering temperatures driven through similar H_2O sorption/desorption phenomena [204]. These coordination polymers $[\{Mn(HL)(H_2O)\}_2Mn\text{-}\{Mo(CN)_7\}_2\cdot 2H_2O$ are formed from the reaction of $\{Mo(CN)_7\}^{4-}$ with Mn(II) ions and enantiomerically pure *R*, *S* or racemic mixture of N,N-dimethylaminol (L), which acts as an ancillary ligand and confers to those materials chiral characteristics. Overall, the different structures show a 3-D cyano bridged Mn–Mo network, which has small channels running along the *c*-direction (Fig. 21a). These channels are filled with water molecules and they are defined by "Mn_4-Mo_4" rings with each $\{Mo(CN)_7\}^{4-}$ unit connecting two different Mn(II) ions. One Mn(II) ion shows a distorted tetrahedral environment consisting of four NC–Mo linkages, while the other has a distorted octahedral coordination sphere with four NC-Mo linkages and two O-atoms, one coming from the L molecule, and the other from an ancillary water molecule. Lattice and coordinated water molecules are readily removed upon heating to afford an apohost crystalline material via a phase transition.

Interestingly, the starting hydrated compound is fully recovered after the exposure of the desolvated phase to air over 50 min. As observed in the previous examples, loss of coordinated water leads to a strong modification of the coordination sphere of one of the Mn(II) ions, which changes from a distorted octahedral environment to five coordinate. This reduced coordination number leads to the shortening of the Mn-NC bonds and gives stronger Mn-Mo interactions within the framework. The hydrated material shows magnetic ordering below $T_C = 85$ K (Fig. 21b), and the ordering temperature is shifted to $T_C = 106$ K in the apohost (Fig. 21c). Since the crystal-to-crystal transformations are fully reversible, magnetic features are recovered when the framework is rehydrated.

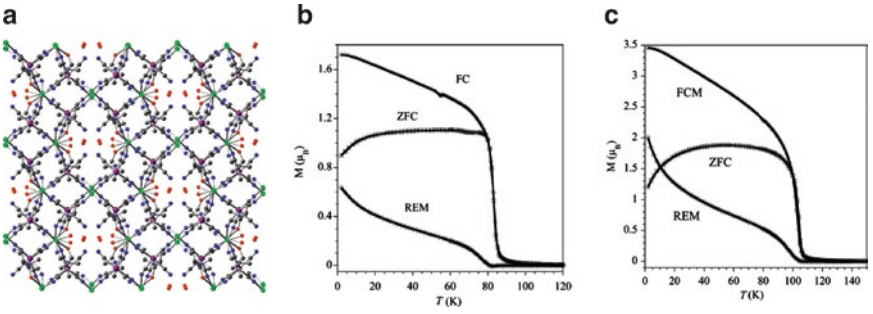

Fig. 21 (**a**) Open-framework architecture of S-$[\{Mn(HL)(H_2O)\}_2Mn\text{-}\{Mo(CN)_7\}_2\cdot 2H_2O$ (water molecules are represented as red spheres). Field cooled magnetization (○, $H = 100$ Oe), zero field cooled (□), and remnant magnetization (◊) as a function of temperature for the hydrated (**b**) and dehydrated (**c**) solids. Reprinted with permission from ref 204. Copyright 2007, American Chemical Society

5.2 Solvent-Induced Modulation of Spin-States

The influence of guest solvent molecules on SCO phenomena has been observed in flexible coordination polymers, and this functionality has been incorporated in dynamic porous solids. SCO is a cooperative phenomenon, where a given metal ion can change its spin state, from HS to LS upon exposure to an external perturbation such as change in temperature, pressure, or light. Structural modifications and both intra-framework and host–guest hydrogen bonding interactions will greatly influence the SCO interconversion in such types of solids.

Kepert and co-workers have reported a series of porous coordination polymers by the reaction of Fe(II) salts with N-based ditopic ligands [166, 205, 206]. Overall, these coordination polymers present comparable 3-D structures resulting from the interpenetration of (4,4)-rhombic grids obtained through the connection of the Fe (II) ions with the ditopic ligands (Fig. 22a). To explain the change occurring in the SCO phenomena in dynamic structures, the coordination polymer $[Fe(bpbd)_2(NCS)_2]\cdot\{Acetone\}$ can be regarded as a reference. In this solid, grid interpenetration is realized at an angle of 90° and generates 1-D channels of dimensions 14.5 × 14.5 Å, which are run along the *c*-axis. This 3-D framework is further stabilized by strong hydrogen bonds involving the diol groups of the bpbd ligand and the sulphur-donor of thiocyanate groups complete the coordination sphere of each Fe(II) ions. Noteworthy is the fact that the acetone molecules filling the channels do not participate in any short hydrogen bonding with the ligands. Consequently, guest departure is completed at 102°C and structural analysis of the apohost reveals minimal changes in the framework atoms structuring the solvated and the desolvated forms (Fig. 22b). Thus, SCO behaviour is only slightly affected by loss of solvent: while the solvated form shows a relatively abrupt one-step full spin transition with $T_{1/2} = 162$ K upon cooling, a slightly shifted similar transition ($T_{1/2} = 156$ K) is observed in the evacuated solid. As expected, both forms show comparable structure contraction, ca. 4% of the unit cell, upon cooling, which is consistent with a full spin transition [205].

Completely different behaviours are observed in the coordination polymers constructed from azpy and bped ligands (Fig. 23), in which guest ethanol molecules

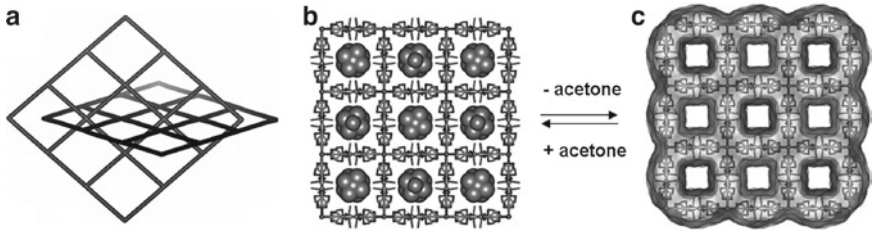

Fig. 22 (**a**) Topological representation of the orthogonal interpenetration of (4,4)-rhombic grids in the series of coordination polymers showing SCO properties. (**b** and **c**) Structure representations for $[Fe(bpbd)_2(NCS)_2]\cdot\{acetone\}$ and $[Fe(bpbd)_2(NCS)_2]$. Reproduced with permission of ref 205 [Neville SM, Moubaraki B, Murray KS, Kepert CJ "A Thermal Spin Transition in a Nanoporous Iron(II) Coordination Framework Material" (2007) Angew Chem Int Ed 46:2059]. Copyright Wiley-VCH Verlag GmbH & Co. KGaA

interact with the host framework through hydrogen bonds. The coordination polymer $[Fe_2(azpy)_4(NCS)_4]\cdot EtOH$ presents two kinds of 1-D channels with dimensions of 10.6 × 4.8 and 7.0 × 2.1 Å, respectively. These channels are filled with ethanol molecules, which interact through hydrogen bonds with the sulphur centres of the thiocyanate ligands bound to Fe(II) ions. As a consequence, guest loss upon heating leads to important structural changes in the apohost. The most significant change is an elongation and constriction of the 1-D channels to new dimensions of 11.7 × 2.0 Å. This structural modification induces enormous changes in the electronic behaviour of this compound. While the as-synthesized sample exhibits a broad half SCO transition at 150 K, the evacuated one shows a constant magnetic moment of 5.1 μB, lacking any SCO transition. Surprisingly, the original SCO properties are recovered after resorption of the guest solvent molecules, this phenomena being also observed with small alcohols such as methanol or propanol (Fig 23a) [166].

Grid interpenetration at an angle of 85.2° is observed in the coordination polymer $[Fe(bped)_2(NCS)_2]\cdot 3EtOH$, which incorporates channels of dimensions 8.4 × 4.7 Å separated by narrower polar windows of dimensions 6.4 × 6.3 Å. Channels and windows are filled with ethanol molecules that interact through hydrogen bonds with OH-groups of the bped ligands, which are also involved in intra-framework interactions through strong hydrogen bonds with the sulphur centres of thiocyanate ligands. The most important structural change upon guest removal is an increase in the interpenetration angle from 85.2° to 90°. Consequently, the accessible void volume changes from 31.0 to 34.9%, and is associated with a dilatation of the cavities and a contraction of the polar windows. Loss of guest molecules leads to new intra-framework interactions, which tend to stabilize the apohost. As in the previous case, these structural modifications are of paramount importance to the SCO interconversion. While the starting material shows a broad and uncompleted SCO interconversion at $T_{1/2} = 137$ K, the $T_{1/2}$ decreases to ca. 125 K in the aphohost with a transition over a wider temperature range (225–270 K) (Fig 23b). Additionally, the fraction of residual HS Fe(II) is as well higher: ca. 53% in the solvated material compared to 37% in the solvated solid [206].

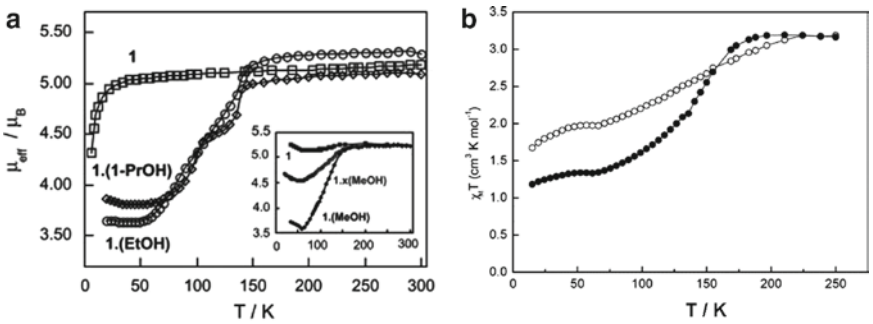

Fig. 23 (**a**) Temperature-dependent magnetic moment of $[Fe_2(azpy)_4(NCS)_4]\cdot x(guest)$, (**1·x**(guest) in the scheme). The inset shows the effect of partial and complete removal of Methanol from **1**·methanol. Reprinted from ref. 166 with permission from AAAS. (**b**) Plot of $\chi_M \cdot T$ versus temperature for $[Fe(bped)_2(NCS)_2]\cdot 3EtOH$ (•) and the corresponding apohost (○) Reprinted with permission from ref 206. Copyright 2008, American Chemical Society

Very recently, a molecule-based nanoporous coordination polymer showing tuneable SCO behaviour near room temperature has also been reported by Aromí, Gamez, and co-workers [207]. In this case, reaction of the $[Fe_2(dpya\text{-}triz)_2(CH_3CN)_2(H_2O)_2]^{4+}$ ditopic SBUs with Fe(II) affords a purple 1-D coordination polymer $\{[Fe_3(dpya\text{-}triz)_2(CH_3CH_2CN)_4(BF_4)_2](BF_4)_4{\cdot}4(CH_3CH_2CN)\}_n$ (dpya-triz = 2,4,6-tris-(di(pyridin-2-yl)amino)-1,3,5-triazine. Overall, packing of 1-D chains results in the formation of channel-like cavities with a cross section of ca. 6 × 4 Å, in which reside lattice solvent molecules and non-coordinated tetrafluoroborate anions. Interestingly, this coordination polymer shows a HS to LS SCO process at ca. 300 K involving 2/3 of the Fe(II) centres. Upon guest removal, a crystal-to-crystal transformation occurs with all the guest and coordinated propionitrile molecules being exchanged with water molecules. The solid turns to yellow and the SCO transition is lost. Interestingly, this phenomenon is fully reversible and both the starting structure and properties are recovered upon immersion in propionitrile or acetonitrile. With the latter solvent, the SCO transition is shifted to lower temperatures ($T_{1/2} = 275$ K).

Similar reversible properties have been found in another compound reported by Real, Bousseksou, and co-workers [208, 209]. $[Fe(pmd)(H_2O)\{Au(CN)_2\}_2]{\cdot}H_2O$ (pmd = pyrimidine) shows a triply interpenetrated structure and a sharp half SCO transition at 165 K with a hysteresis of approximately 8 K. The dehydration process induces large changes in the crystal structure with the pyrimidine ligands, previously bound only through one nitrogen atom, now bridging two Fe(II) ions. This results in the linkage of the three independent interpenetrated frameworks into a unique 3-D network. This conversion results in the suppression of the SCO behaviour, which can be recovered on rehydration. Interestingly, the isostructural $[Fe(pmd)(H_2O)\{Ag(CN)_2\}_2]{\cdot}H_2O$ shows a similar reversible behaviour, but with a shift of the SCO transition to lower temperatures for the dehydrated phase.

5.3 Gas-Induced Magnetic Properties Modulation

Although the number of examples of solvent-induced magnetic properties or spin-state modulation is increasing, cases of coordination polymers in which magnetic properties are modulated upon gas adsorption are rare. While several organometallic compounds containing CO_2 are known [210, 211], the first example of magnetic framework trapping CO_2 during its synthesis was reported by Cornia and co-workers in 1999 [83]. Nevertheless, magnetic properties of the activated framework and eventual reversible trapping were not reported.

The ultramicroporous 3-D MOF $[Cu(F\text{-}pymo)_2(H_2O)_{1.25}]_n$ (F-pymo = 5-fluoropyrimidin-2-olate) reported by Navarro, Parra, Sironi, and co-workers [212] displays a zeolitic gismondine-like topology with helical channels of ca. 2.9 Å diameter. These channels result from the interconnection of two different cyclic motifs, namely metallacalix[8]arenes and metallacalix[4]arenes exhibiting either 1,3-alternate or a pinched cone conformation (Fig. 24a). These are filled with water

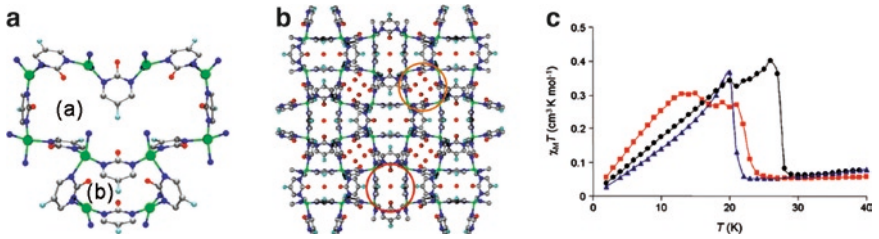

Fig. 24 Structure and magnetic properties for $[Cu(F\text{-}pymo)_2(H_2O)_{1.25}]_n$ (**a**) Metallacalix[8]arenes (**a**) and metallacalix[4]arenes (**b**) cyclic motifs. (**b**) Gismondine-like framework (guest water molecules are represented as red spheres). (**c**) $\chi_M \cdot T$ versus temperature for as-synthesized (*blue*), activated (*red*) and CO_2-loaded (*black*) materials. Reprinted with permission from ref 212. Copyright 2008, American Chemical Society

molecules, which are associated with the framework through strong hydrogen bonds (Fig. 24b). The framework remains crystalline up to 513 K after guest water removal and has a relatively small volume (ca. 13%) available for guest inclusion. At 77 K, the activated solid behaves as a molecular sieve, selectively adsorbing H_2 over N_2, possibly due to size exclusion. The case of CO_2 is even more interesting since these larger molecules are readily incorporated at temperatures as high as 433 K through a transient phase and channels expansion.

Interestingly, the authors have investigated the influence of guest molecules on the magnetic properties in this material (Fig. 24c). The as-synthesized solid shows antiferromagnetic interactions and a weak ferromagnetic ordering below $T_N = 24$ K, which arises from a spin-canting phenomenon related to the non-centrosymetric nature of the framework. While the magnetic ordering temperature is only slightly decreased in the activated material ($T_N = 22$ K), loading with CO_2 has a profound effect on the magnetic properties, since the ordering temperature is increased to 29 K. To explain this result, the authors presume that the structural perturbation exerted by the CO_2 guests may lead to a less distorted environment for the Cu(II) ions with a concomitant increase in overlap between the ligand orbitals and the metal ion magnetic orbitals, thus permitting more efficient magnetic exchange within the framework.

6 Conclusions and Perspectives

As highlighted in the previous sections, many magnetic and porous molecule-based materials with well-defined geometries have been prepared using metal ions and closed-shell and open-shell polytopic organic ligands. Due to the wide availability of organic ligands that can be combined with metal ions, a huge variety of structures is available, the properties of which can be studied for different applications similar to those developed with non-magnetic MOFs in area of catalysis [24–26], gas storage [27–35], and others [36–39]. Nevertheless, new fields of application can be envisioned by exploring the anchoring of these materials onto solid surfaces, or their processability for applications in nanotechnology and in biomedicine.

6.1 Porous and Magnetic Coordination Polymers on Surfaces

In the previous sections, we have reported examples of magnetic and porous coordination polymers. Nevertheless, it is of the utmost importance to harness the properties of such materials in solid-state applications or devices. Therefore, much effort must be devoted to the development of new methods for preparing thin films containing these multifunctional coordination polymers with the aim of directing and controlling the growth of MOFs on surfaces, and to integrate them as novel functional units for bottom-up nanotechnology [213]. The robustness of some porous coordination polymers can be exploited for loading with organometallic precursors of solids that can be subsequently converted into nanosized metal clusters or wires inside the pores [214].

Surface anchoring is a key step, crucial for applications such as the manufacturing of sensor devices. It has been recently shown that the sequential addition of molecular-sized layers to form complex structures is a way of building coordination polymers as well as other heterogeneous nanostructures on surfaces [215, 216]. This approach, named layer-by-layer, allows the building of supramolecular structures from surfaces through the self-assembly of successive monolayers of organic molecules and metal ions interacting via coordination bonds [217]. Therefore, the well-known coordination chemistry of a metal ion in solution might be used to form and control thin film structure and properties at the molecular level.

An example of this approach is represented by the growth of 3-D coordination polymers with SCO properties via stepwise adsorption reactions for multilayer films based entirely on intra- and interlayer coordination bonds Fe(pyrazine)$[Pt(CN)_4]$ [218, 219]. Indeed, after functionalization of the surface with the appropriate anchoring layer the coordination polymer is built in a stepwise fashion, alternating the metal ion (Fe^{2+}), the platinum salt ($[Pt(CN)_4]^{2-}$), and pyrazine. The polymer shows many interesting properties, with the SCO transition accompanied by a variation in the dielectric constant of the material accompanied by a room temperature hysteresis of the dielectric constants. This dielectric hysteretic property may be useful in building molecular memory devices that can store information by high- and low-capacitance states. What must be remarked here is that these appealing properties cannot be exploited in bulk materials, but only in thin films.

The approach of anchoring metal-PTM based frameworks onto solid surfaces has also been undertaken in order to graft porous and magnetic frameworks onto solid supports. So far, the feasibility of the layer-by-layer methodology has been exemplified by the monocarboxylic PTM derivative (PTMMC), the Cu(II) complex of which was successfully grafted onto a carboxylate-functionalized gold surface with its magnetic character remaining intact. Further studies on di- and tri-carboxy substituted PTM radicals coordinated to metal ions are in progress, towards the grafting of a porous multidimensional magnetic structure onto a metal surface [220].

6.2 Porous and Magnetic Coordination Cages

Use of metal-directed self-assembly has afforded many different 0-D discrete structures with internal void space, with the geometry of the organic linker dictating the observed geometry of the material [221, 222]. A variety of structures that include molecular nanosized squares and rectangles [221–223], trigonal [224, 225] and square prismatic capsules [226], as well as tetrahedral [227], octahedral, and higher order suprastructures [228, 229] have been reported. These supramolecular organizations have potential applications as chemical sensors and reaction nanovessels [223, 230–233]. It is only very recently that the first two examples dealing with the preparation of magnetic and porous cages based on open-shell radical ligands and metal subunits have been reported [234, 235]. These studies demonstrated the possibility of incorporating multidimensional metal-organic cages bearing specific functionality with predesigned physico-chemical properties. They also opened the way towards exciting potential applications; since these spin cages are soluble in water their use as new spin probes and as magnetic resonance imaging (MRI) contrast agents could be envisioned.

6.3 Porous and Magnetic Coordination Polymers as Sensors

One of the aims of recent research on coordination polymers is the design of materials combining a set of properties for specific applications. As an example, Corma, Rocha, and co-workers recently reported the rational design and preparation of lanthanide-based porous MOFs showing sensing properties [236]. Their aim was the preparation of rare-earth based MOFs showing hydrophobicity, high adsorption capacity, high thermal resistance, anisotropic photoluminescence, and magnetic properties. The authors succeeded in the preparation of such a MOF by combining an organic aromatic and hydrophobic spacer with lanthanide ions. The change in the fluorescence signal intensity is the result of the interaction of the host with ethanol in the presence of water under ambient conditions. Hence, this lanthanide-based MOF is an example of a rationally-designed sensor based on coordination chemistry.

6.4 Processability of Magnetic Coordination Polymers

Hybrid materials based on gadolinium ions have been investigated as MRI contrasting agents. However, many of these agents show toxicity that prevents their use. One of the approaches to reduce the toxicity of contrast agent is based upon the use of viral capsides as nanocontainers for gadolinium ions bound to the interior of the capside via coordination bonds; i.e., in the form of MOFs [237]. A second approach consists of the reduction of the dose of the drug given to the patient by increasing

the availability of the administrated contrasting agent. So far, good results have been reported by processing MOF-contrasting agent as soluble nanoparticles [238]. Nanoparticles might not only be of use in biomedicine, but also in nanotechnology. Their applications may range among data storage, catalysis, photonics, electronics, microlenses, and biosensors. The principal challenge is in the preparation of nanoparticles showing specific properties, i.e., nanoscale metal-organic particles. Recently, the successful preparation of nanoparticles of Prussian Blue analogues [239], or systems showing magnetic behaviours such as superparamagnetism [240], valence tautomerism [241], SMM behaviour [242] or SCO phenomena [243, 244] has been reported. It is reasonable to think that examples of porous and functional nanoparticles will follow soon [245].

Aknowledgements Authors want to thank the financial support given by the "Plan Nacional de Investigación Científica y Desarrollo e Innovación Tecnológica," Iniciativa Ingenio 2010, Programa Consolider, under Project EMOCIONA (CTQ 2006-06333/BQU), the "Instituto de Salud Carlos III" through "Acciones CIBER," the Generalitat de Catalunya (Project 2009 SGR 516), and the European Commission under the Network of Excellence "MAGMANet" (contract NMP3-CT-2005-515767-2) and the Collaborative Project "SURMOF" (contract STRP032109). V.M. thanks the Spanish Research Council (CSIC) for funding and the Spanish MICINN for a Juan de la Cierva contract.

References

1. Wilson ST, Lok BM, Messina CA, Cannan TR, Flanigen EM (1982) J Am Chem Soc 104:1146
2. Cheetham A, Férey G, Loiseau T (1999) Angew Chem Int Ed 38:3268
3. Natarajan S, Mandal S (2008) Angew Chem Int Ed 47:2
4. Férey G (2008) Chem Soc Rev 37:191
5. Janiak C (2003) Dalton Trans 2781
6. Férey G (2001) Chem Mater 13:3084
7. Cheetham A, Rao CNR, Feller RK (2006) Chem Commun 4780
8. Yaghi OM, O'Keefe M, Ocwig NW, Chae HK, Eddaoudi M, Kim J (2003) Nature 423:705
9. Moulton B, Zaworotko MJ (2001) Chem Rev 101:1629
10. Eddaoudi M, Moler DB, Li HL, Chen BL, Reineke TM, O'Keeffe M, Yaghi OM (2001) Acc Chem Res 34:319
11. Robson R (2000) J Chem Soc, Dalton Trans 37:3537
12. Zaworotko M (2000) Angew Chem Int Ed 39:3052
13. Yaghi OM, Li HL, Davis C, Richardson D, Groy TL (1998) Acc Chem Res 31:474
14. Blake AJ, Champness NR, Hubberstey P, Li WS, Withersby MA, Schröder M (1999) Coord Chem Rev 183:117
15. Rao NR, Natarajan S, Vaighyanathan R (2004) Angew Chem Int Ed 43:1466
16. Park YK, Choi SB, Kim H, Kim K, Won B-H, Choi K, Choi J-S, Ahn W-S, Won N, Kim S, Jung DH, Choi S-H, Kim G-H, Cha S-S, Jhon YH, Yang JK, Kim J (2007) Angew Chem Int Ed 46:8230
17. Park K-M, Iwamoto T (1992) J Chem Soc, Chem Commun 72
18. Kim J, Whang D, Lee JI, Kim K (1993) J Chem Soc, Chem Commun 1400
19. Yaghi OM, Li H (1995) J Am Chem Soc 117:10401
20. Yaghi OM, Li H (1996) J Am Chem Soc 118:295
21. Min KS, Suh MP (2000) J Am Chem Soc 122:6834
22. Kamiyama A, Noguchi T, Kajiwara T, Ito T (2000) Angew Chem Int Ed 39:3130

23. Uemura K, Kitagawa S, Kondo M, Fukui K, Kitaura R, Chang H-C, Mizutani T (2002) Chem Eur J 8:3586
24. Corma A (1995) Chem Rev 95:559
25. Fujita M, Kwon YJ, Washizu S, Ogura K (1994) J Am Chem Soc 116:1151
26. Sawaki T, Aoyama Y (1999) J Am Chem Soc 121:4793
27. Rosi NL, Eckert J, Eddaoudi M, Vodak DT, Kim J, O'Keefe M, Yaghi OM (2003) Science 300:1127
28. Van Den Berg AWC, Otero Areá C (2008) Chem Commun 668
29. Morris RE, Wheatley PS (2008) Angew Chem Int Ed. 47:4966
30. Férey G, Mellot-Draznieks C, Serre C, Millange F, Dutour J, Surblé S, Margiolaki I (2005) Science 309:2040
31. Eddaoudi M, Kim J, Rosi N, Vodak D, Wachter J, O'Keeffe M, Yaghi OM (2002) Science 295:469
32. Li H, Eddaoudi M, O'Keeffe M, Yaghi OM (1999) Nature 402:276
33. Kondo M, Yoshitomi T, Seki K, Matsuzaka H, Kitagawa S (1997) Angew Chem Int Ed 36:1725
34. Kondo M, Okubo T, Asami A, Noro S-I, Yoshitomi T, Kitagawa S, Ishii T, Matsuzaka H, Seki K (1999) Angew Chem Int Ed 38:140
35. Noro S-I, Kitagawa S, Kondo M, Seki K (2000) Angew Chem Int Ed 39:2081
36. Kuznicki SM, Bell BA, Nair S, Hillhouse HW, Jacubinas RM, Braunbarth CM, Toby BH, Tsapatsis M (2001) Nature 412:720
37. Pan L, Adams KM, Hernandez HE, Wang X, Zheng C, Hattori Y, Kaneko K (2003) J Am Chem Soc 125:3062
38. Dybtsev CN, Chun H, Yoon SH, Kim D, Kim K (2004) J Am Chem Soc 126:32
39. Mueller U, Schubert M, Teich F, Puetter H, Schierle-Arndt PK (2006) J Mater Chem 16:626
40. Kitagawa S, Kitaura R, Noro S-J (2004) Angew Chem Int Ed 43:2334
41. Champness NR (2006) Dalton Trans 877
42. Kepert C (2006) Chem Commun 695
43. Maspoch D, Ruiz-Molina D, Veciana J (2007) Chem Soc Rev 36:770
44. Miller JS (2000) Inorg Chem 39:4392
45. Kahn O (2000) Acc Chem Res 33(10):647
46. Buschow KHJ, De Boer R (2003) Physics of Magnetism and Magnetic Materials. Kluwer/Plenum, New York
47. Miller JS, Epstein AJ (2000) MRS Bull 21
48. Maspoch D, Domingo N, Roques N, Wurst K, Tejada J, Rovira C, Ruiz-Molina D, Veciana J (2007) Chem Eur J 13:8153
49. Roques N, Maspoch D, Datcu A, Wurst K, Ruiz-Molina D, Rovira C, Veciana J (2007) Polyhedron 26:1934
50. Caneschi A, Gatteschi D, Sessoli R, Rey P (1989) Acc Chem Res 22:392
51. Lacroix PG (2001) Chem Mat 13:3495
52. Blundell SJ, Pratt FL (2004) J Phys Condens Matter 16:R771
53. Amabilino DB, Veciana J (2001) In: Miller JS, Drillon M (eds) Magnetism: molecules to materials II. Wiley, Weinheim
54. Kahn O (ed) (1996) Magnetism: a supramolecular function. Kluwer, Dordrect
55. Amabilino DB, Cirujeda J, Veciana J (1999) Phil Trans R Soc Lond A 357:2873
56. Cirujeda J, Hernàndez-Gasió E, Rovira C, Stanger J-L, Turek P, Veciana J (1995) J Mater Chem 5(2):243
57. Deumal M, Cirujeda J, Veciana J, Novoa JJ (1998) Adv Mater 10(17):1461
58. Kinoshita M, Turek P, Tamura M, Nozawa K, Shiomi D, Nakazawa Y, Ishikawa M, Takahashi M, Awaga K, Inabe T, Maruyama Y (1991) Chem Lett 1225
59. Takahashi M, Turek P, Nakazawa Y, Tamura M, Nozawa K, Shiomi D, Ishikawa M, Kinoshita M (1991) Phys Rev Lett 67:746
60. Tamura M, Nakazawa Y, Shiomi D, Nozawa K, Hosokoshi Y, Ishikawa M, Kinoshita M (1991) Chem Phys Lett 186:401

61. Hicks RG (2004) Can J Chem 82:1119
62. Hicks RG, Lemaire MT, Öhrström L, Richardson JF, Thompson LK, Xu Z (2001) J Am Chem Soc 123:7154
63. Maspoch D, Ruiz-Molina D, Wurst K, Domingo N, Cavallini M, Biscarini F, Tejada J, Rovira C, Veciana J (2003) Nat Mater 2:190
64. Cao R, Sun D, Liang Y, Hong M, Tatsumi K, Shi Q (2002) Inorg Chem 41:2087
65. Gilroy JB, Koivisto BD, McDonald R, Ferguson MJ, Hicks RG (2006) J Mater Chem 16:2618
66. Kahn O (1993) Molecular magnetism. VCH, New York
67. Fegy K, Luneau D, Ohm T, Paulsen C, Rey P (1998) Angew Chem Int Ed 37(9):1270
68. Miller JS, Zhang JH, Reiff WM, Preston LD, Reis AH Jr, Gerbert E, Extine M, Troup J, Ward MD (1987) J Phys Chem 91:4344
69. Manriquez JM, Yee GT, McLean RS, Epstein AJ, Miller JS (1991) Science 252:1415
70. Miller JS, Calabrese JC, Epstein AJ, Bigelow RW, Zhang JH, Reiff WM (1986) J Chem Soc, Chem Commun 1026
71. Sato O, Cui A, Matsuda R, Tao J, Hayami S (2007) Acc Chem Res 40:361
72. Maspoch D, Ruiz-Molina D, Wurst K, Rovira C, Veciana J (2002) Chem Commun 2958
73. Maspoch D, Ruiz-Molina D, Wurst K, Vidal-Gancedo J, Rovira C, Veciana J (2004) Dalton Trans 1073
74. Maspoch D, Domingo N, Ruiz-Molina D, Wurst K, Hernández JM, Lloret F, Tejada J, Rovira C, Veciana J (2007) Inorg Chem 46:5
75. Maspoch D, Domingo N, Ruiz-Molina D, Wurst K, Tejada J, Rovira C, Veciana J (2004) J Am Chem Soc 126:730
76. Roques N, Maspoch D, Wurst K, Ruiz-Molina D, Rovira C, Veciana J (2006) Chem Eur J 12:9238
77. Wang Z, Zhang T, Otsuka T, Inoue K, Kobayashi H, Kurmoo M (2004) Dalton Trans 2209
78. Wang X-Y, Gan L, Zhang S-W, Gao S (2004) Inorg Chem 43:4615
79. Viertelhaus M, Adler P, Clérac R, Anson CE, Powell AK (2005) Eur J Inorg Chem 692
80. Rettig SJ, Thompson RC, Trotter J, Xia S (1999) Inorg Chem 44:572
81. Wang X-Y, Wei H-Y, Wang Z-M, Chen Z-D, Gao S (2005) Inorg Chem 44:572
82. Wang Z, Zhang B, Fujiwara H, Kobayashi H, Kurmoo M (2004) Chem Commun 416
83. Cornia A, Caneschi A, Dapporto P, Fabretti AC, Gatteschi D, Malavasi W, Sangregorio C, Sessoli R (1999) Angew Chem Int Ed 38:1780
84. Decurtins S, Pellaux R, Antonerra G, Palacio F (1999) Coord Chem Rev 192:841
85. Nikolaï SI, Makhaev VD, Aldoshin SM, Gredin P, Boubekeur K, Train C, Gruselle M (2005) Dalton Trans 3101
86. Gruselle M, Thouvenot R, Malézieux B, Train C, Gredin P, Demeschik TV, Troitskaya LL, Sokolov VI (2004) Chem Eur J 10:4763
87. Coronado E, Galán-Mascaros JR, Gómez-Garcia CJ, Ensling J, Gütlich P (2000) Chem Eur J 6:552
88. Coronado E, Galán-Mascaros JR, Gómez-Garcia CJ, Martínez-Agudo JM (1999) Adv Mater 11:558
89. Larionova J, Mombelli B, Sanchiz J, Kahn O (1998) Inorg Chem 37:679
90. Clemente-León M, Coronado E, Galán-Mascaros JR, Gómez-Garcia CJ (1997) Chem Commun 1727
91. Mathonière C, Carling SG, Yusheng D, Day P (1994) J Chem Soc, Chem Commun 1551
92. Tamaki H, Zhong ZJ, Matsumoto N, Kida S, Koikawa M, Achiwa N, Hashimoto Y, Okawa H (1992) J Am Chem Soc 114:6974
93. Andrés R, Brissard M, Gruselle M, Train C, Vaisserman J, Malézieux B, Jamet J-P, Verdaguer M (2001) Inorg Chem 40:4633
94. Coronado E, Galán-Mascaros JR, Gómez-Garcia CJ, Martínez-Agudo JM (2001) Inorg Chem 40:113
95. Sieber R, Descurtins S, Stoeckli-Evans H, Wilson C, Yufit D, Howard JAK, Capelli SC, Hauser A (2000) Chem Eur J 6:361

96. Lancaster T, Blundell SJ, Pratt FL, Coronado E, Galán-Mascaros JR (2004) J Mater Chem 14:1518
97. Nuttall CJ, Day P (1998) Chem Mater 10:3050
98. Pellaux R, Schmalle HW, Huber R, Fischer P, Hauss T, Ouladdiaf B, Descurtins S (1997) Inorg Chem 36:2301
99. Descurtins S, Schmalle HW, Pellaux R, Huber R, Fischer P, Ouladdiaf B (1996) Adv Mater 8:647
100. Farrel RP, Hambley TW, Lay PA (2004) Inorg Chem 126:32
101. Gruselle M, Train C, Boubekeur K, Gredin P, Ovanesyan N (2006) Coord Chem Rev 250:2491
102. Pointillart T, Gruselle M, Andre G, Train C (2008) J Phys Cond Matter 20:135214
103. Coronado E, Galán-Mascaros JR (2005) J Mater Chem 15:66
104. Coronado E, Day P (2004) Chem Rev 104:5419
105. Coronado E, Galán-Mascaros JR, Gómez-Garcia CJ, Laukhin V (2000) Nature 408:447
106. Lu JY, Lawandy MA, Li J, Yuen T, Lin CL (1999) Inorg Chem 38:2695
107. Yuen T, Lin CL, Mihalisin TW, Lawandy MA, Li J (2000) J Appl Phys 87:6001
108. Armentano D, De Munno G, Lloret F, Palii AV, Julve M (2002) Inorg Chem 41:2007
109. Armentano D, De Munno G, Mastropietro TF, Julve M, Lloret F (2005) J Am Chem Soc 127:10778
110. Pei Y, Journaux Y, Kahn O, Dei A, Gatteschi D (1986) J Chem Soc, Chem Commun 1300
111. Ribas J, Díaz C, Costa R, Journaux Y, Mathonière C, Kahn O, Gleizes A (1990) Inorg Chem 29:2042
112. Vicente R, Escuer A, Ribas J (1992) Polyhedron 11:857
113. Ribas J, Diaz C, Solans X, Font-Badia M (1997) J Chem Soc, Dalton Trans 35
114. Fettouhi M, Ouahab L, Boukhari A, Cador O, Mathonière C, Kahn O (1996) Inorg Chem 35:4932
115. Pereira CLM, Pedroso EF, Novak MA, Brandl AL, Knobel M, Stumpf HO (2003) Polyhedron 22:2387
116. Stumpf HO, Pei Y, Kahn O, Sletten J, Renard J-P (1993) J Am Chem Soc 115:6738
117. Kadam RM, Bhide MK, Sastry MD, Yakhmi JV, Kahn O (2002) Chem Phys Lett 357:457
118. Vaz MGF, Ardisson JD, Speziali NL, Souza GP, Stumpf HO, Knobel M, Macedo WAA (2001) Polyhedron 20:1431
119. Stumpf HO, Ouahab L, Pei Y, Grandjean D, Kahn O (1993) Science 261:447
120. Stumpf HO, Ouahab L, Pei Y, Bergerat P, Kahn O (1994) J Am Chem Soc 116:3866
121. Stumpf HO, Pei Y, Michaut O, Kahn O, Renard JP, Ouahab L (1994) Chem Mater 6:257
122. Cador O, Price D, Larionova J, Mathonière C, Kahn O, Yakhmi J V (1997) Inorg Chem 7:1263
123. Pardo E, Ruiz-Garcia R, Cano J, Ottenwaelder X, Lescouëzec R, Journaux Y, Lloret F, Julve M (2008) DaltonTrans 2780
124. Pereira CLM, Pedroso E, Stumpf HO, Novak MA, Ricard L, Ruiz-García R, Rivière E, Journaux Y (2004) Angew Chem Int Ed 43:955
125. Pardo E, Cangussu D, Dul M-C, Lescouëzec R, Herson P, Journaux Y, Pedroso EF, Pereira CLM, Muñoz M-C, Ruiz-García R, Cano J, Amorós P, Julve M, Lloret F (2008) Angew Chem Int Ed 47:4211
126. Maji TK, Sain S, Mostafa G, Lu T-H, Ribas J, Montfort M, Chaudhuri NR (2003) Inorg Chem 42:709
127. Sain S, Maji TK, Mostafa G, Lu T-H, Chaudhuri NR (2003) New J Chem 27:185
128. Delgado FS, Sanchiz J, Ruiz-Pérez C, Lloret C, Julve M (2003) Inorg Chem 42:5938
129. Konar S, Mukherjee PS, Drew MGB, Ribas J, Chaudhuri NR (2003) Inorg Chem 42:2545
130. Long LS, Chen X-M, Tong M-L, Sun Z-G, Ren Y-P, Huang R-B, Zheng L-S (2001) J Chem Soc, Dalton Trans 1888
131. Zheng Y-Q, Lin J-L, Kong Z-P (2004) Inorg Chem 43:2590
132. Lee E, Kim Y, Jung D-Y (2002) Inorg Chem 41:501
133. Liu T-F, Sun H-L, Gao S, Zhang SW, Lau T-C (2003) Inorg Chem 42:4792
134. Forster PM, Cheetham AK (2003) Angew Chem Int Ed 41:457

135. Guillou N, Livage C, Drillon M, Férey G (2003) Angew Chem Int Ed 42:5314
136. Guillou N, Livage C, van Beek W, Nogués M, Férey G (2003) Angew Chem Int Ed 42:644
137. Miyasaka H, Nakata K, Lecren L, Coulon C, Nakasawa Y, Fujisaki T, Sugiura K, Yamashita M, Clérac R (2006) J Am Chem Soc 128:3770
138. Murugesu M, Wernsdorfer W, Abboud KA, Brechin EK, Christou G (2006) Dalton Trans 2285
139. Wittick LM, Murray KS, Moubaraki B, Batten SR, Spiccia L, Berry KJ (2004) Dalton Trans 1003
140. Moushi EE, Stamatatos TC, Wernsdorfer W, Nastopoulos V, Christou G, Tasiopoulos AJ (2006) Angew Chem Int Ed 45:7722
141. Zheng X-J, Jin K-P, Gao S (2004) Inorg Chem 43:1600
142. Lin WB, Evans OR, Yee GT (2000) J Solid State Chem 152:152
143. Ovcharenko V, Fursova E, Romanenko G, Ivorskii V (2004) Inorg Chem 43:3332
144. Chiang R-K, Chuang N-T, Wur C-S, Chong M-F, Lin C-R (2002) J Solid State Chem 166:158
145. Ma B-Q, Zhang D-S, Gao S, Jin T-Z, Yan C-H, Xu G-X (2000) Angew Chem Int Ed 39:3644
146. Cheng J-W, Zheng S-T, Liu W, Yang G-Y (2008) CrystEngComm 10:1047
147. Xiang S, Wu X, Zhang J, Fu R, Hu S, Zhang X (2005) J Am Chem Soc 127:16352
148. Barthelet K, Riou D, Férey G (2002) Chem Commun 1492
149. Chui SS-Y, Lo SM-F, Charmant JPH, Orpen AG, Williams ID (1999) Science 283:1148
150. Zhang XX, Chui SS-Y, Williams ID (2000) J Appl Phys 87:6007
151. Moulton B, Lu J, Hajndl R, Hariharan S, Zaworotko MJ (2002) Angew Chem Int Ed 41:2821
152. Atwood JL (2002) Nat Mater 1:91
153. Bourne SA, Lu J, Mondal A, Moulton B, Zaworotko MJ (2001) Angew Chem Int Ed 40:11
154. Srikanth H, Hajndl R, Moulton B, Zaworotko M (2003) J Appl Phys 93:7089
155. Chen B, Eddaoudi M, Reineke TM, Kampf W, O'Keefe M, Yaghi OM (2000) J Am Chem Soc 122:11559
156. Cao R, Shi Q, Sun D, Hong M, Bi W, Zhao Y (2002) Inorg Chem 41:6161
157. Garcia-Terán J-P, Castillo O, Luque A, García-Couceiro U, Román P, Lezama L (2004) Inorg Chem 43:4549
158. Li Y, Hao N, Lu Y, Wang E, Kang Z, Hu C (2003) Inorg Chem 42:3119
159. Zheng Y-Q, Lin J-L, Kong Z-P (2004) Inorg Chem 43:2590
160. Liu Y-H, Tsai H-L, Lu Y-L, Wen Y-S, Wang J-C, Lu K-L (2001) Inorg Chem 40:6426
161. Choi HJ, Suh MP (1998) J Am Chem Soc 120:10622
162. Wang X-Y, Sevov SC (2008) Inorg Chem 47:1037 and references cited therein
163. Livage C, Guillou N, Marrot J, Férey G (2001) Chem Mater 13:4387
164. Zhang L-J, Xu J-Q, Shi Z, Zhao X-L, Wang T-G (2003) J Solid State Chem 32:32
165. Choi HJ, Dinca M, Long JR (2008) J Am Chem Soc 130:7848
166. Halder GJ, Kepert CJ, Moubaraki B, Murray KS, Cashion JD (2002) Science 298:1762
167. Real JA, Andres E, Muñoz MC, Julve M, Granier T, Bousseksou A, Varret F (1995) Science 268:265
168. Tian YQ, Cai C-X, Ren X-M, Duan C-Y, Xu Y, Gao S, You X-Z (2003) Chem Eur J 9:5673
169. Masciocchi N, Galli S, Sironi A, Barea E, Navarro JAR, Salas JM, Tabares LC (2003) Chem Mater 15:2153
170. Barea E, Navarro JAR, Salas JM, Masciocchi N, Galli S, Sironi A (2004) Inorg Chem 43:473
171. Masciocchi N, Galli S, Sironi A, Cariati E, Galindi MA, Barea E, Romero MA, Salas JM, Navarro JAR, Santoyo-González F (2006) Inorg Chem 45:7612
172. Pedireddi VR, Varughese S (2004) Inorg Chem 43:450
173. Wang X-Y, Wang Z-M, Gao S (2007) Chem Commun 1127

174. Habib HA, Sanchiz J, Janiak C (2008) Dalton Trans 1734
175. Wang YL, Yuan D-Q, Bi W-H, Li X, Li X-J, Li F, Cao R (2005) Cryst Growth Des 5:1849
176. Zheng Y-Q, Kong Z-P (2003) Anorg Allg Chem 629:1469
177. Konar S, Corbella M, Zangrado E, Ribas J, Chaudhuri NR (2003) Chem Commun 1424
178. Greve J, Jeß I, Näther C (2003) J Solid State Chem 175:328
179. Caneschi A, Gatteschi D, Laugier J, Rey P (1987) J Am Chem Soc 109:2191
180. Roques N, Maspoch D, Luis F, Camón A, Wurst K, Datcu A, Rovira C, Ruiz-Molina D, Veciana J (2008) J Mater Chem 18:98
181. Ballester M (1985) Acc Chem Res 12:1380
182. Maspoch D, Ruiz-Molina D, Wurst K, Rovira C, Veciana J (2004) Dalton Trans 1073
183. Maspoch D, Domingo N, Ruiz-Molina D, Hernández JM, Lloret F, Tejada J, Rovira C, Veciana J (2007) Inorg Chem 46:1627
184. Maspoch D, Ruiz-Molina D, Wurst K, Rovira C, Veciana J (2004) Chem Commun 1164
185. Maspoch D, Domingo N, Ruiz-Molina D, Wurst K, Tejada J, Rovira C, Veciana J (2005) Chem Commun 5035
186. Roques N, Maspoch D, Imaz I, Datcu A, Sutter J-P, Rovira C, Veciana J (2008) Chem Commun 3160
187. Kitagawa S, Kondo M (1997) Angew Chem Int Ed Engl 36:1725
188. Kitagawa S, Uemura K (2005) Chem Soc Rev 34:109
189. Nakatani K, Carriat JY, Journaux Y, Kahn O, Loret F, Renard JP, Pei Y, Sletten J, Verdaguer M (1989) J Am Chem Soc 111:5739
190. Turner S, Kahn O, Rabardel L (1996) J Am Chem Soc 118:6428
191. Kahn O, Larionova J, Yakhmi JV (1999) Chem Eur J 5:3343
192. Larionova J, Chavan SA, Yakhmi JV, Frøystein AG, Sletten J, Sourisseau C, Kahn O (1997) Inorg Chem 36:6374
193. Férey G (2003) Nature Mater 2:136
194. Kurmoo M, Kumagai H, Chapman KW, Kepert CJ (2005) Chem Commun 3012
195. Kurmoo M, Kumagai H, Akita-Tanaka M, Inoue K, Takagi S (2006) Inorg Chem 45:1627
196. Wang Z, Zhang Y, Liu T, Kurmoo M, Gao S (2007) Adv Funct Mater 17:1523
197. Zhang B, Wang Z, Kurmoo M, Gao S, Inoue K, Kobayashi H (2007) Adv Funct Mater 17:577
198. Dunbar K, Heintz RA (1997) Prog Inor Chem 45:283
199. Verdaguer M, Bleuzen A, Marvaud V, Vaisserman J, Seuleima M, Desplanches C, Scuiller A, Train C, Garde R, Gelly G, Lomenech C, Rosenman I, Veillet P, Cartier C, Villain F (1999) Coord Chem Rev 190–192:1023
200. Larionova J, Kahn O, Golhen S, Ouahab L, Clérac R (1999) J Am Chem Soc 121:3349
201. Larionova J, Clérac R, Sanchiz J, Kahn O, Golhen S, Ouahab L (1998) J Am Chem Soc 120:13088
202. Yanai N, Kaneko W, Yoneda K, Ohba M, Kitagawa S (2007) J Am Chem Soc 129:3496
203. Ohkoshi SI, Arai KI, Sato Y, Hashimoto K (2004) Nat Mater 3:857
204. Milon J, Daniel M-C, Kaiba A, Guionneau P, Brandès S, Sutter J-P (2007) J Am Chem Soc 129:13872
205. Neville SM, Moubaraki B, Murray KS, Kepert CJ (2007) Angew Chem Int Ed 46:2059
206. Neville SM, Halder GJ, Chapman KW, Duriska MB, Southon PD, Cashion JD, Létard J-F, Moubaraki B, Murray KS, Kepert CJ (2008) J Am Chem Soc 130:2869
207. Quesada M, De La Peña-O'Shea VA, Aromí G, Geremia S, Massera C, Roubeau O, Gamez P, Reedijk J (2007) Adv Mater 19:1397
208. Bonhommeau S, Molnár G, Galet A, Zwick A, Real JA, Mc Garvey JJ, Bousseksou A (2005) Angew Chem Int Ed 44:4609
209. Niel V, Thompson AL, Muñoz MC, Galet A, Goeta AE, Real JA (2003) Angew Chem Int Ed 42:3760
210. Fu PF, Khan MA, Nicholas KM (1996) J Organomet Chem 506:49
211. Gibson DH, Ye M, Sleadd BA, Mehta JM, Mbadike OP, Richardson JF, Mashuta MS (1995) Organometallics 14:1242

212. Navarro JAR, Barea E, Rodríguez-Diéguez A, Sala JM, Ania CO, Parra JB, Masciocchi N, Galli S, Sironi A (2008) J Am Chem Soc 130:3978
213. Lin C, Kagan CR (2003) J Am Chem Soc 125:336
214. Hermes S, Zacher D, Baunemann A, Wöll C, Fischer RA (2007) Chem Mater 19:2168
215. Shekhah O, Wang H, Strunskus T, Cyganik P, Zacher D, Fischer R, Wöll C (2007) Langmuir 23:7440
216. Shekhah O, Wang H, Kowarik S, Schreiber F, Paulus M, Tolan M, Sternemann C, Evers F, Zacher D, Fischer RA, Wöll C (2007) J Am Chem Soc 129:15118
217. Kosbar L, Srinivasan C, Afzali A, Graham T, Copel M, Krusin-Elbaum L (2006) Langmuir 22:7631
218. Cobo S, Molnár G, Real JA, Bousseksou A (2006) Angew Chem Int Ed 45:5786
219. Molnár G, Cobo S, Real JA, Carcenac F, Daran E, Vieu C, Bousseksou A (2007) Adv Mater 19:2163
220. Shekhah O, Roques N, Mugnaini V, Munuera C, Ocal C, Veciana J, Wöll C (2008) Langmuir 24:6640
221. Lehn J-M (1995) Supramolecular chemistry: concepts and perspectives. VCH, New York
222. Leininger S, Olenyuk B, Stang PJ (2000) Chem Rev 100:853
223. Gianneschi NC, Masar MS III, Mirkin CA (2005) Acc Chem Res 38:825
224. Ono K, Yoshisawa M, Kato T, Watanabe K, Fujita M (2007) Angew Chem Int Ed 46:1803
225. Kuehl CJ, Kryschenko YK, Radhakrishnan U, Seidel SR, Huang SD, Stang PJ (2002) Proc Natl Acad Sci USA 99:4932
226. Yamanoi Y, Sakamoto Y, Kusukawa T, Fujita M, Sakamoto S, Yamaguchi K (2001) J Am Chem Soc 123:980
227. Fujita M, Oguro D, Miyazawa M, Oka H, Yamaguchi K, Ogura K (1995) Nature 378:469
228. Fujita M, Tominaga M, Hori H, Therrien B (2005) Acc Chem Res 38:371
229. Russel S, Seidel SR, Stang PJ (2002) Acc Chem Res 35:972
230. Beer PD, Gale PA (2001) Angew Chem Int Ed 40:486
231. Lützen A (2005) Angew Chem Int Ed 44:1000
232. Hof F, Rebek J Jr (2002) Proc Natl Acad Sci USA 99:4775
233. Pluth MD, Bergman RG, Raymond KN (2007) Science 316:85
234. Company A, Roques N, Güell M, Mugnaini V, Gómez L, Imaz I, Datcu A, Solà M, Luis JM, Veciana J, Ribas X, Costas M (2008) Dalton Trans 1769
235. Nakabayashi K, Ozaki Y, Kawano M, Fujita M (2008) Angew Chem Int Ed 47:2046
236. Harbuzaru BV, Corma A, Rey F, Atienzar P, Jordá JL, García H, Ananias D, Carlos DL, Rocha J (2008) Angew Chem Int Ed 47:1080
237. Liepold L, Anderson S, Willits D, Oltrogge L, Frank JA, Douglas T, Young M (2007) Magn Res Med 58:871
238. Rieter WJ, Taylor KLM, An H, Lin W, Lin W (2006) J Am Chem Soc 128:9024
239. Chelebaeva E, Guari Y, Larionova J, Trifonov A, Guérin C (2008) Chem Mater 20:1367
240. Brinzei D, Catala L, Mathonière C, Wernsdorfer W, Gloter A, Stephan O, Mallah T (2007) J Am Chem Soc 129:3778
241. Imaz I, Maspoch D, Rodríguez-Blanco C, Pérez-Falcón JM, Campo J, Ruiz-Molina D (2008) Angew Chem Int Ed 47:1857
242. Imaz I, Luis F, Carbonera C, Ruiz-Molina D, Maspoch D (2008) Chem Commun 1202
243. Forestier T, Mornet S, Daro N, Nishihara T, Mourib S-I, Tanaka K, Létard J-F (2008) Chem Commun 36:4327
244. Volatron F, Catala L, Rivière E, Gloter A, Stéphan O, Mallah T (2008) Inorg Chem 47:6584
245. Chem Soc Rev (2009) 38: Metal–organic frameworks issue – Reviewing the latest developments across the interdisciplinary area of metal–organic frameworks from an academic and industrial perspective

Index